Towards a cell-based chemo receiver for artificial insect olfaction

By

SANJU THOMAS

School of Engineering

UNIVERSITY OF WARWICK

A thesis submitted to the University of Warwick
for the degree of Doctor of Philosophy

July 2017

To my wife Babitha, children Christina and Joseph for their endless love, support and encouragement.

Table of Contents

List of Figures

List of Tables

Acknowledgment

First and foremost I thank my God and Saviour ***Jesus Christ*** for giving me the ability, strength, motivation and each and everything required to accomplish this great task.

I express my greatest sense of gratitude to my academic supervisor Professor Julian Gardner who has been my beacon light and motivator throughout the metamorphosis of this dissertation. He had confidence in me when I doubted myself, and brought out the good ideas in me. It is my great pleasure to have such a great personality as my guide. I extend my sincere gratitude towards Dr. Marina Cole for her constant help and guidance throughout my project. She deserves many thanks for her continuous support during my study. I would also like to acknowledge the EPSRC for providing me the Doctoral Training Grant during my study.

I would like to thank Dr. Zolton Racz for his advice and support over the course of this research. I am grateful to the staff at the *Microelectronic Support Centre, STFC Rutherford Appleton Laboratory* for their assistance and support in the design and debugging of the CMOS ASIC chip. I am also grateful to all of my friends and colleagues at the *Microsensors and Bioelectronics Laboratory, University of Warwick* including Geraint Rhys Jones, Farah H. Villa-López, Tim Vincent, Dr Barbara Urasinska-Wojcik, Dr Guangfen Wei, and my old colleagues including Yang Jian, Dr Prasanta Guha, Dr Shrey Pathak and Dr Foysol Choudhary for their help and stimulating exchanges of ideas. I would particularly like to thank Mr F. T. Courtney and Mr Ian Griffith for all their assistance in the technical matters throughout the duration of my study.

I remember my dear mother late Mercy Thomas, and sincerely thank my father Thomas K. Ipe who have been an inspiration for me throughout my life. I am also grateful to my brothers Sabin, Tony and my cousin Sherin for the constant encouragement, moral and financial support rendered enormously throughout my course to support my family. Profound respect and thanks to my Pastor S. Manithottam and all other church members for their constant prayer and fellowship supports. Finally, I am in short of words for the immeasurable support and patience of my wife Babitha and my children Christina and Joseph, without which I would not have been able to achieve this. Especially I thank her for the encouragement and motivation she gave during my tough times and for supporting me both financially and spiritually. I would like to express my great appreciation to what she did.

Declaration

The work described in this thesis was conducted by the author according to the university regulations for the degree of Doctor of Philosophy, except where stated otherwise, in the School of Engineering, University of Warwick. This thesis has not been previously submitted in any previous application for any degree. The following are the list of sections with contributions from partners and collaborators.

Section 3.7:	*Design of SAW resonators used in this thesis were performed by Shrey Pathak, University of Warwick.*
Section 4.3.3:	*Experiments performed by Jian Yang, University of Warwick.*
Chapter 5:	*Experiments performed at the Department of Cell Physiology and Pharmacology, University of Leicester, UK in collaboration with Dr. Melissa Jordan.*
Section 6.3:	*Design of SMR sensor performed by Farah H. Villa-López, as part of an EU Project 'Multisensor Platform'. University of Warwick.*

Parts of the work have been presented at international conferences and published in the scientific literatures listed on the next page and reproduced in Appendix D.

List of Author Publications

Peer-reviewed Journal articles:

- W. Xuan, M. Cole, J. W. Gardner, S. Thomas, X. Wang, S. Dong, and J. Luo, "*A film bulk acoustic resonator oscillator based humidity sensor with graphene oxide as the sensitive layer*," J. Micromechanics Microengineering, vol. 27, no. 5, p. 8, 2017.
- F. H. Villa-López, G. Rughoobur, S. Thomas, A. J. Flewitt, M. Cole, and J. W. Gardner, "*Design and modelling of solidly mounted resonators for low-cost particle sensing*," Meas. Sci. Technol., vol. 27, no. 2, p. 25101, 2016.
- S. Thomas, F. Villa-Lopez, J. Theunis, J. Peters, M. Cole, and J. Gardner, "*Particle sensor system using Solidly Mounted Resonators*," IEEE Sens. J., vol. 16, no. 8, pp. 2282–2289, 2015.
- S. Thomas, M. Cole, F. V. Lopez and J. W. Gardner. 2015. "*High frequency surface acoustic wave resonator-based sensor for particulate matter detection*" Sensors and Actuators A: Physical, 244: 138–145. doi:10.1016/j.sna.2016.04.003.

Conference articles:

- S. Thomas, F. V. Lopez, J.W. Gardner, M. Cole, J. Peters and J. Theunis, "*A low-cost acoustic microsensor based system-in-package for air quality monitoring*," IEEE Sensors Conference 2016, 31 Oct-2 Nov, Orlando, USA.
- S. Thomas, M. Cole, A. De Luca, F. Torrisi, A.C. Ferrari, F. Udrea, J.W. Gardner, "*Graphene-coated Rayleigh SAW Resonators for NO_2 Detection*," EuroSensors Conference 2014, September 7-10, Brescia, Italy.
- F.H. Villa-Lopez, S. Thomas, W. Ludurczak, M. Cole and J.W. Gardner, "*Finite Element Modelling of Particle Sensors based on Solidly Mounted Resonators*," IEEE Sensors Conference 2014, November 2-5, Barcelona, Spain.
- S. Thomas, F.H. Villa-Lopez, W. Ludurczak, M. Cole and J.W. Gardner, "*Design, Modelling and Development of Low Cost High Frequency Piezoelectric Particle Sensor*," The Symposium B at E-MRS 2014 Spring Meeting, May 26-30, Lille, France.

- S. Thomas, M. Cole and J.W. Gardner, "*Particulate matter detection based on Acoustic Resonators for air-quality monitoring*", COST Action TD1105- New Sensing Technologies for Air-Pollution Control and Environmental Sustainability 2nd Scientific Meeting, 18-20 December 2013, Cambridge, UK.
- S. Thomas, M. Cole, Z. Rácz, J.W. Gardner, "*Dual High-Frequency Surface Acoustic Wave Resonator for Ultrafine Particle Sensing*," The 12th Annual IEEE Conference on Sensors, November 4-6, 2013, Baltimore, USA.
- S. Thomas, M. Cole, J.W. Gardner, "*High-frequency One-port Colpitts SAW Oscillator for Chemical Sensing*," The 6th International Conference on Advances in Circuits, Electronics and Micro-electronics, August 25-31, 2013, Barcelona, Spain.
- M. Cole, S. Thomas, Z. Rácz, J.W. Gardner, M. Jordan and R.A.J. Challis, "*Cell-based surface acoustic wave sensor with transfected olfactory receptors OR67d and OR22a for a highly specific chemo-receiver*," 22nd Anniversary World Congress on Biosensors, 15-18 May 2012, Cancun, Mexico.
- S. Thomas, S.L.T. Leong, Z. Rácz, M. Cole, and J.W. Gardner, "*Design and Implementation of a High-Frequency Surface Acoustic Wave Sensor Array for Pheromone Detection in an Insect-inspired Infochemical Communication System*," The 14th International Meeting on Chemical Sensors, May 20- 23, 2012, Nurnberg, Germany.
- M.F. Chowdhury, Z. Rácz, S. Thomas, M. Cole and J.W. Gardner, "*ASIC for Hybrid Biosynthetic Infochemical Chemoreceiver*," The 10th Annual IEEE Conference on Sensors, October 28-31, 2011, Limerick, Ireland.

Abstract

Infochemical communication is ubiquitous amongst all living organisms, and particularly important in insects. Because smell being the most common basic means of chemical communication, infochemical blends must be constantly decoded in order to proclaim their readiness to mate, to mark out territorial boundaries, to warn off intruders and predators or, in some cases, to locate food or predators with millisecond precision. The central challenge of the thesis was to mimic nature in both cellular and molecular levels on to a technological platform that aids in the development of a new class of technology employing chemicals alone to communicate over space and time.

This thesis describes a body of work conducted in the development of a miniaturised, smart and label-free cell-based chemoreceiver for artificial insect olfaction, as part of the development of a novel biomimetic infochemical communication system. A surface acoustic wave based microsensor has been utilized to engineer and develop a chemoreceiver system that mimics the cellular and molecular mechanisms occurring during infochemical detection and decoding in insects. Successful recovery of ratiometric information with the aid of polymer-based gas-phase measurements, established the concept of chemical communication. Thus, small scale, high-throughput infochemical communication has been realized by a combination of precise spatiotemporal signal generation using fruit volatiles and insect sex pheromones with highly sensitive detection and signal processing. This was followed by the investigation of the feasibility of using the prototype cell-based biosensor system in a static mode for artificial insect olfaction applications, mimicking the cellular detection in the receptor/antenna apparatus of insects. Finally, as part of the development of a compact and low-power portable chemoreceiver system, the discrete sensor drive and interface circuitry was deployed in an analogue VLSI chip, thereby overcoming the associated measurement complexity and equipment cost, in addition to extending the reach and functionality of point of use technologies.

List of Abbreviations

Abbreviations	Definition
AlN	Aluminium nitride
BAW	Bulk acoustic wave
CMOS	Complementary metal oxide semiconductor
FBAR	Film Bulk acoustic resonator
FPW	Flexural plate wave
GHz	Giga hertz
HPSW	Horizontally polarized shear waves
IC	Integrated Circuit
IDT	Inter digital transducer
IF	Intermediate Frequency
$LiNbO_3$	Lithium Niobate
$LiTaO_3$	Lithium tantalite
LNA	Low noise amplifier
LO	Local Oscillator
LPF	Low pass filter
MEMS	Micro electro mechanical systems
MHz	Mega hertz
Mo	Molybdenum
MOSFET	Metal-Oxide-Semiconductor Field-Effect Transistor
NMOS	n-channel Metal-Oxide-Semiconductor
PCB	Printed circuit board
PDMS	Polydimethylsiloxane
PID	proportional-integral-derivative
PMOS	p-channel Metal-Oxide-Semiconductor
QCM	Quartz crystal microbalance
RF	Radio frequency
R-SAW	Rayleigh surface acoustic wave
SAW	Surface acoustic wave
SAWR	Surface acoustic wave Resonator
SH-APM	Shear-horizontal acoustic plate mode

SH-SAW	Shear horizontal surface acoustic wave
SiO_2	Silicon dioxide
SIP	System-in-package
SMR	Solidly mounted resonator
SV	Shear vertical
TSM	Thickness shear mode
ZnO	Zinc oxide
µm	micro meter

CHAPTER 1

Introduction

The purpose of this first chapter is to introduce the concept of biosynthetic infochemical communication systems upon which the work presented in this thesis has been carried out. This chapter introduces the reader to the field of insect olfaction and chemical communication, detailing how information is transferred between insect species with the help of semiochemicals. The chapter also reviews the chemical sensors based on piezoelectric microsensors and exhibits how Surface Acoustic Wave Resonator (SAWR) and Film Bulk Acoustic Resonator (FBAR) micro sensors have been employed in the area along with their different applications. Next, a brief account of olfactory biosensors (e-tongues) and electronic noses will be given, discussing the technology, current devices, and their applications. Thereafter the aims and objectives of this work presented here have been introduced and the chapter concludes by outlining the structural flow to the thesis.

1.1 Insect-Inspired Communication System

The principal objective of the infochemical communication system is to develop functional equivalents of the cellular, subcellular and molecular machinery that mimic the pathway between pheromone production and detection in insects. This will form the foundation of a new branch of information technology employing chemicals to communicate over space and time. Figure 1.1(a) shows the basic concept and biological inspiration behind the novel infochemical communication technology. The pathways between pheromone production, release and detection in an insect, namely the moth *Spodoptera littoralis*, served as biological blueprints for the development of the artificial biosynthetic modules of the molecular, subcellular and cellular machinery to form the first infochemical communication prototype system [1]. The chemoemitter module shown in Figure 1.1(b) biosynthesise the pheromone components from a common precursor fatty acid (18:CoA) based upon known enzymatic activity within the exocrine system of the moth including chain shortening, desaturation, and functional group modification, within a microreactor. The ratiometric infochemical cues can be programmed through mass flow control and an almost limitless diversity of ligands could be created based on the hierarchy of biosynthetic modules. The volatile infochemical blend is released into the external environment by thermal evaporation. Furthermore, the transmission of time-sensitive and time-registered information is possible by controlling the volatility of the ratiometric compounds. Chemoreception is carried out based on the signalling from transmembrane-domain receptors that are transduced by acousto-electric sensors. The highly specific signals (blend ratios) are processed in a ratiometric neuronal model based on the antennal lobe of moth.

The chemoreceiver module shown in Figure 1.1(b) employing acoustic microsensors, acts as a tuned detector of the emitted volatile chemical mixture capable of recovering the *ratiometrically* encoded information using either complementary olfactory receptors or selective polymer components in the cellular and sub cellular

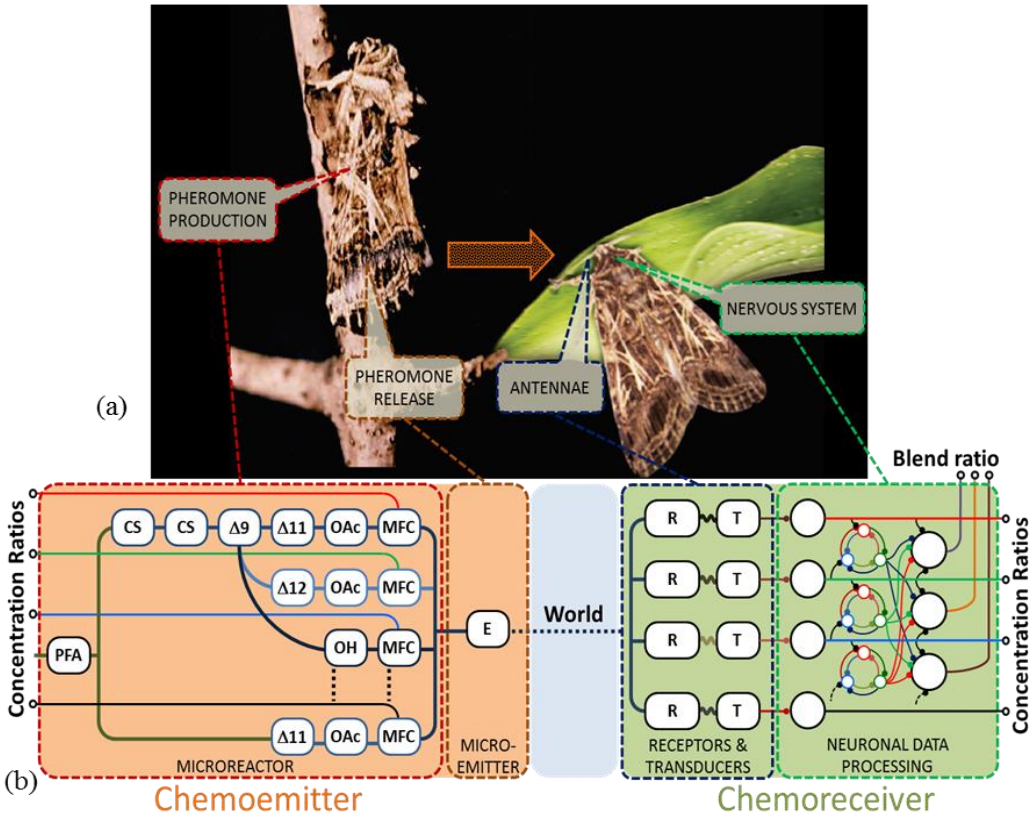

Figure 1.1. (a) A schematic diagram showing the relation between the primary biological components of the pheromone-based insect communication (b) Corresponding bio-inspired modules that form a possible configuration of a biosynthetic infochemical communication system with a chemoemitter and chemoreceiver. Adapted from [192].

level, acousto-electric transduction and a data processing architecture. Its operation simulates the molecular detection in the antennae of insects and the neuromorphic signal processing in the antennal lobe.

This state-of-the-art modular chemoemitter-receiver arrangement, as a unified system, is capable of *infochemical communication* and can serve as the foundation of a new scientific field for labelling, information transmission and biochemical interfacing with possible applications in automatic identification and data capture, product labelling, search and rescue, air silent communication, medical diagnosis and environmental monitoring.

1.2 Mechanism of insect olfaction

Odour information is known to be of vital significance for most animals, especially for insects as they are heavily involved in location and quality determination

of conspecific mates, food and oviposition sites, organize colonies and divide labour. These complex and diverse volatile semiochemicals are detected and identified by the eusocial insects with the help of extremely sophisticated biological systems called olfactory receptor neurons, which are embedded in the hair-like chemosensory sensilla located on the antennae. A synchronous action of the pheromone receptors is essential for the recognition of a broad range of chemicals, allowing the matching of a diversity of chemical odorants. The key specificity in the response to pheromone molecules is due to the specificity of the ligand binding olfactory receptors (ORs) which are responsible for sensing odour molecules, forming the largest G protein-coupled receptor (GPCR) family in mammalian animals. The inherent specificity and sensitivity of ORs makes them major candidates as biological detectors of volatile ligands, which can mimic the sensitivity and specificity of insect olfaction. Thousands of distinct odorants can be recognised and discriminated by the olfactory systems with extreme high sensitivity and specificity through a large family of proteins encoded by olfactory receptor genes.

Even though precise mechanisms of insect olfactory signal transduction remain unclear, there is broad consensus that olfactory signalling in all animals uses canonical G-protein- coupled receptors that activates signal transduction pathways [2]. Insects are equipped with two pairs of olfactory organs, the antennae and maxillary palps, which are decorated with thousands of olfactory hairs called sensilla, each of which may house one or more Olfactory Sensory Neurons (OSN). Research in vertebrate olfactory system has identified that odours stimulate adenylate cyclase activity [3], [4], which led to the subsequent identification of $G_{\alpha}s$ protein [5] and later to the discovery of a distinct variety of genes encrypting seven transmembrane domain G-protein-coupled odorant receptors [6]. In all animals, these ORs signals the identity and quantity of the odorant cues by inducing electrical activity in the primary OSN and encoding information regarding the stimulus that is then relayed to olfactory processing centres in the brain.

The cellular and molecular machinery for olfactory transduction of odorant molecules is located in the olfactory receptor neuron dendrite membrane surface encapsulated in sensilla within sensory hairs [7]. OSN axons in the insect tissue antennae expressing the same odorant receptor converge through specific glomeruli in the primary olfactory centre and transduce the neural signal to the antennal lobe [8].

Literature contains conflicting models of insect olfactory receptor signal transduction claiming that insect odorant receptors are G-protein–coupled receptors [9] or odour-gated ion channels [10]. According to Sato et al. [10], insect ORs form ligand-gated cation channels that are activated rapidly by odours in the absence of G-protein signalling. In part agreeing with the above results, Wicher et al. [9] also revealed that the variable ORx subunit is a G-protein-coupled receptor and that OR83b is a cyclic nucleotide-gated ion channel.

An odorant-specific receptor protein ORx and the cation channel Or83b that conducts the cations Na^+, K^+ and Ca^{2+} form the insect odorant receptor complex that is responsible for olfactory signal transduction. When stimulated by an odorant, ORx activates the channel protein Or83b by triggering two pathways, a fast and short ionotropic pathway and a slow and long-lasting metabotropic pathway. A fast and transient ion conductance is initiated by the direct activation of Or83b by ORx. The metabotropic pathway involves the activation of Gs protein by ORx. The Gs subunit in turn stimulates adenylyl cyclase activity, thereby increasing the production of intracellular cAMP from ATP, which in turn slowly activates a prolonged non-selective cation conductance through the Or83b. Opening of the Or83b channel permits Na^+ and Ca^{2+} (mostly Ca^{2+}) influx resulting in membrane depolarization. Rapid recognition of high odour concentrations is ensured by the ionotropic pathway while the metabotropic pathway allows highly sensitive odour detection with the help of Gs subunit. The Figure 1.2 shows the schematic model of insect OR signal transduction in which an odorant-specific receptor ORx is a G-protein coupled receptor responsible for metabotropic pathway and OR83b is a cyclic nucleotide-gated ion channel.

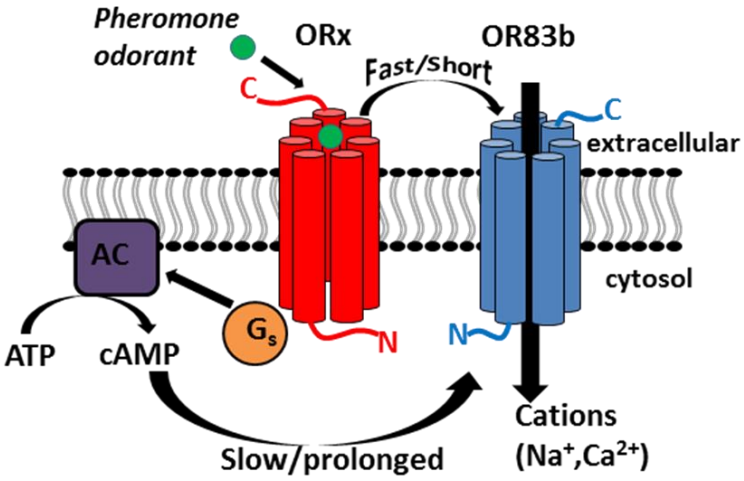

Figure 1.2. The proposed mechanism of olfactory receptor signal transduction. Adapted from [11], [12]

1.3 Piezoelectric microsensors as chemical sensors

In process analytical technology, novel chemical sensors and micro sensors are being developed to quantify a variety of biological processes including gas and vapour detection as well as sensing species in liquids or solutions. The selectivity of these chemical sensors are enhanced by the unique application of selective coatings, such as polymers or enzymes or living cells, used to detect or monitor analytes. Sensors of this type include those of the piezoelectric nature including FBARs, SAWRs, Quartz Crystal Microbalance (QCM) and also those of solid-state origin including ChemFETs, Schottky diodes and chemiresistors [13]. Amongst the various types of sensors available, piezoelectric devices such as surface acoustic wave (SAW) devices (Rayleigh surface acoustic wave (R-SAW), Shear Horizontal surface acoustic wave (SH-SAW), and Flexural Plate Wave (FPW)) [14]–[20] and bulk acoustic wave devices (QCM, Shear Horizontal Acoustic Plate Mode (SH-APM), FBAR) [21]–[24] have been used extensively [25], as they exhibit high sensitivity in mass deposition [26], in addition to the advantages including versatility and reliability [27].

Piezoelectric acoustic sensors provide a direct transduction mechanism to convert the measured physical parameter that is in the form of mechanical strain, into electrical charge variations. Most acoustic wave resonators can be used as sensors, as they are sensitive to mechanical, chemical, or electrical perturbations occurring on the device surface [28]. They can detect not only mass/density changes, but also viscosity

and/or viscoelastic changes [29]–[31], elastic modulus, conductivity and dielectric properties and have been widely used for applications like monitoring of pressure, moisture, temperature, force, acceleration, shock, viscosity, flow, pH levels, ionic contaminants, odour, radiation and electric fields [27], [32], [33]. Acoustic devices have been found to function efficiently to monitor acousto-electric interactions at the solid-liquid interface where the device surface has been derivatised with specific ligands capable of binding species from solution [34], thus forming a highly sensitive biological sensor. As a result, acoustic wave based biosensors have also been extensively used to detect the traces of biomolecules [35]–[39] such as DNA, proteins (enzymes, antibodies, and receptors), cells and tissue (microorganisms, animal and plant cells, cancer cells etc.), biochemical substances or viruses [27].

The quartz crystal microbalance (QCM) which can operate in fluids, offers the possibility to successfully characterize biomolecular systems in their natural aqueous environment [40]. Recent research has shown that QCMs can be used as an electronic nose [41] and as an affinity immunosensor [42]. QCM based biosensor systems have become a suitable tool for in situ measurements in biofluids, particularly, for on-line detection of immunological reactions [43], [44], for surface bioelectrochemistry of redox enzymes [45], adsorption of proteins, and adhesion of vesicles and living cell [26], [46]–[49]. Even though QCMs were the first and the most commonly employed piezoelectric devices especially for biosensing applications, a major drawback is the lack of selectivity since there is no discrimination between the source of the mass changes [25]. In addition, other complications related to QCM biosensors include reduced mass detection limit due to the low operating frequency (range of 5–30MHz), large base-mass due to a thick substrate (0.5–1mm) and large surface area (>1cm^2) which is not easily scalable, resulting in increased cost of fabrication [27]. However, SAW devices and the recently emerged FBAR devices proved to have higher efficiency than their QCM counterpart, as their active layer is about one order of magnitude smaller than that of the QCM, which allows them to operate at higher frequencies and improved sensitivities.

1.3.1 SAWR micro sensors

Initially, surface acoustic wave devices found their applications in electronics and communications industry where they were used as filters and resonators. Lately, they have called the attention of the scientific researchers in biosensing applications [50]. Confinement of acoustic energy in their surface layer of about one wavelength [27], allowed the SAW devices to operate at higher frequencies and hence higher sensitivities than typical QCM biosensors. The surface acoustic wave is generated by the centrally placed inter-digital transducers (IDTs) and reflected by reflector strips fabricated on both sides of the IDTs, and create a standing wave pattern with a distinct resonant peak, thereby reducing the acoustic losses of the device. Figure 1.3 shows the schematic representation of a SAW biosensor functionalised with cells. Selective binding of ligands with the biomarker molecules generate mass change in the path of the travelling wave, resulting in velocity change of the acoustic wave and consequently shifts the SAW resonant frequency. Thus, the resulting perturbation in the acoustic wave propagation on the surface of a piezoelectric crystal is mainly caused by the mechanical parameters of the layer, electrical parameters and the associated atmospheric parameters.

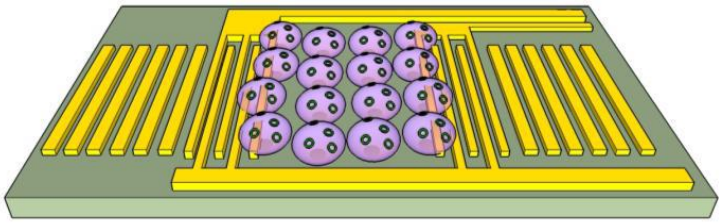

Figure 1.3. The schematic of a cell-coated SAW biosensor

In general, the frequency response of a SAW resonator depends upon the mass density ρ, viscosity η, conductivity σ, and dielectric permittivity ε, of the medium in addition to the temperature, pressure and humidity variations [51]. Hence a change in the frequency can be associated with one of these dependent variables. A dual SAWR sensor arrangement [52] produces a differential frequency output, ameliorating the common mode variations including atmospheric changes like temperature, pressure and humidity [53]. Another advantage of using a dual sensor system is the reduction

of the measured signal frequency from the MHz range to kHz range, which is of essential importance from the view point of removing high frequency noise from the system. Resonant Rayleigh SAW-based sensors, have been used to detect chemical and biological molecules such as volatile organic compounds (VOCs) [47], CO_2 [48], humidity [48], ammonia [49], biomolecules such as proteins, DNA, drugs [35], [50]–[52] and pathogens [53]. Rayleigh SAW devices function well in gaseous or vacuum environments. However, when integrated in microfluidic systems, significant acoustic energy gets dissipated into the liquid causing significant attenuation and hence poor sensitivity and noise which impedes them from liquid sensing applications. Hence, shear-horizontal (SH)-SAW resonators benefitting from transverse displacements polarized parallel to the surface, have the advantage of lower energy loss in liquids [54]. The first SH SAW immunosensor based on $LiTaO_3$ was presented by Rapp et al. in 1993 [55]. Similar to SH-SAW resonators, thickness shear resonators (TSRs), Flexural Plate Wave, shear horizontal Acoustic Plate Mode (SH-APM) and STW-based sensors have also demonstrated better mass sensitivity in liquid biosensing applications where traditional Rayleigh SAW sensors are inappropriate [56].

1.3.2 FBAR micro sensors

A newly emerged but promising bulk acoustic wave resonator structure for highly sensitive biochemical detection is the film bulk acoustic resonator (FBAR) device, initially demonstrated by Lakin and Wang in 1981. An FBAR sensor is MEMS fabricated with sub-micrometer thick piezoelectric films of ZnO or AlN, sandwiched between two metallic electrodes. This device is fabricated on the top of a carrying substrate like silicon, and the acoustic layer and electrodes are fabricated on its top, as sketched in Figure 1.4. FBARs can be used as bio-chemical sensors, in which the mass adsorbed or deposited on the resonator surface, induces a frequency change that can be measured. FBARs can be used as high-Q resonators, essential for highly sensitive micro mass detection. The much-reduced thickness of the piezoelectric film allows the FBAR to operate at a high frequency, up to a few GHz [27], which is about a hundred times higher than QCMs, making it a promising candidate for nanotechnology operation. FBARs are found to be an ideal candidate for gravimetric biochemical measurements in air and liquids, constituting a cheap, disposable and highly integrated

sensor arrays, exhibiting high mass sensitivity and higher operating frequencies. Lower production costs, smaller size, higher sensitivity and multiplexed biomolecule detection are some of the advantages of FBARs over other types of biosensors [57]. The principle of operation of an FBAR biosensor is the change in resonant frequency caused by the resonator mass loading [58], and is the same as that of QCM, except the fact that the device dimensions are at least two orders of magnitude smaller.

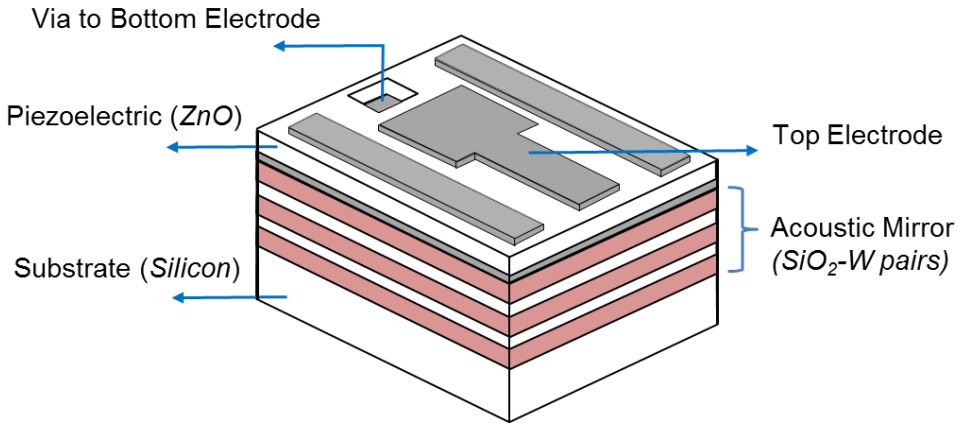

Figure 1.4. The schematic of an FBAR-SMR sensor

Shear mode FBARs are excellent candidates for liquid sensing applications. The temperature compensated second harmonic shear mode is having many advantages such as higher *Q* value in liquids, higher frequency of operation and higher resolution for sensor applications, in comparison with the fundamental shear mode. For an AlN based FBAR, perfect c-axis orientated thin films are grown for a promising excitation in the longitudinal thickness mode. Recently, FBARs with c-axis-inclined AlN and ZnO, working on the principle of thickness-excited shear mode exhibiting high sensitivity, behaving as chemical and biochemical sensors for liquid operation has been reported [59]. Weber et al. (2005) made the very first FBAR biosensor system used in the binding of antibody–antigen in liquid medium and it was found that the sensor performance was much better than that of QCMs [21]. FBAR based label-free biosensors are used in a wide range of applications such as gene sequence analysis, gene profiling and mutation studies, virus and bacteria detection, clinical diagnostics, drug discovery, and counter bioterrorism [60].

1.4 Electronic noses, tongues and their applications

The odour and taste of end products manufactured in the food, beverage, pharmaceutical and personal care industries can be of vital importance for the successful marketing of a product. Ideally these analysis should be carried out by human experts in the field. In practice, this has found to be quite expensive and problematic in several areas. Thus electronic noses and tongues have been developed, based on a combination of sensitive sensors and sophisticated software, operating in a way analogous to the way humans perceive odours and tastes, providing real time solutions for obtaining reliable taste and odour measurement.

Electronic nose and electronic tongues examine different aspects of the sensory perception. The E-nose processes volatile components of aroma/odour while the e-tongue measures dissolved organic and inorganic components (i.e. non-volatile molecules) that remain in the food/beverage. Some of the attributes measured by E-noses include floral, mouldy, estery, acetaldehyde, hoppy and so on, while E-tongue sensors detect all chemical species present directly in a liquid sample [61]. These electronic systems are not only more rapid and objective than human based tasting panels and classical analytical methods such as High-performance liquid chromatography (HPLC) and Gas chromatography–mass spectrometry (GC-MS) instruments, but also they are much more responsive to routine use as in quality control applications. The various types of sensor array inside an e-nose include metal oxide semiconductor (MOX) sensors, conducting polymer sensors, optical sensors, and piezoelectric sensors. The most commonly used sensor array in the design of e-tongues include electrochemical (potentiometric, voltammetric, amperometric, impedimetric, and conductimetric), optical, mass, and enzymatic biosensors [62].

Several biosensors based on electrochemical, calorimetric, optical and electro-acoustic devices utilize olfactory receptors, olfactory neurons, and odorant binding proteins (OBP) as probes due to their adaptable sensitivities. A SAW resonator based "bio-electronic nose" that mimics the biological olfactory system, having the capability to identify odorant molecules with high sensitivity and specificity, overcomes the low-selectivity of the well-known electronic noses reported in the literature [63]. The first report of a flavour sensing system comprising both a so-called

"electronic tongue" based on SH-SAW sensors analysing the liquid phase and a so-called "electronic nose" based on chemFET sensors analysing the gaseous phase has been done by Cole et al. [64]. A 60 MHz dual SH-SAW delay-line based electronic tongue was developed to differentiate the basic tastes of sour, salt, bitter, and sweet, which was placed within a miniature PTFE housing containing the test solution. Without the need for a selective biological or chemical coating, it was possible to correctly classify all the tastes [65]. Natalie et al. demonstrated a combined multisensor system, utilizing sensors operating in liquid (electronic tongue) and in the head space (electronic nose) based on the same sensitive materials: the metalloporphyrins, in order to get chemical information from liquid samples through the analysis of the solution and its head space [41].

1.5 Research objectives

The main objective of the project is to investigate the suitability of high frequency surface acoustic wave sensors to act as a highly specific chemoreceiver for the detection of a wide variety of biochemical reactions. The cell-based biosensor used for artificial insect olfaction applications mimics the cellular detection in the receptor/antenna apparatus of insects. Further sensor signal processing could mimic the neuromorphic signal processing in the insect's antennal lobe and in turn can form a part of an innovative system capable of infochemical communication and can serve as the foundation of a new technological field for labeling, information transmission and biochemical interfacing. The aims of the project are summarized below:

- Development of a novel info-chemical communication system based upon an array of surface acoustic wave resonator sensors employing uniquely ratiometrically encoded chemical signals.
- Demonstrate the encoding, transmission, and decoding of ratiometric information based upon binary mixtures of volatile info chemicals including fruit volatiles and insect pheromones through the recovery of blend ratios by obtaining a classification of chemical ratios, rather than individual components.

- The development of a novel dual surface acoustic wave based whole cell sensor system utilizing transfected ORs, Or22a and Or67d with an automated microfluidic ligand delivery system.
- Determine the possibility to deposit and attach live Sf9 cell lines on to the SAWR sensors to act as a functionalized bio-layer for the detection of specific ligands and to detect the change in intra-cellular calcium levels when the ligand binds to the receptors.
- The design and development of an application-specific integrated circuit (ASIC) for the integration of the olfactory sensor drive, control and interface circuitry using CMOS 0.35µm process, as part of the development of a compact and low-power portable chemoreceiver system.

1.6 Outline of the thesis

The first chapter introduced the concept of biosynthetic infochemical communication system and reviewed the mechanism of insect olfactory signal transduction. A review of piezoelectric microsensors used in chemical sensing including the SAWR microsensors and FBAR microsensors was also presented. The aims and objectives of this thesis have also been presented. Chapter 2 reviews in more detail many of the background technologies used in the project. This includes the fundamental theory of acoustic waves, basic principles of operation of both surface and bulk acoustic waves and their application in biochemical sensing. Furthermore an overview of different acoustic resonator based microsensors is discussed along with the sensing mechanisms.

Chapter 3 describes the design of Rayleigh-SAWR gas sensors and SH-SAWR liquid sensors that are needed for the biochemical detection. This details the operational principle of the microsensor using the equivalent circuit model, system configuration, oscillator circuit design and concepts followed to produce a working design. Chapter 4 discusses the ratiometric infochemical communication system based on polymer-coated surface acoustic wave microsensors. This chapter includes the infochemical communication system setup, ratiometrc signal generation and finally ligand detection of fruit volatiles and insect pheromones. The SH-SAW devices as a high specificity biosensing system with transfected olfactory receptors are described

in chapter 5. The microfluidic system setup and details of all the experimental conditions used are also presented. This is followed by a description of cell deposition and attachment on to the sensor surface and heterologous expression of olfactory receptors. The chapter concludes by an analysis and discussion of the results obtained from the ligand elicited response of olfactory receptors.

Chapter 6 describes the design of the CMOS oscillator for Acoustic resonators using the AMS 0.35 μm standard CMOS process and also outlines the System-in-a-Package implementation of the ASIC SMR sensor. The chapter details the theory, design, layout and simulations of the ASIC chip that has been specifically designed for the 960 MHz solidly mounted resonator sensor. This chapter also includes the characterization of the ASIC oscillator chip, results and discussion of the hybrid sensor system. Chapter 7 concludes the thesis by discussion on how the results have contributed towards the fulfilment of the aims of the project. Lastly, in further work, the latest developments in utilizing surface acoustic wave sensors for ultrafine particle detection for environmental monitoring are presented and possible advancements for liquid phase detection with different cell types for specific applications proposed.

CHAPTER 2

Acoustic waves and resonators: A review

2.1 Introduction

The purpose of this chapter is to introduce the fundamental concepts and properties of acoustic waves as well as their electrical excitation and detection in piezoelectric materials. The basic theory of acoustic waves along with the mathematical model is emphasized in the discussion. Next, a brief comparison between the surface acoustic waves (SAW) and the bulk acoustic waves (BAW) are given, and the various surface acoustic modes are reviewed and discussed. Lastly, an overview of the different types of acoustic resonators, discussing the liquid phase and

gas phase applications with emphasis on device principles and applications are also presented.

2.2 Historical background of acoustic waves

The history of discovery of piezoelectricity and the development of SAW devices is traced from the late 19th century. The first demonstration of the direct piezoelectric effect in quartz was in 1880 by the brothers Pierre Curie and Jacques Curie, when they confirmed that a mechanical deformation in the form of a weight when applied to a quartz crystal, developed a proportional electrical polarization within the crystal [66]. Following the work of the Curie brothers, Hankel suggested the term *piezoelectricity* for this phenomenon. Lippmann predicted the converse piezoelectric effect mathematically based on the fundamental thermodynamic principles and soon before the end of 1881, the Curie brothers demonstrated the existence of this inverse effect [67]. The work was continued and established by Hankel, Lord Kelvin and particularly, Voigt who, in 1894, presented the significance of the crystal geometry, and how the piezoelectric phenomenon could be linked to the piezoelectric crystal atomic structures [68]. Lord Kelvin established a theory of piezoelectricity based on thermodynamic theories and Voigot developed a theory involving elastic vectors and elastic tensors and also published a book on the properties and theory of piezoelectricity [69] The existence of surface acoustic waves on the surface of solid materials exhibiting elasticity was confirmed by Lord Rayleigh in 1885 [51]. The first practical application of the piezoelectric effect was the development of echo-detectors for detecting compressional waves in seawater, developed during the First World War [70], by Langevin. Piezoelectric crystals are commonly used as filters, precision timers and resonators for frequency control in oscillator circuits, thereby playing a critical role in the communications and electronics industry. There are some materials, such as quartz which are naturally piezoelectric, even though others must be polarized in order to make them piezoelectric. During the polarization process, the temperature is elevated while concurrently applying an electric field across the sample, then cooling it down to room temperature with the electric field still applied. The material then displays piezoelectric behaviour.

2.2.1 Piezoelectric Effect

A piezoelectric is a material that develops a net electric polarization in response to an applied pressure and, conversely, develops a strain in response to an electric field. The piezoelectric effect can be demonstrated by the application of either a compressive or tensile stress to the opposite faces of a piezoelectric crystal (Figure 2.1). The asymmetric crystal lattice will get deformed by the applied stress, causing the separation of the centres of gravity of positive and negative charges. As a result of this effect, electrical charges appear on the surface of the electrodes. The generated electrical polarization is dependent not only on the amplitude, but also the direction of the applied stress [71]. Removal of the force releases the strain within the crystal lattice causing the flow of charge, and recreating a zero potential difference between the electrodes. By applying a sinusoidal stress to the opposite faces of a piezoelectric crystal, a sinusoidal piezoelectric voltage is produced between the electrodes, thereby producing electrical energy from mechanical energy [68]. Materials exhibiting this direct piezoelectric effect always exhibit the reverse effect as well, whereby the application of an electrical field creates a mechanical deformation in the crystal, which is proportional to the applied voltage [72]. Hence these crystals are effectively piezoelectric micro actuators. The crystal structure must possess a certain crystallographic asymmetry, for the existence of piezoelectricity.

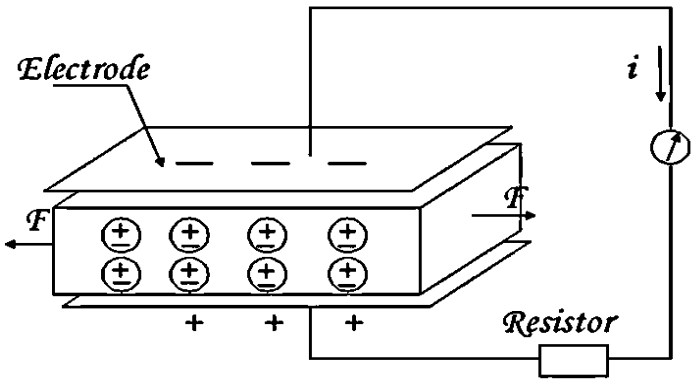

Figure 2.1. Conversion of mechanical energy into electrical energy by piezoelectric effect

Some of the important properties of piezoelectric crystals include: (i) Ideal coupling between the electric circuit and the crystal properties, ensuring that the mechanical wave frequency is equal to the electrical frequency, providing a distortion-

free interface. (ii) Possibility of different crystal cuts with different angles owing to the anisotropic nature of these crystals, providing a range of operating frequencies. (iii) Ability to produce acoustic waves of various types including compressional and shear waves, by varying the angle of propagation [68].

2.2.2 Applications of piezoelectricity

There are several areas where the piezoelectric devices have been utilized for practical and commercial applications. The advantages of piezoelectricity arise from: (i) the conversion of mechanical stress to an electrical signal; (ii) strain generation by an electric signal; (iii) Elastic wave development and detection; (iv) processing and storage of electrical pulses by elastic waves; (v) the existence of electromechanical resonances. Piezoelectric devices could be characterised as follows: *(a) Low frequency devices:* force sensors and transducers, accelerometers, position transducers, spark generators; *(b) Audio devices:* HV transformers, stereophonic pickups, stable oscillators, microphone heads, loudspeakers, audio tone generators; *(c) Radio Frequency Acoustic wave devices:* high-power ultrasonic generators, high-frequency ultrasonic devices, signal processors, resonators, filters, delay lines, electroacoustic devices and signal storage [66].

2.2.3 Inter-digital Transducers

Immense work has been carried out on SAWs since 1965, after White and Voltmer showed that acoustic waves could be generated by an Inter-digital Transducer (IDT), in which two metal comb-shaped electrodes placed on the surface of a piezoelectric substrate produced a field which generated elastic surface waves through a direct interaction. The IDT can be regarded as the cornerstone of SAW technology, according to Gardner et al. [68]. The Figure 2.2 shows a basic configuration of an IDT. The application of an alternating voltage '*V* ' on to the transducers, produces a stress wave that travels along the surface of the crystal in both the directions. In order to obtain constructive interference and in phase stress, the IDTs should work in the most efficient manner. This could be achieved only if the periodicity matches the

wavelength of the SAW occurring at $f = v_p / p$, in which v_p denotes the propagation velocity, f the associated frequency, known as synchronous frequency and p the distance between the IDTs, that is, the periodicity [73]. The transducer efficiency in converting electrical energy to acoustical, or vice versa, is maximised at the synchronous frequency.

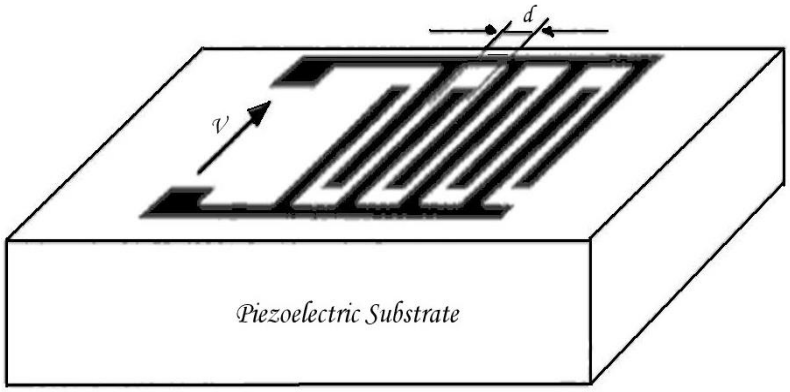

Figure 2.2. Basic IDT structure in a piezoelectric crystal

2.3 Fundamental Physics of Acoustic Waves

2.3.1 Acoustic waves in an elastic medium

Many different types of acoustic waves can propagate in solid materials, and here particular emphasis is given for surface waves. The waves that are generated in a solid is primarily dependant on both the properties of the solid and its boundary conditions. An elastic medium can be modelled as a distributed mass-spring system due to its two main properties including inertia and elasticity. As a result of the interplay of distributed elastic and inertial forces within a solid, an elastic wave is produced. Two types of elastic wave types occurring in solids including bulk longitudinal waves and bulk shear waves, are shown in Figures 2.3 (a) and (b), respectively.

Even in the case of an isotropic media, the phase velocities V_l and V_t for the longitudinal and shear waves respectively, are given by [2.1] and [2.2]

$$V_l = \sqrt{c_{11}/\rho} \qquad 2.1$$

$$V_t = \sqrt{c_{44}/\rho} \qquad 2.2$$

where c_{ij} is the stiffness constant and ρ is the mass density with the subscripts of *i*, *j*, and *k* being *x*, *y*, or *z*. Polarization of the longitudinal (compressional) wave is parallel to the propagation direction whereas that of a shear (transverse) wave is normal to the direction of wave propagation.

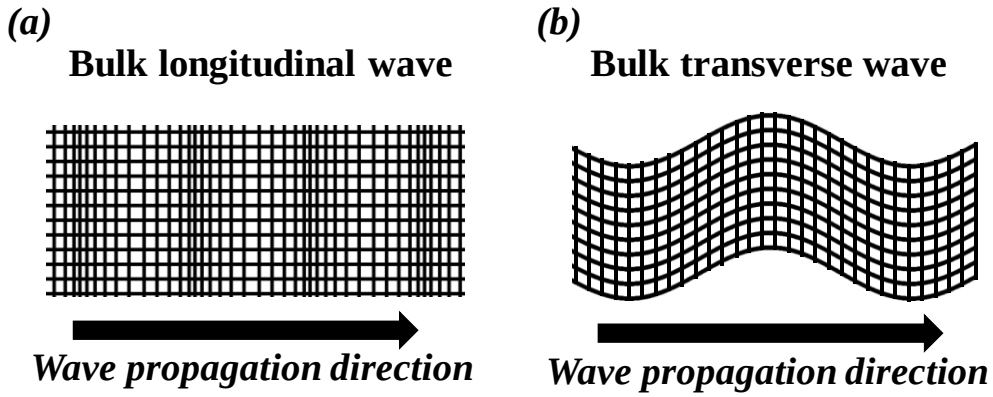

Figure 2.3. Schematic of different types of elastic waves in unbounded solids. (a) Longitudinal wave (b) Transverse wave

Factors including scattering losses due to inhomogeneity in the propagating media, losses due to thermal lattice vibration and energy transfer to neutralise temperature variation caused by volume change, causes the elastic waves to suffer amplitude losses. These losses will be obvious when the wavelength of the acoustic wave is comparable to the size of the scatterers, which proves that attenuation increases with the frequency of the acoustic wave. As a result, higher velocity piezoelectric materials are generally preferred for the excitation and detection of elastic waves in order to reduce the propagation losses. As the piezoelectric materials are generally anisotropic, the direction of propagation and/or polarization decides the properties of an elastic wave.

During the elastic deformation of a solid, the force *F* exerted on each surface is the product of the stress component and the area *A* over which the stress acts, assuming that stress *T* has only changed by a small amount ΔT_i across the elemental lengths $\Delta x, \Delta y, \Delta z$. Using Newton's second law of motion $F = m\ddot{u}$, and adding up all

the acting forces on the solid in all the three directions, where the mass of the elemental volume is given by $\rho\Delta x\Delta y\Delta z$, with ρ being the density of the solid, the *equation of motion* for a solid can be generalised to all three coordinated as :

$$\sum_{j=1}^{3}\frac{\partial T_{ij}}{\partial x_j}=\rho\frac{\partial^2 u_i}{\partial t^2} \qquad 2.3$$

For small deformations, mechanical stress *T* (force per unit area *F/A*) exerted within an elastic solid produces a strain *S* (ratio of the stressed length to its unstressed length) that is linearly proportional to the applied stress. This proportionality is known as Hooke's Law, relating the elongation of an elastic material to the tensile force. For simple compressional stress and strains along the same axis, this relation can be shown as

$$T=cS \qquad 2.4$$

where c is the *elastic stiffness constant*, also known as Young's Modulus (*Pa* or N/m^2). A generalised three dimensional form of the equation 2.4 for the case of a non-piezo electric solid is shown as:

$$T_{ij}=\sum_{k,l=1}^{3}c_{ijkl}S_{kl} \qquad 2.5$$

where c_{ijkl} is the elastic stiffness constant, which will symbolise the elastic behaviour of a solid in the small-deformation limit. This equation 2.5, called the *elastic constitutive relation*, can also be expressed using reduced notation as shown below.

$$T_I=\sum_{J=1}^{6}c_{IJ}S_J \qquad 2.6$$

The S_{kl} in equation 2.5 is equivalent to $\partial u_k/\partial x_l$, due to the symmetry property of the strain matrix. Differentiating equation 2.5 with respect to x_j gives

$$\sum_{j=1}^{3}\frac{\partial T_{ij}}{\partial x_j}=\sum_{j,k,l=1}^{3}c_{ijkl}\frac{\partial^2 u_k}{\partial x_j\partial x_l} \qquad 2.7$$

Equating the right hand sides of the equations 2.3 and 2.7 , it can be written as follows:

$$\rho \frac{\partial^2 u_i}{\partial t^2} = \sum_{j,k,l=1}^{3} c_{ijkl} \frac{\partial^2 u_k}{\partial x_j \partial x_l} \qquad 2.8$$

This is called the *non-piezoelectric wave equation*, which describes the propagation of plane acoustic waves in a non-piezoelectric, elastic material. The solution to the above equation 2.8 consists of three propagating wave types: a quasi-compressional wave having polarization in the direction of wave propagation, and two quasi-shear waves, both having polarizations perpendicular to the propagation direction.

2.3.2 Piezoelectric Interactions

Application of an electric field to a non-piezoelectric dielectric elastic solid will result in an accumulation of surface charge density, which is proportionally related to electric field intensity, *E* by

$$D = \varepsilon_r \varepsilon_o E \qquad 2.9$$

where ε_r is relative dielectric permittivity and ε_o is the permittivity of free space and is equal to 8.856 $\times 10^{-12}$ F/m. The above equation [9] no longer holds well when the dielectric is a piezoelectric material. Application of an electric field will produce both electrical and mechanical effects within a piezoelectric material, giving rise to a mechanical deformation also and vice versa. This can be mathematically expressed by extending the equation 2.9 as shown:

$$D = e_{ikl} S_{kl} + \varepsilon_{ik}^{S} E_k \qquad 2.10$$

where ε_{ik}^{S} is measured at constant or zero strain. Here S_{kl} is the strain matrix, D is the electrical displacement density, E_k is the electric field intensity and e_{ikl} is the piezoelectric constant in units of C/m^2.

Furthermore, the equation 2.4 no longer holds true for the case of a piezoelectric material. Application of an electric field creates a coupling between the electrical and mechanical parameters, resulting in the mechanical deformation and

vice versa. This can be mathematically expressed by extending the equation 2.4 as shown:

$$T_{ij} = c^{E}_{ijkl} S_{kl} - e_{kij} E_k \qquad 2.11$$

Equations 2.10 and 2.11 are often referred to as piezoelectric constitutive equations, and can be expressed in matrix notations as shown below.

$$D = [e][S] + [\varepsilon]E \qquad 2.12$$

$$[T] = [c][S] - [e^T]E \qquad 2.13$$

where $[e^T]$ is the transpose of the piezoelectric constant $[e]$.

The electromechanical coupling coefficient K^2 for surface acoustic wave propagation in a piezoelectric material can be formulated as

$$K^2 = \frac{e^2}{c\varepsilon} \qquad 2.14$$

where the *constants* e, c, ε are the piezoelectric constant, elastic constant and dielectric permittivity, respectively, whose values depend on the crystal cut and the SAW propagation direction.

2.3.3 Acoustic Wave Damping

None of the energy loss mechanisms were taken into consideration during the derivation of the wave equation (equation 2.8). In general, acoustic wave propagation in a piezoelectric crystal is characterised by reduction in wave amplitude, due to the effect of several damping factors. These attenuating factors include mechanisms such as photon scattering, Raman scattering and thermodynamic scattering. The entropy caused by the photon scattering being the most dominant one, introduce a viscous term into the elastic constitutive relation (equation 2.5) for the crystal, which is modified as:

$$T_I = \sum_{J=1}^{6} \left(c_{IJ} S_J + \eta_{IJ} \dot{S}_J \right) \qquad 2.15$$

where η_{IJ} , the viscosity tensor has the same symmetry as the elastic stiffness tensor c_{IJ}. In a harmonic motion, $\dot{S}_J = j\omega S_J$, which implies that wave attenuation may be accounted for by representing the elastic constants c_{IJ} by complex elastic constants $c_{IJ} + j\omega\eta_{IJ}$. Hence equation 2.13 can be written as

$$T_I = \sum_{J=1}^{6} \left(c_{IJ} + j\omega\eta_{IJ} \right) S_J \qquad 2.16$$

The wave equation (equation 2.8) can thus be written as

$$\rho \frac{\partial^2 u_i}{\partial t^2} = \sum_{j,k,l=1}^{3} \left(c_{ijkl} + j\omega\eta_{IJ} \right) \frac{\partial^2 u_k}{\partial x_j \partial x_l} \qquad 2.17$$

The spatio-temporal solution to this lossy wave equation is given by

$$u_2 \left(x,t \right) = A e^{j(\omega t - k x_i)} e^{-\alpha x} \qquad 2.18$$

where α is the attenuation coefficient of the acoustic wave.

For the case of shear wave propagation in a lossy material, it can be deduced that the presence of the viscous damping factor contributes to a second order perturbation of the wave velocity and a first-order contribution to the attenuation. The attenuation coefficient α for the y-polarized shear wave is given as:

$$\alpha = \frac{\omega^2 \eta_{44}}{2\rho v^3} \qquad 2.19$$

where η_{44} is the viscous damping coefficient of the shear wave. This also establishes the fact that attenuation of an acoustic (both bulk and surface) wave is proportional to the square of the frequency of the acoustic sensor. This emphasizes the importance of using high quality materials for acoustic sensors operating at higher frequencies.

The wave equation for piezoelectric material can be easily derived from the piezoelectric constitutive relations, and is written in terms of the displacements u_i coupled with the electric potential, ϕ. Hence equation 2.13 can be written as

$$T_{ij} = \sum_{k,l=1}^{3} c_{ijkl} \frac{\partial u_l}{\partial x_k} + \sum_{k=1}^{3} e_{ijk} \frac{\partial \phi}{\partial x_k} \qquad 2.20$$

where the electric field component, $E_k = -\partial\phi/\partial x_k$

Applying the equation of motion (equation 2.3) to equation 2.20,

$$\sum_{j,k,l=1}^{3} c_{ijkl} \frac{\partial^2 u_l}{\partial x_k \partial x_j} + \sum_{j,k=1}^{3} e_{ijk} \frac{\partial^2 \phi}{\partial x_k \partial x_j} = \rho \frac{\partial^2 u_i}{\partial t^2} \qquad 2.21$$

Comparing the above equation 2.21 with the non-piezoelectric wave equation, it can be observed that an additional term involving the electrical potential ϕ is present in the wave equation in the piezoelectric media, which is considered to be a source responsible for the generation of an acoustic wave, on the application of a time varying electrical potential. Conversely, the acoustic wave displacements generate an electric potential through which the wave can be electrically detected.

2.4 Acoustic Waves: Classification

The mode of wave propagation through or on a piezoelectric substrate describes the type of acoustic wave devices designed. The substrate material properties, the crystal cut, and the electrode structure used in the transformation of electrical energy into acoustic energy are the basic factors that determine the type of acoustic wave generated in a piezoelectric material, which may be specific to the required application. Acoustic waves are categorized predominantly by their velocities and displacement directions. Depending on the material and boundary conditions of the piezoelectric substrate, many combinations are possible. The input IDT of the sensor provides the electric signals which are needed for the particle displacement forming an acoustic wave. The mechanical wave propagates through the substrate and reaches the other IDT, where it is converted back to an electric field. Acoustic waves can be categorised based on: (a) the particle displacement relative to the propagation direction of the wave as longitudinal or shear, (b) the particle displacement relative to the device surface as vertical or horizontal. The longitudinal (compressional) waves have particle displacement parallel to the wave propagating direction as shown in Figure 2.4, while the transverse (shear) waves have particle displacements that are perpendicular to the direction of wave propagation [50] as shown in Figure 2.5. Shear

horizontal waves are characterised by transverse displacements polarized parallel to the sensor surface, whereas shear vertical waves displays transverse displacements perpendicular to the sensor surface [74].

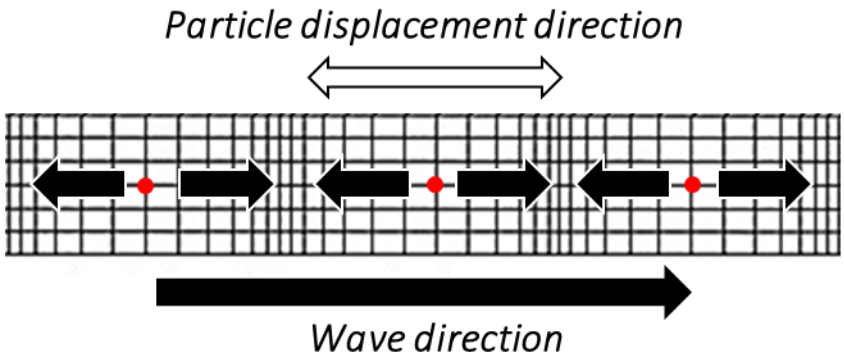

Figure 2.4. Pictorial representation of longitudinal wave showing the particle displacement direction with respect to the direction of wave propagation

The acoustic waves could either travel along a sensor surface forming a surface acoustic wave, or travel through the bulk of the substrate or be guided by reflections from multiple surfaces, as in a plate wave. Those waves travelling through the substrate are called bulk waves and the most commonly used BAW devices are the Thickness Shear Mode (TSM) resonator and the SH-APM devices. Waves travelling along the substrate surface are termed as surface acoustic waves (SAW) and the most commonly used ones are the SAW sensors and the shear horizontal SAW (SH-SAW) sensors [74].

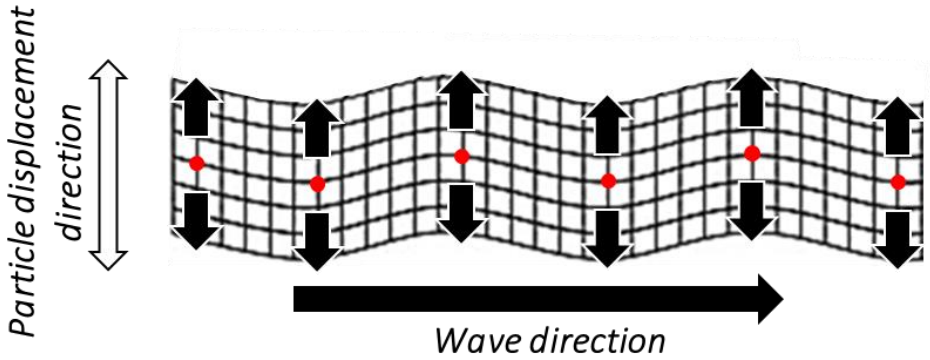

Figure 2.5. Pictorial representation of shear wave showing the particle displacement direction with respect to the direction of wave propagation.

Bulk acoustic waves

Acoustoelectric devices and technology have had a major impact on today's cutting-edge communication systems and are gaining more popularly for their performance since the study of the bulk acoustic wave (BAW) crystal resonator devices in the 1930s. Bulk acoustic wave travels in the bulk of the material and interacts with the external environment through the opposite surface of the material. Some of the commonly used BAW devices include quartz crystal microbalances (QCM), thin film resonators including film bulk acoustic resonators (FBAR) and solidly mounted resonators (SMR) and cantilevers. Bulk acoustic wave sensors may utilize either the longitudinal or shear wave. In order to minimize acoustic radiation into the plate, the shear wave is used in most cases. The acoustic resonance frequencies of an unloaded plate is obtained when the plate thickness is an odd multiple of a half-wavelength [75]. Thus, the resonance frequencies, the bulk wave phase velocity and the boundary conditions at the plate's surfaces are determined by the plate thickness.

2.4.1.1 Shear Horizontal Acoustic plate mode

Acoustic Plate Modes (APMs) are the allowed waveguide modes, that are excited and received on a piezoelectric plate surface with the help of IDTs, resulting in displacements that are either transverse to the propagation direction (shear horizontal (SH) and shear vertical (SV)) or parallel to the propagation direction (longitudinal (L) modes). The SH-APMs are useful for liquid-based biosensing applications [76], as they have displacements parallel to the crystal plane with no surface normal wave component and hence they do not dissipate energy into the fluid [77]. These devices offer the advantage of using the back surface as the sensing active area, which isolates the IDT from the testing liquid, preventing potential problem of chemical attack [69]. They have a similar configuration as that of Rayleigh SAW devices, but with a thin wafer of a few acoustic wavelengths, which acts as an acoustic waveguide (as shown in Figure 2.6). Shear horizontal waves are generated by the IDTs that propagate through the bulk at angles to the surface. These waves reflect between the plate surfaces as they progress through the plate between the input and output IDTs. Hence both surfaces of the plate undergo displacement, allowing detection to occur on either side [68].

The resonant frequency of the SH-APM is determined by the plate thickness and the IDT finger spacing. The SH-APMs generated in the Z-cut X propagating $LiNbO_3$ piezoelectric crystal have much higher piezoelectric coupling than the ST cut Quartz [77]. The addition of a biosensing film to the sensing surface of the piezoelectric plate modifies the sensing properties of these devices. These devices have been used for measuring mass change in liquid media and also for detecting biological molecules [78]. Ricco and Martin, being the first to utilize a SH-APM device specifically, confirmed a correlation between the sensor response and liquid viscosity [79]. A liquid-based chemical sensor capable of detecting low concentrations of Cu^{2+} ions in solution has been fabricated by chemically modifying the sensing surface with ethylene diamine ligands [34]. In addition, Schweyer et al. reported that these sensors have been effectively used in the detection of microgram levels of mercury, which is acceptable for Safe Drinking Water Act compliance testing [80].

The sensitivity of an SH-APM device with an isotropic plate is given by

$$S_n = -J/\rho d \qquad 2.22$$

where $J = 1/2$ for the mode $n = 0$ and $J = 1$ for higher plate modes ($n > 0$), ρ is the plate density and d is the plate thickness [50]. As the plate thickness decrease, the frequencies of higher plate modes increase, which in turn result in high sensitivity in high order modes, at the cost of increased transmission losses [81]. Though SH-APMs are more sensitive to mass loading than the TSM resonators, they are less sensitive than surface wave sensors due to the following two reasons. Firstly, mass sensitivity depends on the plate thickness, with sensitivity increasing as the device is thinned [82]. But for SH-APM devices, the minimum plate thickness is limited by the available manufacturing processes. Secondly, the wave energy is not maximised at the sensing surface of the plate, reducing the sensitivity [74].

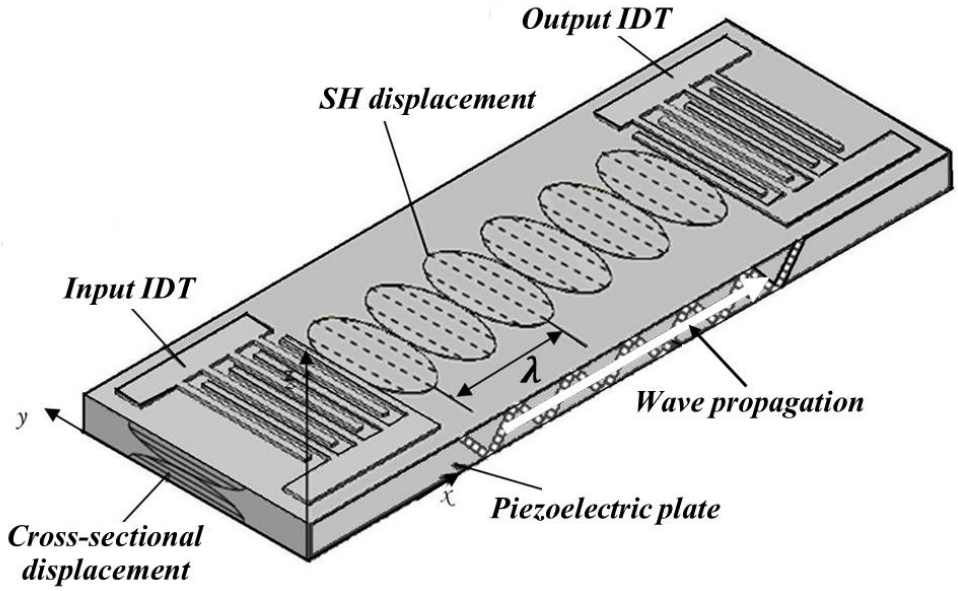

Figure 2.6. Shear horizontal Acoustic Plate mode (SH-APM) device. Adapted from [69].

2.4.1.2 Thickness Shear Mode

TSM devices, also widely referred to as a quartz crystal microbalance (QCM), is the widely accepted, oldest, and simplest bulk acoustic wave device. TSMs generate bulk transverse waves that travel normal to the plate surface with particle displacements parallel to the surface (in-plane). The resonant wavelength λ is determined by the equation 2.23 given by

$$\lambda = \frac{2d}{n} \qquad 2.23$$

where $n = 1,3,5\ldots$ and 'd' is the plate thickness. Also the frequency increases as the thickness of the plate decreases. These devices consist of thin metal electrodes, on both sides of an AT cut quartz plate forming a single electrical port [83]. Figure 2.7(a) shows the top view of a QCM and Figure 2.7(b) shows the cross-sectional view illustrating the direction of the shear wave displacement within the device. These are considered as resonators because the crystal resonates when a standing wave pattern is created. These devices resonate on the application of a voltage between the electrodes, causing shear deformation of the crystal. Maximum displacement is

observed at the crystal surfaces, making the device sensitive to surface mass loading and other perturbations. The sensor forms part of an oscillator circuit, where the oscillation frequency trails the crystal resonance, identifying the mass deposition on the sensor surface. Benefits of TSM devices include simplicity of manufacture, ability to withstand harsh environments, good sensitivity, robustness and temperature stability [74]. Moreover, the presence of a shear component facilitates the use of these devices in liquid sensing applications. The TSM resonator was shown to operate as a vapour sensor in the late 1960s. A major disadvantage of TSM devices is their low mass sensitivity, which can be improved by making the devices very thin and thereby increasing the operating frequency. Recent efforts to produce high-frequency TSM resonators utilizing piezoelectric films and bulk silicon micromachining techniques [83] have resulted in the development of thin film resonator technology.

The governing equation for the QCM operation was empirically derived by Sauerbrey in 1959 [84] which demonstrated the principle of quartz crystal microbalances (QCM) by relating the change in resonance frequency of a quartz crystal plate to the mass attached on to its surface.

$$\Delta f = -\frac{2 f_0^2}{A\sqrt{\rho\mu}}\Delta m \qquad 2.24$$

where Δf is the resonant frequency shift, Δm is the change in mass of the sensing surface, and A is the sensing area of the QCM electrodes and ρ and μ are the density and shear modulus of the crystal. Even though this is the fundamental equation for QCM-based sensors, it can only be suitable for a crystal with negligible thickness and only in a gaseous atmosphere. Such limitations give rise to significant alterations to the basic model when the detection is done in the liquid phase. Thus, in 1985, Kanazawa and Gordon [85] derived a similar relationship of QCM in contact with liquid given by equation 2.25.

$$\Delta f = -f_0^{3/2}\left(\eta\rho/\pi\mu_q\rho_q\right)^{1/2} \qquad 2.25$$

where f_0 is the resonant frequency, η and ρ are the viscosity and mass density of the liquid, correspondingly, μ_q and ρ_q are the shear modulus and density of the quartz

substrate, respectively. This equation introduces an important parameter relating to liquid sensing, that is, the viscosity of the medium, in addition to the mass.

From the above two equations, it is evident that a higher resonant frequency improves the sensitivity of the QCM. However, the resonant frequency of the QCM is limited by the thickness of the quartz crystal, resulting in a fundamental mode in the low MHz range.

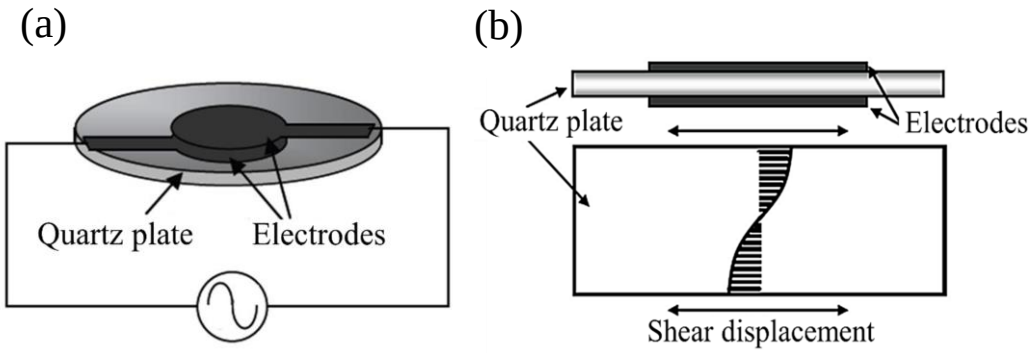

Figure 2.7. Thickness Shear Mode resonator device: (a) top view (b) cross-sectional view illustrating the direction of the shear wave displacement. Adapted from [69]

2.4.2 Surface Acoustic Waves

The surface acoustic wave discovered by Lord Rayleigh in the 19th century has particle displacements both in the wave propagation direction as well as in the perpendicular direction. In a surface wave mode, the acoustic energy is confined close to the surface (roughly within one wavelength) and the attenuation increases exponentially with increasing depth; resulting in surface waves that are extremely sensitive to external mass loading and perturbations in gaseous environments. The commonly used surface acoustic wave sensors are the Rayleigh surface acoustic wave (Rayleigh SAW) device and the shear-horizontal surface acoustic wave (SH SAW) device, also referred to as surface transverse wave (STW) sensor. Other acoustic wave devices that are auspicious for sensors include the flexural plate wave (FPW) and the Love wave devices.

2.4.2.1 Rayleigh SAW waves

The SAWs were first described by the British scientist Lord Rayleigh in 1887 in which acoustic energy is confined very near the surface of an isotropic solid (Figure 2.8). This mode of wave propagation, now known as the Rayleigh wave, has by far become the most widely known and used. Due to the surface confinement of energy to a few wavelengths thick zone close to the crystal surface, Rayleigh waves has been utilized in sensor applications, allowing them to be excited by surface electrodes in piezoelectric crystals and making the wave extremely sensitive to surface perturbations. These waves have both a surface-normal component and a surface-parallel component with respect to the direction of propagation. The electromagnetic field related to the acoustic wave travels in the same direction. The wave velocity is determined by the substrate material and the crystal cut orientation. Surface waves from a quartz crystal have been engaged for various sensor applications due to its temperature stability and high sensitivity to surface loading. One of the major applications of Rayleigh wave devices is bio/chemical sensing. After the first use of SAW devices as a gas sensor in 1979 by Wohltjen and Dessy [86], many researchers have been exploring the possibilities of using SAW devices for the detection of vapour phase molecules with selective polymer coatings. Later on, with the development of stable antibody immobilization methods, their application extended to biosensor and immunosensor detection [87].

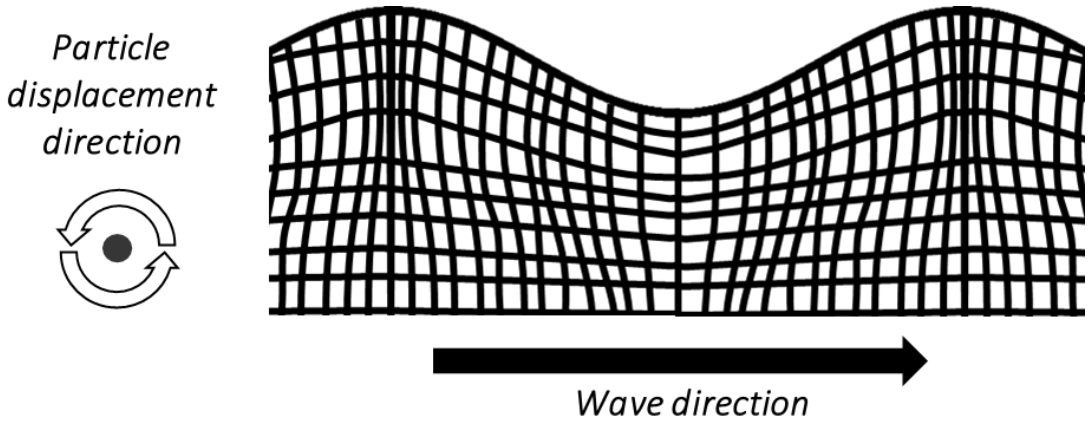

Figure 2.8. Rayleigh wave propagation showing the surface deformation profile and the particle displacement direction.

When surface acoustic waves are used for liquid based applications, electromagnetic energy is radiated into the liquid due to its surface-normal particle

displacement, causing excessive damping. As a result of this attenuation in liquid, they are less exploited for liquid-phase sensor devices [27]. Lithium Niobate ($LiNbO_3$) substrates were generally used for the SAW fluidic-systems because SAWs can be efficiently excited within the wafer plane.

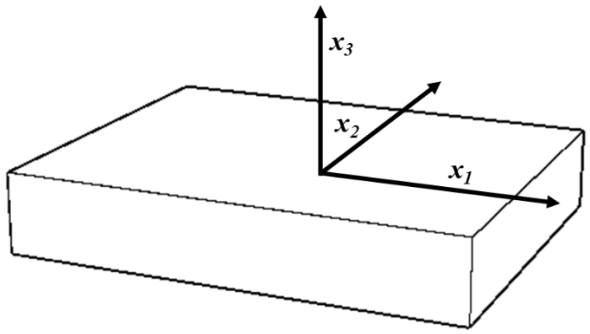

Figure 2.9. Co-ordinate system showing the propagation vector for SAWs.

Consider the SAW propagation geometry axes of a piezoelectric crystal as shown in the Figure 2.9. Rayleigh SAWs propagate parallel to the sensor surface with a phase velocity V_R and their displacement and amplitude decay with distance from the surface ($x_3 > 0$). Considering the propagation direction as x_1 axis, the (x_1, x_3) plane is defined as the sagittal plane, the solution for the surface waves is in the form of a linear combination of partial waves as shown below.

$$u_i = A_i \exp(-kx_3)\exp\left[-j\omega\left(t-\frac{x_1}{V_R}\right)\right] \qquad 2.26$$

$$\varphi = B\exp(-kx_3)\exp\left[-j\omega\left(t-\frac{x_1}{V_R}\right)\right] \text{ and } x_3 > 0 \qquad 2.27$$

Here, ω is the angular frequency of the electrical signal, $k = 2\pi/\lambda$ is the wave number and wavelength is given by $\lambda = 2\pi V_R/\omega$.

These are the generalised Rayleigh waves as all the three particle displacement components exist. The crystal symmetry and other electrical and mechanical boundary conditions enforce further constraints on the wave solutions. Since the Rayleigh waves

do not vary in the x_2-direction, the displacement vectors have no component in the same direction and the solution is given as follows.

Assuming displacements u_1 and u_3 to be of the form given by

$$u_1 = A\exp(-bx_3)\exp\left[jk(x_1 - ct)\right] \qquad 2.28$$

$$u_3 = B\exp(-bx_3)\exp\left[jk(x_1 - ct)\right] \qquad 2.29$$

and $u_2=0$

where the elastic half-space for $x_3 \leq 0$, B and A are unknown amplitudes, k is the wave number for propagation along the boundary (x_1 - axis) and c is the phase velocity of the wave. Physical consideration requires b could be complex with a positive real part. Substituting into Navier-Stokes equation gives [88]

$$\nabla.\tau - \rho\frac{\partial^2 u}{\partial t^2} = 0 \qquad 2.30$$

Using the generalised Hooke's law for an isotropic elastic solid, two homogeneous equations in A and B are obtained. For a non-trivial solution, the determinant of the coefficient matrix gets cancelled, giving two roots for b in terms of the longitudinal and transverse velocities. Substituting these roots in the homogeneous equations for A and B gives the amplitude ratios, giving rise to a general displacement solution as given by above equation. These displacements are as shown in Figure 2.10. It can be noticed that u_3 is in phase quadrature with u_1, and hence the particles have an elliptical motion. Due to the change in sign of u_1 at a depth of about 0.2 wavelengths, the ellipse has got different directions above (retrograde motion) and below (prograde motion) this point. Hence u_1 and u_3 can be shown as:

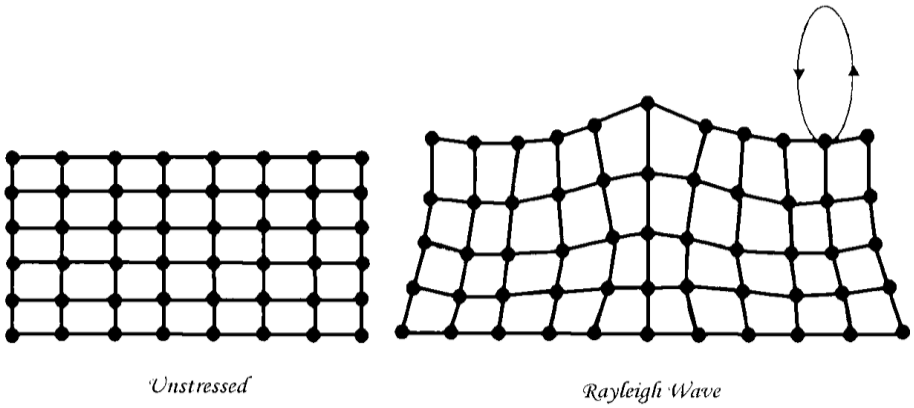

Figure 2.10 Rayleigh wave particle displacements on sagittal plane

$$u_1 = \left[A_1 \exp\left(-b_1 x_3\right) + A_2 \exp\left(-b_2 x_3\right) \right] \exp\left[jk\left(x_1 - ct\right) \right] \qquad 2.31$$

$$u_3 = \left(-b_1 / jk\right) A_1 \exp\left(-b_1 x_3\right) + \left(jk / b_2\right) A_2 \exp\left(-b_2 x_3\right) \exp\left[jk\left(x_1 - ct\right) \right] \qquad 2.32$$

where, $b_1 = k\left(1 - c^2 / v_l^2\right)^{1/2}$ and $b_2 = k\left(1 - c^2 / v_t^2\right)^{1/2}$

Also, the longitudinal velocity v_l and transverse velocity v_t are given by

$$v_l = \sqrt{\frac{\lambda + 2G}{\rho}} \qquad 2.33$$

$$v_t = \sqrt{\frac{G}{\rho}} \qquad 2.34$$

where the Lames' constants $G = E_m / 2\left(1+\nu\right)$ and $\lambda = \nu E_m / \left[\left(1+\nu\right)\left(1-2\nu\right)\right]$ with ν being Poisson's ratio and E_m being Young's modulus.

2.4.2.2 Shear-horizontal surface acoustic waves

Shear horizontal surface acoustic waves (SH SAWs) are suitable for liquid-phase operation as they do not radiate energy into liquids avoiding any damping effects due to the fact that these waves have particle displacements that are transverse to the propagation direction and parallel to the surface plane (Figure 2.11 illustrates the propagation of a SH surface acoustic wave). By the use of a different crystal cut of a substrate, a shear horizontal surface acoustic wave (SH-SAW) instead of a vertical Rayleigh wave could be yielded. The transverse displacements of SH-SAWs, which

are polarized parallel to the sensing surface, prevent the SH-SAW energy being radiated into the liquid. Out of the several substrate types such as $LiTaO_3$, $La_3Ga_5SiO_{14}$ and Quartz that exhibit SH-SAWs, the liquid sensing systems using $LiTaO_3$ substrate have been explored extensively. In general, the SH-SAW is sensitive to mass-loading, viscosity, conductivity and permittivity of the adjacent liquid.

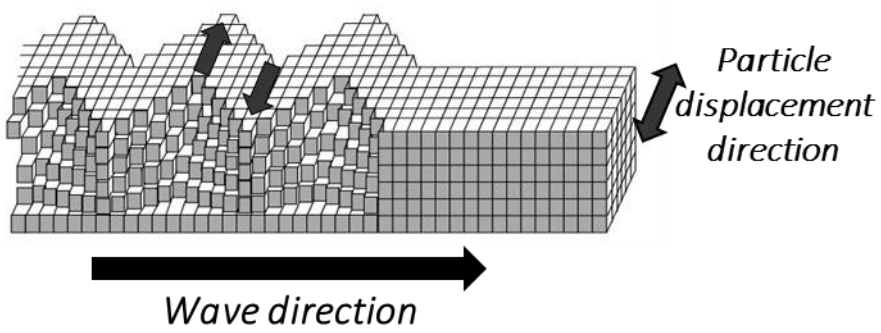

Figure 2.11 Shear Horizontal Surface Acoustic Wave propagation. Adapted from [68]

Comparable to the SH-SAW is another type of acoustic wave called the surface transverse wave (STWs, i.e., shear bulk modes confined to the device surface by periodic metallic gratings), which is also a horizontally polarized shear wave (HPSW) developed by Baer et al. In order to solve the problem of high dielectric mismatch, a thick shielding layer was added on the sensor surface to reduce the high DC influence of water on the IDTs. These SH-SAW devices in ST-cut quartz crystal have a thin solid film or grating added to the surface to prevent wave diffraction into the bulk of the plate, the mass of which slightly reduces the wave velocity and these are also called STW sensors. Using this approach, lower attenuation values were achieved that potentially allowed the sensor to operate with a simple oscillator circuit in a bio sensing investigation [55]. As the STW device operates with surface shear horizontal particle displacements, it can be used for detection in both gas and liquid media. The spacing of the IDTs determine the resonance frequency of this device and its typical operating frequency is in the range of 30-300 MHz.

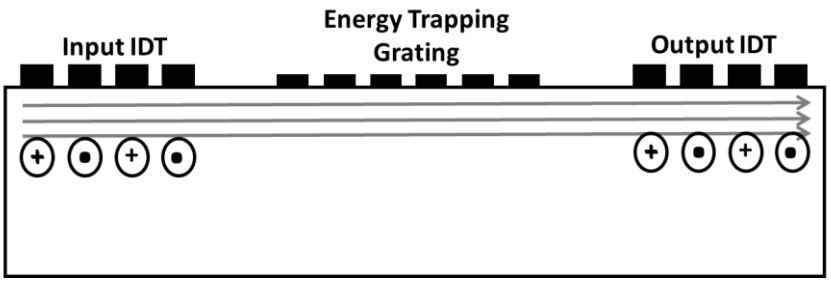

Figure 2.12. STW propagation employing an energy trapping grating between IDTs

The particle displacement solution for a shear horizontal (SH) or acoustic plate mode (APW) is simply a plane shear wave having parallel propagation to the surface, with its amplitude independent of x_3 (see Figure 2.12) inside the material. The phase velocity is denoted by v_t and the particle displacement associated with the n^{th} order SH mode (propagating in the x_1 direction) has only an x_2-component and is given by

$$u_2 = u_0 \cos\left[\frac{n\pi}{b}\left(x_2 + \frac{b}{2}\right)\right]\exp\left[j(\omega t - \beta_n x_1)\right] \qquad 2.35$$

where b is substrate thickness, u_2 is the surface particle displacement, n is the transverse modal index (0,1,2,3…) and t is time. The propagation of the displacement profile down through the waveguide length (in the x_1 direction) is described by the exponential term in the equation with angular frequency ω, wave number β_n *and* unperturbed propagation velocity of the lowest-order mode v_0 and is given as

$$\beta_n = \sqrt{\left(\frac{\omega}{v_0}\right)^2 - \left(\frac{n\pi}{b}\right)^2} \qquad 2.36$$

2.4.2.3 Love waves

A special class of SH-SAW sensors, called Love wave sensors, have proven to be the most sensitive acoustic sensor for liquid based sensing applications [74]. The Love wave effect is the acoustic resonance of a deposited waveguide layer on the top of an SH-SAW device, such that the energy of the shear horizontal wave is focused in that coating. Originally, the related physical effect was discovered by Love, who proposed that these waves were SH waves confined to a superficial layer of an elastic

half-space deposited on a substrate made of another material with different acoustic properties and infinite thickness in comparison to the original wave guide layer. These transverse waves brought shear stresses into action as shown in Figure 2.13.

Overlaying a thin film on the surface of a substrate having the appropriate properties of a guiding layer, Love waves propagate near the surface which supports SH waves. The propagating energy is located in the waveguide layer and in the substrate face close to the interface because it is a surface wave. The shear acoustic wave velocity within the waveguide layer is lower compared to that of the substrate, which results in the acoustic wave being guided through the layer. Also, a reduction in attenuation can be obtained by adjusting the waveguide layer thickness to an optimum value. The first Love wave device for biosensor measurements based on quartz with a PMMA wave-guiding layer was presented in 1992 by Gizeli et al. The adsorption of IgG was investigated at the sensor surface, and anti-IgG and protein A were used as analyte [89]. Recently, devices based on Love waves have received increasing interest. A Love wave device based on sputtered SiO_2 with an optimal layer thickness was first presented by Du et al. in 1996 [55]. In comparison with the SH-SAW devices, SH-SAWs are limited by high noise levels and background interference from reflection off the lower surface. The waveguide layer (usually SiO_2) in a Love mode device confines the wave over the device top layer, eliminating the disadvantages associated with a similar SH device.

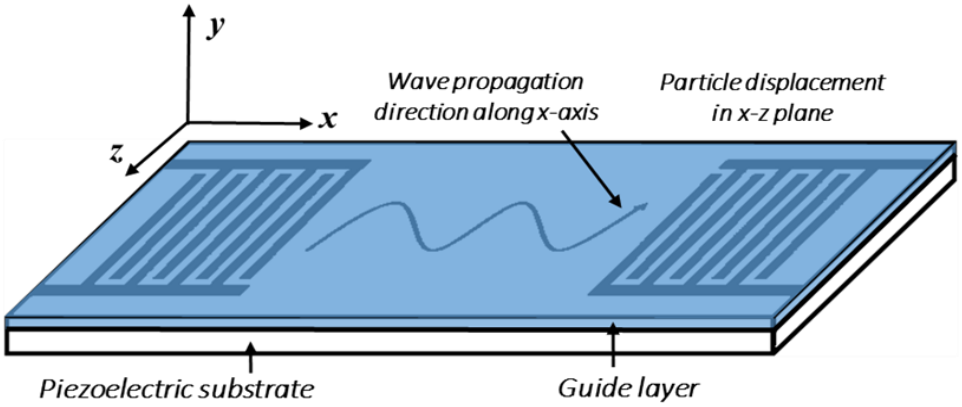

Figure 2.13 Love wave propagation.

With the exception that the Love waves propagate in waveguide layer on the IDT top surface, these waves have the same principle of generation as that of the SH-SAW waves. These devices' resonance frequency is determined by the IDT finger spacing and the shear velocity in the waveguide layer. Obviously, the variation in the layer's electrical and mechanical properties caused by the measurand, can be determined by monitoring the love waves with a high concentration of energy in the layer [90].

2.4.2.4 Flexural Plate Waves

In an FPW device (see Figure 2.14) an acoustic wave is excited in a thinned membrane. The velocity of an FPW is much lower than that of most liquids which lie in the range from 900 to about 1500 ms^{-1}, allowing a low loss operation in gas and liquids. A slow propagation of the FPW prevents any radiation from the plate, making the devices function well in the liquid environment, and hence form a good candidate for biosensing and chemical sensing applications. The mass per unit area of the thin plate is significantly increased on mass-loading (due to adsorption of chemical vapor molecules on the plate) and fluid loading, which is measured as a decrease in the phase velocity of the acoustic wave. However, when the tension in the plate is increased, an opposite effect occurs, resulting in an increase in the phase velocity.

The FPW devices typically consist of a silicon substrate, a dielectric membrane layer (such as silicon nitride, silicon dioxide, oxy-nitride, aluminium nitride and diamond) and the piezoelectric thin film (usually zinc oxide) sputtered on the membrane layer. The membrane is released by the back etch of the silicon wafer and the IDTs are patterned on top of the piezoelectric material, which will transmit a shear wave as in the case of SH-SAW waves. Any surface perturbations change the wave velocity and dampen the acoustic vibration. The spacing of IDTs and thickness of the substrate are the parameters that define the resonance frequency of these devices, with typical operation frequencies in the range of 2-20MHz. Unlike the other acoustic wave devices, the frequency of operation does not determine the detection sensitivity; but instead the relative magnitude of the perturbation to the corresponding membrane parameter will decide the sensitivity of the FPW device. In the case of mass, the sensitivity is the ratio of the added mass to the membrane mass. Since very thin membranes can be achieved, very high mass sensitivities can be accomplished, even

higher than other acoustic sensor modes [50]. Low operational frequencies, very high detection sensitivity, cheaper driving circuitry, possibility of large scale low cost system integration are some of the advantages of the FPW devices. However, due to the reduced thickness, FPWs are quite fragile.

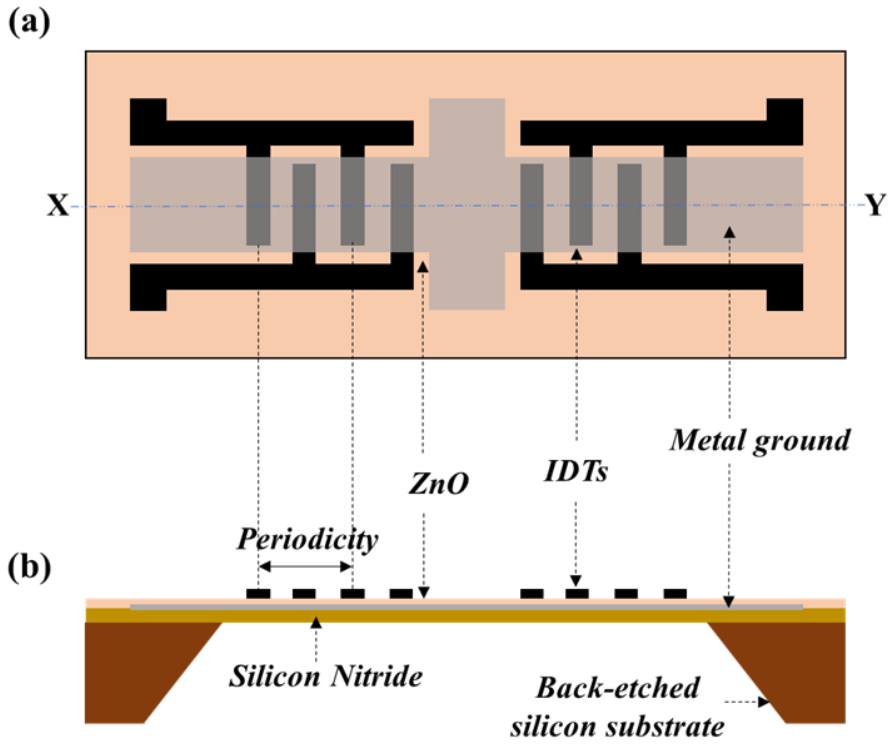

Figure 2.14. Schematic of a typical flexural plate wave device (a) Top view of the chip (b) Cross-sectional view along X-Y line. Adapted from [32]

2.5 SAW substrate materials

Acoustic wave devices provide a robust and relatively economical means for the implementation of a wide-range of biochemical sensing applications. Acoustic wave devices grounded on piezoelectric substrates have been successfully explored for the real-time and rapid detection of bio-chemicals where the device is in direct contact with the solution [91]. Hence these sensors had a successful commercial market for several decades. Any change in the propagation characteristics due to the propagation of the acoustic wave through or on the surface of the material, will affect the wave performance such as velocity. By measuring the frequency characteristics of

the sensor, the changes in the velocity of the wave can be monitored and correlated [92]. The acoustic wave sensors utilizes the piezoelectric effect to stimulate electrically an acoustic wave at an input IDT and receive the wave at the output IDT [93]. Piezoelectric materials can generate an electric field on application of a mechanical force and conversely produce a stress on application of an electric field. Some of the commercially available piezoelectric materials include quartz (SiO_2), $LiTaO_3$, $LiNbO_3$, AlN, ZnO, lead zirconium titanate (PZT), piezo polymers and diamond [66]. Piezoelectric materials allow various crystallographic cut angles that minimize the temperature coefficient of AW devices; which include the ST cut for SAW devices and *AT* and *BT* cuts for TSM devices [68].

YZ-lithium niobate substrates with relatively high values of electromechanical coupling coefficient (K^2) generally find application in wideband SAW filters [94]. These crystals suffer from a very large temperature coefficient of delay (approximately 80 ppm/^{o}C) and consequently, it is thermally fragile and temperature compensation is required when using this substrate to detect anything other than temperature changes [95]. Temperature variations will result in phase shifts around the feedback loop, when the devices are used in an oscillator configuration. This reduces the stability of the oscillator. The 128^o rotated X-propagating $LiNbO_3$ is an improved design over the Y-Z counterpart [96].

ST-cut Quartz (i.e., stable temperature cut) is the most commonly used in SAW oscillator designs, narrowband filters, and delay lines as it is identified as having negligible temperature coefficient of delay resulting in stable operation even though it has a value of K^2 which is about 40 times less than for $LiNbO_3$ [86], [97]. However, $LiTaO_3$ substrates have a higher K^2 than ST-quartz, but poorer temperature stability [98]. $LiTaO_3$ exhibits unique electro-optic, pyroelectric and piezoelectric properties combined with more stable temperature and reasonable mechanical and chemical stability than $LiNbO_3$ [95]. This makes $LiTaO_3$ well-suited for numerous applications including SAW oscillators, electro-optical modulators, pyroelectric detectors and optical waveguides [96].

Langasite ($La_3Ga_5SiO_{14}$) is a relative newcomer to the field of SAW piezoelectric crystals [95]. In addition to the low TCD suitable for temperature stable applications, it has a higher coupling coefficient (K^2*=0.3%)* than quartz, with a slightly smaller SAW velocity (*v=2400 m/s*) [55]. In view of the ability to obtain compact device size due to the comparatively smaller SAW velocity, bismuth germanium oxide

($Bi_{12}GeO_{20}$) has found use in long delay-line applications [66]. The piezoelectric coupling of Gallium Arsenide (GaAs) is slightly less than that of Quartz, while its attenuation is higher. The suitability of GaAs for extremely high speed electronics makes it an ideal candidate for developing monolithic mass-sensitive acoustic wave devices integrated with high frequency (GHz based) electronic components on the same substrate [83]. Additionally, with the aid of thin film piezoelectrics, AW devices and integrated electronic drive circuitry could be merged into the same silicon substrate. The possibility to grow extremely thin piezoelectric films, typically by RF sputtering (e.g., ZnO and AlN) has helped in the development of very high frequency based bulk resonators like FBAR devices [99].

The anisotropic nature of SAW piezoelectric substrates or the improper alignment of an IDT with the required crystal cut could lead to an undesirable second order effect known as beam steering. In order to avoid this effect, it requires the use of piezoelectric substrates with crystal cuts such that the SAW velocity is either a maximum or a minimum along that particular cut [100]. Other high temperature materials include berlinite ($AlPO_4$), lithium tetraborate ($Li_2B_4O_7$) and gallium phosphate ($GaPO_4$), operable up to 1000°C as they have a high Curie temperature [95]. Moreover, high acoustic velocity based newer materials are being developed including sapphire, diamond-like carbon, silicon, NbO_3 compounds and PMN-PT [101], [102].

2.6 Practical design aspects of SAW devices

Surface acoustic wave (SAW) sensors are commonly engaged in the detection of various gases and volatile organic compounds and have been effectively used in both liquid phase and vapour/gas phase. A SAW sensor utilizes IDTs with/without the use of reflection gratings in order to launch surface acoustic waves that travel through a chemically sensitive film on a piezoelectric substrate. The primary sensing is due to mass loading on the absorbent film resulting in a shift in the operating frequency. As the sensitivity of the AW devices are proportional to the square of the operating frequency, the SAW sensor devices typically find their applications at radio frequencies in the range of hundreds of MHz [52].

The SAW devices comprise of two major groups: the non-dispersive delay line two-port devices and secondly the SAW resonators; which are either two port or one port devices.

2.6.1 SAW Delay line

Unlike the bulk wave devices, SAW devices focus their energy on the sensor surface rather than scattering the energy through the substrate material to the opposite surface. SAW delay lines have been successfully employed for biosensing and microfluidic systems. A SAW delay line consists of two IDTs forming electrode pairs on the surface of a thin piezoelectric film, one to launch the SAW and the other to detect it. The Figure 2.15 shows the 'delay-line' configuration of the SAW device. There is a space or delay line between the input and output IDTs [54]. Application of an electrical voltage to the input IDT creates oscillating mechanical strains in the piezoelectric substrate forming travelling surface waves. The surface wave launched by the input IDT, caused by the piezoelectric effect will be converted back into a sinusoidal voltage signal voltage of different phase and amplitude by the receiving IDT. These differences are related to changes in the SAW velocity and attenuation and can be correlated to changes in the mass loading, viscosity and temperature of the substrate.

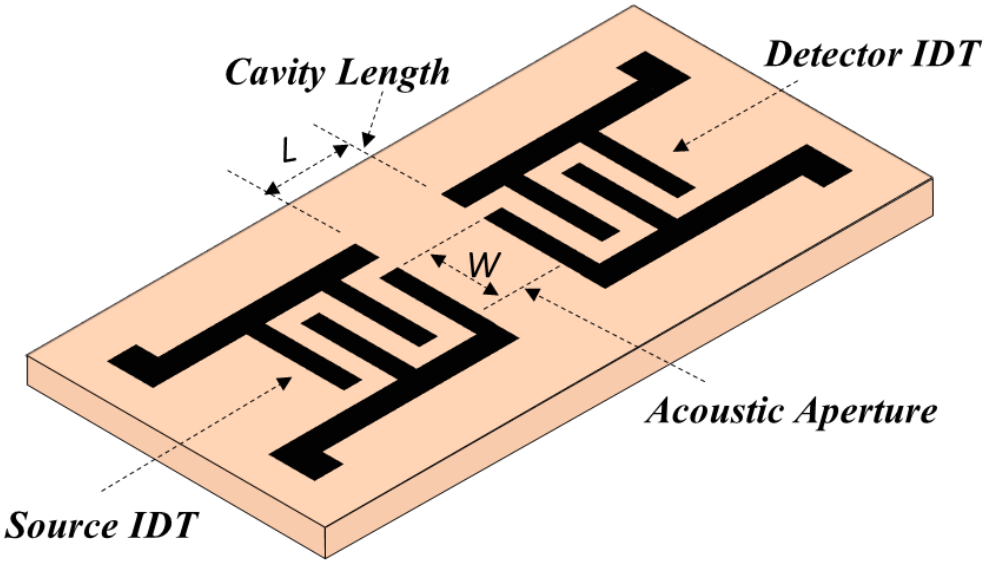

Figure 2.15. SAW delay line device with IDTs metallised onto the top of the substrate

2.6.2 SAW resonator configuration

In order to improve the proficiency of the SAW delay lines, reflection gratings are placed alongside the input and output IDTs of a SAW device. The acoustic waves are generated by the centrally placed IDTs and reflected by reflection gratings fabricated on both sides of the actuation IDTs. The reflection gratings constructively reflect the SAW waves emitted from the excited IDTs, giving rise to a SAW standing wave pattern within the IDT. Device losses are reduced due to this energy trapping, which in turn creates a distinct series resonant peak, when compared to a delay line. A SAW resonator device is preferred because of its high *Q* value, which results in low noise level and better stability [103]. Practical and commercial applications usually exploit the synchronous resonators [104] and are becoming increasingly attractive for narrow-band filtering applications.

SAW resonators may be configured electrically as one port or two port networks, whose operation is based around the cautious use of SAW reflection gratings. A one port SAW resonator consists of a single IDT which is covered on both sides by the reflection gratings (shown in Figure 2.16(a)). The surface waves emitted from both sides of the excited IDT are constructively reflected at the centre frequency by the reflection gratings, giving rise to a standing wave pattern around the IDT. A two-port SAW resonator consists of two IDTs, one forming the input IDT and the other one forming the output IDT, forming a resonant cavity between the IDTs for the generation of a standing wave pattern, with the aid of reflection gratings as shown schematically in Figure 2.16(b). Such a device is considered to be uniform and symmetric with respect to the centre of the synchronous structure.

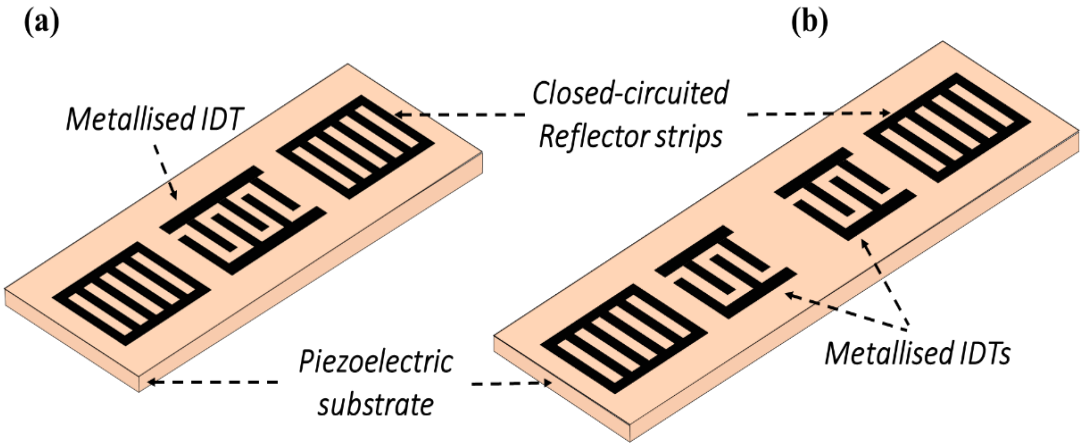

Figure 2.16. Schematic layout of surface acoustic wave based resonator (a) One port SAW resonator (b) Two port SAW resonator

2.7 Detection mechanisms of AW sensors

Immobilization of analytes on to the chemically sensitive coating/film changes the physico-chemical properties of the coating, in turn, perturbing the associated AW device. These perturbations resulting from the interaction of the coating with the analytes constitute the basis of detection and quantitation. In addition, the ultimate sensor performance also depends on the sensor configuration including the substrate material, acoustic mode and operating frequency of the device.

Intrinsic film properties used for the detection of chemical analytes include density, elastic stiffness (modulus), viscoelasticity, viscosity, electrical conductivity, and permittivity. Furthermore, a sensor response can be initiated based on extrinsic variable changes such as temperature and pressure also, affecting the acoustic wave either directly or via changes in the film's intrinsic properties. All the detection mechanisms are not of practical importance to all sensor types and also several mechanisms can operate simultaneously to produce a response. Thus the range of detection mechanisms could lead to a high degree of flexibility and a broad range of potential analytes. Recently, equivalent circuit models have been used for sensor response evaluation and to obtain the relative importance of a given transduction mechanism for a specific sensor application. These transduction principles engaged in analytical applications include changes in the velocity and/or the amplitude of the

acoustic waves. Although the preferred measurement is generally the wave velocity, sometimes wave attenuation is also used to indicate a particular interaction and more importantly, aids in differentiating one sort of perturbation from another [72]. The choice of a coating appropriate for a given sensing application requires consideration of the principal detection mechanism to be utilized for the sensing application.

2.7.1 Mass Loading

The changes in oscillation frequency by the addition or removal of mass at the sensor surface are the most commonly used detection mechanism. The wave velocity is perturbed by simple mass loading, without producing any attenuation effects, making it a unique mechanism when compared to other detection mechanisms. A vast majority of sensing applications utilise changes in mass loading as this effect is accessible to all acoustic wave modes. Because of the predominance of mass changes in causing velocity shifts, several resonant sensor types (eg. TSM and SAW) have been referred to as gravimetric sensors. Sorptive interactions (including adsorption and absorption) or chemical reactions between the analyte and sensing film result in surface mass changes and hence are used in both liquid and gas phase applications. The absolute mass sensitivity of an uncoated sensor depends on factors including the piezoelectric substrate type, operating frequency, device dimensions and the acoustic mode utilised. A very general description of the relation between mass-loading and frequency shift, with a linear dependency predicted in all cases for acoustic wave devices is given as

$$\Delta f_m = -KS_m \Delta m_A \qquad 2.37$$

where S_m is a device specific constant dependant on the above-mentioned factors, K is a geometric factor for the sensing area being perturbed, and Δm_A is the change in mass/area on the device surface.

For AW sensing in liquids, the effective surface mass depends on the thickness of the liquid/coating layer coupled to the propagating AW, which in turn is dependent on the density and viscosity of the contacting liquid and the operating frequency. Mass accumulation on the thin-film coatings on the sensor surface results in a proportional frequency decrease as in equation 2.35. The majority of the AW sensors used in bio-

chemical sensing use coatings that interact with the analytes, hence causing a change in mass. Thus, this sensing mechanism offers a great freedom and flexibility in the selection of suitable coating materials, including a wide range of organic polymers. However, the downside in engaging this detection mechanism is providing selectivity.

2.7.2 Mechanical properties

Analyte interactions can cause changes in the mechanical properties of the coating/film, which in turn produce changes in both frequency and the attenuation of the acoustic wave. Moreover, these changes can either increase or decrease either or both of the above mentioned AW propagation parameters depending on the relationship between film thickness, acoustic wavelength, and the complex modulus of the film at its operation frequency and temperature. The mechanical properties of a thin film coating can be generally classified as either elastic or viscous in nature, both of which are interdependent in most of the cases. Hence they are therefore treated together as viscoelastic properties. Many thin film materials, including most polymers, are generally treated as viscoelastic materials to fully account for their interactions with AW sensors.

The case of purely viscous interactions have been observed in certain AW devices coated with liquid absorbent, low molecular weight polymer films, when contacted with liquids [105]. When the force exerted by a Newtonian liquid on the crystal is considered to be equal and opposite to the force exerted by the crystal on the liquid, the condition for the shift in the resonant frequency of the perturbed wave as a result of liquid loading on to the crystal surface was predicted by Kanazawa and Gordon as follows [85]:

$$\Delta f_s = -\frac{f_s^{3/2}}{N}\left(\frac{\rho\eta}{\pi\mu_q\rho_q}\right)^{1/2} \qquad 2.38$$

where ρ and η are the density and absolute viscosity of the liquid, μ_q and ρ_q are the shear modulus and density of the quartz crystal and N is the mode index (integer).

Where the mechanical effects are effectively treated as purely elastic, the frequency of a SAW device is disturbed by modulus changes according to the equation 2.37 [32].

$$\Delta f_e = S_e f_0^2 \Delta\left(\frac{4h\mu}{v^2}\left(\frac{\lambda+\mu}{\lambda+2\mu}\right)\right) \qquad 2.39$$

where S_e is a substrate-related constant, h is the coating film thickness, v is the surface-wave velocity, and μ and λ are the shear modulus and Lamé constant (bulk modulus) of the coating, respectively. A Δ shows that a change in the entire term is used in calculating the elastic perturbation, which applies to either the deposition of the elastic material or changes in the elastic moduli and/or thickness of a film already present on the device surface.

Due to the capability to reversibly sorb vapours and liquids, organic polymers are considered as the most commonly used coating for the AW sensors. The magnitude of a purely elastic polymer based perturbation is proportional to the product of shear modulus and thickness of the coating. In the majority of the works published on polymer coated SAW vapour sensing, the polymer's elastic modulus has been considered small enough for the modulus effects to be neglected; and most of these studies did not, however, consider viscoelastic effects at all. But, realistically, the effective modulus of a polymer increases with the frequency of applied stress [72].

The exposure of a polymer to an analyte must generally be considered in terms of the viscoelastic changes of the coating. In some cases, the absorption of the analyte causes largely elastic perturbations, resulting in a modulus decrease, thereby enhancing the magnitude of the negative frequency shift associated to mass loading. Latest research advocates a greater role for changes in the stiffness or viscosity of the film and, in some cases, contradictory. Bartley and Dominguez reported that an increase in frequency could be obtained due to internal stress created during vapour sorption in polymers [106]. In addition to the mass loading and elastic stiffness effects, a third term was included in the sensor response expression, to account for the increase in frequency if compressive stresses were created within the coating upon vapour sorption. However, this term is expected to be about an order of magnitude less than the mass-loading term, for typical polymers. The viscoelastic contributions on polymer-based mass loading in the case of an acoustic sensor response are an issue that is yet to be resolved. Moreover, exploiting these effects to improve bio-chemical selectivity and detection sensitivity requires further categorization of sensor response, in terms of both velocity and attenuation changes.

2.7.3 Electrical properties

Chemical sensing applications using AW devices based on piezoelectric substrates create an electric field as the wave propagates through the substrate. This field can interact with mobile charge carriers linked with a surface coating on the sensor surface, affecting both the velocity and amplitude of the wave. Changes in acoustic velocity $\frac{\Delta v}{v_0}$ and attenuation $\frac{\Delta \alpha}{k}$ due to the interaction of charge carriers are given by the following equations [32], [107]

$$\frac{\Delta v}{v_0} = -\frac{K^2}{2}\frac{\sigma_s^{\,2}}{\sigma_s^{\,2} + \left(v_0 c_s\right)^2} \qquad 2.40$$

$$\frac{\Delta \alpha}{k} = \frac{K^2}{2}\frac{v_0 c_s \sigma_s}{\sigma_s^{\,2} + \left(v_0 c_s\right)^2} \qquad 2.41$$

where σ_s is the sheet conductivity of the film, K^2 is the electromechanical coupling coefficient squared, $c_s = \varepsilon_0 + \varepsilon_s$, where ε_0 and ε_s are the air and substrate dielectric permittivities respectively, v_0 denotes the propagation velocity. The peak in attenuation, as well as the maximum rate of velocity decrease, occurs at a critical sheet conductivity, and is defined as $\sigma_c \equiv v_o c_s$. The magnitude of the acoustoelectric response is proportional to K^2, and is thus dependant on the substrate.

Application of this detection mechanism in the design of a chemical sensor requires the careful selection of the piezoelectric substrate material. Changes in the wave velocity and attenuation depends on the square of the electromechanical coupling coefficient of the substrate, K^2, which varies by orders of magnitude from one crystal to the other. The value of K^2 for YZ – $LiNbO_3$ is 0.048, which is 40 times higher than that of ST-quartz (K^2=0.0011). Thus, in order to choose this type of detection mechanism, $LiNbO_3$ is a more suitable candidate than quartz.

When the analyte interacts with the sensor coating, the conductivity of the coating film is increased, resulting in a decrease in frequency. The conductivity change enhances frequency shifts due to mass loading effects or decreased modulus. To isolate the conductivity effects from mass and mechanical effects, a reference device coated

with an initial metal layer could be used, thereby shorting the electric field (this does not reduce the sensitivity to mass loading). The coating film layer is then applied on the top of the metal film. The signal from this device is then compared with the signal from the actual sensing device (with no metal layer) to obtain the differential frequency, which depends only on the conductivity changes [69].

2.7.4 Thermal effects

The velocity of acoustic wave in piezoelectric media is sensitive to changes in temperature. As a result, the need of a temperature control and/or compensation is very much essential for most practical sensors. For most chemical sensing applications, substrates with small/negligible temperature coefficient of delay are selected, which include ST-cut Quartz for SAW sensors, and AT-quartz for TSM sensors.

There are situations where the AW temperature sensitivity is of great potential for biosensing applications, but value is thus far undemonstrated. Certain pyroelectric materials such as $LiTaO_3$, ZnO and VO_x ($2<x<3$) cause a charge to build up in the crystal lattice, when there is a change in temperature [108]. This enthalpimetric property of acoustic wave devices have been used in the measurement of heat developed during chemical reactions occurring at a sensor surface. The most common claims include the detection of biological ligands via enzyme-catalysed reactions [109] that generate significant amounts of heat (up to 100 kcal/mole [110]). Without the need for an additional pyroelectric layer, enthalpimetric measurements could be carried out using temperature sensitive AW devices. It is possible to obtain maximum sensitivity by the careful selection of the substrate material. YZ-cut $LiNbO_3$ forms a suitable candidate for SAW sensors, as it possess very large temperature coefficient of 80 ppm/^oC. Sensitivity could be enhanced by minimizing the thermal mass of the AW device and its coating, relative to the sensing active area.

2.8 Summary

This chapter provides the necessary background to the basic principles governing waves and SAW devices. The basic equations describing the propagation of different types of wave in elastic solids have been presented along with expressions

for particle displacements. Rayleigh and SH modes were given particular emphasis and other different types of SAW modes compared. Also covered in this chapter are information about the substrate materials and the various detection mechanisms for SAW sensors. The materials detailed in this chapter will help understand the SAW sensor design and application of this study in other chapters.

.

CHAPTER 3

Design and Characterisation of SAW devices

3.1 Introduction

The previous two chapters had introduced the theoretical framework of acoustic waves, focusing on the fundamental physics of acoustic waves (Chapter 1) followed by a review of the different types of acoustic waves and resonators (Chapter 2). This chapter introduces the basic design principles of the SAW sensors design used for VOC detection in gaseous medium and cell-based detection in liquid medium. Even though a variety of SAW devices are commercially available on the market, high frequency SAW sensors often require tailored application-specific-configurations, which can even be a challenging task for RF experts.

Firstly, the sensor model based on the perturbation theory which in turn relates the mechanical and electrical properties of an analyte are discussed. This is followed by the discussion of the fundamental guidelines for the SAW resonator design and the various layout configurations.

3.2 Acoustic Wave Perturbation

In acoustic wave sensor applications, as the device interacts with the environment, the change of wave velocity *'v'* and/or the induced attenuation '*x'* is detected. Wave velocity and attenuation changes are fundamentally related to variation in wave energy density and power dissipation, respectively. The power density '*P*' is defined as power per area carried by a wave, which is related to the wave energy density *'U'* (energy/volume) stored in a lossless medium. The transit time for the wave passing across a unit cube is given by $\tau = 1/v$

The travelling of the wave increases the energy density within the cube and is given by the product of the incident power and transit time: $U = P\tau = P/v$ Thus,

$$P = Uv \qquad 3.1$$

The equation relates the changes in wave energy density to the changes in wave velocity in a lossless medium, where *P* remains constant. Differentiating equation 3.1 gives

$$\frac{\Delta v}{v_0} = -\frac{\Delta U}{U_0} \qquad 3.2$$

where v_0 and U_0 represent the unperturbed velocity and energy density, respectively. The fundamental relation between wave velocity and energy density in a system with a characteristic frequency of excitation is given by the above equation as the fractional change in wave velocity is equal to the negative of the fractional change in energy density. A reasonable explanation is that in the case of a system excited at a definite frequency, the adjustment of the wavelength occurs in order to maintain the peak kinetic wave energy and the peak potential wave energy the same [72]. As a result, changes in the medium that influence the wave energy density will also cause changes of the wave velocity.

Based on the energy conservation principle, power dissipated by the wave P_d should be balanced by a reduction in power transmitted by the wave *P*, and thus in a lossy media,

$$P_d = -\frac{\partial P}{\partial x} \qquad 3.3$$

Since energy density and power flow are proportional to the square of wave amplitude, in a lossy medium, $P(x) = P_0 e^{-2\alpha x}$, so that

$$\frac{\partial P}{\partial x} = -2\alpha P \qquad 3.4$$

Combining both the equations 3.3 and 3.4, the relation between the wave attenuation and power dissipation in the medium, given by

$$\alpha = \frac{P_d}{2P} \qquad 3.5$$

Wave attenuation α is half the ratio of power dissipated to power transmitted by the wave. Both velocity and attenuation changes are independent of wave amplitude, as they depend on ratios of energy and power, and not on absolute values. Acoustic wave perturbations change both energy storage and power dissipation resulting in a combination of velocity and attenuation changes.

The continuous propagation of a wave in the *x*-direction is given as

$$u(\mathrm{x,y,z,t}) = u(\mathrm{y,z})\,\mathrm{e}^{j\omega t - \gamma x} \qquad 3.6$$

where γ is a complex propagation factor indicating both attenuation and wavenumber:

$$\gamma = \alpha + jk = \alpha - j\frac{\omega}{v} \qquad 3.7$$

Changes in wave propagation, when frequency is constant is show by

$$\Delta\gamma = \Delta\alpha - jk_0\frac{\Delta v}{v_0} \qquad 3.8$$

In normalised form, it can be shown as

$$\Delta\gamma' = \frac{\Delta\gamma}{k_0} = \frac{\Delta\alpha}{k_0} - j\frac{\Delta v}{v_0} \qquad 3.9$$

where k_0 is the unperturbed wavenumber. The second part of the equation 3.9 makes it clear that $\Delta\alpha/k$ and $\Delta v/v_0$ are consistently normalised factors of changes in the complex propagation factor γ caused by a general perturbation.

As perturbations generally involve reduction in stored energy and dissipation of power, a perturbation-based complex power transfer P_T from the wave can be defined which accounts for power dissipation P_d and changes in stored energy ΔU as,

$$P_T = P_d + j2\omega\Delta U \qquad 3.10$$

Thus, a change in the complex propagation factor γ is related to the complex power transfer P_T as:

$$\Delta\gamma' = \frac{\Delta\alpha}{k_0} - j\frac{\Delta v}{v_0} = \frac{P_T}{2k_0 P} \qquad 3.11$$

3.3 Perturbation mechanisms for R-SAW Devices

Use of SAW devices for sensing applications or thin film characterization, produces perturbations of the wave velocity and attenuation, resulting from the interactions between the SAW and the surface sensing layer. As a surface acoustic wave propagation gives rise to both mechanical deformation and an electrical potential, it can be inferred that both mechanical and electrical coupling occurs between the SAW and the surface film layer. SAW-film interactions due to mechanical coupling between the wave and the film include *mass loading* caused by the change of surface mass by the SAW surface displacement and *elastic* and *viscoelastic* effects caused by the deformation of surface film by the wave. Interactions between the wave and film based on electrical coupling include acoustoelectric effects between electric fields generated by the SAW and charge carriers in a conductive film.

3.3.1 Mass Loading

SAW response due to changes in mass density on the device surface is the most utilized interaction in sensor applications. The synchronous movement of a thin or rigid surface layer by the acoustic wave cause an increase in the kinetic energy density, U_k, without any energy dissipation. This change of kinetic energy will change the

wave propagation velocity without affecting the attenuation. The change in average kinetic energy per area of the sensor surface is

$$\Delta U_k = \frac{\rho_s}{4}\left(v_{xo}^2 + v_{yo}^2 + v_{zo}^2\right) \qquad 3.12$$

where v_{xo}, v_{y0} and v_{zo} are the SAW particle velocities at the surface and ρ_s is the surface mass density [32]. The relation between particle velocity v_i and particle displacement u_i is given as $v_i = j\omega u_i$. An increase in kinetic energy density results in a decrease in wave velocity, according to equation 3.2. Combining equations 3.1, 3.2 and 3.13, an expression for wave velocity change arising from surface mass loading is obtained as

$$\frac{\Delta v}{v_0} = -\frac{\omega v_o \rho_s}{4}\left(\frac{v_{xo}^2}{\omega P} + \frac{v_{yo}^2}{\omega P} + \frac{v_{zo}^2}{\omega P}\right) \qquad 3.13$$

The quantities in parenthesis ($v_{io}^2/\omega P$) being independent of wave amplitude and depending only on the substrate material, remains a constant [111]. The expression for the mass-induced SAW velocity change is obtained by grouping all the substrate-dependant constants together and is a follows [32]:

$$\frac{\Delta v}{v_0} = -c_m f_0 \rho_s \qquad 3.14$$

where the mass sensitivity factor c_m is given by:

$$c_m = \frac{\pi v_o}{2}\left(\frac{v_{xo}^2}{\omega P} + \frac{v_{yo}^2}{\omega P} + \frac{v_{zo}^2}{\omega P}\right) \qquad 3.15$$

The above equation shows that the fractional velocity change f_0 varies with the operating frequency of the device. However there are no attenuation effects, as the mass layer is assumed to be lossless.

3.3.2 Acoustoelectric Response

In addition to the mechanical wave, a layer of electric charge is also developed at the surface of a piezoelectric material when a SAW propagates through the device.

This bound charge is the source of the wave potential ϕ, which generates an evanescent electric field as shown in Figure 3.1.

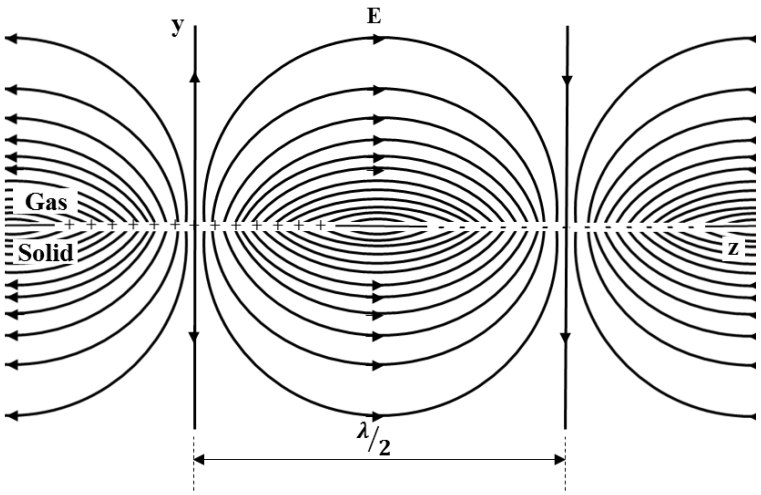

Figure 3.1. SAW-generated evanescent electric field on a piezoelectric crystal surface. Adapted from [72]

In order to compensate for this layer of bound charge generated by the SAW propagation, the charge carriers within the conductive film will get redistributed. The wave generated time varying surface charge is denoted by an *ac* source and the current generated per area of surface, is [107]

$$I_0^2 = 2K^2 \omega k^2 \left(\varepsilon_0 + \varepsilon_s\right) P \qquad 3.16$$

where K^2 is the electromechanical coupling coefficient squared and ε_0 and ε_s are the air and substrate dielectric permittivities, respectively; k and P are the wavenumber and power density. The effect of wave/charge carrier coupling produces two types of currents, including the wave generated conduction currents in the film and the displacement currents in the adjacent dielectric media. The displacement currents generated in the air and substrate originate from the capacitances of $k\varepsilon_0$ and $k\varepsilon_s$ respectively. Conduction currents in the film are obtained from the shunt capacitance $k^2\sigma_s$, where σ_s is the sheet conductivity of the film, which is in turn related to the bulk conductivity σ and thickness of the film h_f by $\sigma_s = \sigma h_f$. The wave-generated evanescent electric field stores energy, in the absence of a sensing conductive film. The complex power flow in this case is given [32] as

$$P_{T1} = \frac{I_0^2}{2j\omega k\left(\varepsilon_0 + \varepsilon_s\right)} \qquad 3.17$$

In the presence of a conductive film, the power flow becomes

$$P_{T2} = \frac{I_0^2}{2\left[k^2\sigma_s + j\omega k\left(\varepsilon_0 + \varepsilon_s\right)\right]} \qquad 3.18$$

The difference in power flows gives the effect due to acoustoelectric interactions, which is measured when the film conductivity changes.

$$P_T = P_{T2} - P_{T1} = -\frac{I_0^2}{2}\frac{k^2\sigma_s}{j\omega k c_s\left(k^2\sigma_s + j\omega k c_s\right)} \qquad 3.19$$

where $c_s = \varepsilon_0 + \varepsilon_s$. Substituting equation 3.16 into 3.19 gives the complex power transfer P_T. Substituting this power transfer equation into equation 3.11 will provide the equation for the complex propagation factor γ. By equating the real and imaginary components, the following relationships are obtained [107].

$$\frac{\Delta v}{v_0} = -\frac{K^2}{2}\frac{\sigma_s^2}{\sigma_s^2 + \left(v_0 c_s\right)^2} \qquad 3.20$$

$$\frac{\Delta \alpha}{k} = \frac{K^2}{2}\frac{v_0 c_s \sigma_s}{\sigma_s^2 + \left(v_0 c_s\right)^2} \qquad 3.21$$

It can be noticed that the acoustoelectric effect is proportional to K^2, showing its substrate dependency. The greatest attenuation rate and the maximum decrease of fractional velocity is obtained at a critical sheet conductivity, defined by $\sigma_c \cong v_0 c_s$.

3.3.3 SAW Response from elastic and viscoelastic films

While considering the mass-loading response (detailed in section 3.3.1) of the surface acoustic device, the mass-layer was treated as an infinitely thick layer, which suffered only SAW-induced translational motion. This translational motion could only bring about a velocity change relative to the areal mass density; but no attenuation response was predicted, as there is no power loss involved during film translation. However, an actual viscoelastic film having finite thickness and elastic properties

could bring about SAW-induced film deformation. This involves energy storage and power dissipation, resulting in velocity and attenuation changes.

Two different regimes of film performance can be recognized. This can be identified from the ratio of film strain obtained from cross-film displacement gradient to those obtained from the in-plane gradients, given by [112]

$$R = \frac{Afv_0\rho h}{|G|} \qquad 3.22$$

where ρ is the film density, h is the thickness, G is the shear modulus and $A=1.9$ for ST-cut quartz [113]. Based on the value of R, films can be divided into: *acoustically thin* and *acoustically thick* surface film.

3.3.3.1 Acoustically thin films

When the surface film is sufficiently thin (small h) and stiff (large $|G|$) compared to the oscillation frequency, such that $R << 1$, the film is acoustically thin; where in-plane displacement gradients govern over the surface-normal gradients. There is a synchronous movement of the entire film with the substrate surface, resulting in constant displacements across the film thickness, and only gradients in the plane of the film arise. The mechanical impedances at the substrate/film interface associated with film translational and strain modes [112], produces the SAW velocity and attenuation changes arising from acoustically thin films.

3.3.3.2 Acoustically thick films

Thick and soft films behave as acoustically thick $(R \geq 1)$ where the inertial deformation becomes substantial so that surface-normal gradients also arise. The upper portion of the film tends to lag behind the film/substrate interface, inducing non-uniform strains within the film. This inertial distortion of the film produces varying displacements across the film thickness. The thick-film displacement is obtained by the superposition of waves created at the substrate-film boundary and released into the film. The radiated waves are reflected downward by the upper film surface resulting in phase shift and attenuation of the transmitted waves. This changes the mechanical impedance seen at the substrate/film interface. Therefore, a distributed model is used for the acoustically thick film, in which the substrate-film boundary impedance

depends upon the *interference* between the waves generated at the bottom of the film and those reflected from the top of the film.

3.4 Perturbation mechanisms for SH-SAW Devices

The basic principle of operation considered when designing an acoustic biosensor is that perturbations that affect SH-SAW propagation on a non-metallized free surface are related to both the mechanical and the acoustoelectric properties of the adjacent liquid [76]. Depending on whether or not the sensing area is covered with a thin conducting metallic layer (e.g. gold), various perturbations affecting the propagation of the SH-SAW produce different effects. The shear horizontal wave propagating on a metallized surface are affected only by the mechanical properties of the adjacent liquid, and the electrical effects are nullified by the electrically shorted surface, i.e. the penetration of the electric potential into the adjacent medium is negligible [114]. In such a case, only the SH-SAW particle displacement interacts with the liquid. Conversely, the propagation of an SH-SAW on a non-metallised, free (non-shorted) surface will have both the electrical and mechanical effects based on the adjacent liquid, where both the particle displacement and the surface acousto-electric potential, interact with the liquid. Figure 3.2 shows the normalised SH particle displacement 'u' (shown by the curves u_m and u_f for metallised surface and non-metallised free surfaces respectively) and electric potential 'ϕ' at the 36° Y-cut X propagating $LiTaO_3$ substrate and water interface (shown by the curves u_m and u_f for the cases of a metallised surface and non-metallised free surfaces respectively) [115]. For liquid phase applications, these electrical and mechanical effects are associated with two different types of penetration depths (δ) namely the electric penetration depth and the mechanical penetration depth, respectively.

Propagation of an acoustic wave along or near the surface of a piezoelectric crystal produces an associated electric field which extends outside the crystal surface, interacting with the adjacent medium. Thus, when a SH-SAW is propagated on a $LiTaO_3$ substrate, an acoustoelectric potential is created on the surface of the piezoelectric, which extends into the adjacent liquid. Penetration depth is defined as the extent of the penetration of this potential into the adjacent medium (liquid) so that

a measurable change can be detected using the SH-SAW sensor. This extension of the acousto-electric potential that is capable of monitoring electric or acousto-electric variations was calculated by Kondoh et al., to be approximately 1/7th of the wavelength of a SH-SAW for a non-metallized free surface [76], as shown by the curve ϕ_f in Figure 3.2. This electric potential is zero for the SH-SAW travelling on a shorted surface as shown by the curve ϕ_m in Figure 3.2. The occurrence of a chemical reaction within this penetration depth causes the piezoelectric potential to be changed, due to changes in the electrical conductivity and dielectric permittivity of the adjacent media, giving corresponding characteristic changes in the SH-SAW propagation.

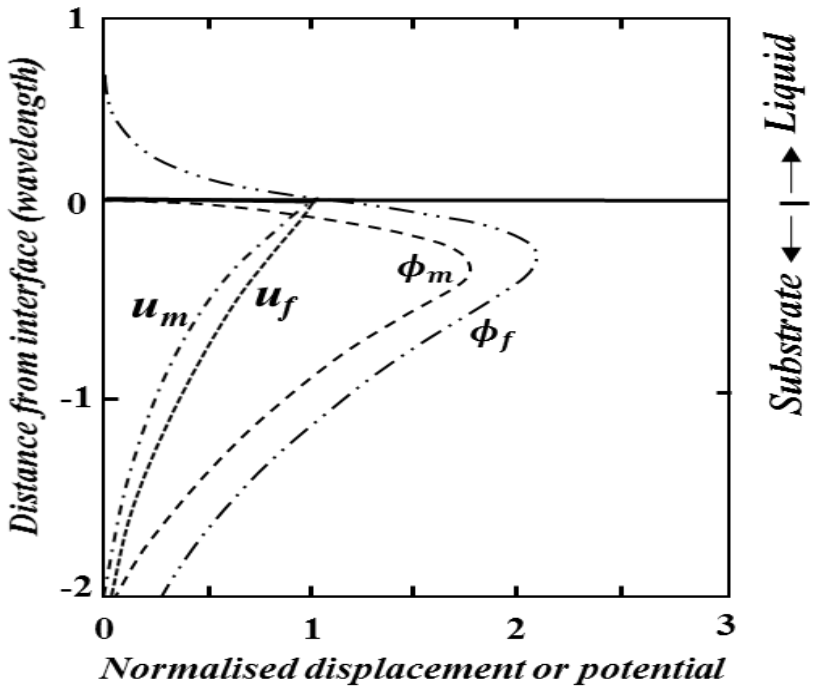

Figure 3.2. Normalized SH-SAW particle displacement (u) and potential (ϕ) profiles at the crystal/water interface for metalized (m) and metal free surface (f). Adapted from [76], [98]

For the case of a shorted SH-SAW sensor, the wave potential being zero, the surface wave particles travelling on the shorted surface only interacts with the adjacent medium. This adjacent medium is the liquid that is in contact with the sensor surface, allowing the monitoring of only mechanical perturbations due to mass density and viscosity. The effective liquid thickness, (δ_m), coupled to the acoustic wave is given by employing the formulae [116]:

$$\sigma = \sqrt{\eta / \pi f_0 \rho} \qquad 3.23$$

where η and ρ are the adjacent liquid viscosity and density respectively, and 'f_0' is the resonant frequency of the device. Thus, loading an SH-SAW sensor with liquid, will create an additional particle interaction mechanism through viscous coupling.

3.4.1 Mechanical Perturbations

Auld's perturbation theory [117] for gases helps with the derivation of changes in the SH-SAW due to mechanical perturbations, which can also be extended to the liquid phase. The perturbation formula for a liquid sensor is given by [95], [117]

$$\frac{\Delta\gamma}{k} = -\frac{jv}{4\omega P}\left(v_p^{*} \cdot Z_{Alr}^{'} \cdot v_p + v_p \cdot Z_{Alr}^{*} \cdot v_p^{*}\right) \qquad 3.24$$

Here k is the wave number, v is the phase velocity, ω is the angular frequency, P is the power flow per unit width, v_p *is* the particle velocity vector, Z_{Al} is the acoustic surface impedance and $\Delta\gamma$ is the perturbation of complex propagation constant γ. Also, ´ indicates a perturbed quantity and * indicates a complex conjugate. γ is defined in terms of k as :

$$\gamma = k - j\alpha \qquad 3.25$$

From the above equation, $\Delta\gamma$ is obtained as:

$$\frac{\Delta\gamma}{k} = -\frac{\Delta v}{v} - j\frac{\Delta\alpha}{k} \qquad 3.26$$

Equating both the equations 3.25 and 3.26 and separating real and imaginary parts provide the variation of the complex propagation in terms of the velocity and attenuation changes as shown below [98].

$$\frac{\Delta v}{v} = \frac{v}{4\omega P}\left(v_p^{*} \cdot Z_{Ali}^{'} \cdot v_p - v_p \cdot Z_{Ali} \cdot v_p^{*}\right) \qquad 3.27$$

$$\frac{\Delta\alpha}{k} = \frac{v}{4\omega P}\left(v_p^{*} \cdot Z_{Alr}^{'} \cdot v_p + v_p \cdot Z_{Alr} \cdot v_p^{*}\right) \qquad 3.28$$

Here the subscripts r and i represent the real and imaginary components of the acoustic surface impedance, Z_{Al}.

The SH-SAW liquid interactions based on mechanical perturbations at the sensor surface include effects of mass loading and viscoelasticity.

3.4.1.1 Mass Loading in Liquid

The uniform loading of an isotropic thin film of thickness *h* and density ρ on to the metallised sensor surface in a liquid will provide the velocity shift and attenuation change as follows [115]:

$$\frac{\Delta v}{v} = -\frac{vhv_2^2}{4P}\left(\rho' - \frac{\mu'}{v^2}\right) \qquad 3.29$$

$$\frac{\Delta \alpha}{k} = 0 \qquad 3.30$$

Here, μ′ is the Lamè constant of the film and v_2 is the particle velocity component of the shear horizontal mode. It has been assumed that the liquid properties do not change before and after perturbation. The equations 3.29and 3.30 agree to Auld's equations for the gas phase.

3.4.1.2 Viscous Coupling

The liquid loaded on to the metallized surface of the SH-SAW sensor is presumed to be a Newtonian fluid with a viscosity of η and density ρ_l. By substituting the surface acoustic impedance into equations 3.27 and 3.28, the following expressions are obtained [115]:

$$\frac{\Delta v}{v} = \frac{vv_2^2}{4\omega P}\left(\sqrt{\frac{\omega\eta'\rho_l'}{2}} - \sqrt{\frac{\omega\eta\rho_l}{2}}\right) \qquad 3.31$$

$$\frac{\Delta \alpha}{k} = \frac{vv_2^2}{4\omega P}\left(\sqrt{\frac{\omega\eta'\rho_l'}{2}} + \sqrt{\frac{\omega\eta\rho_l}{2}}\right) \qquad 3.32$$

Here v_2 is the particle velocity component of the shear horizontal mode.

3.4.2 Acousto-electric interactions

The electric potential associated with the SH-SAW propagating on a piezoelectric surface extends several micrometers into the adjacent liquid. This

electric field affects the electrical properties of the materials within the liquid. As a result of this interaction, the velocity and/or attenuation of the SH-SAW propagation changes. The major electrical properties associated with the adjacent liquid are dielectric permittivity and conductivity. The expression for the complex permittivity is given by

$$\varepsilon_l = \varepsilon_r \varepsilon_0 - j\frac{\sigma}{\omega} \qquad 3.33$$

Here, ε_l and ε_0 are the permittivities of the unperturbed liquid and that of the free space, and ε_r is the relative permittivity of the unperturbed liquid. The conductivity σ of the unperturbed liquid is considered to be zero. Thus its electrical properties are given by:

$$\varepsilon_l = \varepsilon_r \varepsilon_0 \qquad 3.34$$

After perturbation, the complex permittivity ε_l changes to ε_l' and is given by:

$$\varepsilon_l' = \varepsilon_r' \varepsilon_0 - j\frac{\sigma'}{\omega} \qquad 3.35$$

Here ε_r' and σ' are the relative permittivity and conductivity of the measurand, respectively after the perturbation. The velocity and attenuation changes of the SH-SAW in the presence of a liquid is given below as [118]:

$$\frac{\Delta v}{v} = -\frac{K_s^2}{2}\frac{\left(\sigma'/\omega\right)^2 + \varepsilon_0\left(\varepsilon_r' - \varepsilon_r\right)\left(\varepsilon_r'\varepsilon_0 + \varepsilon_P{}^T\right)}{\left(\sigma'/\omega\right)^2 + \left(\varepsilon_r'\varepsilon_0 + \varepsilon_P{}^T\right)^2} \qquad 3.36$$

$$\frac{\Delta \alpha}{k} = \frac{K_s^2}{2}\frac{\left(\sigma'/\omega\right)\left(\varepsilon_r\varepsilon_0 + \varepsilon_P{}^T\right)}{\left(\sigma'/\omega\right)^2 + \left(\varepsilon_r'\varepsilon_0 + \varepsilon_P{}^T\right)^2} \qquad 3.37$$

Here K_s^2 is the electromechanical coupling coefficient when the free (non-metallised) sensor surface is loaded with the unperturbed liquid and $\varepsilon_P{}^T$ is the effective permittivity of the SAW crystal. The velocity and attenuation changes in the above equations show that they are proportional to the square of electromechanical coupling coefficient, which implies that substrates with a higher K_s will produce a high sensitivity. The following two parametric relations in the form of circle equations [65] can be obtained by eliminating the permittivity or conductivity from equations 3.36 and 3.37.

$$\left[\frac{\Delta v}{v}+\frac{K_s^2}{4}\frac{\varepsilon_0\left(2\varepsilon_r^{'}-\varepsilon_r^{'}\right)+\varepsilon_P{}^T}{\varepsilon_r^{'}\varepsilon_0+\varepsilon_P{}^T}\right]^2+\left[\frac{\Delta\alpha}{k}\right]^2=\left[\frac{K_s^2}{4}\frac{\varepsilon_r\varepsilon_0+\varepsilon_P{}^T}{\varepsilon_r^{'}\varepsilon_0+\varepsilon_P{}^T}\right]^2 \qquad 3.38$$

$$\left[\frac{\Delta v}{v}+\frac{K_s^2}{2}\right]^2+\left[\frac{\Delta\alpha}{k}-\frac{K_s^2}{4}\frac{\varepsilon_r\varepsilon_0+\varepsilon_P{}^T}{\sigma^{'}/\omega}\right]^2=\left[\frac{K_s^2}{4}\frac{\varepsilon_r\varepsilon_0+\varepsilon_P{}^T}{\sigma^{'}/\omega}\right]^2 \qquad 3.39$$

Electrical properties of the tested liquid including permittivity and conductivity can be obtained from the measured values of velocity shift *Δv/v* and attenuation change Δα/k by solving equations 3.38 and 3.39.

3.5 External environment effects

In addition to the electrical and mechanical effects, acoustic-wave devices are also sensitive to several physical parameters such as temperature, pressure, acceleration and stress. As a result of this wide range of measurand parameters, acoustic wave devices are considered to be suitable for a wide range of different sensing applications. However, each sensing application requires the exploitation of only one of these parameter sensitivities, thus making all other responses undesirable. Thus it is required to carefully control and eliminate the sensor cross-sensitivities [72].

3.5.1 Temperature effects

Temperature has a direct influence on the operation of all acoustic wave devices. The substrate density changes with temperature, resulting in a change of the velocity of the acoustic wave. Since acoustic velocity change is the most common factor of acoustic perturbation in a SAW device, there is a temperature-dependant component to the sensor output signal. There are three main techniques to reduce the effects of temperature variation on acoustic devices that includes selection of low-temperature-coefficient substrate cut, application of a temperature sensor and compensation circuitry and active control of sensor temperature [72].

Supposing a linear thermal increase in the substrate, then the acoustic path length *d* and the sensing length in liquid *l* will vary linearly as

$$d=d_o\left(1+\kappa\Delta T\right) \qquad 3.40$$

where, d_o is the length at a reference temperature T_o, ΔT is the change in temperature $(T - T_o)$, κ is the expansion coefficient and d is length at the final temperature T. The variation in the length Δd will increase the time constant by $\Delta \tau_o$, increasing the total delay time. A similar variation occurs to the sensing length l as well.

3.6 Generalised perturbation model for SAW device

A surface acoustic wave propagating on the piezoelectric sensor surface creates an electric field on the surface, which extends into the adjacent medium and subsequently measures the electrical parameters (dielectric permittivity and conductivity) of the adjacent medium, in addition to detecting the mechanical properties, including the viscosity and mass density. However, when the surface is electrically shorted, the electric potential becomes zero, thus measuring only the mechanical parameters. In general, the changes in the velocity and attenuation of a SAW sensor can be established to be functions of several parameters (denoted by $\psi(\rho, \eta, \sigma, \varepsilon, T)$), based on the discussions in sections 3.3 and 3.4.

$$\left(\frac{\Delta v}{v}\right)_{Free} = \psi(\rho, \eta, \sigma, \varepsilon, T) \qquad 3.41$$

For a shorted SAWR device, the electrical terms may be neglected leaving behind only the mechanical terms, as shown below.

$$\left(\frac{\Delta v}{v}\right)_{Shorted} = \psi(\rho, \eta, T) \qquad 3.42$$

Using the differential theorem, the total frequency shift, Δf, can be related to changes in the dependent parameters.

$$\Delta f_{Free} = \left\{ \frac{\partial f_{liq}}{\partial \rho_{liq}} \Delta \rho_{liq} + \frac{\partial f_{liq}}{\partial \eta_{liq}} \Delta \eta_{liq} + \frac{\partial f_{liq}}{\partial \sigma_{liq}} \Delta \sigma_{liq} + \frac{\partial f_{liq}}{\partial \varepsilon_{liq}} \Delta \varepsilon_{liq} \right\} \qquad 3.43$$

$$\Delta f_{Shorted} = \left\{ \frac{\partial f_{liq}}{\partial \rho_{liq}} \Delta \rho_{liq} + \frac{\partial f_{liq}}{\partial \eta_{liq}} \Delta \eta_{liq} \right\} \qquad 3.44$$

Thus, it can be concluded that the frequency response of a *free* SAW resonator depends upon the mass densityρ, viscosityη, conductivityσ, and dielectric permittivityε, of the medium, therefore a change in the frequency can be associated with one of these dependent variables.

3.7 SAW sensor design[1]

Surface acoustic wave resonator devices are realized by employing either one or two IDTs bounded by reflection gratings. SAW chemical sensors are usually configured as either a delay line or a resonator. SAW resonator devices are more attractive because they have narrow bandwidths, therefore higher Q-factors than delay lines, and, consequently, better signal-to-noise ratios. Moreover, SAW resonator based oscillator circuits offer better stability than the ones based on delay lines. The layout of a SAWR-based chemical microsensor is shown below. This section covers the design aspects for the Rayleigh mode SAW gas sensor and SH-SAW liquid sensors fabrication. Initially, the fundamental procedures for the SAW design are reviewed which is followed by the design parameters and a brief description of each configurations. The crucial block components in SAW resonator design are the inter-digital transducers (IDTs) and the reflectors, discussed below.

3.7.1 Interdigital Transducer Design

The excitation and detection of different types of surface acoustic waves and other plate waves on piezoelectric substrates is most readily accomplished by the use of an IDT [119]. The comb like IDT structure, as shown in Figure 3.3(a), is made from lithographically patterned metal film which is thick enough to offer low electrical resistance and thin enough to avoid any excessive mechanical load to the AW.

The electrode geometry (width, thickness, aperture), periodicity of the finger pairs and the total number of finger pairs generally define an IDT. A finger pair consists of two consecutive electrodes that are connected to different polarities. The

[1] *Design of SAW resonators used in this thesis were performed by Shrey Pathak, University of Warwick.*

electrical impedance of the AW device, the operating frequency, bandwidth and sensitive area are determined by the IDT [72].

When an RF voltage is applied to an IDT, synchronously varying deformation of the piezoelectric substrate generates an AW. The most efficiently excited wavelength λ equals the IDT periodicity '*p*'. An unperturbed AW velocity is always a constant and is equal to the product of wavelength and frequency. Thus, the IDT finger spacing governs the resonant frequency given by $f_o = v/p$.

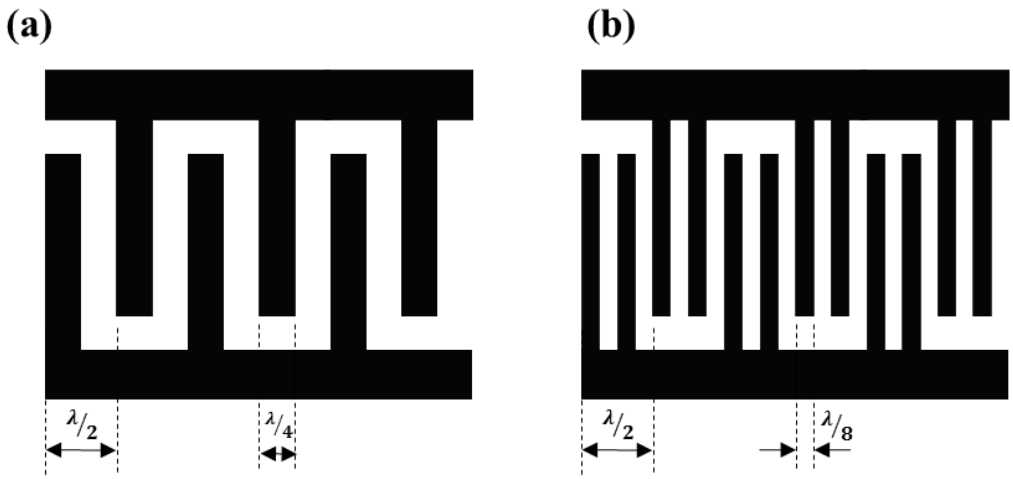

Figure 3.3. Characteristic features of (a) solid finger IDT (b) Split finger IDT

Another design parameter that relates to the acoustic wavelength is the finger width *w*. The most commonly used configuration is the solid finger type, which can facilitate the fabrication of transducers in the gigahertz range with lower transducer loss [120]. These electrodes possess a rectangular shape with a λ/4 width. Hence, consecutive fingers are uniformly spaced apart with equal gaps of λ/4 between them. Acoustic aperture is the length of the overlapping finger pairs and has to be chosen carefully in order to avoid optical radiation in the transducer resulting in diffraction of the acoustic beam before reaching the output IDT. This parameter determines the IDT impedance and previous works and literatures recommend apertures of at least 50 wavelengths. It has also been previously reported that successful 50Ω impedance IDTs could be achieved with an acoustic aperture of 72 wavelengths.

The generation of an AW is the cumulative effect of all the fingers, and hence the number of finger pairs is a critical design parameter. The number of finger pairs is calculated based on complex input and output power matching conditions and will be discussed in the following sections. It can also be noted that the bandwidth (*BW*) of the transducer is inversely proportional to the number of finger pairs (*N*) according to the relation: $BW \propto f_0/N$ where f_0 is the centre frequency. Increasing the number of finger pairs could provide a narrow bandwidth, which is suitable for applications such as resonators and delay lines, to avoid spurious responses and to achieve a higher stability. However, a trade-off should be made when choosing the number of fingers in an IDT. In practice, it is not advisable to increase the *N* over 100 to decrease the *BW* of the transducer. This could bring about extra mass loading and scattering effects due to the electrodes [72]. Also the impedance of the IDT will be also affected by the number of electrodes. Several other IDTs configurations and electrode geometries including apodization and split-fingering (As sketched in Figure 3.3(b)) could be used to shape the frequency response and to further enhance the performance of the IDT.

Depending upon the application type, finger reflections may have a desirable or undesirable effect on the SAW performance. In the case of solid electrodes IDT, all the metal fingers in the receiving IDT will be in phase at the centre frequency, so that the reflected SAW signal gets summed, resulting in maximum reflections at the centre frequency. (As sketched in Figure 3.4(a)). Unless compensated for, these reflections occurring at both ends of a λ/4 electrode usually degrade the amplitude and phase response of the IDT. For mechanical reflection, this structure is equivalent to a grating with periodicity $p_1=\lambda/2$, and Bragg reflection occurs at the fundamental resonance frequency of the SAW device [71].

In this work, two types of IDT geometries were utilized: the solid finger electrodes (as detailed above) for the design of R-SAW devices, and the split finger IDT for the design of SH-SAW devices. A standard technique used for the removal of the undesirable finger reflections associated with solid IDTs is to employ the split fingers IDTs design, as shown in Figure 3.3b. For the case of a split-electrode IDT with finger width and spacing of λ/8, different path lengths are such that the SAW reflections from each split-electrode pair cancel out, at the centre frequency, rather than being added up as of a single electrode IDT (as sketched in Figure 3.4(b)).

However, a disadvantage of using split-finger IDT is that due to the narrower strip width, an increased lithographic resolution is required for fabricating this IDT. Even though they require a higher definition, they have the capability to suppress the Bragg reflection at the SAW resonance frequency because the periodicity is $\lambda_0/4$ for mechanical reflection [71].

The use of split-finger IDTs may change some of the IDT design parameters including the effective electromechanical coupling coefficient K_e^2 associated with a substrate. Also, the capacitance C_T of a split-electrode IDT is 1.4 times larger than for a corresponding solid IDT.

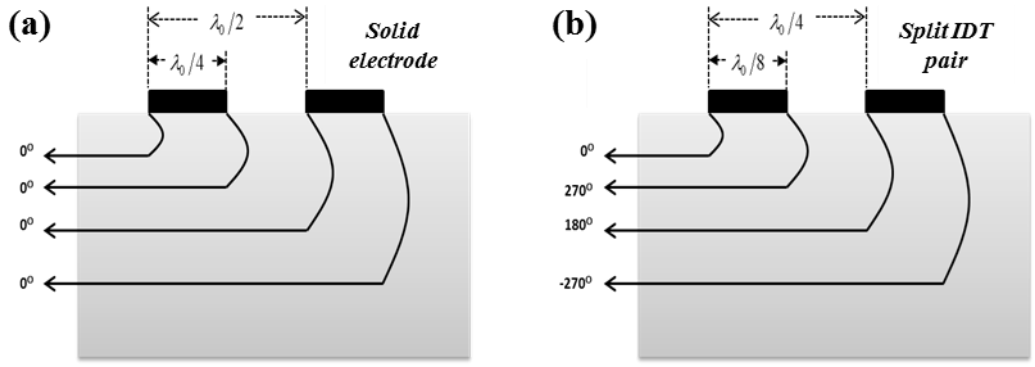

Figure 3.4. (a) Maximised SAW reflections for a solid finger IDT. (b) Minimal SAW reflections in the case of a split finger-pair IDT

3.7.2 Reflectors

Reflection gratings are periodically spaced discontinuities deposited on the surface of the piezoelectric substrate, in order to obtain a near-total reflection of the acoustic wave. The use of these metallic gratings causes electrical reflection in addition to providing mechanical reflection of the AW. At the centre frequency, the periodicity of the grating produce a cumulative reflection from the front and back edges of discontinuities, when the metallization ratio $\eta = 0.5$ is used. The number of reflector strips required for near-total reflectivity depends on the type of reflection mechanism used. Three types of SAW gratings include elements of shallow etched grooves, open-circuited (unconnected) or short-circuited thin metal strips deposited on the surface of the piezoelectric substrate as sketched in the Figure 3.5(a), (b) and (c) respectively. For the design of the sensors used in this work, metal gratings made of

short circuited strips have been chosen as reflector blocks, where all the strips are connected in parallel.

Various reflection mechanisms related to the SAW reflection grating are associated with piezoelectric shorting, geometric discontinuities, electrical regeneration and mass loading. They can be broadly classified into mechanical and electrical discontinuities, based on the nature of effects involved.

The variations in impedance existing at both the edges of each grating element produce the so-called mechanical SAW reflections. They can be generated by the *geometric discontinuities* imposed by etching groves onto the substrate or by depositing metal strips on its surface. The effect is weak for thin films and usually smaller than piezoelectric shorting or regeneration. However, this effect becomes significant for strips with film-thickness ratios $h/\lambda > \sim 1\%$. Another mechanism that can produce mechanical reflections is the *strips mass loading effect*, which is brought about by the differences in density and elastic properties between the metal film and the substrate. This will produce reflections only when using shallow groove gratings filled with heavy metal films (like gold) to substantially increase the reflection coefficient [100].

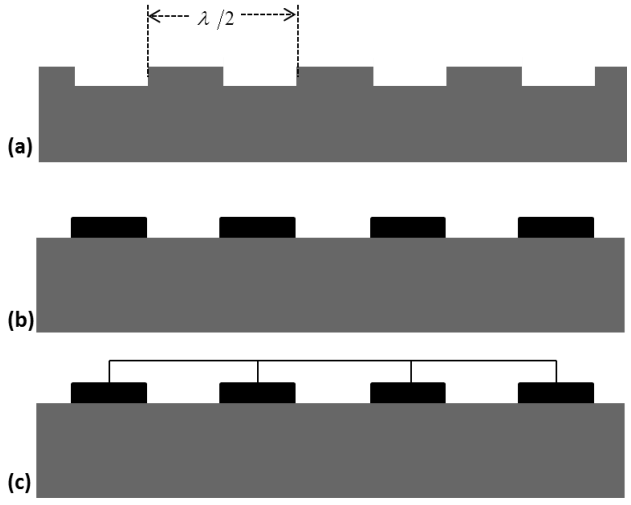

Figure 3.5. Types of SAW reflector gratings (a) Shallow grooves etched into piezoelectric substrate (b) Open-circuited metal strips (c) closed circuited metal strips

The piezoelectric nature of the SAW crystals produces the reflections due to electrical discontinuities. *Piezoelectric shorting* occurs when the electric field related

to the SAW propagation is short-circuited by the conductivity of the metal strips, thus producing a SAW perturbation. This effect is significant only for materials with large coupling coefficient K^2, such as $LiNbO_3$ or $LiTaO_3$. Additionally, *electrical regeneration* is another effect that can bring about electrical reflections. An electric potential is created between the adjacent strips, when the surface waves are incident on a grating structure. This potential regenerates a surface acoustic wave in addition to the reflected component due to piezoelectric shorting.

3.7.3 Design parameters

The transfer response of a two port SAW resonator will depend on several parameters. Some of the critically influential parameters include the spacing between each reflection grating and its adjacent IDT; grating reflectivity and loss; separation between reflection gratings; number of IDT fingers; IDT film thickness and resistivity; K^2 and C_0 values of the piezoelectric substrate; and the operating frequency. Hence, in order to attain constructive interference and to obtain a SAW standing wave pattern at the resonant frequency, the individual structures need to be placed at precise distances from each other. In this section, the various spacing parameters have been calculated.

For a given substrate, the wave propagation velocity, *v*, can be considered as a physical constant. Since $v=f\cdot\lambda$, the frequency, *f*, of the sensor determines the wavelength, λ, of the acoustic wave. In order to create a standing wave pattern, all electrode fingers must be positioned above the wave maxima; therefore, the minimum distance between the two IDTs, (i.e. cavity length), d_t should be equal to $\lambda/4$, which can be expanded by half-wavelengths, thus $d_t = \lambda/4 + n\lambda/2$, where *n* is an arbitrary integer. Furthermore, depending on the sign of the substrate reflection coefficient and grating connection, the optimal spacing between the IDT and the reflector grating are varied by $\lambda/8$ from that of the synchronous spacing between the structures. Because the standing wave patterns are periodic, the reflector grating can be moved out by an integer number of acoustic half-wavelengths [100]. Hence, the IDT-reflector spacing is determined by the optimal spacing formula: $d_r = \lambda/8 + m\lambda/2$, where *m* is an arbitrary integer.

The number of reflectors, N, is determined using $R = \tanh(N|r|)$ where R is the total reflection coefficient which relates the ratio of reflected to incident surface waves entering the reflection grating, r is the reflectivity of a single shorted reflector strip, which can be calculated from $r = -0.5h/\lambda$, where h is the thickness of metallization, and N is the number of electrode finger pairs [100].

The IDT static Capacitance C_T is given by the relation:

$$C_T = NC_s = NC_oW \qquad 3.45$$

where N is the number of IDT finger pairs, C_s is the capacitance/finger-pair, C_0 is the capacitance/finger pair/unit length (values for different substrates are shown in the Table 3.1) and W is the acoustic aperture.

Table 3.1. Acoustoelectric properties of SAW substrate materials [100], [121]

Substrate, Cut, Propagation Direction	**Acoustic Velocity (m/s)**	**Electromechanical coupling coefficient (K^2) (%)**	**C_s (pF/cm)**
Quartz ST X	3158	0.11	0.5
Lithium Niobate Y Z	3488	4.8	4.6
Gallium Arsenide Z X+22.5º	2763	0.022	1.2
Lithium Tantalite 36° Y X	4161	4.7	4.4

The unperturbed radiation conductance, G_a at the resonant frequency, f_0 with negligible finger reflections is obtained by

$$G_a(f_0) = 8K^2 f_0 N_p^2 C_s \qquad 3.46$$

where K^2 is the piezoelectric coupling constant (0.11% for ST-quartz). In order to compensate for the reduction in radiation conductance due to IDT finger reflections, a

large number of fingers are normally required for substrates with low K^2 coupling factors. This helps to increase the radiation conductance to sufficient levels for input/output impedance matching [100].

3.7.4 SH-SAW Sensors: Design and layout

The cell-based SH-SAW micro-sensors were micro-fabricated using 100 nm thin gold electrodes on a 36°-rotated Y-cut X-propagating $LiTaO_3$ substrate using a combination of conventional photolithography and lift-off. The employed design considerations, especially the large sensing areas, allow ligand sensing in liquid environments and enable the deposition, culturing and characterization of Sf9 cells at a reasonably high acoustic frequency. An SH-SAW device frequency of 60 MHz was selected based on the required wave penetration depth (i.e. the distance of the area of interest in the Sf9 cells) and the required method of operation. SAW resonator based sensors, being more sensitive than delay lines, require only much simpler interface circuitry to obtain a frequency output. The design specifications of the 2-port SH-SAW resonator to be used in a cell-based chemoreceiver are detailed in the Table 3.2.

Table 3.2. Design parameters for the SH-SAW resonator for cell-based chemoreceiver

SAW Resonator Type	***Two Port-Free***	***Two Port-Shorted***
Frequency [MHz]	60.56	60.56
Wavelength , λ [µm]	68	68
IDT split-finger Width [µm]	8.5	8.5
Number of finger pairs per IDT	5.5	5.5
Acoustic Aperture [µm]	3400 [50 λ]	3400 [50 λ]
Cavity length [µm]	5015.26 [73.75 λ]	5015.26 [73.75 λ]
Number of stripes per reflector pair	100	100
Distance between IDT-Reflectors [µm]	42.5	42.5

A metallised version of the 60 MHz SH-SAW device was included in the study, in order to be able to measure the purely mechanical effects by nullifying the

electrical effects during ligand detection. Thus, two different operating configurations were designed, namely free and metallized, for the two port resonator SH-SAW configuration for being used in the detection of biological analytes. The sensing area of the *free* resonator was left bare without any metallization, with the intention of coating the device with a biological coating layer. In contrary to the *metallised* sensing area, the use of a free sensing area allows the measurement of the both the electrical and mechanical effects occurring during ligand addition. On the *free* surface both the SSBW and Leaky SH-SAW propagate on a 36^{o} rotated Y-cut X propagating $LiTaO_3$ crystal [71].

The sensors were designed in dual configuration to eliminate environmental and common mode interferences on the sensing signal, such as changes in ambient temperature or pressure. This allows differential measurements in which one device of the pair is functionalized with transfected cells and the other serves as a reference (e.g. normal cells). Measuring the difference between the signals of the two devices ensures that the measured responses are produced purely by the functionalized coating. The reference resonator was either left bare or deposited with control Sf9 cells, with the intension of forming a control signal. The photograph of the 60MHz SH-SAW device is shown in Figure 3.6.

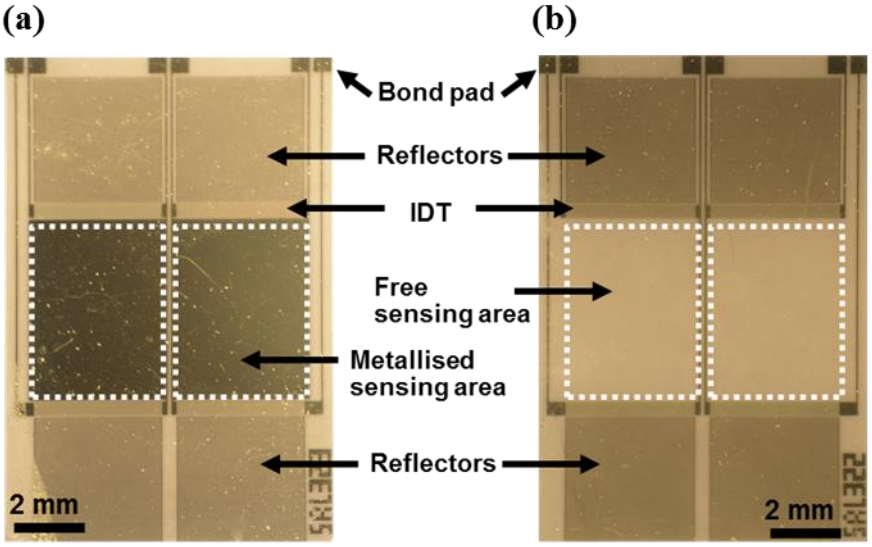

Figure 3.6. Optical micrographs of three variations of a 60 MHz $LiTaO_3$ SH-SAW resonator with (a) metallised sensing surface, (b) free sensor surface

3.7.5 R-SAW Sensors: Design and layout

In addition to the development of liquid phase $LiTaO_3$ based SH-SAW biosensors for cell-based ligand detection, quartz based gaseous phase SAW sensors have also been designed. The SAWRs were fabricated in aluminium on an ST-cut quartz substrate using UV lithography (PacTech, Germany). Unlike $LiTaO_3$ SAW devices that employ shear horizontal surface acoustic waves, gas phase sensors utilize Rayleigh waves. These devices provide high vapour phase sensitivity because of the fact that Rayleigh waves have a surface-normal displacement component. The R-SAW sensors, being very robust and low maintenance devices, will be used as an alternative to cell-based ligand sensing. They are functionalized with different types of polymer coatings with parts-per-billion (ppb) range sensitivity. Similar to the liquid phase devices, two-port R-SAW resonators have also been designed in a dual configuration, so as to enable differential operation. Table 3.3 lists the major design specifications of the quartz based 262 MHz SAWR devices. The optical micrograph of a 262 MHz Rayleigh mode dual SAW resonator sensor is shown in the figure 3.7.

Table 3.3. Design parameters for the SAW resonator for gas phase detection

SAW Resonator Type	***Two Port-Free***
Frequency [MHz]	262.98
Wavelength , λ [µm]	12
Number of finger pairs per IDT	60.5
Acoustic Aperture [µm]	720
Delay path length [µm]	303
Cavity edge-edge [µm]	1764
Number of stripes per reflector pair	600
Distance between IDT-Reflectors [µm]	7.5

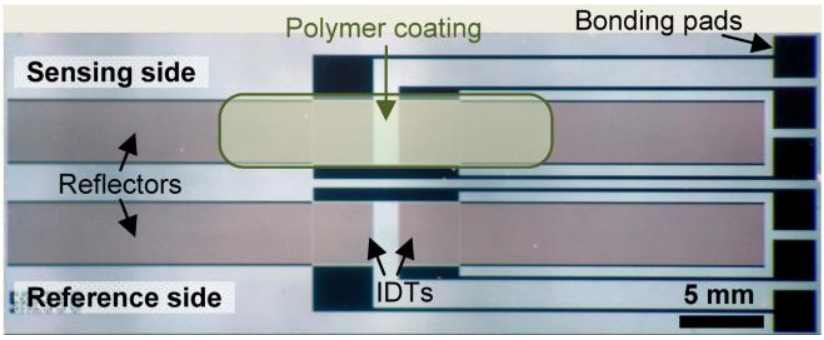

Figure 3.7. Optical micrograph of a 262 MHz Rayleigh mode dual SAW resonator sensor for gas phase measurements

3.8 RF characterisation of sensor devices

The measurement of the frequency response of an AW device provides a better understanding of the sensor response to an external perturbation such as chemical/biological sensing. Additionally, this also allows the design of a stable and accurate measuring system for the particular type of resonator. Obtaining the frequency response of a device before and after modifying the sensor surface, (eg. by the addition of a liquid layer or deposition of a polymer layer), will provide the user with more information regarding the physical properties of the contacting liquid or layer, than measuring the oscillation frequency alone. The frequency response of a SAW resonator is defined by the magnitude and phase of its signal output obtained by the application of a constant magnitude input signal as a function of frequency. The magnitude and phase of the generated acoustic wave changes as a function of time, due to the effect of different mechanical and electrical perturbations. The characterization of high frequency SAWR devices are usually performed with a network analyser, which analyses the electrical proprieties of the devices in terms of reflection and transmission signals. The measurement of the various reflection and transmission parameters is done by characterising the scattering parameters (S parameters), which describes the signal flow within the test sensor.

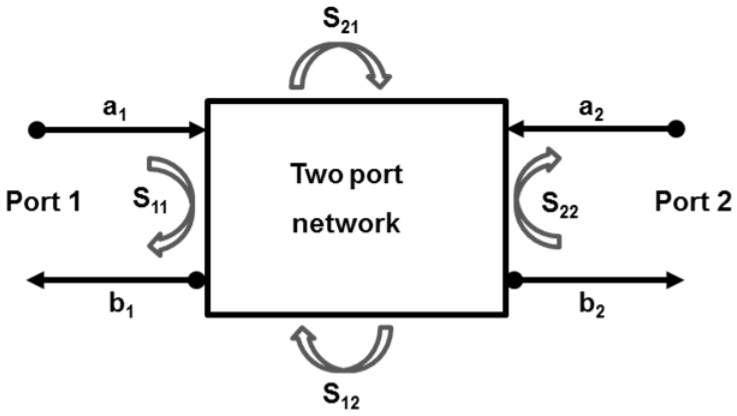

Figure 3.8. Signal flow diagram of a two-port network used to define S parameters

As shown in the figure 3.8, a_1 is the incident signal from the port 1 of the network analyser, and b_1 is the reflected signal from the sensor device into the port 1 of the analyser. Similarly, a_2 and b_2 are the incident and reflected signal to and from the sensor device, respectively. Thus the two-port device has four S-parameters, namely S_{11}, S_{22}, S_{12} and S_{21}. The S-parameters are computed and measured using the equations 3.47, 3.48, 3.49 and 3.50, where S_{11} and S_{22} shows the reflection coefficients at port 1 and 2 respectively while S_{21} and S_{12} shows the transmission coefficients between the ports 1 and 2. The reflection and transmission coefficients of the two port SAW microsensors was measured using an E5071B RF Network Analyser, which has a frequency range of 300kHz to 8.5GHz.

$$S_{11} = \frac{Reflected}{Incident} = \frac{b_1}{a_1}\bigg|_{a_2=0} \qquad 3.47$$

$$S_{22} = \frac{Reflected}{Incident} = \frac{b_2}{a_2}\bigg|_{a_1=0} \qquad 3.48$$

$$S_{21} = \frac{Transmitted}{Incident} = \frac{b_2}{a_1}\bigg|_{a_2=0} \qquad 3.49$$

$$S_{12} = \frac{Transmitted}{Incident} = \frac{b_1}{a_2}\bigg|_{a_1=0} \qquad 3.50$$

As the two port SAW devices are having an input port and an output port unlike the one port devices, the transmission coefficients are found to be more effective than the reflection coefficients. Even though the reflection coefficients can be of great help in diagnosing any IDT related problems, estimation of transmission parameters are more useful in sensing applications, as it helps to determine the insertion loss within the SAWR resonator.

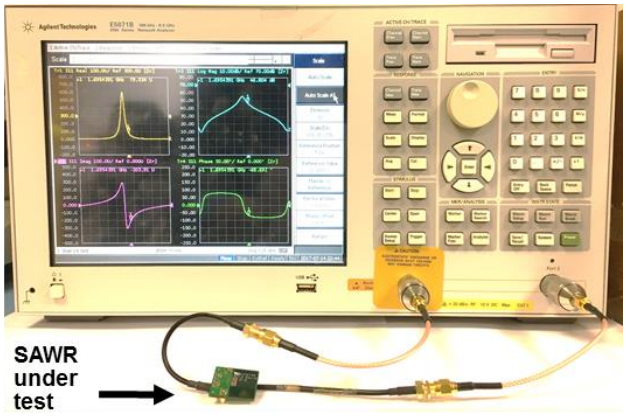

Figure 3.9. SAW resonator connected to the E5071B Network Analyser to measure the device frequency response.

3.8.1 Transmission characteristics of SH-SAW sensors

SH-SAW sensors were characterized using the network analyser (connected as shown in Figure 3.9) and transmission parameters over the same frequency range (50 MHz to 70 MHz) are shown in the Figures 3.10 to 3.13. The insertion loss for the metallised (shorted) SH-SAW resonators when the devices are not loaded is shown in the figure 3.10. It can be noted that the attenuation at the designed frequency of operation is about 8 dB. The plot showing the attenuation curve for the same metallised SH-SAWR when the device is loaded with a PDMS microfluidic chamber is shown in Figure 3.11. When comparing the above two plots (Figures 3.10 and 3.11), it can be observed that the extra attenuation added to metallised SAWR is only about 2 dB, which can be easily addressed by the amplifier gain within the oscillator loop.

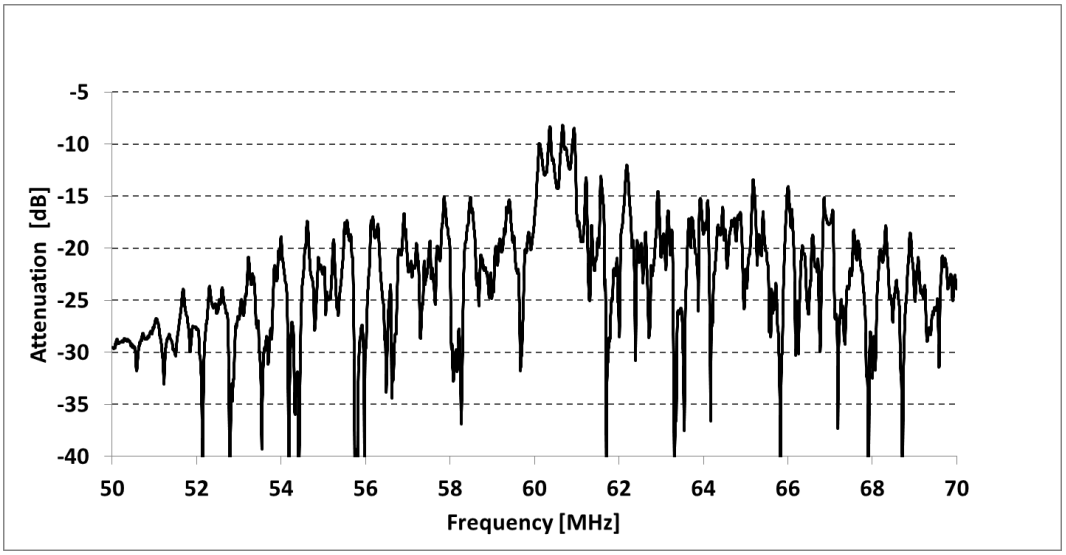

Figure 3.10. Attenuation vs. frequency plot for a 60 MHz metallised SH-SAW resonator without mass loading.

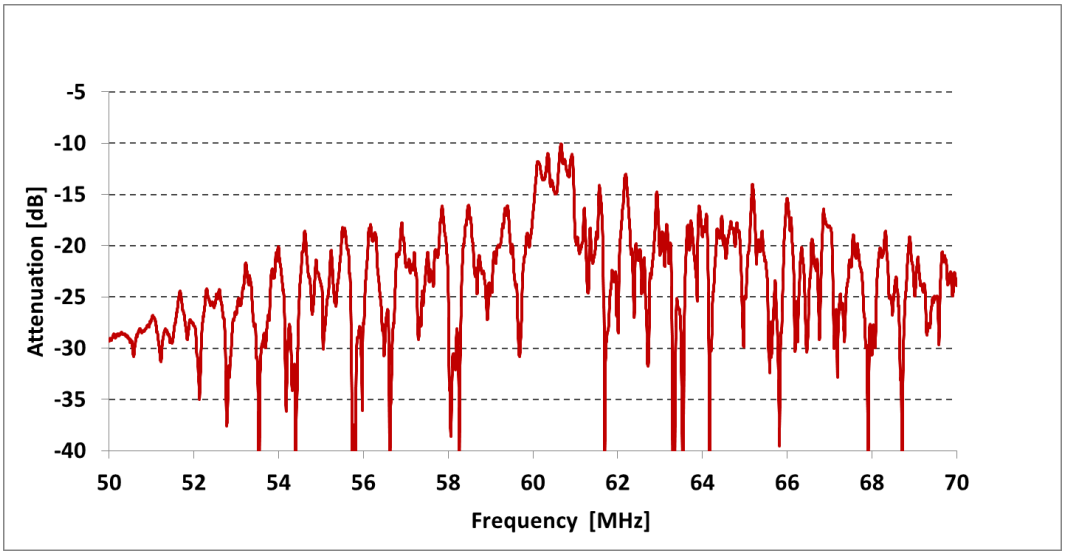

Figure 3.11. Attenuation vs. frequency plot for a 60 MHz metallised SH-SAW resonator with PDMS chamber on the sensor surface.

The Figures 3.12 and 3.13 shows the attenuation curves for the non-metallised free SH-SAW devices before and after PDMS loading on the sensor surface, respectively. It can be noted that loading the sensor surface with PDMS microfluidic reservoir increases the attenuation by about 2 dB, similar to the metallised devices.

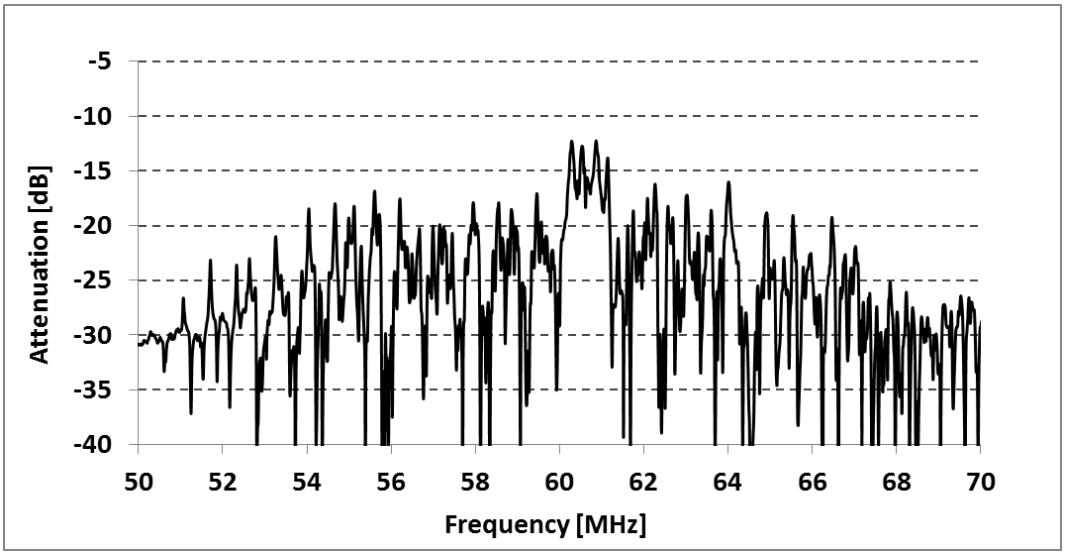

Figure 3.12. Attenuation vs. frequency plot for a 60 MHz free SH-SAW resonator without mass loading.

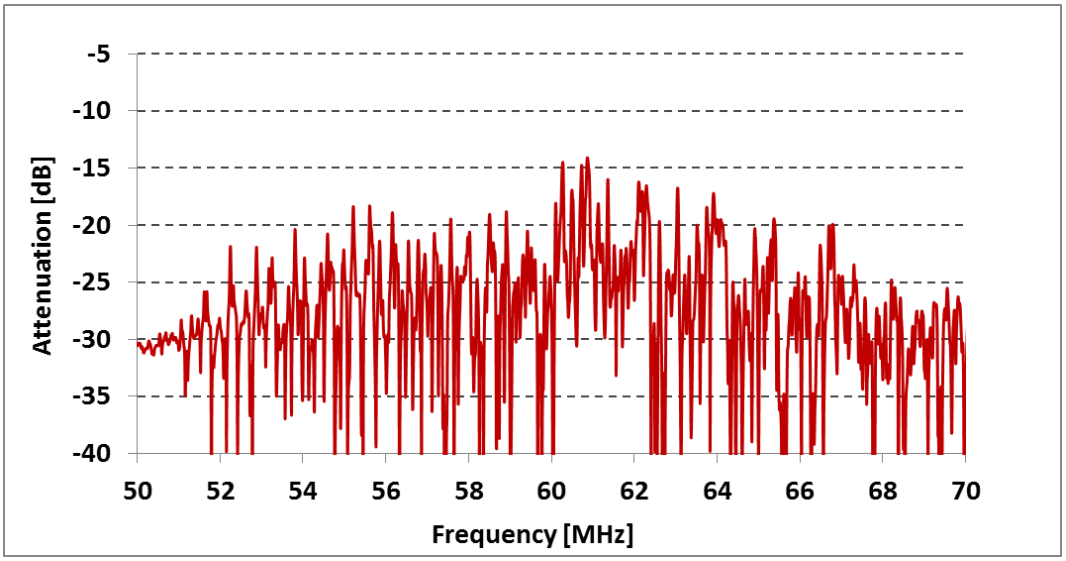

Figure 3.13. Attenuation vs. frequency plot for a 60 MHz metallised SH-SAW resonator with PDMS chamber on the sensor surface.

By comparing the transmission coefficients of the free and metallised SH-SAWRs in Figures 3.10 and 3.12 shows that the attenuation is significantly reduced when the sensing surface is metallized. The transmission coefficient of the metallised device shows that metallisation of the propagation path traps and localizes the acoustic wave to the surface, thereby reducing the insertion loss, comparing to the free devices.

3.8.2 Transmission characteristics of R-SAW sensors

The Figure 3.14 shows the S21 magnitude plot of the 262 MHz free R-SAW resonator depicting the typical device insertion loss of about 9 dB. This indicates that the energy dissipation due to IDT based acousto-electric conversion, is very low.

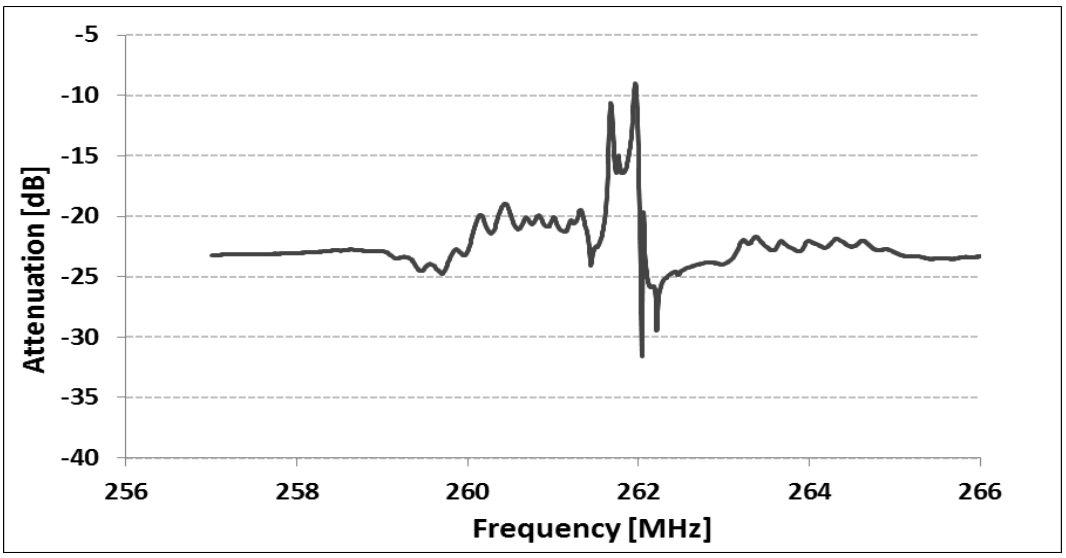

Figure 3.14. Attenuation vs. frequency plot of an unloaded 262 MHz free R-SAW resonator.

The transfer characteristics of the oscillator circuit is shown in Figure 3.15, which shows that there are only two distinct peaks above zero dB, across the region of interest, near to the desired oscillation frequency region. Out of the two available peaks, the one which satisfies the total oscillator phase shift of 0 degree for the entire feedback loop, will be the actual frequency of operation of the sensor device. The entire phase of zero degrees is obtained by adding together the phases from the amplifier, filter and other circuit components. As devices suffer from individual differences, the actual frequency of operation could deviate from the designed frequency by a few kilohertz.

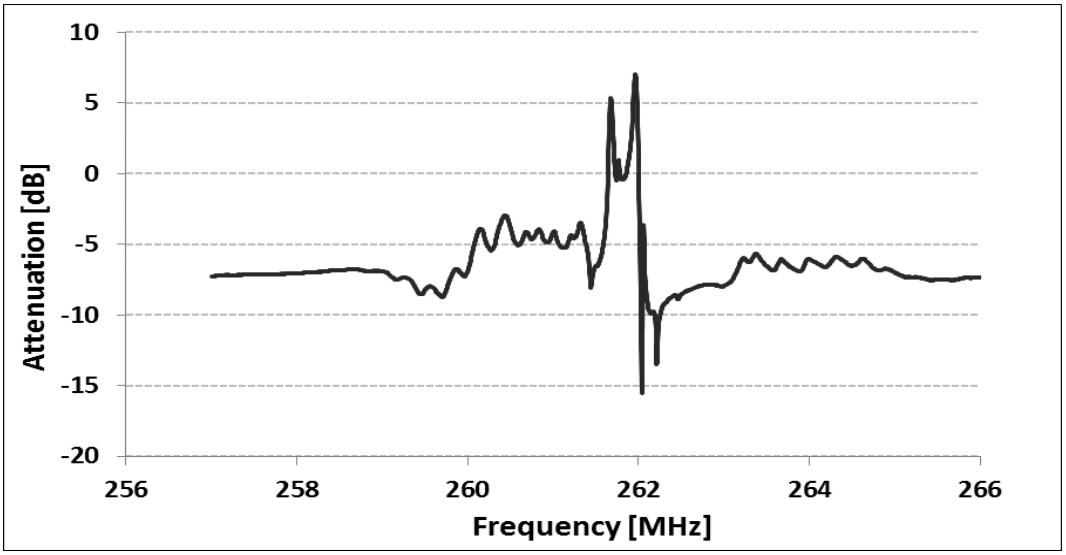

Figure 3.15. Transfer characteristics of the oscillator loop around the resonator frequency of 262 MHz.

3.9 SAWR Oscillator circuit design and implementation

Since the use of a comparable reference sensor is the most popular method for compensation [82], the designed 2-port SAW sensor operates in a dual configuration. As explained in the section 3.7.4, one side of each dual device acts as a reference signal, while the other side is used for the detection of the ligand/gas molecules. This differential signal has a reduced noise level and improved signal stability by maintaining a high signal to noise ratio. Figure 3.16 (a) shows the schematic block diagram of the dual SAW oscillators and Figure 3.16 (b) shows the photograph of the 262 MHz dual SAW resonators driven by separate oscillator boards.

The SAWR sensors were driven by amplifier based independent feedback-oscillator circuits consisting of surface mount amplifiers, a low pass filter, and the buffer circuitry. The oscillator PCBs are four layered with separate grounding planes which takes account of the phase shifts associated with the RF signal path within the resonator circuitry loop. It also reduces the RF cross talk, thereby improving noise sensitivity.

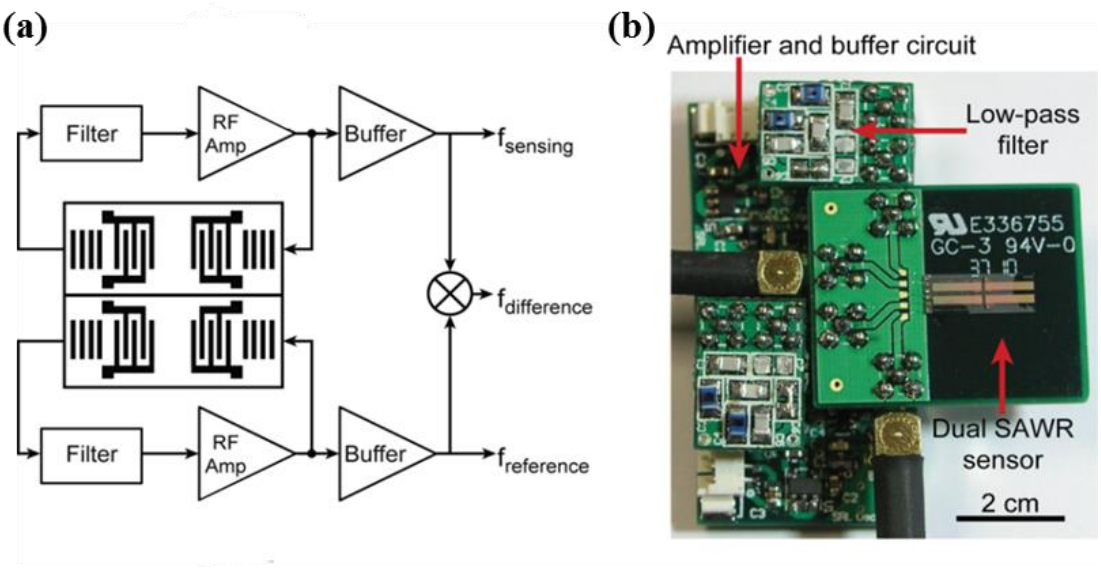

Figure 3.16 (a) Schematic block diagram of the Dual setup of the SAW resonators based oscillator circuitry. (b) Photograph of the 262 MHz dual SAW resonators driven by separate oscillator boards.

A schematic layout of the RF oscillator circuit is shown in Figure 3.17 comprising low pass filter, amplifier and buffer stages. The entire SAWR oscillator system is having a modular arrangement, so as to maintain the signal integrity and reduce the high-frequency signal cross talk. The amplifier board, low pass filter board and the SAW sensor board are plugged-in together to constitute the oscillator feedback system.

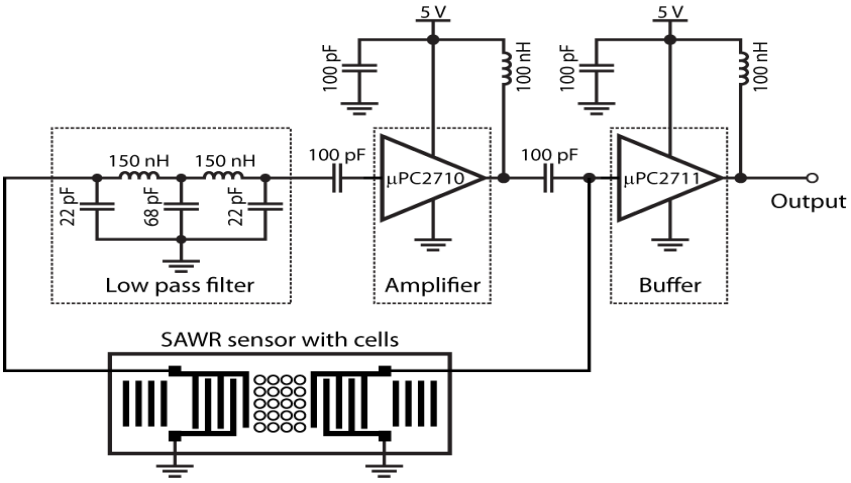

Figure 3.17. Schematic circuit diagram showing the 2-port SAWR sensor with the matched feedback-loop oscillator circuit for frequency read-out.

3.9.1 SAW sensor board

The SAW sensor boards are plug-in boards that are designed and fabricated to accommodate the SAW resonator dies. They provide contact pads for wire-bonding the SAWR sensors, and also serve as platforms for the PDMS microfluidic chambers. The SAW devices are used as the frequency and phase selective elements in the feedback loop of the oscillator circuit because they provide a maximum signal transmission at the designed resonant frequency of operation with very low attenuation.

3.9.2 Oscillator board

A dual feedback-loop type oscillator circuit utilizing broad-band radio frequency amplifiers and the SAW devices as the frequency selective elements is realised in the oscillator board. Two conditions to be satisfied for the circuit to oscillate includes a total loop gain of the circuit greater than 1 and secondly, the phase shift in the loop must be equal to 0°, as stated by the Barkhausen criterion (Barkhausen criterion will be discussed in detail in section 6.4). Each two-port oscillator circuit contains an RF bipolar amplifier µPC2710, which is a low cost Silicon Monolithic Integrated Circuit (IC) suitable for high gain (in excess of 30 dB) applications and with a high bandwidth of 1.5 GHz. The µPC2710 IC is featured by flat gain characteristics and low power consumption. It also has internal impedance matching provided to compensate for signal losses in the feedback loop due to the insertion loss of the SAW sensor (typically <10 dB), mass-loading during operation (~4 dB), attenuation by the filter, the signal paths and imperfect impedance matching (~1-2 dB). A µPC2711 silicon based wideband amplifier with 2 GHz bandwidth was used as an output buffer for the oscillator loop.

3.9.3 Filter board

The filter boards are employed to narrow the frequency band of operation of the oscillator board and also to achieve the desired frequency shift. A fifth-order low-pass Butterworth filter is used to remove oscillations at unwanted harmonic (higher)

frequencies. These daughter boards are realised using passive elements that can provide the required filtering as well as phase shifting.

The SAW biosensor serves as the resonating element in the feedback loop of the oscillator circuitry. The external phase shift and frequency selective filter and the SAW sensor board can be plugged into vertical connectors on the oscillator board. Figure 3.18 shows the photograph of the overall dual 262 MHz SAWR oscillator with surface mount amplifier, filter and buffer circuitry. The frequency output of the oscillator circuit is measured and recorded via the µPC2711 voltage buffer using a commercial FQ4 interface (JLM Innovation, Germany), which is connected to a computer via the USB port.

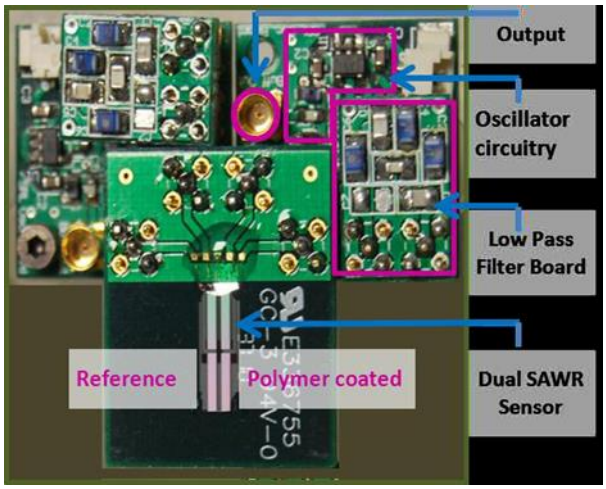

Figure 3.18. Photograph of a dual 262 MHz SAW resonator sensor with surface mount amplifier, filter and buffer circuitry.

3.10 Summary

This chapter covered the basic theory behind the perturbation effects occurring in an acoustic sensor. Detailed analysis of the various perturbation mechanisms were discussed for polymer-coated Rayleigh SAW sensors. In addition, the electrical and mechanical parameters affecting the fractional velocity and attenuation change in a SH-SAW based liquid sensor were also analysed. The basic operational principle and detailed theoretical design parameters affecting the sensor response of a two port SAW resonator has been presented. The various design details of the sensors along with the dimensions and layouts have also been detailed. The next chapter details the SAWR

based ligand detection of fruit volatiles and insect pheromones in a gaseous environment.

CHAPTER 4

SAWR Ratiometric infochemical detection

4.1 Introduction

The basics of infochemical communication and the mechanism of insect olfaction have been reviewed in the chapter 1, which acts as the backbone for the work detailed in this chapter. This chapter details the development of a prototype infochemical communication system based on polymer-coated surface acoustic wave microsensor arrays. The system described here is capable of detecting the ratio of predefined volatile compounds and recovering the ratiometric information deployed in the environment. The design of Rayleigh SAW resonators that has been employed in the detection of odorants have been previously detailed in Chapter 3. General characterization of different semiochemicals and their concentration ratios has been carried out by using SAW sensors, which rapidly measures trace levels of molecules in air utilizing the concept of receptor-ligand interaction on a sensor surface. Employing SAWRs to study the semiochemistry helps in the development of a superior biosensing technology that is capable of discriminating between various semiochemicals.

Intraspecific communication in insects is achieved by the use of semiochemicals; these odour signals are able to modify behaviour such as conspecific mate finding, location of food, and other social interactions [1]. The odour signals received from the olfactory sensory neurons on the antenna are translated to a complex behavioural pattern within the antennal lobe of the insect olfactory system. The well-studied infochemical-mediated behaviour of the moth '*Spodoptera littoralis'* , both from a behavioral and neurophysiological point of view, served as the biological inspiration for the work described in this chapter [122] [123]. The behavior of this moth species is grounded on a precisely controlled blend of well-established info-chemicals (eg. sex pheromone), and also the biosynthetic stages of generation of these pheromones have been well-defined [1]. The work presented in this chapter arises from an EU-funded FP6-032275 project called "Biosynthetic Infochemical Communication" [2].

Insects, in particular moths, rely on blends of several chemical compounds to communicate using their sophisticated low-power chemical signaling and processing systems [91]. As species-specific blend ratio is crucial for male orientation to a female emitter [124], specificity is achieved by specific blends of pheromone components with variation in molecular chain length, unsaturation level, functional group and total number of compounds; rather than by chemically unique structures [125]. These infochemical signal blends are produced by generating a spatially and temporally defined combination of several semiochemicals that are often biosynthesized in the insect's pheromone gland. The female moths usually release minute quantities of pheromone blends into the air, which are detected several miles away, by the extremely sensitive and feathery antennal system of the male moths. Component-specific receptor proteins present in the antennal sensory neurons of the male moths are activated by these odor cues, producing electrical potentials conferring information about the odorant molecule [126]. These electrical signals are processed into a unified, ratiometric signal within the antennal lobe of the brain [127].

An artificial system based on moth-pheromone communication has been developed to demonstrate pheromone-based ratiometric information encoding, transmission and decoding. This innovative modular system consists of a microsystem, called *chemoemitter* module, which is capable of releasing a predefined ratio of volatile compounds utilizing an artificial gland; mimicking pheromone

production and release in a female moth. An array of polymer-coated piezoelectric Surface Acoustic Wave Resonator (SAWR) sensors has been utilized here, which helps in the detection of the pheromone blends released into the environment. The sensor array forms the chemoreceiver module, which in turn mimics the molecular detection in the insect antenna. The signal processing in the antennal lobe of the insect brain is simulated by recovery of ratiometric information contained in the odor cues by the use of a biologically constrained signal processing model. The modular arrangement of the chemoemitter and chemoreceiver [128] sections of an infochemical communication system prototype is shown in Figure 4.1, which details the relationship between the biological and technological counterparts.

As pheromones play an important role in triggering a pre-encoded behavior in an insect, several works have been identified in the recent years using various pheromone compounds and their species-specific blends as detailed in [129]–[131]. The ratio between the two pheromone isomeric components (E)-11 and (Z)-11-tetradecenyl acetate (E11 and Z11-14: OAc) from two populations of the redbanded leafroller moth *Argyrotaenia velutinana* has been analysed by Miller and Roelofs in 1980 [132]. Most moth pheromones are biosynthesized with specific ratios according to small variations on a given subject, which makes it possible to mimic the "generating" and "sensing" process of moth pheromones. There are at least two distinct pheromone components known in the moth species *Spodoptera littoralis*, which are well defined. (i.e, Z9-14:OAc and E11-14:OAc). Hence, the two pheromones Z9-14: OAc and E11-14: OAc have been utilized in our work to demonstrate the recovery of ratiometric information using our infochemical system.

This chapter reports on the detection of the biosynthetic ligands using the SAWR sensor system and the decoding of ratiometric information using real-time data processing methods. Several features of SAWR sensor signals have been extracted as an approach for rapidly decoding ratiometric infochemical signals in real-time. With complementarily tuned sensors and advanced neural network algorithms, the presented infochemical system, having the potential for autonomous operation, mimics pheromone-based communication between insects.

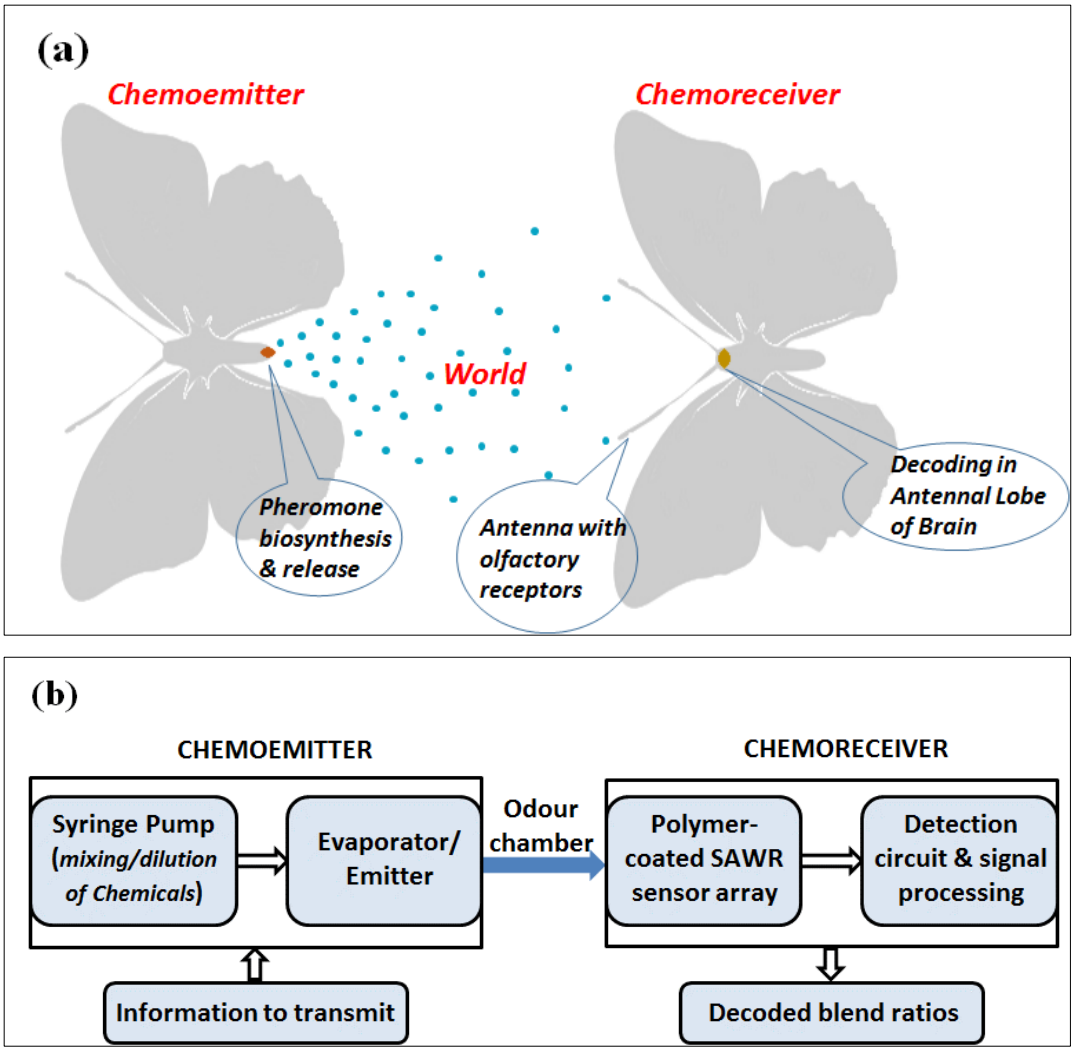

Figure 4.1. (a) Diagram showing the relation between the primary biological components contributing in pheromone-based insect communication (b) corresponding bio-inspired modules that form a biosynthetic infochemical communication system.

4.2 SAWR Sensor Array

Acoustic wave devices are commonly employed as gas sensors as they operate by detecting the effect of sorbed molecules on the propagation of acoustic waves. After the introduction of organic vapour sensors by King in 1964 using coated bulk wave resonators [133], a variety of other piezoelectric acoustic wave devices including SAW devices, flexural plate wave devices, and horizontally polarized shear wave devices have also been utilized to create acoustic chemical sensors. The quartz-based

SAWR chemical sensors (although other piezoelectric materials such as lithium niobate, lithium tantalite or zinc oxide can be used) are coated with chemically selective functional coatings to accumulate vapor molecules from the gas phase at the device surface. Sorption of vapor molecules into the sorbent coating changes the propagation of the acoustic wave bringing about changes in the wave velocity, which can be measured indirectly, as a frequency shift in the resonant frequency, with improved accuracy, selectivity and sensitivity. The chemoreceiver detects and recovers the ratiometric chemical information via an array of robust, and highly sensitive SAWR devices hosting polymer layers. The 263 MHz SAW resonators fabricated on ST-cut quartz substrates using Al electrodes are designed in a dual configuration [16], as discussed in section 3.9. More details of the design parameters and fabrication of the Rayleigh based 262 MHz SAW resonator has been reported in section 3.7. In order to obtain highly stable and precise frequency measurements while detecting the SAW propagation characteristics, the SAW resonator is driven by simple feedback based oscillator circuits, details of which are presented in section 3.8.

4.3 Ratiometric Infochemical Communication

4.3.1 Experimental System Setup

The design and realization of a biosynthetic infochemical communication prototype system [134][135][136][1] has been carried out by mimicking the communication structure and system architecture of insect communication. This system consists of functionally comparable modules comprising a chemoemitter, an odour chamber and a chemoreceiver for encoding, transmitting and decoding ratiometric infochemicals, respectively. The chemoemitter system comprises of a neMESYS high-precision multi-channel syringe pump (cetoni GmbH, Korbussen, Germany) connected to a bioinspired micro machined evaporator (developed by MESA+) termed ‘artificial gland’[137], [138]. A precise mix of predefined volatile compounds in programmable ratios of concentration is delivered to the SAWR chemoreceiver with the help of the syringe pump and micro evaporator.

As the pheromone blends have a higher boiling point of 135^{o}C, it was essential to keep the micro evaporator at elevated temperatures. However, raising the

temperature of the micro evaporator would result in condensation within the chamber walls. As a trade-off, in order to balance out these factors, the artificial gland membrane was maintained at an optimum temperature of 120^{o}C with the aid of an external PID controller. Thus the liquid-based pheromone blends are released as volatiles, into the environment as time-sensitive and time-registered information via controlled thermal volatilization using the artificial gland and its associated controller. The Perspex odour chamber (14×14×40 cm^3 volume) which forms the wind tunnel is coupled to a membrane venting pump, in order to transport the odour cues to the piezoelectric SAWR sensor arrays situated at the opposite side. The horizontally arranged three dual SAWR sensors which forms the chemoreceiver module helps in the detection and decoding of the ratiometric information. The SAW sensors are associated with their individual discrete oscillator circuits, which in turn is connected to commercial interface circuitry for real-time frequency measurements (JLM Innovation, Germany). The real-time resonant frequencies of 6 channels (each SAWR oscillator) were recorded individually during the measurements. Figure 4.2 shows a schematic block diagram of the pheromone based communication system comprising of the chemoemitter module, the wind chamber and the chemoreceiver module. A prototype of the insect-based pheromone communication system has been fabricated as shown in Figure 4.3[a]. Photographs of the three sets of the dual polymer-coated SAWR sensor array used inside the test chamber is shown in Figure 4.3[b].

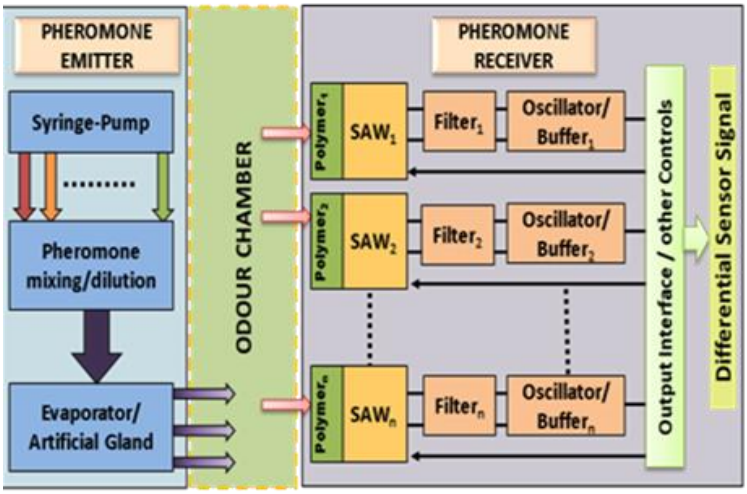

Figure 4.2. Block diagram of pheromone-communication system detailing various modules within chemoemitter and chemoreceiver modules.

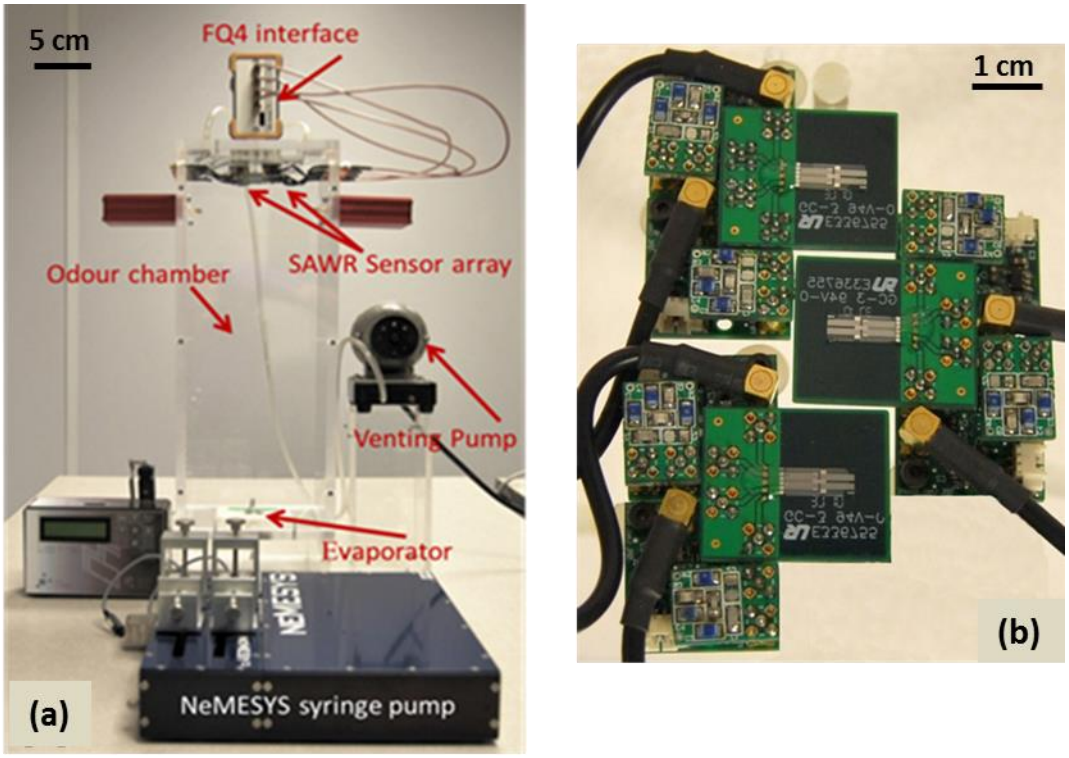

Figure 4.3. (a): Prototype of an infochemical test chamber containing syringe pump, micro-evaporator and array of four polymer-coated SAWR sensors. (b): Photograph of the polymer coated SAWR sensor array used inside the test chamber.

4.3.2 Polymer selection and Coating

Polymers are commonly used as chemical coatings for acoustic devices to detect volatile organic compounds because of their high sensitivity, fast vapour diffusion and reversible reactions, and stable operation at ambient conditions [1]. The overall detection of the volatile is mainly dependant on both the transduction mechanism and the adsorption processes. Vapour adsorption is dependent on the partition coefficient relating the vapour concentration in the polymer film and in the contacting gas molecules [139], as denoted by the Figure 4.4. The interactions between the polymer and the gaseous ligands are non-covalent and depending on the molecular structures, that could include dipole/dipole interactions, dipole/induced dipole interactions or hydrogen bonding. The entire solvation process can be modelled in two steps; the initial step being the formation of a cavity in the polymer, which is an endothermic reaction involving the breaking of non-covalent bonds between polymer chains. The second step involves the formation of new bonds between the polymer

and the solute, during the insertion of the solute molecule into the cavity, resulting in an exothermic reaction [139].

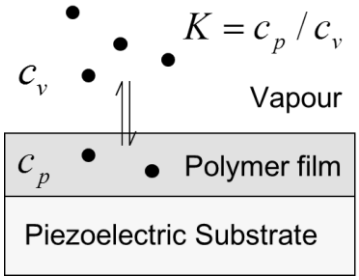

Figure 4.4. Diagram illustrating the partitioning of gas molecules into SAWR-polymer coating. The ratio of concentrations of analyte in the layer, c_p, and in vapour phase, c_v, is called the partition coefficient, K.

The absorption of vapours into the bulk of the polymer results in a decrease in the resonant frequency of the SAWR sensor, which is attributed by the mass of the vapour. However, Grate et al. reported that the dynamic modulus of the polymer also decreases on the addition of ligands onto the bulk of the polymer; which additionally causes a SAWR frequency decrease several times greater than the frequency decrease caused by the mass of the vapour [140]. These effects will be applicable only if the polymer film thickness is very thin. If the polymer coating is thicker, film resonance effects occur, which could produce positive frequency shift on the addition of ligands to the polymer. The linear solvation equation [140]–[142] calculates the partition coefficient of the vapour concentration, as given by:

$$\log K_p = k + rR_2 + s\pi_2^H + a\alpha_2^H + b\beta_2^H + l\log L^{16} \qquad 4.1$$

where *k* is a constant, R_2 is the excess molar refraction, π_2^H is the polarizability, α_2^H is the hydrogen-bond acidity, β_2^H is the hydrogen-bond basicity, and L^{16} is the gas-liquid partition coefficient on analyte at 298 K, while *r*, *s*, *a*, *b* and *l* are polymer-related parameters.

For a given vapour, the highest sensitivity can be achieved by finding a coating (with parameters *r*, *s*, *a*, *b*, and *l*) that maximizes K_p. In typical applications, K_p can be an amplification factor of which can be as high as few hundreds. Of course, to obtain the highest selectivity, polymers must be chosen to have the least correlation for a range of analytes rather than the highest sensitivity. Even though there are theoretical arguments supporting the linear solvation behaviour for the selection of polymeric compounds, other factors such as ease of acquisition, solubility in a suitable solvent,

immunity to changes in physical state and ease of coating application were also considered while selecting the polymers.

Due to the high sensitivity, fast volatile diffusion, reversibility and ambient temperature operation, gas chromatographic polymers such as polystyrene-co-butadiene (PSB), polyethylene-co-vinyl acetate (PEVA), polycaprolactone (PCL), and polyvinylcarbazole (PVK) were identified to be optimal to form thin chemical coating for the detection of volatile based pheromone blends. These solvating volatile blends collect and focus the solute molecules selectively in the polymer film, based on the partition coefficient magnitudes, thereby improving sensitivity and selectivity in vapour detection [1].

Polymer deposition was carried out by the process of spray coating, due to its simplicity and robustness. This process involves the ejection of fine liquid particles by a jet stream of carrier gas onto the substrate. A 0.25 weight (%) mixture was made by dissolving the polymer compounds in toluene by stirring it on a hotplate (SEA MS-506, Scientific & Educational Aids Ltd., Windsor, UK) for nearly 24 hours. An airbrush (Iwata HP-BC1P, Anest Iwata Corp., Yokohama, Japan) was used to spray the polymers onto the SAWR sensing surfaces, while covering the other regions of the resonator using a PDMS mask. During coating, the change in the resonant frequency of the device was monitored in order to provide an accurate control over the thickness of the deposited polymer film.

Recurrent sprayings were applied on to the sensor until a stable frequency drop of approximately 100 kHz was achieved, after the evaporation of the solvent. A stable frequency shift of about 100 kHz was obtained during the deposition of all the polymers, so as to obtain a uniform thickness for the functional layer. Maintaining a uniform thickness during polymer coating within the sensor array would prevent the sensors showing varied responses due to different polymer thicknesses. Figure 4.5 shows the frequency shifts obtained during different polymer coating on the 262MHz R-SAW sensors for gas phase chemical detection, which shows that there is a uniformity (of about 100 kHz) in the frequency shift shown by all the sensors during their corresponding polymer deposition. The relationship between the resonant frequency of a SAW device and the deposited polymer coating has been realized with high reproducibility and is given by [143]:

$$h = \frac{\Delta f}{(k_1 + k_2) f^2 \rho} \qquad 4.2$$

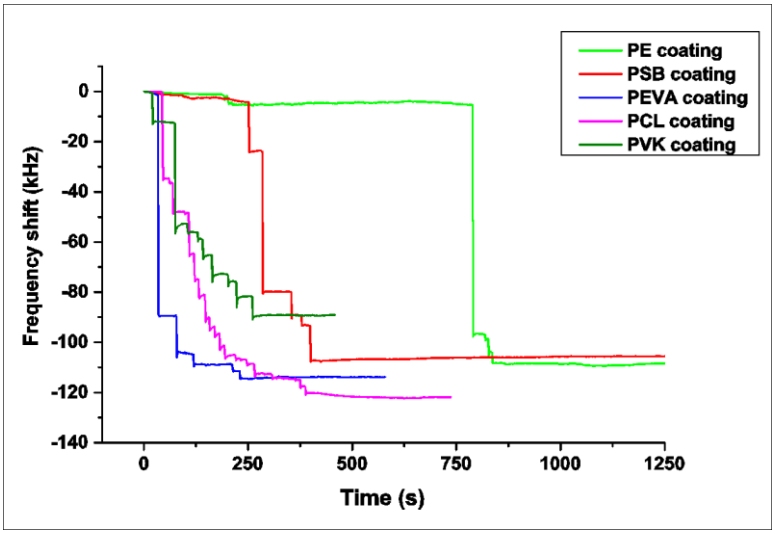

Figure 4.5. Frequency shifts obtained during different polymer coating on the 262MHz R-SAW sensors for gas phase chemical detection

As the polymer layer is a thin, non-conductive coating, the SAW sensor response is dominated by mass effects, neglecting the electrical and viscoelastic terms. In the above equation, Δf represents the shift in frequency due to the addition of the polymer film of thickness *h*, f being the resonant frequency of the SAW device, ρ being the coating density, k_1 and k_2 being the material constants for the ST cut quartz substrate ($k_1 = -8.7\times10^{-8}$ m^2skg^{-1} and $k_2 = -3.9\times10^{-8}$ m^2skg^{-1}). The theoretically calculated thickness of the polymer film based on the above equation is about ~15 nm. Atomic-force microscopy (AFM) imaging has been carried out for the polymer coated SAWR devices as shown in Figure 4.6. This analysis shows that the average thickness of the polymer film is ~ 20 nm which is comparable to the theoretically predicted thickness. The Figure 4.7 shows the polymer coating on the sensing device of a 262 MHz Rayleigh mode dual SAWR sensor.

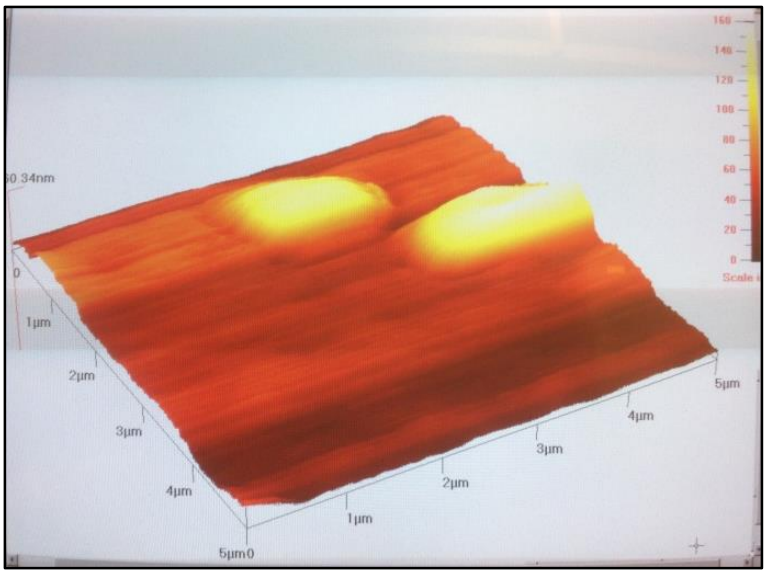

Figure 4.6. AFM image of polymer coating on SAWR surface showing thickness of the polymer layer.

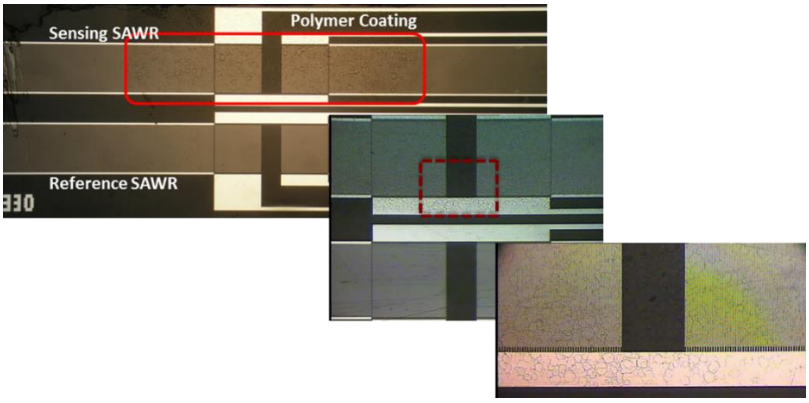

Figure 4.7. Optical micrograph of a 262 MHz Rayleigh mode dual SAWR indicating the polymer coating on the sensing device.

4.3.3 Feasibility study using fruit volatiles

Although the ultimate goal is to use the SAWR chemoreceiver module for the detection of predefined volatile pheromone compounds and recovering the ratiometric information deployed in the environment utilizing polymers that are sensitive and selective to pheromones, the first feasibility and performance studies of the chemoreceiver unit were performed using the major components of fruit volatile blends as analytes instead of *Spodoptera littoralis* sex pheromones. Fruit volatiles are used as low cost, commercially available alternatives to real pheromones that are extremely expensive even in small quantity. Considering that tens of millilitres are

needed for the initial testing of the prototype chemoreceiver/emitter unit, financially it is very reasonable to use these simple chemicals. There is no behavioural data directly connecting these volatiles to *Spodoptera littoralis*. Nonetheless, these common plant compounds are behaviorally relevant as they are detected by many species of insects (e.g. *Rhagoletis pomnella)*. As 3-methylbutan-1-ol and ethyl acetate make up a major portion of the plant compounds, these chemicals were selected for the initial odour testing[2].

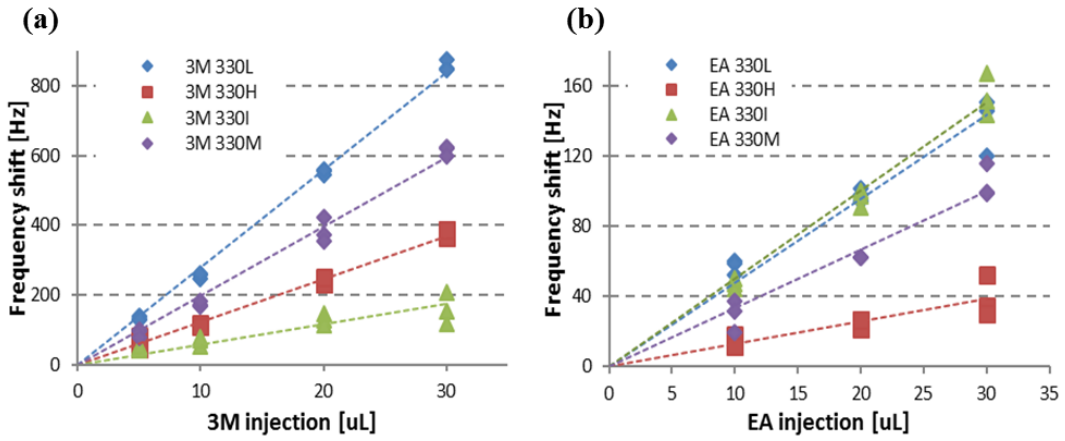

Figure 4.8. Concentration dependent differential frequency responses of four polymer-coated dual SAW resonators to two fruit volatiles: (a) isoamyl alcohol (b) ethyl acetate. Adapted from [128].

The frequency response of the polymer coated SAWR sensors were measured to various levels of fruit volatile concentration in random repeated sequences, using the developed infochemical communication prototype. Concentration dependent differential frequency responses of four polymer-coated dual SAW resonators to two different fruit volatiles isoamyl alcohol and ethyl alcohol is depicted in Figure 4.8(a) and (b), respectively. It was established that the sensor response is highly linear and reproducible indicating the reliability of the system and an appropriate measurement technique. Based on the satisfactory results from the preliminary tests using the fruit volatiles, ratiometric information transmission using pheromone compounds was attempted.

[2] Experiments carried out with the help of Jian Yang, University of Warwick.

4.3.4 Polymer-SAWR Responses

The functionality of the developed infochemical chemoreceiver system is demonstrated by establishing the minimum sensitivity of the system and verifying the linearity of the polymer-coated SAWR sensors. As a result, the frequency response of the SAWR sensors to various levels of sex pheromone concentration was measured. The chemoemitter was utilized to inject different volume concentrations (diluted with hexane) of pheromone E11-14:OAc into the odour chamber in randomized repeated sequences. The typical frequency response of a polymer coated dual SAWR sensor to an injection of 1:2 ratio of pheromone blends of Z9-14:OAc and E11-14:OAc respectively is shown in Figure 4.9.

It should be observed that injection of the volatiles generated a frequency shift in both the coated and the uncoated devices, due to the addition of volatile molecules on the surface of the SAWR sensor. However, the differential signal suggests that the response of the polymer coated SAWR is much greater than the reference signal. Hence, a differential signal is preferred to ameliorate the common-mode signals and also to determine the sensitivity of the polymer coated device.

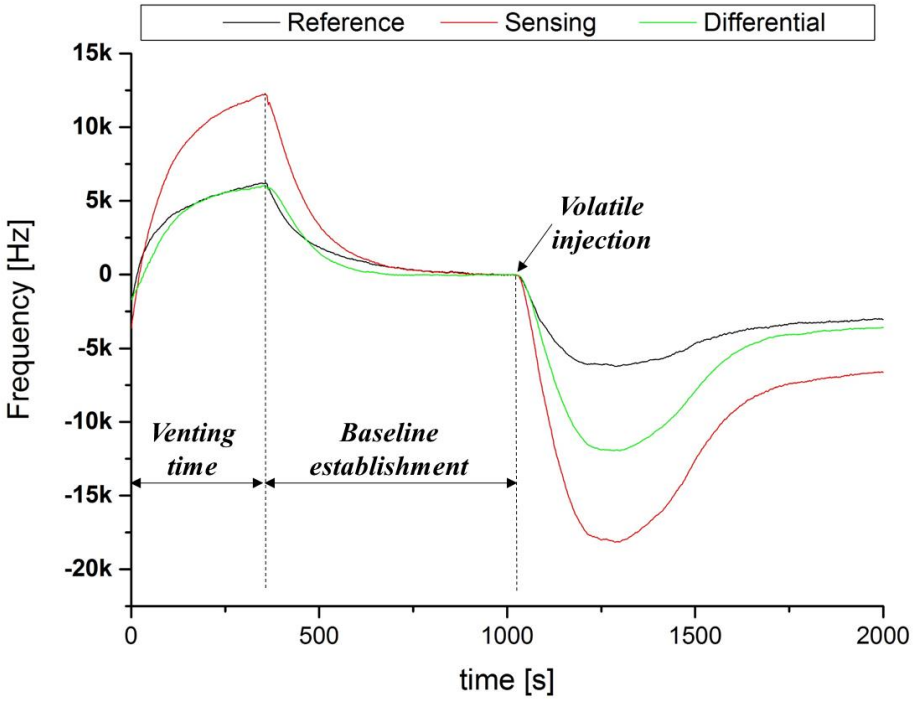

Figure 4.9. SAWR responses obtained during a typical ratiometric measurement, (0.33µl Z9-14: OAc and 0.66µl E11-14:OAc) showing sensing, reference and difference signals of a PSB-coated dual sensor

The response of the sensor array to different volumes of volatile pheromone compounds are shown in Figure 4.10(A). Average sensitivities of the SAWR devices to the volatile E11-14: OAc computed from the trend-line slopes in Figure 4.10(A), are 7.5, 12.5, 5 and 35 Hz/µl for the PCL, PSB, PVK and PEVA polymer coatings, respectively. The trend-lines obtained for each of the sensors proved that all of them operated in their linear region for the given concentrations. These investigations on polymer-SAWR sensitivity have shown that PEVA exhibited superior sensitivity, followed by the PSB. However, the other two types i.e., PVK and PCL polymers responded minimally and almost similar to that of the PSB response. Thus, instead of employing all the three polymers PSB, PVK and PCL, only PSB was chosen for the pheromone analysis. In addition, polyethylene (PE) based SAWRs were also employed, as polyethylene showed a high affinity to pheromones [144]. The Figure 4.10(B) shows the response of polyethylene-coated SAWR sensor to different volume concentrations of the sex pheromone E11-14:OAc, which follows a linear pattern.

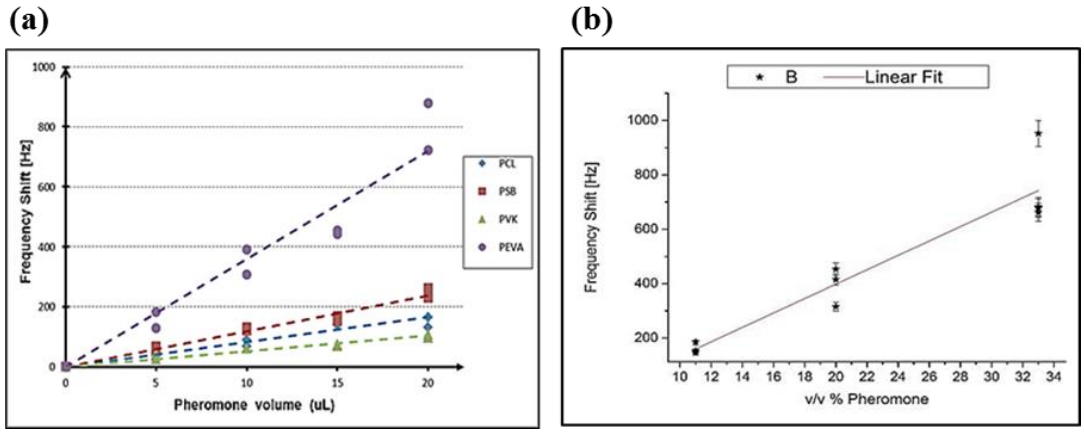

Figure 4.10. Frequency response of: (a) four polymer (PCL, PEVA, PSB, PVK) coated SAWR sensors to different volumes of (10% v/v) pheromone. (b) Polyethylene based SAWR sensors for different concentrations of pheromones.

From the above sensor responses to various polymers, it can be inferred that the observable frequency shift of the SAWR due to vapour or gas sorption is directly proportional to the partition coefficient by the following relation:

$$\Delta f = K_p C_v \qquad 4.3$$

Since the partition coefficient K_p is dependent on the boiling point of the liquid blend, it should be noted that the chemical concentration of the volatile present in the sensor polymers are neither the same as those in the air nor indeed those in the initial liquid blends. The precise blend concentration is only dependent upon the partial pressures of the individual chemical compounds in air; hence this difference. However, this difference does not cause a problem, as it is not required to determine the actual precise concentration of the compounds in the liquid. The purpose of these experiments mainly concentrate on qualitative classification of the blend ratios by encoding and decoding information, and thus presenting the preservation of blend information between source and receiver [1].

4.3.1 Ratiometric signal generation

Precisely controlled dilution of the pheromone compounds is performed by the syringe pump, to produce the infochemical blends with encoded ratiometric information. These infochemical ratios were injected instantaneously by the two

microliter precision syringes, into the artificial gland (micro evaporator) through capillary tubes. They are then carried to a micro-reservoir (0.375 µL) through rectangular microfluidic channels, where they are blended together. As the micro reservoir is located under a silicon membrane (5 mm × 5 mm × 40 µm) perforated with 37636 micro machined via-holes, the binary blend reaching the reservoir passes through the silicon membrane, where it gets evaporated from tiny droplets formed on the via-hole opening.

Table 4.1. Ratios of the two pheromones used to demonstrate the basic principle of ratiometric infochemical communication

Ratios	**1:0**		**2:1**		**1:1**		**1:2**		**0:1**	
Categories	**R1**	**R6**	**R2**	**R7**	**R3**	**R8**	**R4**	**R9**	**R5**	**R10**
E11-14: OAc (µl)	1	2	0.66	1.33	0.5	1	0.33	0.66	0	0
Z9-14: OAc (µl)	0	0	0.33	0.66	0.5	1	0.66	1.33	1	2

The ratiometric data is encoded using mixtures of two kinds of pheromone compounds namely E11-14: OAc and Z9-14: OAc with different ratios. Ten different binary volatile pheromone blends within the range of volumes of 0 to 2 µl were used to encode ratiometric data and are detailed in the Table 4.1. This pheromone based information is encoded into five different ratios such as 1:0, 2:1, 1:1, 1:2 and 0:1, but in two levels of volume concentration ranges. Thus, in total, ten different ratios of two sex pheromones were utilized for the demonstration of the basic principle of ratiometric information encoding and decoding, utilizing the infochemical communication system. The dosing volumes were chosen to be very small (of 1 µl and 2 µl), so as to accommodate the slow evaporation rate of the pheromone compounds. In order to remove polymer memory effects and other unaccounted factors, blends were injected with a constant flow rate of 0.25 µl/s in randomized sequence, for each of the batches.

4.4 SAWR Response Repeatability

In order to demonstrate the repeatability and reproducibility of the measurement system, relative standard deviation (RSD) percentages of the sensor responses are obtained (with the assistance received from Dr Guangfen Wei,

University of Warwick, UK). The average value and standard deviation of sensor

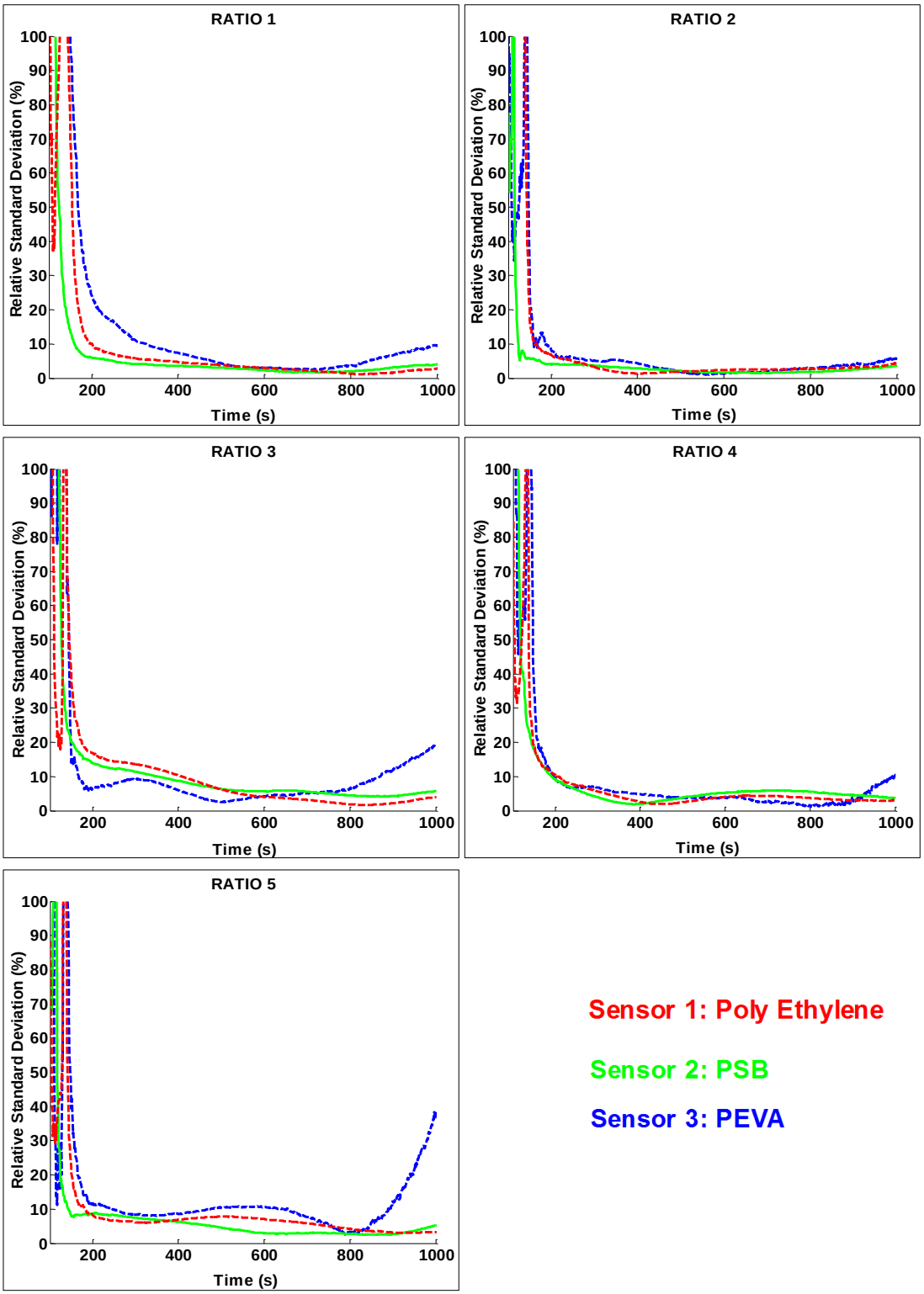

Figure 4.11. The deviation level of the SAWR sensor responses to each category of the low concentration (R1-R5) pheromone blends.

responses to each category of ratios at each time are calculated. In order to see the repeatability of sensors more clearly, the deviation level is computed through dividing

the standard deviation by the average value, which shows the statistical deviation percentage of the sensor responses from the average. The percentage deviation level of the SAWR sensor responses to each category of the low concentration (R1-R5) pheromone blends are shown in Figure 4.11. It can be observed from this figure that, the deviation percentage is random and widely distributed before the injection and also at the time of injection of the pheromone ratios (around the baseline). After the injection of pheromone, the deviation level starts to decrease. Thus, when the sensor starts to respond, the deviation level decreases rapidly and reaches a relative stable level. The lowest deviation is located around the maximum response points and the deviation level increases towards the end of the measurements.

4.5 Ratiometric decoding

Separation and classification of the ratiometric pheromone mixtures was performed using principal component analysis (PCA). The sensor response to various chemical concentrations was approximated to a suitable model as shown:

$$\Delta f_x = K_{xy} C_y + K_{xz} C_z \qquad 4.4$$

where ***x*** shows the polymer sensor, ***y*** and ***z*** are the chemicals with concentration *C*, having regression coefficients *K*. The equation 4.4 shows that, by utilizing two or more sensors, it is possible to determine the concentrations of the analytes uniquely. However, ratiometric decoding involves the classification of chemical ratios, rather than individual chemical components. Hence, features that are related to the chemical ratio recovery is of high importance. The data analysis using PCA was carried out in collaboration with Dr Zoltan Racz of University of Warwick, UK.

Table 4.2. Correlation coefficients for the response profiles of polymer coatings

	PE vs. PSB	***PSB vs. PEVA***	***PE vs. PEVA***
Mean Correlation Coefficient	0.963	0.975	0.902

The difference in sensitivity of a polymer to an analyte when compared to other polymers in the sensor array is an important characteristic in the selection of a polymer. Thus, in order to quantify the statistical correlation between the responses of one polymer to that of another, the correlation coefficients have been calculated, which is shown in Table 4.2. If the correlation coefficient is having a value of +1, this specifies that the two sensors are completely correlated. The results indicate that both the polymers respond in a similar manner, making it impossible to discriminate between the different blends. However, if the value is zero, it shows that both the sensors have completely different responses. From the Table 4.2, it can be inferred that PE shows the least cross-sensitivity in responses (as it has the lowest value of correlation coefficient) when compared to the other two polymers PEVA and PSB which are sharing highly correlated response profiles.

The ratiometric decoding capability of the system was evaluated by utilizing the steady state differential frequency shifts at 150, 350, 550 and 750s as the key features in a PCA. The corresponding PCA is plotted in Figure 4.12, with Sensor 1 (f_1), Sensor 2 (f_2) and Sensor 3 (f_3) as the three major axes. It was observed that the data points are randomly distributed initially. With time, the data points of each category cluster together. Starting from 350s, the high volume ratio points are separated clearly from the low volume ratio points, as visible in Figure 4.12(b). Also, it can be observed that the low volume mixtures (R1–R5) become linearly separable earlier than the high volume ratios, as evident from Figure 4.12(c). Because of the relatively large response to the higher concentrations, it is difficult to see the clusters of the low concentration ratios. The Figure 4.13 shows the scatter plots at t= 550 s and 750 s for the low-volume ratios (R1-R5) alone, where the clusters are clearly visible. It takes another 200s for the high volume ratios to achieve linear separation. It can be appreciated that after 750s, all the low and high volume ratios are not only linearly

separable, but also they form relatively tight clusters. Thus, ratiometric recovery based on stationary sensor responses was carried out by using the steady state differential frequency shifts, as the key sensor feature.

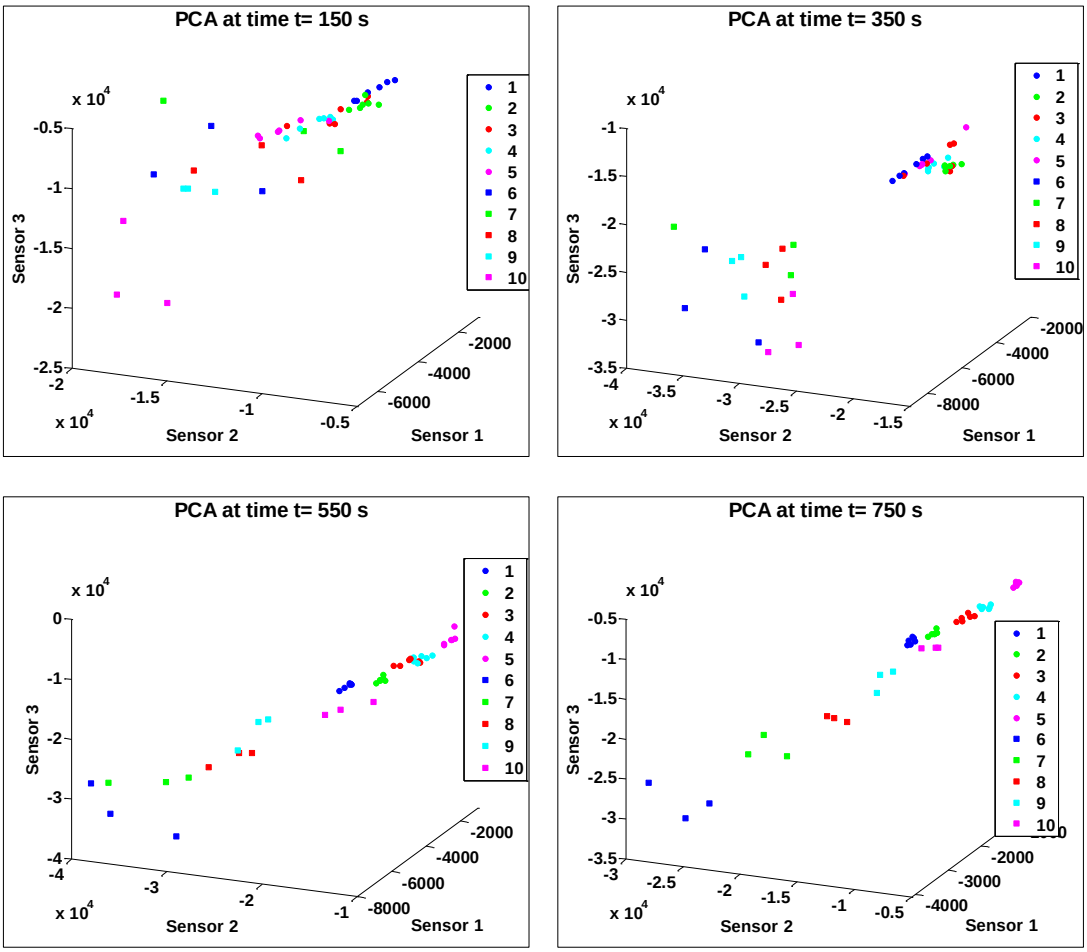

Figure 4.12. PCA plots of the original data at specified time, demonstrating the performance of ratiometric decoding.

The system produces the same response in the steady state for a given ratio, irrespective of the volume-dependence of the different ratios. This is illustrated in

Figure *4.14*, where, the data points are obtained from steady state frequency shifts normalized according to dosing volume. From this figure it can be observed that, for each of the ratios, the data points relating to both lower and higher volumes, form a single cluster. This proves that ratio recovery is independent of absolute concentration of each blends. Additionally, for a normalised data-set, ratiometric classification could be performed merely on the basis of the first principal component

of the steady state frequency responses, as it contains almost all the measurement variance, which is also evident from

Figure *4.14*. Overall, the SAWR based chemoreceiver system is capable of recovering ratiometric information based on only a single-dimensional information, independent of blend concentration or volume.

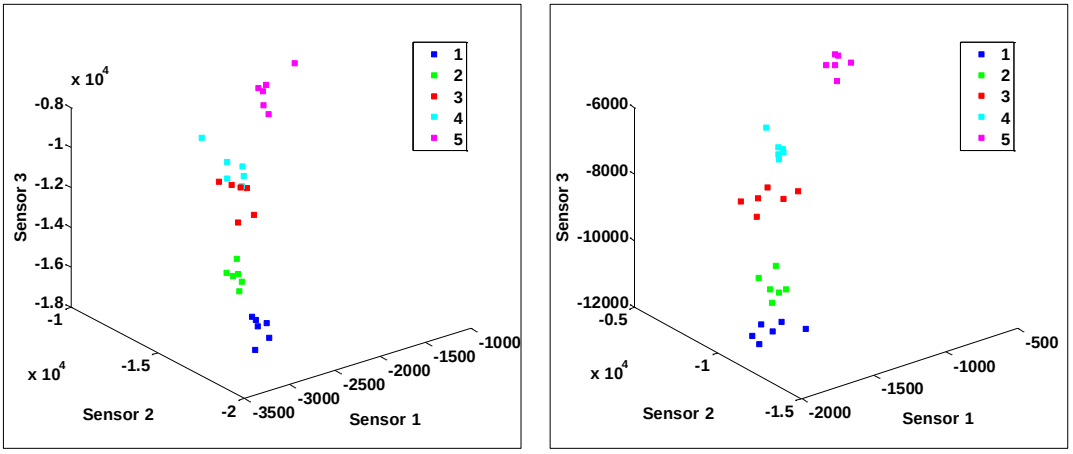

Figure 4.13. PCA based on standardised frequency shifts for the low volume ratios at time: (a) t=550 s and (b) t=750 s.

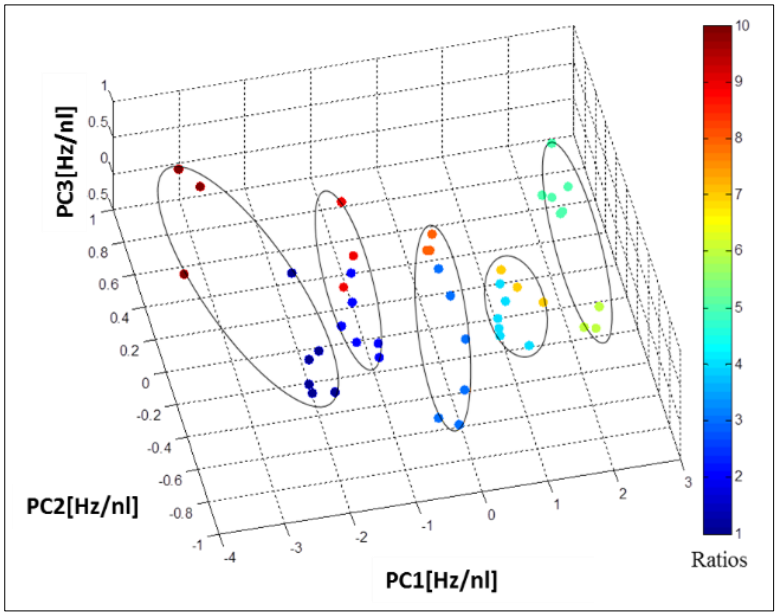

Figure 4.14. PCA based on frequency shifts (steady state) normalized according to dosing volume

The time development of the ratiometric clusters is obtained by plotting the first two principal components of the instantaneous frequency shifts as a function of time and is as shown in Figure 4.15. Even though the curves are entangled initially at the time of injection of the volatiles, each ratio category clusters as time increases after ~550s. An evaluation of the sensor stability, noise and repeatability could be obtained from this plot, which shows the PCA trajectory for all the ten different low and high volume ratios.

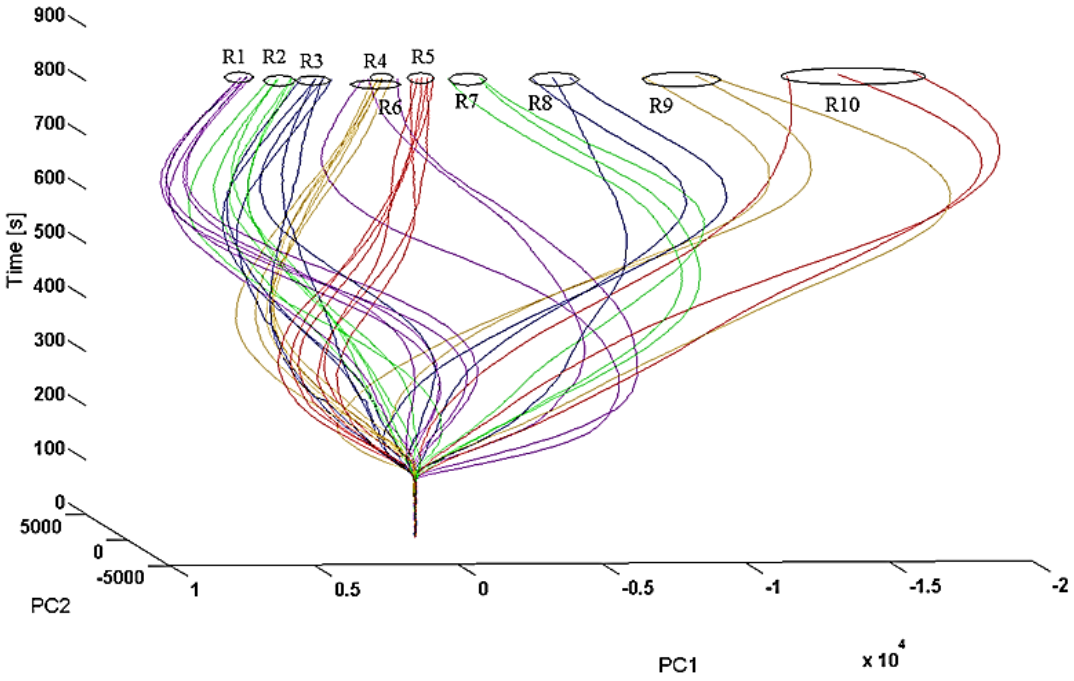

Figure 4.15. Trajectory plot of the PC1 versus PC2 calculated based on the instantaneous differential frequency of 3 sensors.

Volatile blends with low volume ratio show little deviation over time and tend to form distinct trail groups as early as 550s after injection. However, ratios with high volume content vary significantly and could take as much as 750s for the trajectory groups to form. As both the high and low volume mixtures had the same flow rate, the longer delay in separation is due to the greater vaporisation time rather than due to decreased SAWR system performance and sensitivity. Hence for the high volume blend ratios, longer time is needed to differentiate the ratios due to the greater liquid delivery and higher boiling point (135˚C) of the pheromones.

4.6 Summary

In this chapter, the ratiometric decoding of a biomimetic infochemical communication system have been presented, with pheromones as the information transferring media. Information have been ratiometrically encoded and released into the wind tunnel using binary mixtures of two kinds of pheromones with different ratios and concentrations. These uniquely encoded chemical signals were successfully detected by an array of polymer coated SAW sensors, which forms a selective chemoreceiver.

In conclusion, the system described has shown to recover the ratiometric information successfully, thus demonstrating the complete insect-based infochemical communication system. The sensor response time, and consequently decoding rate, could be improved by reducing spatial scales utilizing nano-engineered VLSI systems, thereby improving temporal precision. Such a biomimetic system can serve as the foundation for a new form of information transmission for broadband chemical communication influencing a range of applications such as environmental monitoring, product labelling, medical diagnosis and nanoscale communication.

CHAPTER 5

Cell-based SAWR with Olfactory receptors

5.1 Introduction

Biosensor assay technologies are widely employed today to measure the activation of cell receptors in response to their corresponding ligands; often through the use of a fluorescent label. Ligand-stimulated responses often produce downstream signalling events, triggering small physiological changes in the cell, such as a change in cell mass, cell size, intra-cellular ionic conductivity, or viscoelasticity (i.e. turgidity). Acoustic wave based biosensors are proving to be a valuable tool in different biosensing applications ranging from immunoassays for detecting the breast cancer biomarkers to detection of interleukin-6 in the human serum [54], and offer a real alternative to conventional fluorometry. Acoustic methods have also been used to monitor the growth of bacterial biofilms in serums [145]. Recently, a study was

reported detailing the development of SAW-based biosensors for functional assays of olfactory receptors [146]. The study of cell-substrate interactions has also been reported for monitoring events such as cell adhesion and motility, in which the sensors respond not only to net mass changes, but also to difference in cell volume and physiological conditions [35], [147].

As part of a study into chemical communication between insects, the work presented here utilizes a SH-SAW based sensor system functionalized with specific insect odorant receptors (ORs) introduced into Sf9 cells to detect acousto-electrically the binding of associated ligands. The principal objective is to develop a highly-specific chemoreceiver as a complementary module to the previously reported chemoemitter in a pheromone bioreactor [148], [149]; thus creating a complete infochemical communication system employing volatile chemical compounds to transmit information over space and time. Using this system, multiple channels of information are encoded using mixtures of infochemical ligands in precisely controlled ratios.

The sensor system comprises a dual 60 MHz $LiTaO_3$ shear-horizontal SAW resonator (SAWR) in which one channel can probe *Spodoptera frugiperda* (Sf9) cells expressing the olfactory receptors of Or22a or Or67d from *Drosophila melanogaster*, and the other probe wild-type cells (thereby acting as a reference channel). An automated micro-fluidic system has been constructed that delivers ligands reproducibly to the cell-based sensors. The SAW sensor response to the ORs can be explained by a change in acoustic coupling associated with physical parameters, such as an increase in intra-cellular ionic conductivity when the ligands bind to the ORs. Hence, these SAW-based biological sensor can be used as a selective chemo-receiver as part of a novel info-chemical communication system. Such a system mimics pheromone-based communication between insects. Possible future applications in the field of environmental monitoring, automatic identification & data capture, product labelling, search & rescue, air silent communication, and autonomous robot control could be identified. Here, the cell-based chemoreceiver for the acousto-electric transduction based responses to specific ligands has been described in detail.

5.2 Cell-based SH-SAWR Biosensor

The basic principle of operation of a cell-coated SAWR biosensor containing a cartoon representation of different penetration depths within a cell being probed is detailed in Figure 5.1. The symmetrical two-port resonator configuration comprises an input IDT, an output IDT and two highly reflecting grating structures. Electrically generated surface acoustic waves are contained by the reflectors and create a standing wave, thus the acoustic energy is mainly confined to the area between the IDTs. Changes in the resonant frequency of the SAW device indicate changes in the liquid medium acoustically coupled to this sensing region of the substrate.

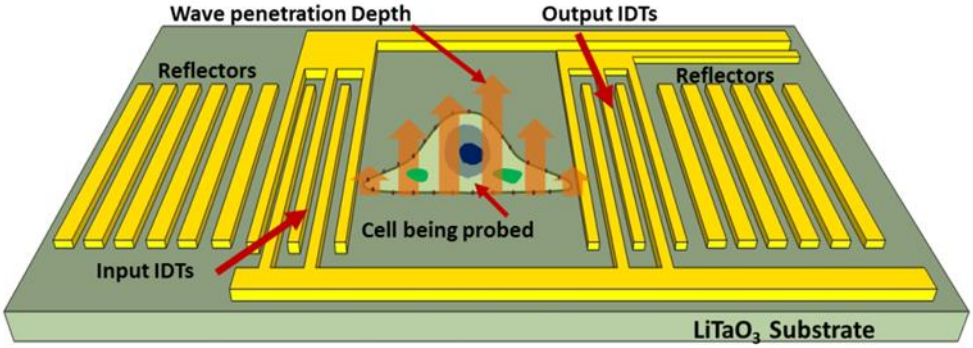

Figure 5.1. Schematic of a cell-coated 2-port surface acoustic wave resonator (SAWR) biosensor including a cartoon representation of different penetration depths within a cell being probed.

The acousto-electric potential associated with the acoustic wave on the surface of the sensor extends into the adjacent medium and the extent of the penetration of this potential determines a change in medium properties (relating to conductivity and dielectric permittivity), resulting in a change in the propagation characteristics of the SH-SAW sensor. As the work described in this chapter is related to determining the conductivity changes associated with a cell-based biosensor, it is important to have the electrical penetration equal to the approximate size of the Sf9 cells used in the detection. Thus a 60 MHz SH-SAW sensor has been used for the detection of the cell-based ligand-receptor interaction. Such a resonant frequency will have an electrical penetration depth of about 10 μm, which is in the similar range of the diameter of a single Sf9 cell, so as to detect the electrical changes occurring within the cells.

Thus, by depositing cells on the sensor surface, physical changes on the cell membrane or inside the cells induced by the ligand-receptor interaction are detected by surface acoustic waves that – depending on the frequency – penetrate varying distances into the cell (e.g. bilipid layer, part or all of the cytoplasm). The proposed mechanism of olfactory receptor signal transduction is described in detail elsewhere where it is proposed that in insects Or83b receptor is widely expressed and is thought to co-assemble with other ORs to form functional units that can bind odorants (either directly or indirectly) and generate an intracellular response [150].

In section 3.6, it has already been deduced that a change in the SAW frequency can be associated with one/more of the several dependent variables including the mass density ρ, viscosity η, conductivity σ, and dielectric permittivity ε, of the medium. This theory can now be extended to the case where the adjacent surface comprises a set of cells with liquid between them. In practice, complete coverage of the sensing surface area with cells is not easily achievable. So, it has also been assumed that the cells cover a given surface area of the sensor and the volume fraction, f_c, in the skin depth is simply given by (see Figure 5.2)

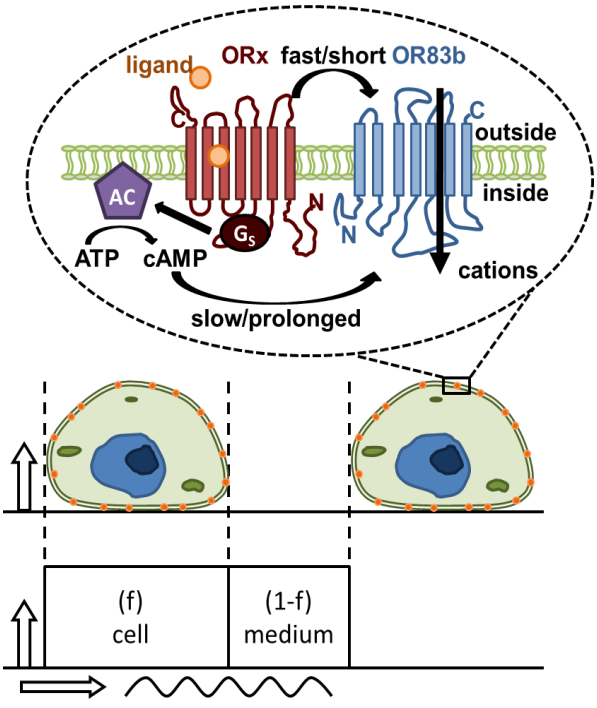

Figure 5.2. A bi-compartmental model used to estimate the theoretical sensor response.

$$f_c = \frac{Volume_{cells}}{Volume_{cells+liquid}} \qquad 5.1$$

Hence the change in frequency response for a *free* SAWR device partly covered with cells and the remaining fraction covered with liquid medium is represented as

$$\Delta f_{F/cell/Liquid} = f_c \left\{ \frac{\partial f_{cell}}{\partial \rho_{cell}} \Delta\rho_{cell} + \frac{\partial f_{cell}}{\partial \eta_{cell}} \Delta\eta_{cell} + \frac{\partial f_{cell}}{\partial \sigma_{cell}} \Delta\sigma_{cell} + \frac{\partial f_{cell}}{\partial \varepsilon_{cell}} \Delta\varepsilon_{cell} \right\} + (1-f_c)\left\{ \frac{\partial f_{liq}}{\partial \rho_{liq}} \Delta\rho_{liq} + \frac{\partial f_{liq}}{\partial \eta_{liq}} \Delta\eta_{liq} + \frac{\partial f_{liq}}{\partial \sigma_{liq}} \Delta\sigma_{liq} + \frac{\partial f_{liq}}{\partial \varepsilon_{liq}} \Delta\varepsilon_{liq} \right\} \qquad 5.2$$

For a single *shorted* SAWR sensor,

$$\Delta f_{S/Cell/Liquid} = f_c \left\{ \frac{\partial f_{cell}}{\partial \rho_{cell}} \Delta\rho_{cell} + \frac{\partial f_{cell}}{\partial \eta_{cell}} \Delta\eta_{cell} \right\} + (1-f_c)\left\{ \frac{\partial f_{liq}}{\partial \rho_{liq}} \Delta\rho_{liq} + \frac{\partial f_{liq}}{\partial \eta_{liq}} \Delta\eta_{liq} \right\} \qquad 5.3$$

By employing a dual SAWR configuration with both *free* devices, it is possible to remove the fraction of the reference liquid. This condition holds best when the reference SAWR coated with wild–type cells has the same volume fraction of cells as that of the SAWR coated with cells transfected with olfactory receptors.

Thus, for a dual sensor system with free path, equation 5.2 becomes,

$$\left(\Delta f_{F/cell+OR/liquid} - \Delta f_{F/cell/liquid}\right) \approx f_c \left\{ \frac{\partial f_{cell}}{\partial \rho_{cell}} \Delta\rho_{OR} + \frac{\partial f_{cell}}{\partial \eta_{cell}} \Delta\eta_{OR} + \frac{\partial f_{cell}}{\partial \sigma_{cell}} \Delta\sigma_{OR} + \frac{\partial f_{cell}}{\partial \varepsilon_{cell}} \Delta\varepsilon_{OR} \right\} \qquad 5.4$$

Also for a dual sensor system with shorted path, equation (6) becomes

$$\left(\Delta f_{S/Cell+OR/Liquid} - \Delta f_{S/Cell/Liquid}\right) \approx f_c \left\{ \frac{\partial f_{cell}}{\partial \rho_{cell}} \Delta\rho_{OR} + \frac{\partial f_{cell}}{\partial \eta_{cell}} \Delta\eta_{OR} \right\} \qquad 5.5$$

where the subscript 'OR' refers to the change in each term due to ligand binding to the receptor. Equation 5.4 forms a mathematical model describing the cell-based dual sensor system that estimates the expected frequency response out of the four loading terms associated with it which includes the change in the mass density of the cell when the ligand binds, the change in viscosity, the change in cell conductivity and the

change in dielectric permittivity. In addition, the cell volume fraction is assumed to be a constant, i.e. the cells do not swell when a ligand binds onto the receptors.

5.2.1 Dual Biosensor System

The operating frequency of the SAW sensors is set through geometric design to define a penetration depth between say the typical thickness of the cell membrane and cell diameter in order to target the region of interest [16]. The dual SAWR sensors ensure that the measured responses are produced purely by the functionalized cells [53], [114]. An optical micrograph of a dual SAWR device is shown in Figure 5.3. The sensitivity of a cell-coated SAWR biosensor utilizing cellular conductivity changes as the main sensing mechanism have proved to be several times greater than identical systems relying on mass loading effects [151].

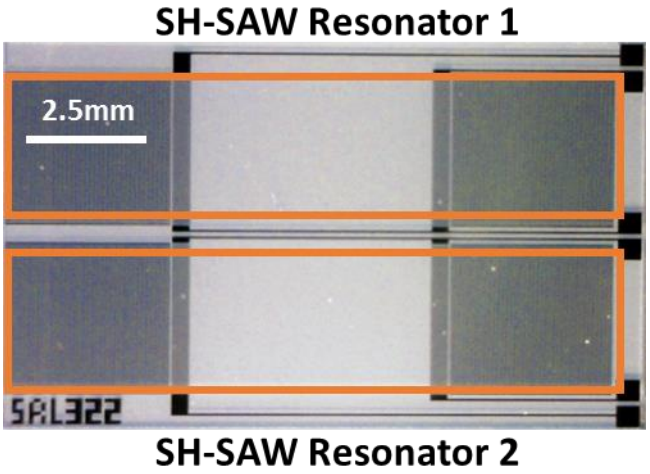

Figure 5.3. Optical micrograph of the 60 MHz SH-SAW devices, arranged in a dual configuration

In this study the cell-based SH-SAW resonator is designed to a frequency of 60 MHz and was micro-fabricated using 100 nm thin gold electrodes on a 36°-rotated Y-cut X-propagating $LiTaO_3$ substrate. The choice of $LiTaO_3$ as the substrate material was based on its relatively high electromechanical coupling coefficient of 4.7% and a relatively low temperature coefficient of delay of 32 ppm/ºC. The sensing surface of the resonator was functionalized with Sf9 insect cells.

The design specifications of the 2-port SAWR are detailed in the section 0. The estimated potential penetration depth of the surface acoustic wave at 60 MHz is approximately 10 μm which should enclose the entire cytoplasm.

5.3 Insect cell-based expression system

One of the most efficient expression systems for invertebrate receptors, Sf9 cells of *Lepidopteran* origin (*Spodoptera fugiperda*) was used in this work to establish an insect cell-based system. These cells provide favourable conditions for membrane targeting and the heterologous expression of insect olfactory receptors from Drosophila [152], [153], and also for the functional characterization of ORs from moth species [154], [155]. Sf9 cells endogenously express the Orco receptor, hence there is no need to co-express this receptor, and ligand potency is much greater when compared to mammalian expression systems. Also, the Sf9 cell-line is much more tolerant of culture condition variations (e.g. precise control of CO_2) than mammalian cells and can be grown at 28°C, allowing it to grow and survive on SAW devices making it much more adaptable even for some lengthy experiments. These cells not only readily grow on piezoelectric substrates, but also more importantly, adhere to the SAWR substrate within a short period of time (<1 h) at the desired confluency, eliminating any lengthy and contamination-prone cell growth processes.

As the foremost model organism for olfactory research [156], *Drosophila melanogaster* ORs have been routinely expressed in a variety of cell-based systems, including *Xenopus* oocytes e.g. [10], mammalian embryonic kidney cells (HEK) e.g. [9], [157], and insect ovarian tissue (*Spodoptera frugiperda* Sf9) e.g. [152], [153], [158], [159]. The full complement of olfactory receptors and their odour perception profiles in *D. melanogaster* has been identified [160]. Subsequently, a series of physiological and behavioural experiments have recognized the receptor Or67d as the male-specific odorant receptor responsible for mediating a response to the pheromone 11-cis-vaccenyl acetate (CVA) [161], [162]. Heterologously expressed olfactory receptor Or22a is functionally active when expressed in Sf9 cells, and is able to detect the fruit volatile ethyl butyrate (EB) in an aqueous medium [152], [163].

5.4 Microfluidic system setup

For precise, reliable and reproducible ligand delivery to the cell-based sensors, an automated micro-fluidic system has been constructed. This microfluidic implementation ensured continuous operation without maintenance, environmentally controlled aseptic interior, interfaces to low power electronics, and dimensions small enough to fit in a CO_2 incubator. The schematic diagram of the designed automated microfluidic system is depicted in Figure 5.4. Sterile medium reservoirs contain the solutions for cell growth and sub-culturing, line cleaning, and analyte delivery.

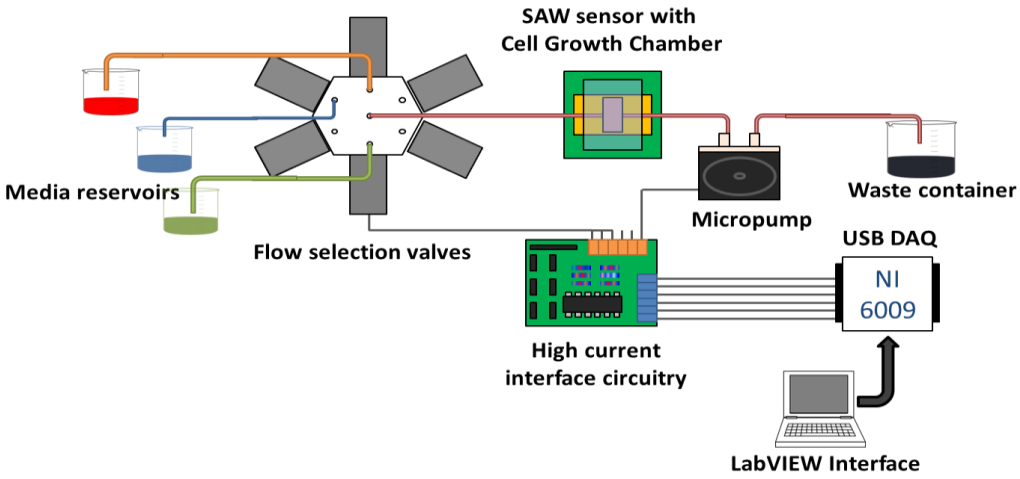

Figure 5.4. Block diagram of an automated microfluidic system for Sf9 cell culturing and characterization

5.4.1 Microfluidic chamber design

The automated microfluidic system works in conjunction with a microfluidic liquid reservoir made from PDMS, and is formed on top of the PCB-mounted 60 MHz SH-SAW device. This PDMS based liquid chamber is placed over the sensing area of the SAW device, while the rest of the device is sealed off by the PDMS. Split PDMS chambers having inlet/outlet holes with gauge 20 (0.81 mm) diameter have been utilized as the liquid chambers. The PDMS chambers are designed such that liquid will not contact with the sensor IDTs. Several reservoirs shapes were considered including rectangles and domes, and some with different reservoir heights. There are several other advantages for the PDMS chamber over the MSL/SU-8 design, in

addition to the fact that it produces only a small attenuation when used in the sensor system. PDMS acquires the shape of the mould and the SAW device with nanometre precision, using soft lithography. A single step process allows the channel formation and surface passivation and the resulting microfluidic chamber has excellent sealing without the need of an external support. The optical transparency of PDMS enables real time monitoring of cell activity using a light microscope. Additionally, the biological compatibility and chemical resistivity of PDMS to most solvents and aqueous solutions makes it a suitable candidate for the liquid phase detection. This feature protects itself from the several types of cell culturing solutions and oil.

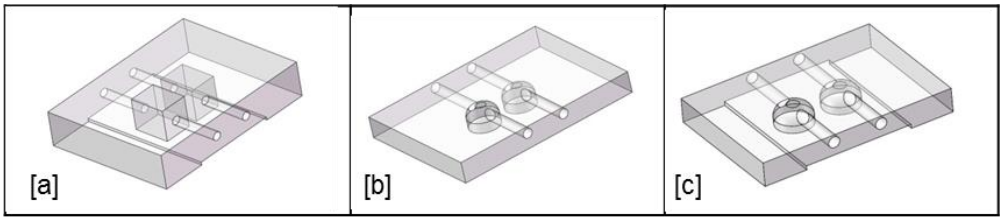

Figure 5.5. Various designs of PDMS chambers used to form the microfluidic reservoir.

Figure 5.5 shows the different designs of PDMS microfluidic chamber used for the delivery of the ligands to the cell based sensor. The PDMS micro-reservoir which contains two separate chambers for each of the SAW sensor present in the dual device is having separate inlet and outlet holes. This chamber confines the liquid under test to the sensing area of the SAW Resonator. The tubings connecting the different liquid containers to the PDMS chamber were of the size 1/16 inch inner diameter, which mitigates the generation of air bubbles from the connectors. The rectangular shaped reservoir with the greatest chamber height (shown in figure 5.5 [a]) was found to produce the lowest attenuation, when mounted on the top of the sensor device.

5.4.2 Experimental Setup

The microfluidic system comprises a pulse-driven micro-pump (KNF Neuberger, Germany) used to pump the liquids through the C-Flex® tubing with 1/50 inch inner diameter into the PDMS cell growth chamber on the sensor surface and eventually into the waste container, a 4-inlet manifold solenoid mixing valve for controlling the liquid flow from the reservoirs, and a NI-6009 multifunction data acquisition board (National Instruments, USA). A LabVIEW user interface controls

the operation of the valves and the pump via the data acquisition board that is connected to a custom high current amplifier interface to match the power requirements of the valves and the pump. A bio-compatible incubator (Stuart SI60D, Bibby Scientific Ltd, Stone, UK) is used to ensure temperature stability. The flow rate of the system can be varied by changing the pulse frequency of the pump drive. An implementation of the microfluidic system including the SAW sensor with growth chamber, the main sensor interface board and a DinoLite digital microscope (IDCP, Naarden, The Netherlands) is shown in Figure 5.6.

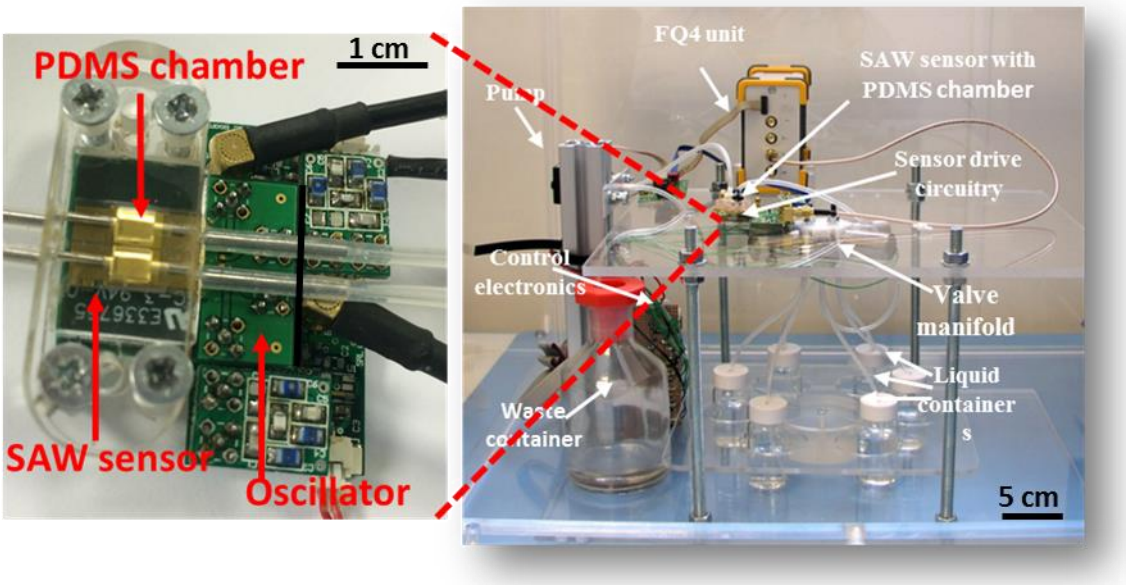

Figure 5.6. (a) Photograph showing the dual SAWR sensor inside a PDMS chamber and the associated oscillator circuitry on surface mount printed circuit boards, and (b) the computer-controlled microfluidic cell measurement system with valve and pump control, and interface electronics.

5.4.3 Cell culture, transfection and calcium assay[3]

The Sf9 cell line transfected with the olfactory receptors Or22a or Or67d was used to form a biological functional layer on a SH-SAW resonant biosensor system thus enabling the detection of various semiochemicals, including fruit odours (i.e. EB) and pheromones (i.e. CVA) at low concentrations. This design utilized the fact that transfected cells change their physical properties (e.g. cytoplasmic Ca^{2+} concentration)

[3] Cell culture, transfection and calcium assay has been carried out at the Department of Pharmacology, University of Leicester, by Dr. Melissa Jordan, as part of the iCHEM Project.

upon ligand binding to the olfactory receptors. Sf9 cells were grown as an adherent culture in T-25 flasks at 28°C using Sf-900 II serum free medium (Life Technologies). For transient transfection of Sf9 cells the protocol published by Kiely et al. [152] was followed.

Preparation of cells for calcium imaging was performed as published in Kiely et al. [152], except that cells were grown on coverslips and transferred to a PDMI-2 micro incubator open perfusion chamber for the duration of the assay. The assay buffer consisted of 12 mM NaCl, 21 mM KCl, 18 mM MgCl2, 3 mM CaCl2, 170 mM d-glucose, 1 mM probenecid and 10 mM PIPES, having a pH of 7.2. Imaging was performed on an Olympus FV500 confocal microscope.

5.5 Measurement Protocol

Ligand-induced perturbations in the surface acoustic wave propagation characteristics were monitored indirectly by placing the sensor in a feedback-loop of a radio frequency (RF) oscillator arrangement and measuring the resonant frequency [15]. Initial measurements were carried out to monitor and verify cell deposition and attachment to the SAWR surface based upon the sensor responses. Since Sf9 cells endogenously express G-protein-coupled receptors that are activated by octopamine, an invertebrate neurotransmitter, the response of wild (i.e. non-transfected) cells to octopamine was used to establish a protocol to measure ligand-elicited cellular responses. For these measurements, a dual SAWR sensor was used in which one resonator was coated with the wild cells and the other was left uncoated to serve as the reference channel. Following this, responses from dual SAWR sensors coated with Or22a or Or67d expressing cells were recorded. In these experiments one resonator of the dual device was functionalized with Sf9 cells expressing olfactory receptors and the other side (reference) with non-transfected Sf9 cells. A schematic of the biomimetic antenna detailing the above steps is shown in Figure 5.7. Detailed descriptions of the experiments and the associated results are given below in the following sections.

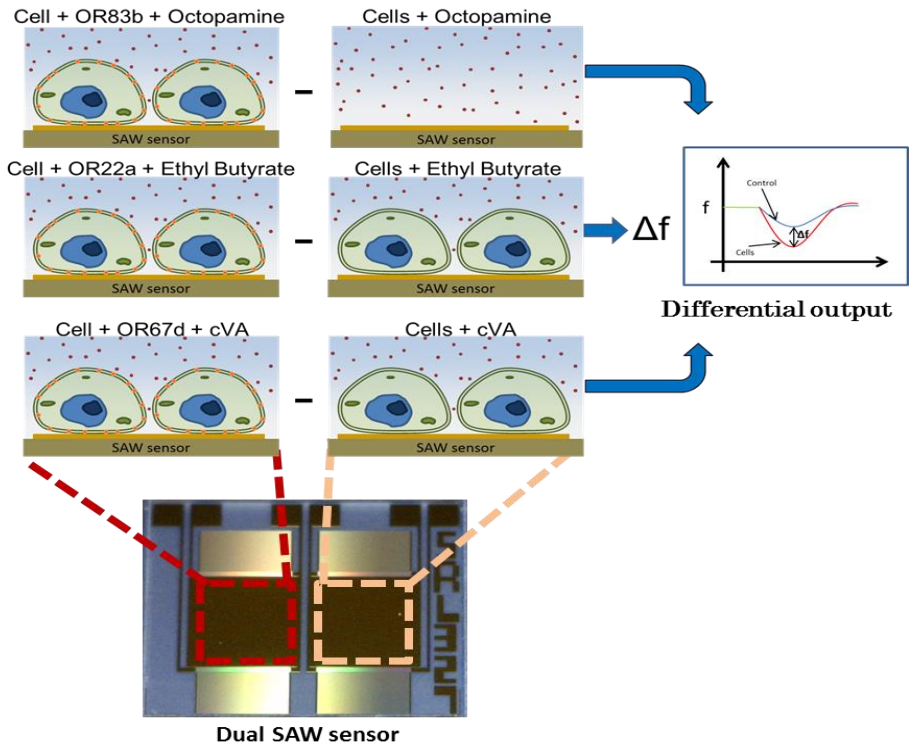

Figure 5.7. Schematic of the biomimetic antenna realized using SAWR biosensing system with transfected Olfactory Receptors.

5.6 Monitoring Sf9 cell deposition and attachment

The Sf9 cell deposition and adherence was measured in real-time by measuring the dual SAWR sensors frequency response. The cell deposition procedure was first started by attaching the PDMS cell growth chamber on to the sensor surface and connecting the entire setup to the microfluidic system followed by closure of the incubator door for maintaining ambient initial temperature. In order to establish a stable base line for the SAWR sensor and to prepare the sensor surface for the deposition of live cells, the cell culture growth medium Sf-900 II was pumped through the tubes into the PDMS growth chamber. The system was allowed to stabilize for about 20 minutes to alleviate the effect of sensor drift caused by temperature changes due to the discrete oscillator circuitry. After establishing a stable baseline, 10 µl of Sf9 cells at the appropriate concentration in growth medium were injected directly onto the sensing SAW surface through the cell growth chamber using a Hamilton syringe without disturbing the entire set up.

The cells were left to settle and adhere to the surface of the sensor for 60 to 90 min during which time they secrete extracellular matrices and develop cellular processes. Cell attachment to a $LiTaO_3$ shorted device shows a moderate shift in frequency (as compared to the control) of around 2300 Hz and these cells have shown more tolerance to variation in culture conditions than HEK cells. Thus, the Sf9 cell-line have shown to settle and attach themselves to the surface of the $LiTaO_3$ piezoelectric substrate within a short period of time (1 hour) at the desired confluence, thereby excluding the need for prolonged infection-sensitive cell growth processes. In addition, preliminary experiments have also been performed by Jordan et al. to determine the Sf9 cell viability on the SAWR surface and found out that the cells were alive for more than three days duration [163]. This also proves that Sf9 cells can be used as a bio-functional layer for SAW resonator based biosensor applications.

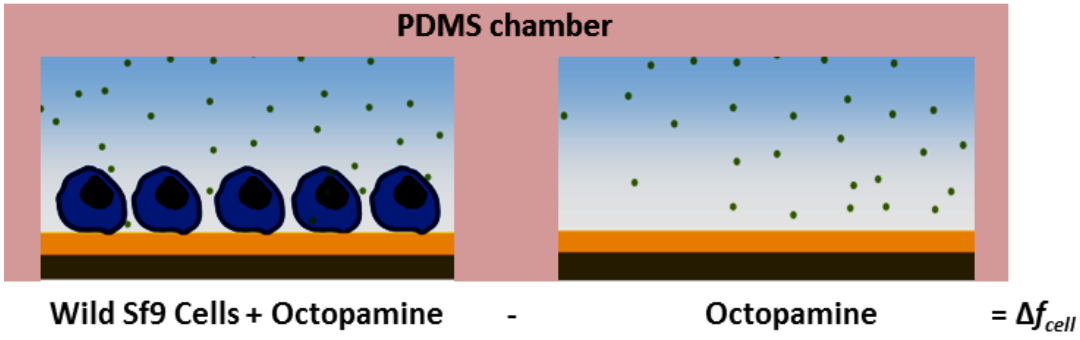

Figure 5.8. Dual Bio-SAW sensor where the sensing device is coated with wild sf9 cells while reference device is left uncoated.

As the Sf9 cells endogenously express the Orco (Or83b) co-receptor, initial calibration experiments were performed using wild non-transfected Sf9 cells forming the sensing layer on one SAW sensor, while the other sensor was left blank which forms the reference sensor, thus providing a dual sensor arrangement. Such an arrangement is shown in Figure 5.8, where one sensor is coated with wild Sf9 cells, giving rise to a differential signal, which is free of common mode variations. The endogenously expressed GPCR, within the non-transfected Sf9 cells is activated by the ligand octopamine. On addition of octopamine, a robust differential frequency response is recorded from a dual free SAW sensor based on Sf9 cells.

5.6.1 Cell adherence to various SAW device surfaces

The adherence and growth of Sf9 cells on the surface of SAW devices was assessed, using $LiTaO_3$ based 60 MHz free and shorted (with gold) SAW resonator devices. The Sf9 cell-adhesion on to the SAWR sensor was monitored in real-time, until the stable condition was reached. Scanning electron microscopy of Sf9 cells that had been incubated on the surface of SAW devices revealed that within a short period of time the cells form strong attachments to the device surface (Figure 5.9[a]) through multiple filopodia (cell projections) that are just about visible in Figure 5.9[b] and Figure 5.9[c] as shown in [163]. Additionally, investigation of cell growth on various SAW device surfaces has also been studied by Jordan et al., [163] which reports that the Sf9 cells were able to form a tightly adherent monolayer on the SAWR surface and were able to grow on these devices over extended periods of time (>72 h). This proves the suitability of Sf9 cells for use as a biological functional layer on SAW resonator devices. The cell adherence and growth pattern observed in SAW resonators were found to be similar for both free and gold-coated devices. The Figure 5.10 shows the Sf9 cell adherence profiles for both free and shorted SAW device surfaces.

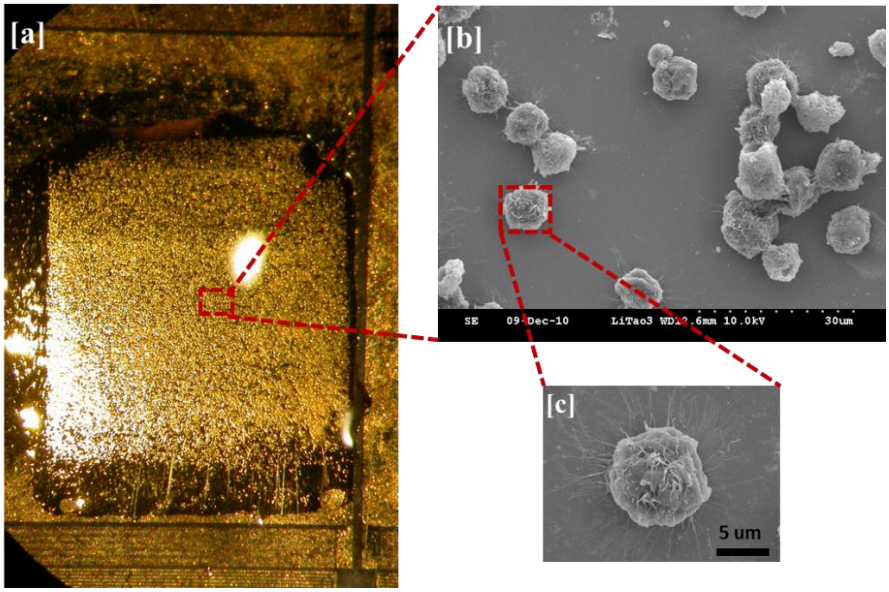

Figure 5.9. Scanning electron micrograph of Sf9 cells attached to the free surface of the $LiTaO_3$ SH-SAWR sensor.

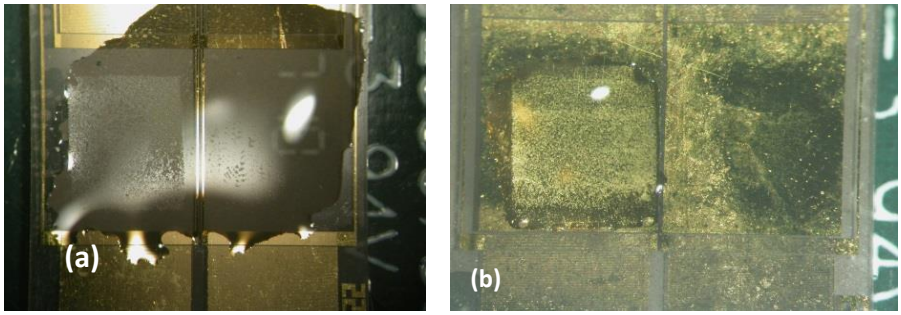

Figure 5.10. Sf9 cell adherance to one side of the dual SAWR sensors, showing both free (a) and gold-coated (b) $LiTaO_3$ SAWR surfaces.

5.6.2 SAWR response to Sf9 cell adhesion

The Sf9 cell deposition experiments were carried out on SAWRs with metalized sensing areas. Hence, it is claimed that the obtained frequency shift is mainly due to the large mass change associated with the deposition of thousands of 10 µm diameter cells over the sensing area, due to the fact that the SAWR sensing areas were metallized. The actual frequency response change when the Sf9 cells attach themselves to the metallized area on one side of dual shorted SAWR sensor is shown in Figure 5.11. When the sensing area is covered with a thin conducting layer (e.g. gold) it forms an electrically-shorted SAW device, i.e. the penetration of the electric potential into the adjacent medium is negligible [159]; therefore, only the mechanical properties of the liquid determine the sensor response. By neglecting the electrical terms and viscosity term in equation 5.2, the change in frequency response of a metalized SAWR when the cells have attached is given by simply,

$$\Delta f_{shorted} \approx \mathrm{f}_c \left[\left\{ \frac{\partial f_{cell}}{\partial \rho_{cell}} \Delta \rho_{cell} \right\} - \left\{ \frac{\partial f_{liq}}{\partial \rho_{liq}} \Delta \rho_{liq} \right\} \right] \qquad 5.6$$

In other words, the shift in frequency is the difference in the added mass of the cells subtracted from the mass of the displaced liquid. By analyzing the above equation, it can be observed that if the mass density of the cells was identical to that of the liquid medium then there would be no sensor response at all. Clearly this is not the case with the cell density is much higher than that of the liquid. The actual mass sensitivity terms depend upon the penetration depth with generally

$$\left\{\frac{\partial f_{cell}}{\partial \rho_{cell}}\Delta\rho_{cell}\right\} \leq \left\{\frac{\partial f_{liq}}{\partial \rho_{liq}}\Delta\rho_{liq}\right\} \qquad 5.7$$

Calibration measurements were performed in order to determine the value of the mass (density) sensitivity term. About 35,000 cells settle on the active sensing area each with a cell mass of *ca.* 500 pg. As the cells got attached to the sensor surface, the same volume of the cell growth medium (Sf-900 II) got displaced from the PDMS chamber. The volume of the displaced media is approximately 17 x 10^{-12} m^3 which is the same as the volume of the cells attached to the sensor surface. As the mechanical penetration depth of the sensor is about 72 nm, only a very small percentage of the attached cell volume, which is in contact with the sensor surface (approximately 1-2% of the entire cell volume), lies within the skin depth of the sensor. Owing to the fact that the mass density of the cells are smaller than that of the displaced medium (as depicted in equation 5.7), the cells attached onto the sensor surface contribute to a change in mass of ca. 0.2 µg, while the displaced growth medium produces a mass change of about 0.3 µg inside the skin depth. Both these effects contribute to a resultant differential frequency shift according to the equation 5.6**.**

The change in resonant frequency of a SAW resonator due to mass loading (neglecting the viscoelastic and other electrical effects due to the adjacent liquid) has been characterized by the classic Sauerbrey equation, which is given by

$$\Delta f = -\frac{2 f_0^2}{\sqrt{\rho_s \mu_s}}\frac{\Delta m}{A} \qquad 5.8$$

where f_0 is the resonant frequency of the SAW device, A is the active area of the sensor, ρ_s is the substrate density, μ_s is the substrate shear modulus and Δm is the change in mass. Based on equation 5.8, the mass sensitivity of the 60 MHz $LiTaO_3$ SAW resonators has been calculated to be about 25 Hz/ng.

Thus the resultant frequency shift due to mass changes obtained from both the contributions from the cells and from the displaced medium could be calculated to be about –2.5 kHz for 35K cells on the 60 MHz SAWR biosensor. This frequency shift is mainly due to the large mass change associated with the deposition of thousands of 10 µm diameter cells over the sensing area. However, it can be observed that the overall calculated shift (-2.5 kHz) is slightly more than the actual observed stable

condition corresponding to a frequency shift of about 2.35 kHz as shown in Figure 5.11. Some of this difference may be accounted for by the viscosity of the cells being higher than the buffer solution.

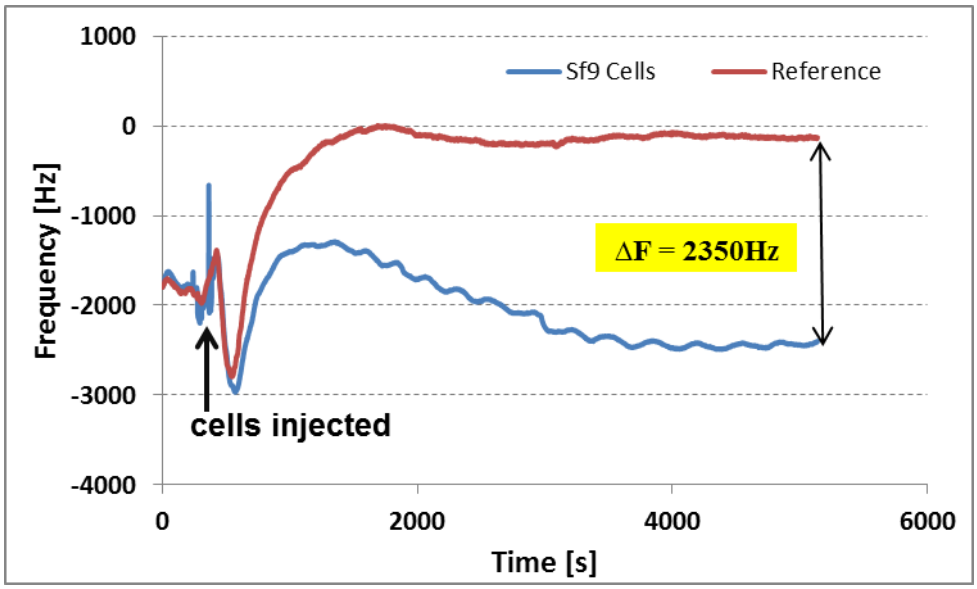

Figure 5.11. Frequency response of a 60 MHz dual shorted SAWR sensor during the deposition and stable attachment of about 35,000 Sf9 cells on the metallized sensing area.

5.7 Endogenous receptors in wild Sf9 cells

5.7.1 Response due to free SAWR biosensor system

The Sf9 cell-line endogenously expresses the OR co-receptors that have a high ligand- potency. Preliminary results showing the detection of secondary cellular responses using a functionalized Sf9 cell coating were obtained. These ligand-binding experiments were performed using the same assay buffer that was used for the fluorescent calcium imaging. Octopamine interacts with endogenous receptors (GPCRs) present in the cell membrane of Sf9 (wild type) cells, triggering intracellular responses within the cell due to the opening of ion channels. This response was recorded as a change in frequency response on the addition of 100 µM octopamine because endogenous receptors open calcium gates and so change the intra-cellular ionic concentration which has been confirmed by fluorescent markers. Figure 5.12 shows the *free* SAWR resonator biosensor response to 100 µM octopamine with a differential output (from control channel) of *ca*. -115 Hz. A major part of this

frequency shift is produced as a result of an increase in the ion concentration of the cell (i.e. conductivity) on ligand binding. As these free devices are also susceptible to mechanical effects including mass density changes and changes in the cell-stiffness (visco-elasticity) or cell size, there will be a small contribution to frequency shift due to these mechanical changes. As the response due to the additional ligand mass *(Detailed explanation is given in the section 5.11.)* is negligible (< 1 Hz), the remaining frequency shift will be associated with another mechanical effect, such as an increase in the cell stiffness (visco-elasticity) or cell size due to an increase in the intra cellular ionic concentration.

Thus, for a dual sensor system with free path, the frequency shift associated with additional ligand mass could be avoided (as it is negligible). Hence, it is possible to express the approximate shift in frequency response associated with simply a change of the conductivity (ion concentration) inside the cells with the control by:

$$\Delta f_{oct} \approx \mathrm{f}_c \left[\left\{ \frac{\partial f_{cell}}{\partial \sigma_{cell}} \Delta \sigma_{OR} \right\} - \left\{ \frac{\partial f_{liq}}{\partial \sigma_{liq}} \Delta \sigma_{liq} \right\} \right] \qquad 5.9$$

where the subscript 'OR' refers to the change due to ligand binding to the Orco receptor. The above equation 5.9 shows that the net shift in frequency is obtained as the difference between the added conductivity of the cells due to octopamine addition and conductivity of the displaced liquid. As the change in conductivity of the liquid associated with µM levels of octopamine will be negligible, equation 5.9 can be reduced to:

$$\Delta f_{oct} \approx \mathrm{f}_c \left\{ \frac{\partial f_{cell}}{\partial \sigma_{cell}} \Delta \sigma_{cell} \right\} \qquad 5.10$$

The small reduction in signal in the reference channel suggests that there may be other effect such as slight change in temperature on injecting the octopamine within the flow system.

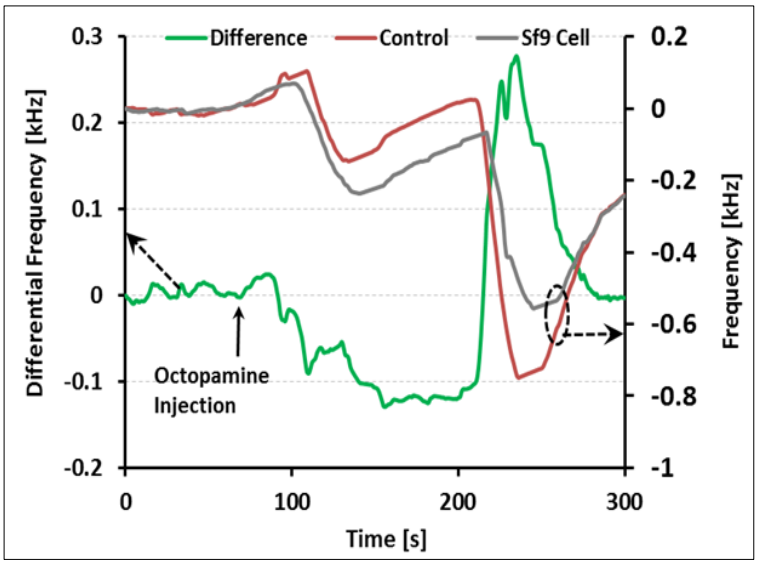

Figure 5.12. Frequency response of a 60 MHz free dual device to 100 μM octopamine.

5.7.2 Response due to shorted SAWR biosensor system

In order to prove the reliability of the free SAWR sensor response due to ligand addition on the Sf9 cells, similar experiments have been performed using shorted SAWR sensors also. Measurements on shorted SAWRs gave a lower, but still measurable response. Figure 5.13 shows the shorted SAWR resonator biosensor response to 100 μM octopamine with a differential output (from control channel) of *ca*. +30 Hz. As the shorted sensors are susceptible to mechanical effects alone, the frequency shift obtained should reflect the mechanical effects such as mass changes and changes in viscoelasticity of the cells. However, in section 5.7.1, it has been noticed that the frequency shift associated with additional ligand mass is negligible; and hence it is neglected. Hence, the obtained frequency shift of about +30 Hz is not due to the additional ligand mass (< 1 Hz), but must be associated with another mechanical effect; such as an increase in the cell stiffness (visco-elasticity) or cell size being higher than the buffer solution.

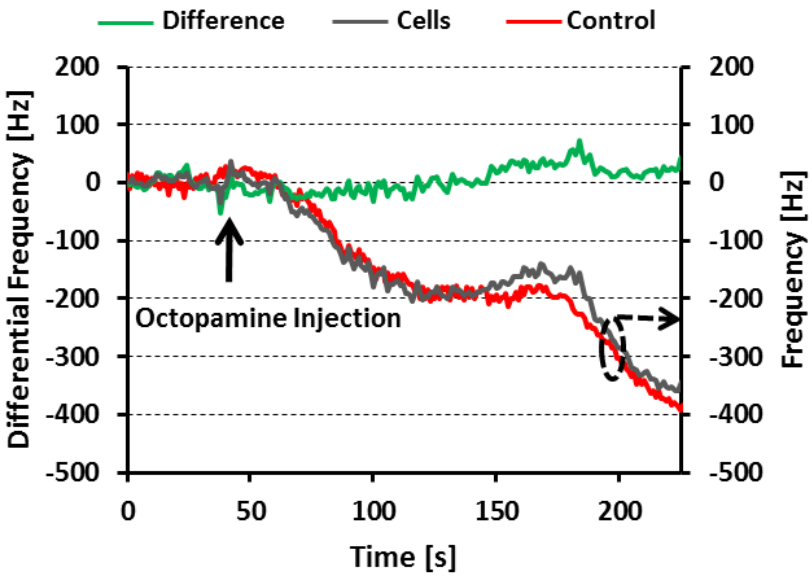

Figure 5.13. Frequency response of a 60 MHz shorted dual device to a solution of 100 μM octopamine. The actual response is the difference between the two signals from the cells and control channels.

5.7.3 Ionomycin response on SAWR biosensor system

In order to measure a physiological event that was more likely to induce a maximal calcium response within the cellular cytoplasm, ionomycin, a Ca^{2+} ionophore that facilitates the movement of Ca^{2+} ions across the cell membrane is added to the Sf9 cells. This will cause the cells to swell, with an excessive Ca^{2+} ions flowing into the cells. Differential frequency response of a free 60 MHz SAWR device to the addition of a solution of 5 μM ionomycin has been shown in the Figure 5.14 to be about -230 Hz, which will induce a maximal calcium response within the cell cytoplasm. The actual response is the difference between the two signals from the cells and control channels and this response can be mathematically expressed using equation 5.9, as explained in section 5.7.1. As ionomycin will cause the excessive influx of Ca^{2+} ions into the cells, the net shift in frequency obtained is higher than that of ligand binding, because of the abnormal increase in the added conductivity of the cells.

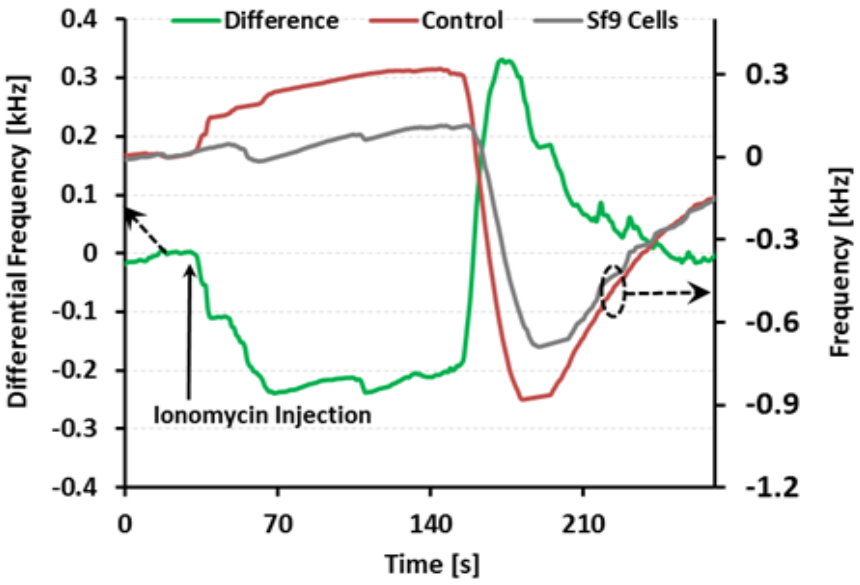

Figure 5.14. Frequency response of the 60 MHz free SAWR device to a solution of 5 μM ionomycin to induce a maximal calcium response. The actual response is the difference between the two signals from the cells and control channels.

5.8 Heterologous expression of olfactory receptor proteins

Lipid-mediated transfections were carried out with both Or22a and Or67d to provide a successful heterologous expression of Or22a and Or67d in Sf9 cells. The permeabilised cells that were transfected with the constructs containing the tagged olfactory receptors exhibited a fluorescent signal associated with protein expression, as reported by Jordan et al. [163]. Thus the two olfactory receptor proteins, Or22a and Or67d, have been successfully expressed on to the Sf9 cell machinery, which was verified by western blotting and immunocytochemistry results.

5.9 SAW sensor response to transfected Sf9 cell layer

The Sf9 cells provide optimal conditions for membrane targeting and functional characterization of insect ORs and have been employed in recent studies [152], [163]. These cells were transfected with functional olfactory receptors, namely Or22a and Or67d. Mimicking the octopamine response measurements, transfected Sf9 cells were employed for the detection of specific ligands in experiments. The main alteration to these experiments was that both sides of the dual *free* sensor were injected with the same volume of Sf9 cells. Only one device is coated with Sf9 cells transfected

with olfactory receptor, which forms the sensing SAWR; while the other device is injected with wild Sf9 cells, which forms the control SAWR. This setup eliminates non-specific cell response from the differential signal. Figure 5.15[A] shows the dual SAW sensor arrangement with sensing device expressing olfactory receptor based Sf9 cells and the reference device expressing cells without receptors, both of which are kept alive by the cell growth buffer medium. This figure also details the fluorescence imaging of the wild type cells (Figure 5.15[B]) and the heterologously expressed Sf9 cells (Figure 5.15[C,D]).

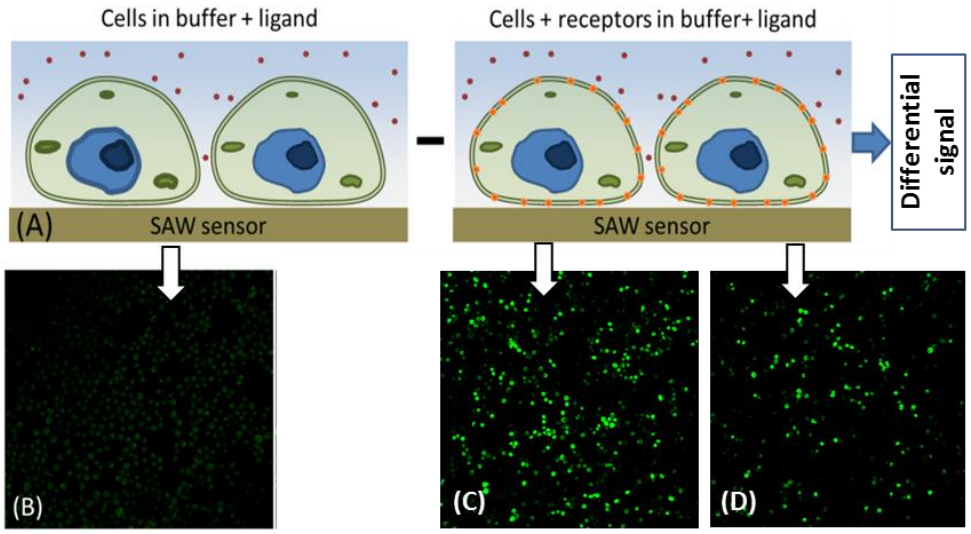

Figure 5.15. (A) Dual SAW sensor design with sensing device expressing olfactory receptor based Sf9 cells and the reference device expressing cells without receptors. Confocal fluorescence images of Sf9 cells with olfactory receptors (ORs) Or22a (C), or Or67d (D) without exogenous receptors (B).

5.9.1 Ligand elicited response of olfactory receptors

Sf9 cells were transfected with the olfactory receptor Or22a and the cells were exposed to the fruit volatile EB as the Or22a receptors can be stimulated by the ligand EB. A large shift of 900 Hz in frequency was observed (as shown in Figure 5.16) between the control and the transfected cells on the addition of 10 µM of EB over the 60 MHz free SAWR sensor using the automated system. Finally, the wild cells were transfected with the receptor Or67d and their response to the pheromone ligand CVA (100 µM) was also characterized. A large frequency shift of *ca*. 600 Hz was demonstrated as shown in Figure 5.17. The frequency change profiles showed some

similarity between the two sides of the dual sensor, the cells expressing Or67d or Or22a ORs demonstrating a much steeper decrease in frequency, due to an increase in cell conductivity on the addition of the particular ligands.

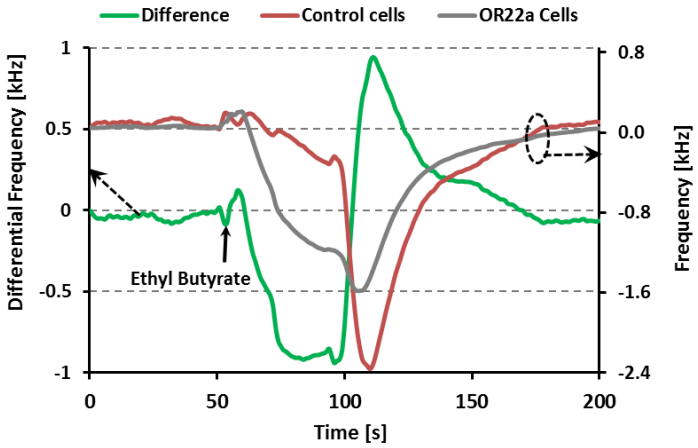

Figure 5.16. Frequency responses of dual free 60 MHz SAW biosensors coated with Or22a expressing Sf9 cells to 10 µM of the fruit volatile ethyl butyrate (EB). The actual response (left scale) is the differential signal shown by the green curve.

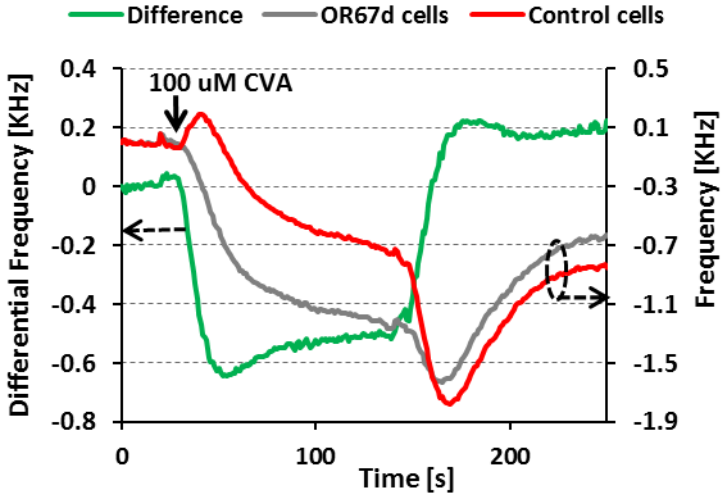

Figure 5.17. Frequency responses of dual free 60 MHz SAW biosensors coated with Or67d expressing Sf9 cells to 100 µM of the insect pheromone 11-cis-vaccenyl acetate (cVA). The actual response (left scale) is the difference between the two signals from the cells and control channel shown by the green curve.

5.9.2 Ionomycin response of olfactory receptors

The dual sensor system where the sensing device is coated with OR-transfected Sf9 cells and the other control device coated with wild Sf9 cells were exposed to ionomycin, in order to detect the physiological change occurring in both the transfected and the wild Sf9 cells. As ionomycin should have the same effect on both cell types, it was expected that this response would be very similar between the two sensors and both the wild and transfected cells showed an almost similar response profile as shown in both the OR22a–based sensor system (Figure 5.18) and OR67d–based sensor system (Figure 5.19). This means that there was a minimum differential response between the reference and the sensing devices, as both types of cells (i.e., wild and transfected) should express similar physiological changes when exposed to ionomycin. Thus there would be an excess of Ca^{2+} ions flowing into both the wild and transfected cells, resulting in a decrease in frequency shift for each sensor. Ideally, this should produce the very minimum shift in frequency between the reference and sensing devices. Thus, it can be observed that, the stable frequency difference is the least (of about 230 Hz), between the wild and transfected cells for both the OR-based systems.

The SAWR response to ionomycin can also be validated by verifying the single SAWR responses for each of the sensor types. The wild sf9 cell-coated SAWR within the OR22a and OR67d-based systems have an individual frequency shift of 800 Hz each. The transfected cell-coated SAWRs within the OR22a and OR67d-based systems have an individual frequency shift of *ca*. 1 kHz each. This symbolizes that ionomycin will produce a similar physiological effect on all types of cells, irrespective of whether they are transfected or wild type cells. As this physiological effect brings about an excessive Ca^{2+} ion flow into the cell cytoplasm, it can be inferred that the SAWR response is mainly due to the increase in cell conductivity, occurred due to the Ca^{2+} ion flow. The small difference between the two sensors could be caused by variation in the exact number of cells attached to the sensor as this is quite a difficult factor to control.

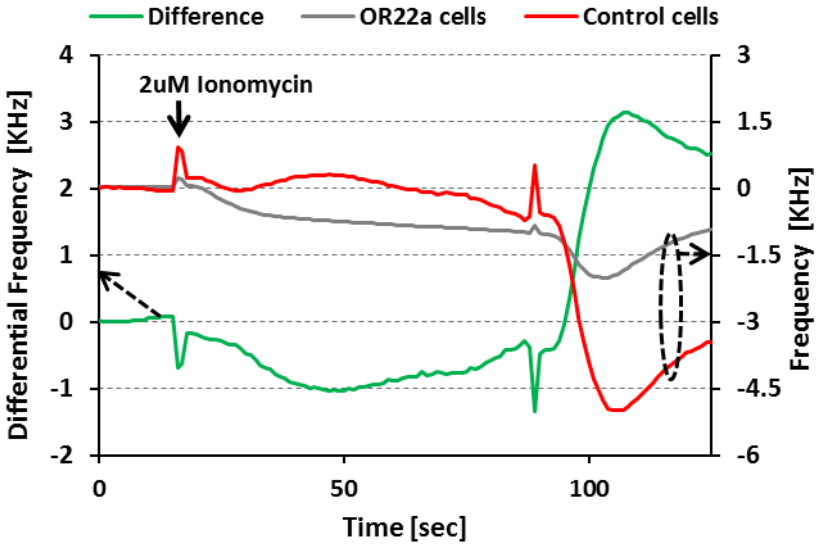

Figure 5.18. Sf9 cells expressing Or22a respond to the addition of 2 µM Ionomycin, which is indicated by the solid black arrow. The stabilized shift in frequency is obtained at a time=88 s.

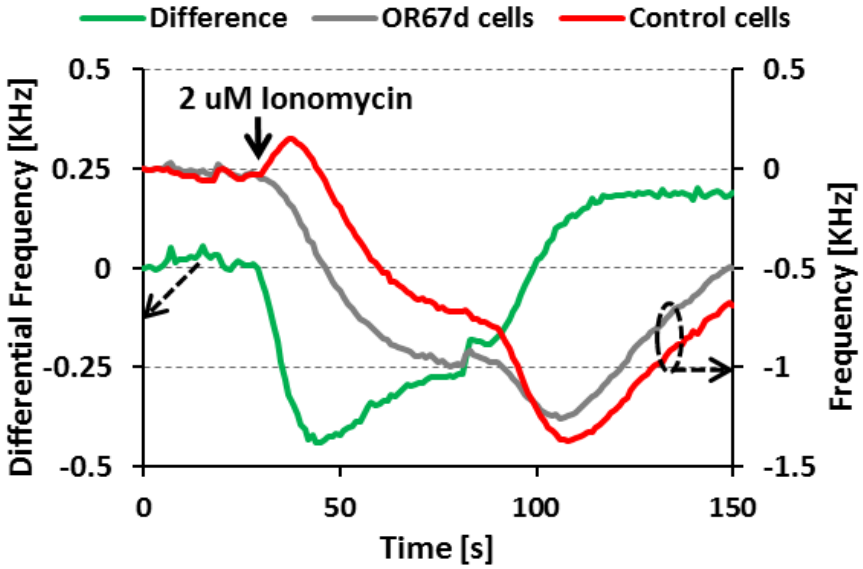

Figure 5.19. Sf9 cells expressing Or67d respond to the addition of 2 µM Ionomycin, which is indicated by the solid black arrow. The stabilized shift in frequency is obtained at a time=84 s.

5.10 Functional assay of ORs in Sf9 cells using calcium imaging[4]

Single-cell fluorescence calcium imaging was used to assess the performance and functionality of the endogeneously and heterologously expressed ORs. The cells were first loaded with a fluorescent Ca^{2+} indicator, Fluo-4 AM (Invitrogen), after which a receptor (endogeneous or transfected) will be stimulated by its appropriate ligand. They were exposed to octopamine for the endogeneous receptor (Orco), or the fruit volatile Ethyl Butyrate for Or22a receptor, or the pheromone compound Cis-Vaccenyl Acetate for Or67d receptor. Odorant-specific receptor activation results in an increase in the intracellular calcium concentration (observed as an increase in fluorescence).

The functional analysis was first performed with non-transfected Sf9 cells, which endogenously express a GPCR called the Orco receptor, stimulated by the ligand octopamine. On addition of 50 µM octopamine, an increase in the Ca^{2+} concentration inside the cell cytoplasm could be recorded as detailed in Figure 5.20. The same figure also shows response to the addition of 2 µM of ionomycin. The addition of ionomycin to the Sf9 cells induces a maximal calcium response within the cellular cytoplasm. It causes the cells to burst out, with an excessive Ca^{2+} ions flowing into the cells. The red arrow in Figure 5.20 shows the Ca^{2+} imaging of an individual Sf9 cell, stimulated with 50 µM octopamine. The endogenous octopamine receptor within Sf9 cells releases Ca^{2+} ions into the cell cytoplasm, when stimulated with octopamine addition, shown by black arrow. Ionomycin addition (green arrow-B) induces a maximal calcium response. The activated cell is shown in the four static images, showing the cell shape before and after octopamine addition (images D and E) and also before and after ionomycin addition (images F and G).

Similar functional tests were carried out with Sf9 cells expressing transfected odorant receptors. On stimulation with 100 µM Ethyl Butyrate, Sf9 cells expressing Or22a showed a 1.5 - 3 fold increase in fluorescence over background (Figure 5.21[a]),

[4] *Calcium assay described in section 5.10 has been carried out at the Department of Pharmacology, University of Leicester, with the help of Dr. Melissa Jordan, as part of the iChem Project.*

whilst on stimulation with 100 µM CVA, Sf9 cells expressing Or67d show a robust 3-8 fold increase in fluorescence over background as shown Figure 5.21[b]. However, the cells responding to CVA do not show the expected large ionomycin response. This may be due to Ca^{2+} stores already being depleted by the large CVA-stimulated response.

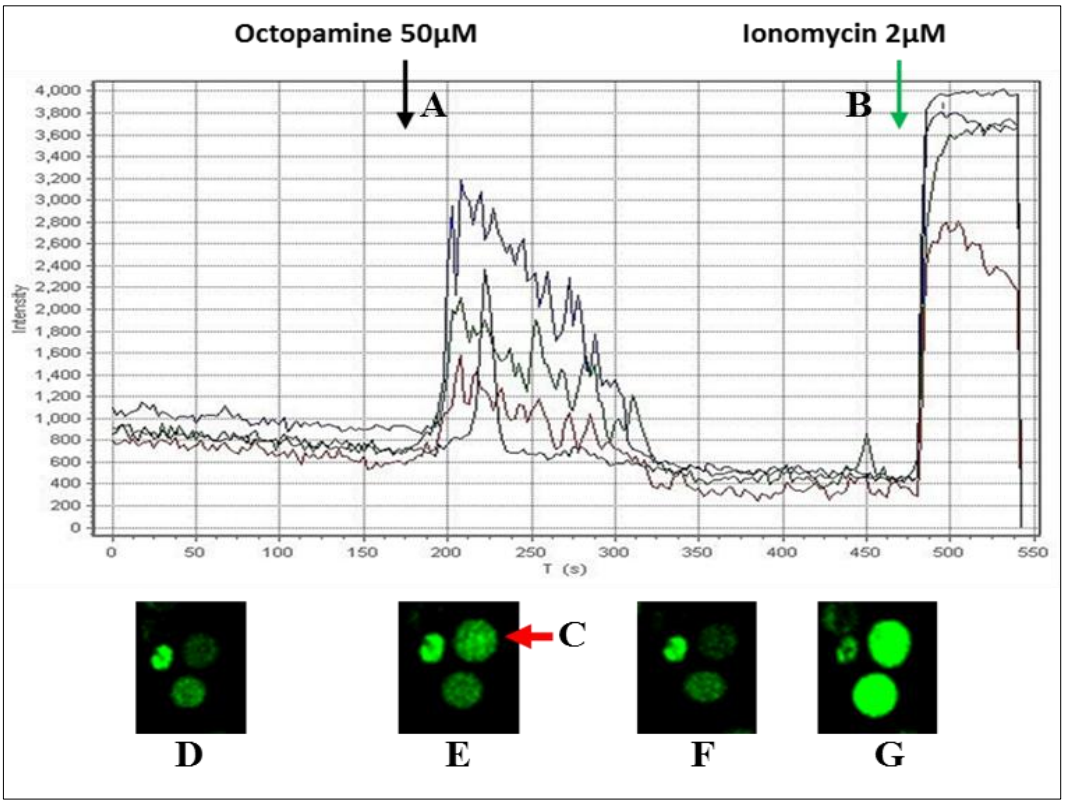

Figure 5.20. Fluorescent calcium imaging traces from representative individual Sf9 cells expressing endogeneous receptors. Arrow-A show the response of Sf9 cells to the addition of 50 µM Octopamine. Arrow-B show the response of Sf9 cells to the addition of 2 µM Ionomycin. The images D and E show the cell shape before and after octopamine addition respectively and the images F and G show the cell shape before and after ionomycin addition respectively.

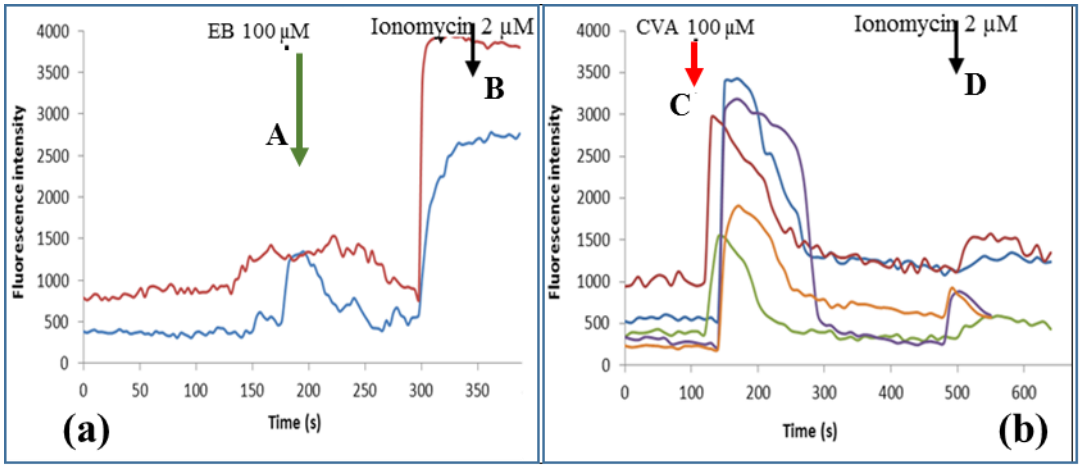

Figure 5.21. ***(a)*** *Sf9 cells expressing Or22a respond to the addition of 100 µM ethyl butyrate (arrow-A). 2 µM ionomycin was added 100s later to elicit a large increase in cytoplasmic calcium (arrow-B).* ***(b)*** *Sf9 cells expressing Or67d respond to the addition of 100 µM 11-cis vaccenyl acetate (arrow-C).*

5.11 Result Discussion

The SAWR sensors detect biochemical and physiological reactions occurring within the deposited cells which are dependent on the SAW penetration depth which is in turn defined by the resonant frequency of the SAW sensor. By exploiting this concept, it is possible to detect a wide variety of biochemical reactions based on cell-ligand interactions. A significant part of the SAWR response can be explained[5] here by the change in acoustic coupling associated with the increase in intra-cellular ionic conductivity caused by a small transient increase in intracellular Ca^{2+} level when the ligand binds to the receptor.

The mass of the attached ligand to the olfactory receptors has been estimated initially, which shows that it will have a relatively small contribution. The mass of the ligand is about 1,000 Da and with *ca*. 100k receptors per cell the mass of ligands is 100 MDa or about 1.7×10^{-16} g or 0.2 fg. Therefore, our set of about 35,000 cells on the 60 MHz SAWR sensing surface should change their total mass by ~10 pg. It had been previously estimated that the absolute mass sensitivity of our SAWR was about 25 Hz/ng or 40 pg/Hz. Thus, it can be concluded that a mass change of 10 *pg* will

[5] Mapping of SAWR sensor outputs with theoretical calculations performed in collaboration with Professor Julian Gardner (University of Warwick).

produce a frequency shift of less than 1 Hz, which is immeasurable by the 60 MHz SAWR system.

The response of the *free* SAWR sensor has been evaluated from the change in the intra-cellular concentration of calcium (Ca^{2+}) ions which is typically about 10 nM (before ligand binding) and with the binding of the ligand increases the concentration to about 1.5 µM. The conductivity of the cells is assumed to be similar to that for a strong electrolyte and so the Kohlrasuch equation applies.

According to the Kohlraush's law, the molar or equivalent conductivity of an electrolyte at infinite dilution is the sum of molar or equivalent conductivity of cations and anions produced by the electrolyte at infinite dilution.

$$\Lambda_m^o = n^+ \lambda_c^o + n^- \lambda_a^o \qquad 5.11$$

where n^+ and n^- are the number of cations and anions respectively. Also, λ_c^o and λ_a^o are the equivalent conductivity of cations and anions at infinite dilutions respectively (limiting molar conductivity).

The molar conductance at infinite dilution for a strong electrolyte like $CaCl_2$ is given by

$$\Lambda_{CaCl_2}^o = \lambda_{Ca^{2+}}^o + 2\lambda_{Cl^-}^o \qquad 5.12$$

The limiting molar conductivities of $Ca^{2+}$and Cl^- are given as 11.9 mS m^2 mol^{-1} and 7.63 mS m^2 mol^{-1} respectively. In this case, the conductivity increase within the cells can be estimated from the limiting molar conductivities of Ca^{2+} and Cl^- . The estimated increase in ionic molar conductivity of calcium ions (and hence twice chloride ions) is obtained from the cell fluorescent calcium imaging during octopamine addition to Sf9 cells (Figure 5.20); and is *ca*. 0.2 µM. This equates to an increase in ion concentration of *ca*. 5.4 µS/m on octopamine binding to the cells.

Based on the above calculations, the frequency coefficient of the free 60 MHz $LiTaO_3$ SAWR has been calculated to be about 20 Hz/µS m^{-1} and expect a frequency

shift of *ca*. 54 Hz associated with a 1 µM increase in cell conductivity due to the attached ligands. From the above calculated conductivity coefficient, the change in conductivity occurred inside the transfected Sf9 cells during the ligand (EB/CVA) attachment to the OR22a/OR67d receptors have been calculated to be about 45 µS/m (1.7 µM) for the OR22a coated SAWR system which resulted in a frequency shift of ~ 900 Hz and about 30 µS/m (1.2 µM) for the OR67d coated SAWR system which resulted in a frequency shift of ~ 600 Hz.

From these calculations, it can be concluded that it is possible to measure the change in cell conductivity; but not the change in cell mass on ligand binding. Consequently, employing SAWRs with an operating frequency of 60 MHz, the penetration depth is ideal here for probing the whole Sf9 cell structures.

In such a biosensor configuration, the differential SAWR output should be free of both non-specific responses and common mode variations because these are cancelled out due to the use of a reference or control channel. However, it is also possible that other physical properties, such as the shape of the cell or its visco-elasticity, could change as a result of ligand binding. The overall response profile of this dual SAWR device was fairly reproducible across multiple experiments when adding the various types of ligands (i.e. octopamine, CVA, EB). However, there was not a high level of consistency in the magnitude of the frequency levels across the different types of sensors. This could be due to several reasons, including a variation in the uniformity of the cell distribution on the sensing area which causes variations in the cell attachment profile or a change in the cell shape during ligand binding resulting in a change in the number of cell interactions occurring.

Thus, there also appears to be a small mechanical effect that is not associated with the increase in cell mass. Further investigations will be carried out to determine whether this effect is linked to any physical properties, such as a change in the cell shape/size or its visco-elasticity; during ligand attachment.

5.12 Summary

The development of a novel dual surface acoustic wave based whole cell sensor system utilizing transfected ORs, Or22a and Or67d with an automated

microfluidic ligand delivery system has been described in this chapter. The deposition and attachment of the Sf9 cell line on to the SAWR sensors are defined, which acts as a functionalized biolayer for the detection of specific ligands.

Basic equations governing the physical response of free and shorted SAWR sensors are presented and estimates have been made for sensor response based on mass and conductivity loading. The study shows that it is possible to detect the change in intra-cellular calcium levels (*ca*. 1.5 μM) when the ligand binds to the receptors.

Finally, the SAWR based system described here may be considered as the chemoreceiver part of an info-chemical communication system. Further studies are being carried out elsewhere on the detection of specific blends of chemicals that are used by insects to either locate specific foods (e.g. fruit odour EB) or sexual mates (e.g. pheromone CVA) and thus demonstrate the complete insect-based infochemical communication system.

CHAPTER 6

VLSI integration of Acoustic sensors

6.1 Introduction

Commercially available instruments for e-nose applications are generally large in size and expensive. The measurement complexity and equipment cost associated with acoustic sensor based detection could be overcome by CMOS integration, leading to the development of a portable and smart sensor system. Investigation of the possible integration of the sensor and associated interface circuitry into a single hybrid system has been carried out. This chapter details the design, simulation and development of an ASIC to interface acoustic resonant micro sensors such as SAWs and FBARs.

Solidly mounted FBAR sensors, were utilized for the development of a hybrid acoustic sensor system. These SMR devices make use of thin film technology to operate at higher resonant frequencies and therefore higher sensitivities can be achieved compared to other devices. The footprint of SMR devices is much smaller to

that of SAWs and QCMs and unlike SAW devices, SMRs are compatible with low-cost silicon technologies making them suitable for monolithic integration.

6.2 Sensor System Design

A compact and low power portable acoustic sensor system has been designed and implemented by integrating the bulk acoustic wave microsensors and the associated circuitry into a single hybrid microelectronic system. As part of this integration, an ASIC comprising a high-frequency analogue front-end and a series of interfacing circuit blocks were designed and fabricated. The basic functional layout of the hybrid microsensor system comprising of dual SMR resonators and an active CMOS interface circuitry is shown in Figure 6.1. The frequency shift related to the detection of analytes is obtained as a digital output suitable for micro-controllers. The frequency measurement system consists of an oscillator circuit that utilizes the FBAR resonator as a frequency determining element. The oscillator is a simple Pierce oscillator [164] implemented with CMOS inverters. The oscillator signals are amplified using a CMOS inverter based RF amplifier. The signals from the active and reference sensors are fed to the analogue frequency mixer and then to a low-pass filter which provides a differential frequency output. The analogue output signal is translated into a digital square wave with the help of an on-chip comparator. The output signal frequency of the comparator is externally measured by using a frequency counter provided by a microcontroller. The design and implementation of the major circuit blocks are detailed in the following sections.

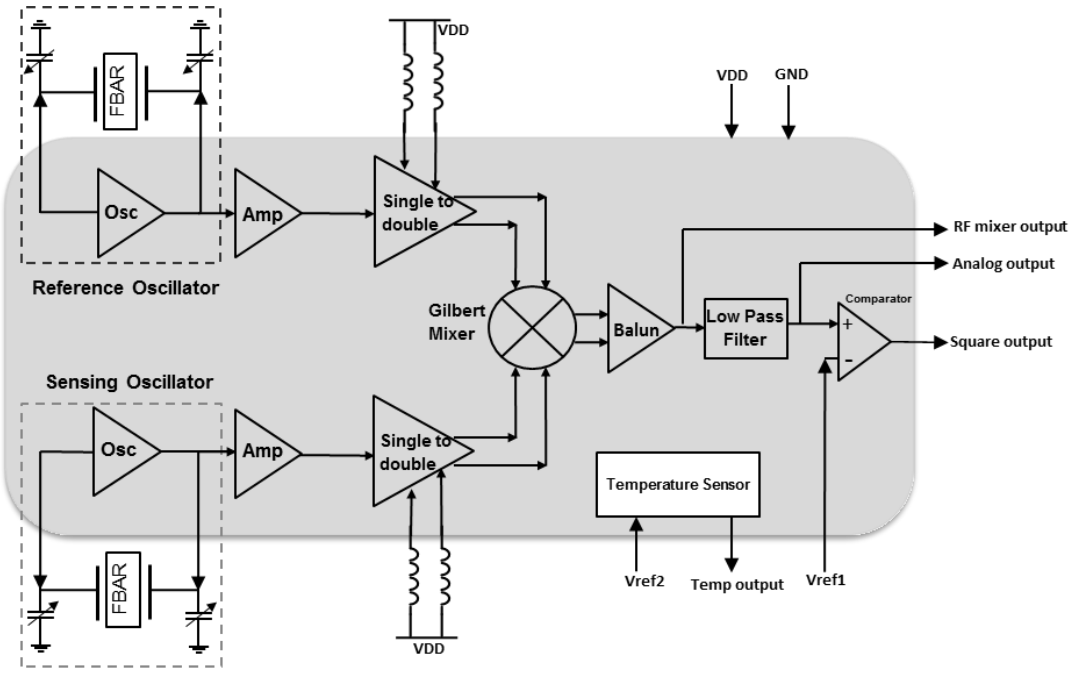

Figure 6.1. Global architecture of the FBAR-CMOS microsensor system. Two FBARs oscillators provide a differential low frequency output is obtained using a mixer, low pass filter and a comparator within the CMOS chip.

6.3 SMR[6] as a tuning element

The SMR is a promising candidate for the development of an RF MEMS sensor system allowing CMOS-MEMS co-design. The SMR employed here consisted of a 2.96 µm thick ZnO piezoelectric layer, resonating at a frequency of 894 MHz. The top and bottom aluminium electrodes have a thickness of 200 nm. Three pairs of molybdenum and SiO_2 layers formed an acoustic mirror that reflects and traps the acoustic wave over the resonant frequency range.

The SMRs were designed in a coplanar waveguide (CPW) structure with a characteristic impedance of 50 Ω for maximum power transfer. The resonance (series) and anti-resonance (parallel) behaviour of the SMR has been modelled using the Modified Butterworth-Van Dyke model (MBVD) [165]. The COMSOL simulated transmission (S_{21}) parameters of the SMR shown in Figure 6.2[a] was used [166] to design the oscillator circuitry, because the SMRs were not fabricated and characterised

[6] *The solidly mounted resonator has been made at the University of Cambridge, by Farah H. Villa-López, University of Warwick, UK, as part of an EU Project 'Multisensor Platform'.*

at the time of the chip design included in this chapter. The mBVD model, shown in Figure 6.2[b], gives a more realistic evaluation of the SMR performance, and extraction of device properties from electrical measurements.

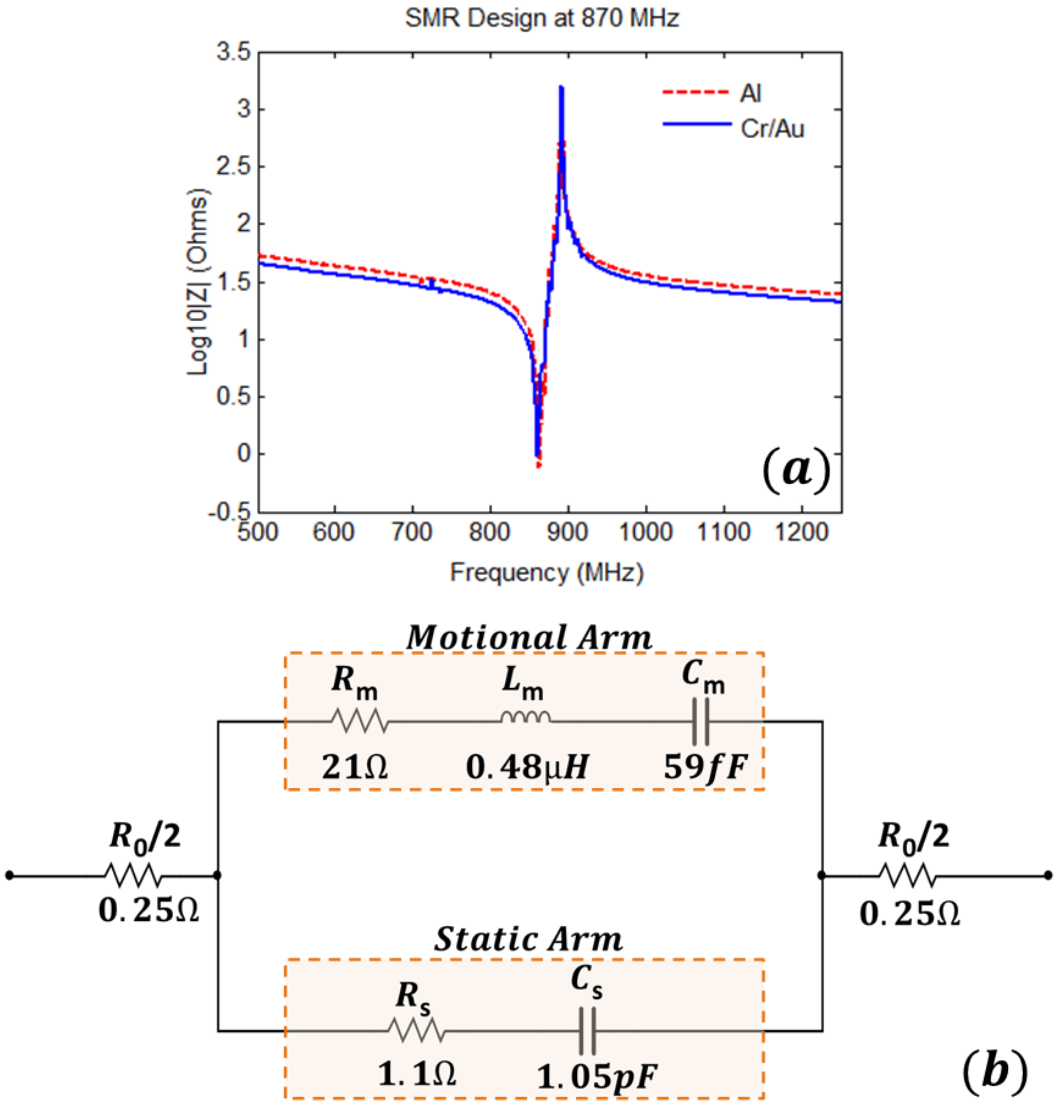

Figure 6.2. (a) Simulated frequency response of an SMR modelled using a 2D finite element model. Adapted from [166]. (b) Modified-Butterworth Van Dyke model of SMR.

The model comprises two parallel branches, namely the static capacitance arm and the motional arm. The static capacitance arm models the large parallel plate capacitor formed by the FBAR structure using the capacitance C_s and the dielectric losses in the material is modelled using the resistance R_s. R_o represents the electrical resistance of the two electrodes. The motional arm models as a series LCR circuit, representing the electro-acoustic properties of the piezoelectric layer. At the series

resonance frequency, the impedance is at a minimum, as L_m and C_m have equivalent impedance but opposite phase. This series resonance is obtained from the motional arm and is given by

$$f_s = \frac{1}{2\pi\sqrt{L_m C_m}} \qquad 6.1$$

The parallel resonance frequency is given by

$$f_p = \frac{1}{2\pi}\sqrt{\frac{1}{L_m C_m}}\left(1+\frac{C_m}{C_s}\right) \qquad 6.2$$

The above equation shows that a parallel resonance is determined by the combination of the static and motional arm. Even though the mBVD model gives accurate results close to resonances, it does not include effects caused by resonant overtones, electrode and acoustic reflector loading, and environmental loading [167]. The electrical parameters [168] associated with the mBVD equivalent model of the 870 MHz SMR are detailed in Figure 6.2[b].

6.4 Oscillation conditions

An oscillator consists of an amplifier and a frequency-dependent feedback network capable of providing frequency selection as shown in the basis block diagram in Figure 6.3. As the amplifier, with an open loop voltage gain $A_v(j\omega)$ is inverting, the phase shift through the amplifier is approximately 180°. The feedback network provides an additional 180° phase shift. So the total phase shift associated with the closed loop is 360°, resulting in a positive feedback system.
From Figure 6.3, it can be seen that

$$v_0 = A_v(j\omega)v_d \qquad 6.3$$

$$v_f = \beta(j\omega)v_o \qquad 6.4$$

And

$$v_d = v_i + v_f \qquad 6.5$$

From equation 6.5, the closed loop voltage gain $A_{vf}(j\omega)$ is given by

$$A_{vf}(j\omega) = \frac{v_o}{v_i} = \frac{A_v(j\omega)}{1-\beta(j\omega)A_v(j\omega)} \qquad 6.6$$

where the quantity $\beta(j\omega)A_v(j\omega)$ is referred as the loop gain. A system is said to oscillate only when there is an output signal without applying an input signal. Thus, from equation 6.6, it follows that the denominator is equal to zero. That is,

$$1-\beta(j\omega)A_v(j\omega) = 0 \qquad 6.7$$

which results in

$$\beta(j\omega)A_v(j\omega) = 1 \qquad 6.8$$

The equation 6.8 proves that the loop gain must be unity for the oscillations to occur.

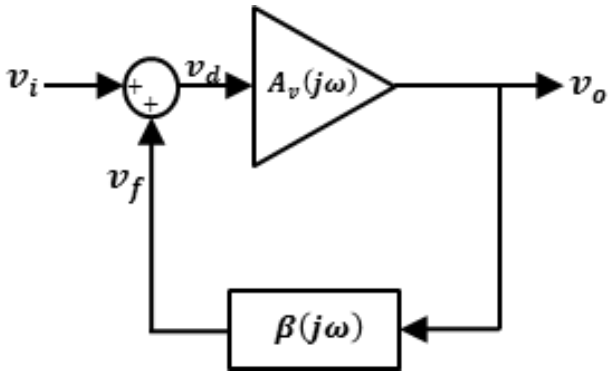

Figure 6.3. Basic feedback model of an oscillator system.

Thus, for a system to have steady state oscillations, it should satisfy the following two conditions such as a unity loop gain and a total phase shift of 360°. This relation is referred to as the Barkhausen criterion. When implemented as a circuit, this means that the amplifier gain should be sufficiently large enough to compensate for the FBAR losses and other parasitic losses. In addition, the feedback path formed by the resonator, load and stray capacitances, including the output load resistance, should provide the required phase shift at the frequency of oscillation. As the FBAR mBVD model is almost similar to that of crystal resonators, all the topologies [53], [169]–[172] designed for crystal oscillators can also be applied almost directly for the design of FBAR oscillators; except for the fact that the FBAR resonance frequency is at RF.

The FBAR oscillator system has been implemented using a CMOS based Pierce topology. A simple three stage inverter-based Pierce oscillator is chosen in this ASIC design due to the benefits of self-biasing, current-reuse, high oscillation amplitudes, low-power and tunability.

6.5 Discrete Oscillator and interface circuitry

Acoustic wave perturbations are obtained as change in attenuation and velocity changes of the bulk wave. The real-time detection of these perturbations require complex and bulky circuitry, which are quite inappropriate to be used in integrated microsystems. By using an SMR sensor as a resonating element within a simple oscillator circuit, monitoring of the acoustic velocity changes could be a achieved indirectly with great measurement [91] precision. Thus, a Colpitts oscillator configuration with a grounded base configuration has been used to drive the SMRs, resonating at a frequency of ~970 MHz to obtain good frequency stability and sensitivity.

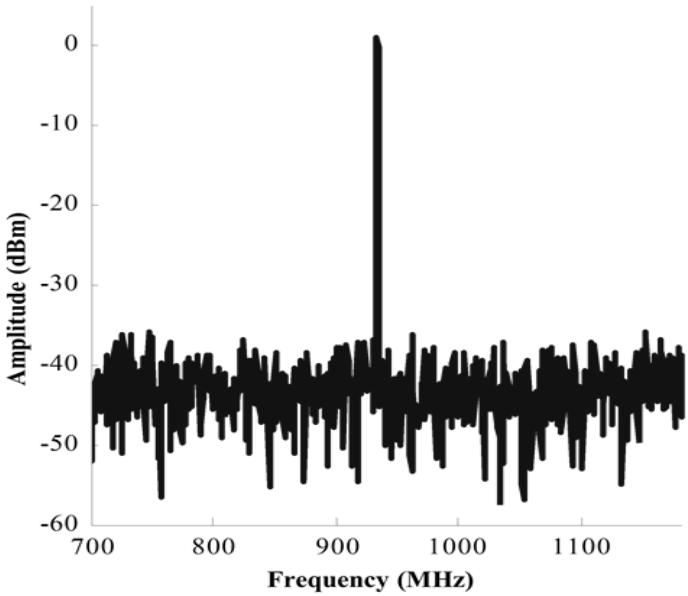

Figure 6.4. SMR-Colpitts oscillator output spectrum showing a resonant frequency of 933 MHz.

The Colpitts oscillator used the SMR in a 1-port configuration by grounding the output port unlike the Pierce oscillator in which a 2-port configuration is established [170]. The SMR device behaves as an inductor between its series and parallel frequencies of operation. Gain is provided to the oscillator by the NPN RF

Transistor BFR92P, which also allows the circuits to operate at higher frequencies by reducing the parasitic capacitances when compared to a nominal operational amplifier. The output voltage is amplified with the aid of a commercial RF amplifier chip UPC2771. The high frequency output from the RF amplifier is taken to a frequency divider IC chip HMC434E, which divides the high frequency by eight. This divider output voltage is again amplified and sent to the mixer circuit for obtaining the differential signal. The schematic of the Colpitts oscillator circuit along with the output amplifier and frequency divider circuit is shown in the Appendix B.

The LC tank oscillation energy and the wideband noise energy at the SMR´s resonance frequency stored in the device, create the initial start-up oscillator frequency. A standing electrical wave is created inside the SMR resonator, when the Barkhausen's criterions are satisfied within the oscillator loop. As more SMR energy flows, more current flows through the device, causing the oscillations to move towards the resonance frequency of the SMR [172]. Figure 6.4 shows the output spectrum of an SMR based Colpitts oscillator circuit showing the resonant frequency peak of 933 MHz obtained by a Tektronix MDO3012 Mixed Domain Oscilloscope.

An interface board consisting of the mixer circuitry (Analog Devices HMC207AS8) and the associated drive circuitries including the Low Pass Filter (SCLF-10+ MiniCircuits) and the comparator chip (ADCMP600) is detailed in the schematic diagram shown in Appendix C. The reference and the sensing SMR oscillators are mixed using the passive mixer chip to obtain the differential signal. The amplified mixer output is passed through the LPF to remove the unwanted high frequencies, common mode variations and other harmonics. This sinusoidal differential output is converted to a digital square signal having the same frequency with the aid of the comparator chip, which in turn is sent to a microcontroller for digital processing.

6.6 Pierce FBAR Oscillator

As part of CMOS VLSI implementation of an RF oscillator and drive circuitry for an acoustic FBAR resonator, a simple oscillator circuit was designed, implemented, and measured using an AMS 0.35μm CMOS C35B4C3 process (Europractice Multi-Project Wafer Run). The general configuration of a Pierce

oscillator circuitry for the construction of a crystal oscillator is depicted in Figure 6.5, which shows that amplifier is placed in a feedback loop configuration with an acoustic resonator. Here the amplifier provides sufficient gain to compensate for the losses due to the resonator and parasitic elements in the system. When the system satisfies the Barkhausen criterion for sustained oscillations by achieving a unity loop gain at the required 360 degree loop phase, it starts oscillating at the target oscillation frequency. This topology [164] is utilized in the implementation of the CMOS inverter-based FBAR oscillator.

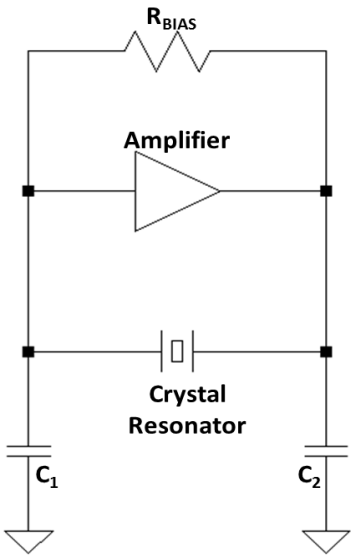

Figure 6.5. The schematic of a Pierce oscillator circuitry for the realization of an acoustic crystal oscillator

The Pierce oscillator is a derivative of the Colpitts oscillator, as both of them uses two capacitors and one inductor as the reactive elements that form the feedback circuit [167]. In the case of an FBAR Pierce oscillator, the FBAR itself acts as an inductor at all frequencies between the series and parallel frequency of operation. The inverting amplifier provides the 180 degree phase shift in addition to providing enough gain to compensate for the FBAR losses. The FBAR and its output impedance along with the discrete capacitors form a pi-network filter that provides the additional 180 degree phase shift, allowing only the resonant frequency to pass through it. Thus, Barkhausen criterion is satisfied and sustained oscillations are obtained using an FBAR resonator.

6.6.1 CMOS Oscillator Designs

One of the advantage of Pierce oscillator circuit is that sustained oscillations are obtained without the use of an inductor and hence it can be realised using CMOS technology. As the impedance of the FBAR resonator at parallel resonance frequency is much larger than that at the series resonance (as evident from Figure 6.2[a]), the Pierce oscillator was chosen to operate at the parallel resonance of the FBAR. Parallel resonance operation is also suitable for low phase noise operation; allowing a higher *loaded Q* [173]. The amplifiers are commonly implemented using digital CMOS inverters and the capacitors may be provided explicitly or can be provided by the device, interconnect and pad capacitances [174].

In order to obtain a relatively high frequency of operation (approximately 890 MHz) for the operation of the FBAR resonator, RF models of NMOS (n-channel Metal-Oxide-Semiconductor) and PMOS (p-channel Metal-Oxide-Semiconductor) field-effect transistors namely *nmosrf* and *pmosrf* that were present in the AMS kit were employed in the design of the oscillator. The CMOS oscillator circuit was realized by utilizing two different iterations of oscillator designs with four possible configurations, in order to increase the possibility of producing an efficient oscillator circuit, having the required gain to start-up the oscillations [167]. Figure 6.6 shows the two versions of the Pierce oscillator circuit. Both of them are similar in operation, but the latter one providing a better amplifier gain than the former. Both the above designs were verified with two different configurations on the basis of providing parallel capacitors either on-chip or through the utilization of inherent parasitic capacitances.

The single-inverter based CMOS Pierce oscillator circuit, as shown in Figure 6.6(a), uses an n-channel MOSFET (Metal-Oxide-Semiconductor Field-Effect Transistor) as the active device forming the gain stage. The FBAR resonator along with the load capacitances forms the feedback stage, which allows only the oscillation frequency to pass through it. The large resistor R_{poly} is used to provide the optimal operating point, so that the maximum allowable voltage swing is obtained at the amplifier output. The modified Butterworth-Van Dyke circuit model of the FBAR depicted in the Figure 6.2[b], serves as a resonant tank model for the design of the oscillator. The FBAR behaves as an inductor at frequencies between the series and

parallel resonant frequencies of the resonator. The capacitances C_1, C_2 along with C_m and C_s forms a tuned circuit along with FBAR resonator at an effective parallel resonant frequency, which also helps in oscillator start-up. As a result, wideband noise energy at the resonance frequency will get stored in the FBAR device. This results in the generation of a standing electrical wave inside the resonator. As the energy builds up in the FBAR, increased current flow through the resonator [175]. This causes the start-up oscillation frequency to move into the direction of the FBAR´s resonance frequency, where it satisfies the Barkhausen criterion [172].

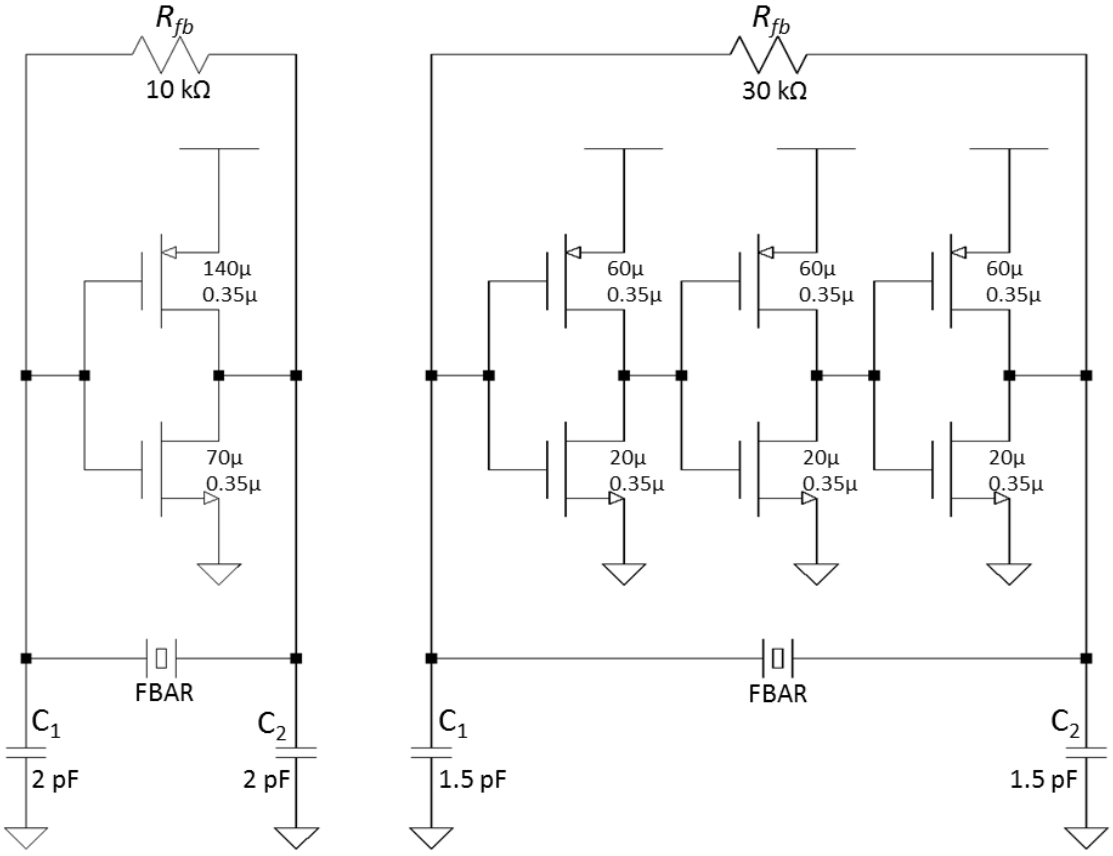

Figure 6.6. Inverter based CMOS Pierce oscillator design iterations: (a) Schematic of the single-inverter based Pierce oscillator (b) Three-inverter based FBAR oscillator schematic.

During oscillation, the inverter experience a high load impedance, due to its operation at parallel resonant frequency. This high FBAR impedance forms a parallel combination with the feedback resistor and the output impedance of the NMOS device. By performing AC analysis of the circuit, the loop gain at the resonant frequency can be obtained as

$$A_L \approx -2g_m \left(R_{fb} \parallel R_p \right) \qquad 6.9$$

where A_L is the loop gain of the circuit, R_{fb} is the feedback resistor, R_p is the FBAR impedance at parallel resonance frequency and g_m is the transconductance of both the NMOS and PMOS devices [174], [176]. We have assumed that the output impedance of the NMOS device is infinite, and that the parallel capacitors $C_1 = C_2$.

Since $R_{fb} >> R_p$, the above equation can be approximated as

$$A_L \approx -2g_m R_p \qquad 6.10$$

From the above equation, it can be observed that the transconductances of both the PMOS and NMOS devices adds up to obtain the loop gain. But the same drain currents flow through both the devices. Thus only about half the current is needed to produce the required transconductance of the circuit [177]. As a result, the power consumption will be reduced.

The circuit shown in Figure 6.6(b) is largely identical to that of the single-inverter based circuit, except the fact that it includes three inverter cascade stages in order to improve the amplifier gain. Here also there is no need for any reference currents, as the circuit is self-biased. Since current flow is not controlled by any current source, the circuit allows rail-to-rail oscillation. With an increase in gate voltage amplitude, the current subsequently increases above the bias current of 3.4 mA. As a result, the oscillator amplitude grows, until the transistors exhibit non-linear behaviour that limits the signal amplitude. Hence, a three-inverter cascade-based Pierce oscillator is used in this work, in order to provide additional gain. This extra gain is needed to compensate for the high resonator losses and also to obtain a gain that is greater than unity. In doing so, the oscillation conditions are met, ensuring a good oscillator start-up.

Both the inverter circuits shown in Figure 6.6 were identified in two different configurations on the basis of providing the discrete parallel capacitors either on-chip or through the utilization of inherent parasitic capacitances. In the first configuration, the discrete capacitors were implemented on-chip using the *cpolyrf* model identified

by the Poly1-Poly2 module stack of the AMS 0.35 µm CMOS process. For the implementation of the second iteration of the oscillators, no explicit parallel capacitors were provided and these capacitors were realised by the parasitic capacitors including the resonator capacitance, MOSFET internal capacitance, interconnect and pad capacitance.

Pre and post layout simulations of CMOS ASIC oscillator have been performed using the Cadence SpectreRF circuit simulator. The hybrid CMOS-FBAR oscillator ensures sufficient gain to overcome the FBAR insertion losses and provides sustained oscillation [178]. The post layout SpectreRF simulations of the oscillator circuit after parasitic extraction are shown in the Figure 6.7. The output voltage levels during transient simulation are shown in the Figure 6.7(a). The voltage gain (20 dB modifier) at the fundamental resonant frequency is 0 dB, as demonstrated from the periodic steady state analysis of the oscillator circuit, as shown in Figure 6.7(b). The periodic steady-state analysis solves for all of the harmonics produced by the oscillator system as it has a single input frequency [179]. Figure 6.7(c) shows the loop gain magnitude and phase at the FBAR oscillator frequency. Close inspection of the magnitude and phase curves show that the oscillator satisfies the Barkhausen criterion for sustained oscillations, because there is a gain of 0 dB (unity) and a phase of 360 degree, occurring simultaneously at the oscillator frequency.

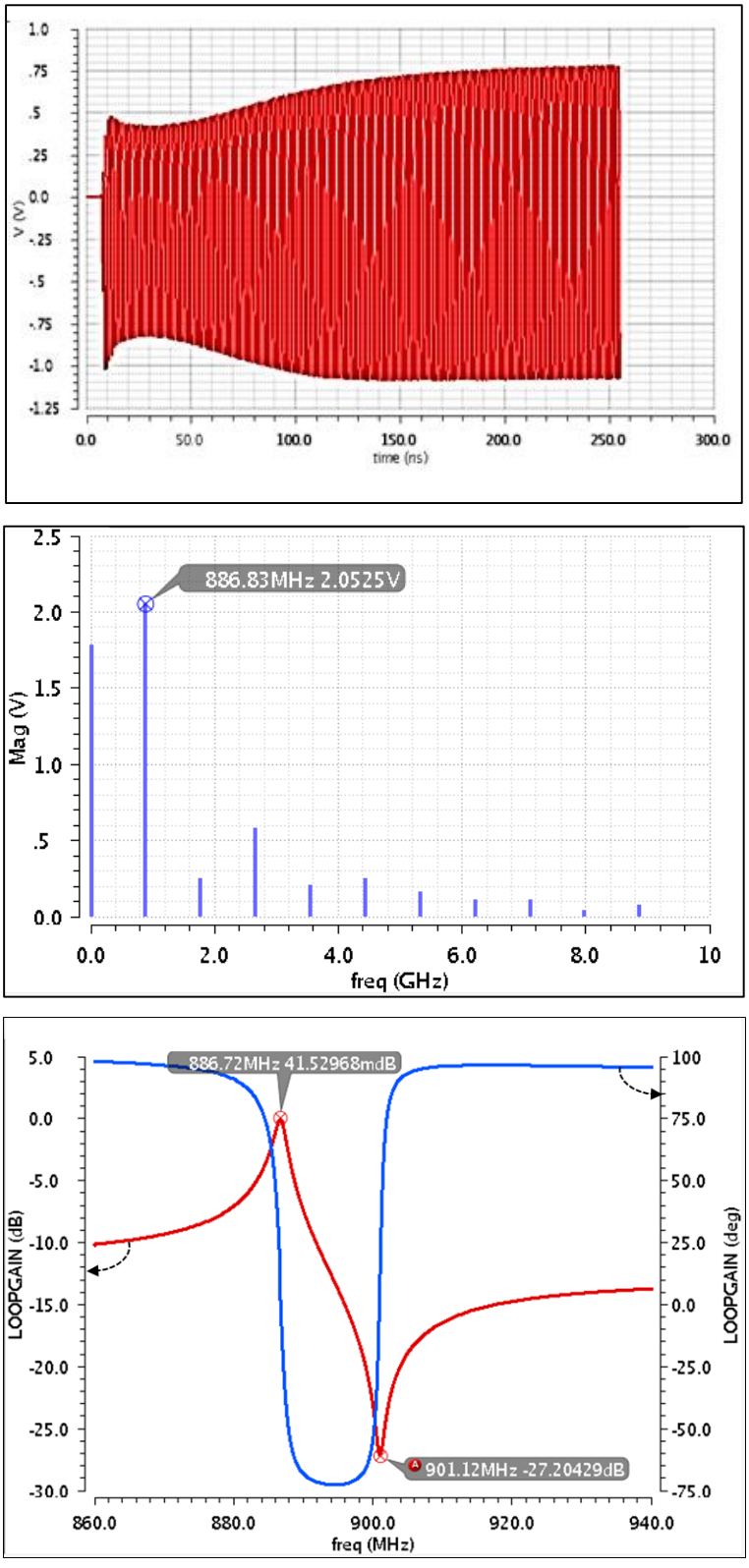

Figure 6.7. Post layout SpectreRF simulation results of CMOS Oscillator detailing (a): Transient stability (b): Periodic Steady state analysis (c): Loop gain magnitude and phase.

6.7 Mixer Input Baluns

The dual-sensor system is designed to operate in a dual configuration in which one sensor forms the sensing device, whilst the second one is used as a reference channel; thereby eliminating common mode interferences on the baseline signal (as detailed in section 3.9). Each single sensor is fundamentally an FBAR-based CMOS oscillator resonating at ~890 MHz. Both the sensing and the reference oscillator outputs are fed to separate buffer amplifiers in order to prevent loading, which in turn are connected to on-chip active baluns separately, so as to generate a differential signal from the single ended oscillator output signals.

In RF sensing applications, a differential approach is usually preferred over a single ended signal due to its advantages such as less susceptibility to noise and electromagnetic coupled disturbances in addition to benefits such as better common mode rejection ratio and power supply rejection ratio. Additionally, there is an increased signal to noise ratio due to twice the swing of a single-ended signal, which helps in lowering the power dissipation. Moreover, certain circuits such as RF based frequency mixers also require differential signals for their efficient function [178], [179]. Due to the above-mentioned reasons, ASICs operating in the high frequency domain utilize a differential approach within the chip, and hence an intermediate stage able to convert single ended signals to differential signal is essential. Several CMOS solutions have been proposed in literatures for realizing baluns that can convert a differential to single-ended signal, but the reverse problem has been approached occasionally[180] [181]. As a result, several off-chip baluns were extensively utilized by developers in communications system design [182]. The balun implemented in this design uses a cascode topology in which the two amplifying stages are formed in a common source (CS) and common gate (CG) configurations, as demonstrated in [181], [183]. The Figure 6.8 gives a simplified schematic of the single-ended to differential-ended Amplifier, used in the ASIC implementation. The Figure 6.9 shows the transient response of the simulated differential oscillator signals obtained at the differential outputs of the balun. The periodic steady-state response of the circuit obtained at the fundamental resonant frequency shown in Figure 6.10 confirms the peak output voltage levels obtained during transient simulation.

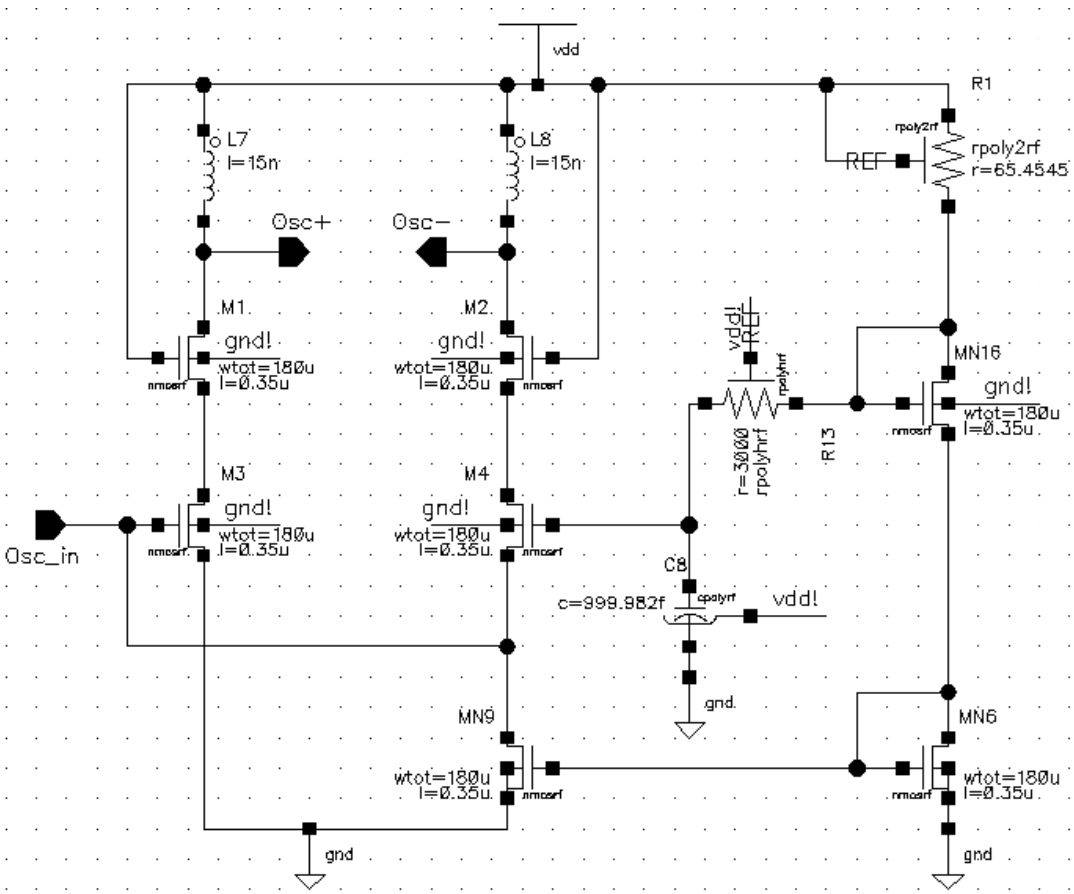

Figure 6.8. Schematic of the single-ended to Differential-ended Amplifier.

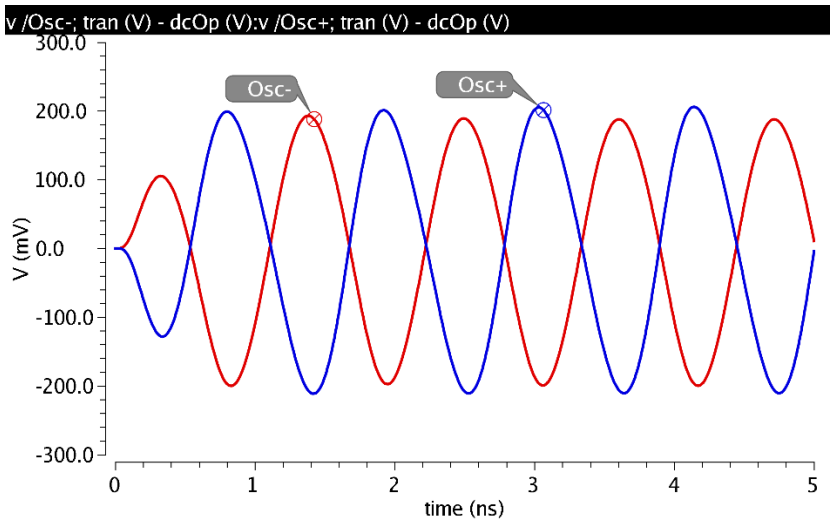

Figure 6.9. Transient response of the simulated differential oscillator signals obtained at the differential outputs of the single-ended to Differential-ended Amplifier.

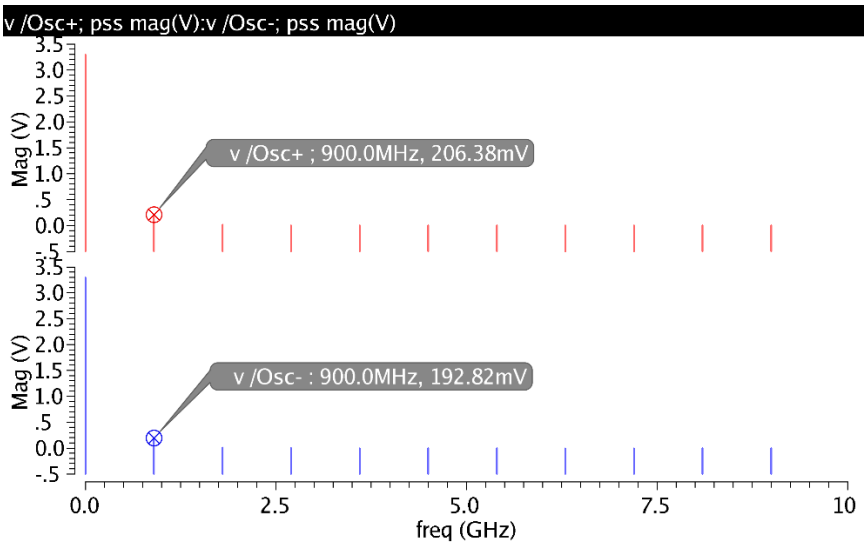

Figure 6.10. Periodic steady-state response of the output spectrum showing the peak voltage magnitude at the fundamental resonant frequency.

6.8 Down-conversion Mixer circuitry

The high frequency signals of the sensing and reference FBAR oscillators are mixed using an analog mixer in order to obtain a low frequency differential output that is easier to measure at high resolution. Such a differential sensor measurement allows the elimination of common mode variations of temperature and other process variations. An analogue mixer which can receive high frequency sensor signals at both the RF (Radio Frequency) and LO (Local Oscillator) input terminals and also provides a differential intermediate frequency (IF) signal at the output port, has been utilized in this ASIC chip. Hence the mixer used in the drive circuitry is based on the Gilbert-cell topology. The dual-ended high frequency output from the sensing FBAR based balun is applied to the balanced RF input and the dual-ended signal from the reference FBAR based balun is connected to the LO input of the Double Balanced Gilbert cell mixer [184].

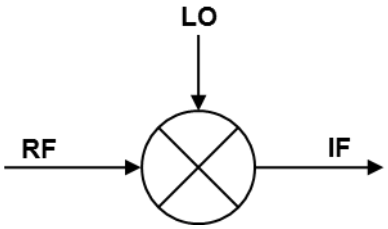

Figure 6.11. Typical symbol of a mixer circuit.

Mixers must be either time varying or non-linear elements so as to translate a signal from one frequency to another. The Figure 6.11 shows the typical symbol of an ideal mixer. An IF signal is obtained by multiplying the RF and the LO signals, as evident from the figure. The multiplication of two signals in an ideal mixer is illustrated in equation shown below:

$$\left(V_1 c\cos\omega_1 t\right)\left(V_2 c\cos\omega_2 t\right)=\frac{V_1V_2}{2}\left(c\cos\left(\omega_1+\omega_2\right)t+c\cos\left(\omega_1-\omega_2\right)t\right) \qquad 6.11$$

From the equation, it is clear that multiplication results in an output comprising of sum and difference frequencies of the inputs [185]. Also, the output amplitude is proportional to the product of the RF and LO amplitudes. Hence, any amplitude modulation occurring to the RF input signal could be transferred to the IF signal, by keeping the LO amplitude a constant. However, due to this same principle, some unwanted signal modulation effects also occur at the output, due to the non-linearity effects of the mixers and amplifiers. Suppression of this cross-modulation effects is achieved by improving the linearity of the mixer circuit [182]. An advantage of Gilbert-cell mixers is that they maintain high isolation between ports due to their double balanced structure. The Figure 6.12 shows the simplified circuit diagram of a Double balanced Gilbert cell mixer, which uses a linear, time-varying circuit to achieve time-domain multiplication. The RF signal is connected to two pairs of long-tailed differential amplifier pairs (M1A-M1B pair and M2A-M2B pair) which perform a voltage to current conversion. Both these differential amplifiers are provided with inductive degeneration, which helps in noise degradation, due to their low thermal noise. Also, the increase in inductive reactance with increase in frequency removes high frequency harmonic and intermodulation components in a mixer [182]. Their drain terminals have a cross connection to a set of four transistors M3, M4, M5 and

M6. These four transistors are controlled and are driven by the LO signal, which allows the switching of alternate transistor pairs at a time, so as to form a multiplication function and to provide the switching effect.

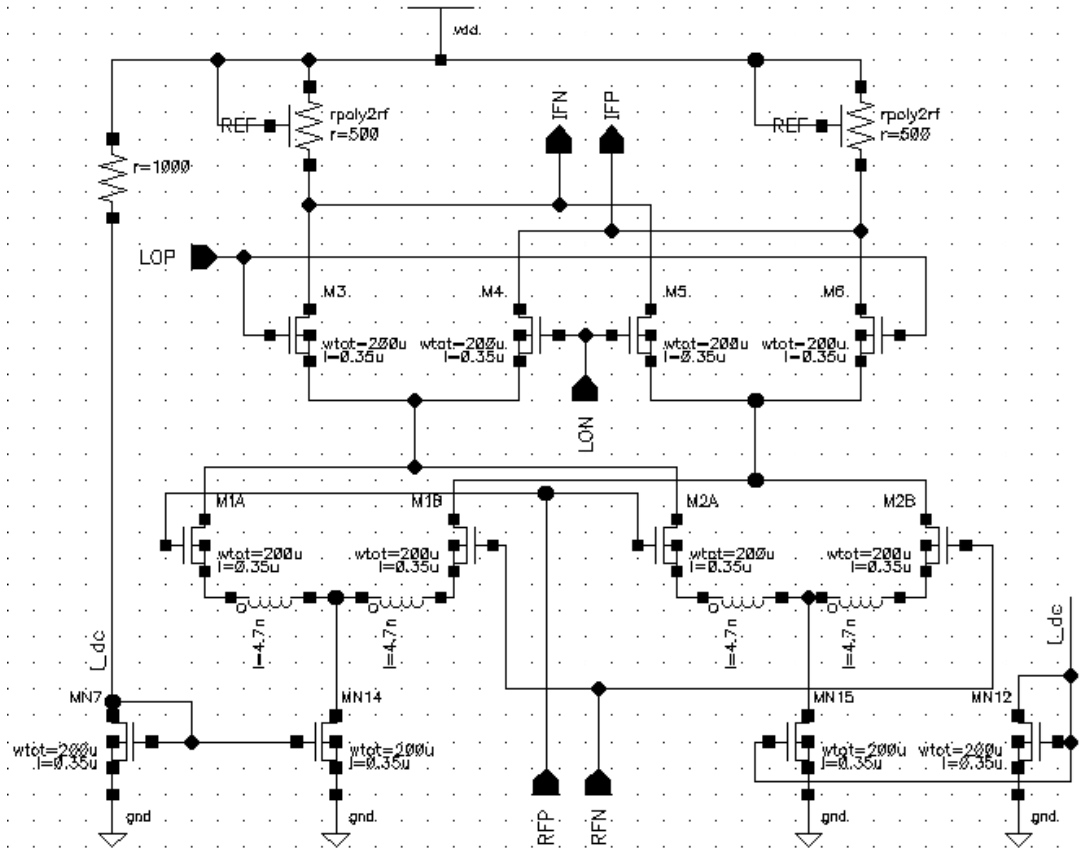

Figure 6.12. Circuit schematic of the Gilbert Cell Double balanced mixer.

Severe non-linearities limit the ceiling of the RF input signal entering a mixer circuit and is identified by determining the 1-dB compression point, which measures the linearity of the mixer circuit. This compression point establish the value of the RF signal power above which the IF output exhibits some non-linear behaviour, deviating from its linear nature. The SpectreRF simulation of the post-layout mixer circuit shown in Figure 6.13[a] demonstrates the signal curve and an ideal linear slope, and calculates a value of -2.11796 dBm for the 1 dB compression point.

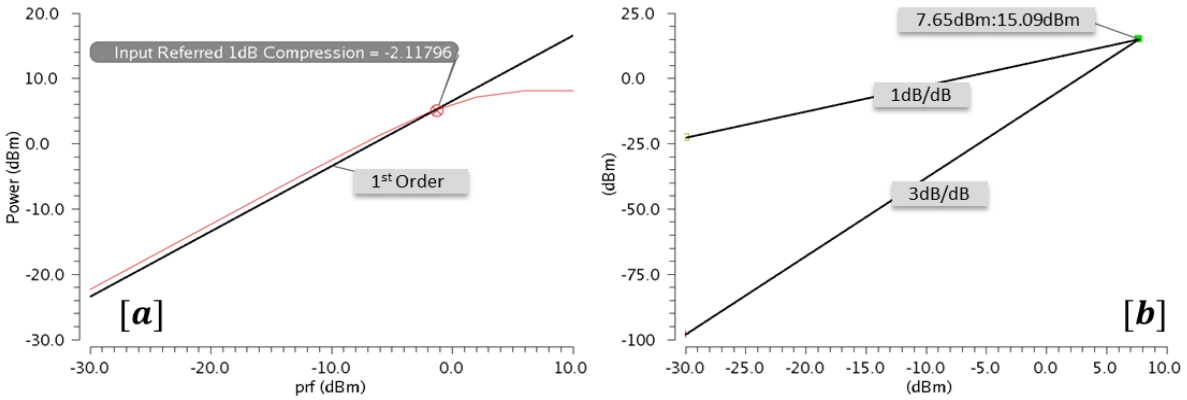

Figure 6.13. Plot showing the input RF power versus output IF power characterising the mixer linearity. (a) Demonstrates the 1 dB compression point of the mixer. (b) Demonstrates the input and output third-order intercept point of the mixer.

Practical mixers often suffer from intermodulation (IM) effects due to the effect of an interferer signal at the RF input. Thus the IF output will contain unwanted third order IM products which are having frequencies of $2\omega_{RF1} \pm \omega_{RF2}$ and $2\omega_{RF2} \pm \omega_{RF1}$. The difference frequency terms interfere with the IF passband range while the sum frequency terms will be removed by filtering [182]. The third order intercept shows the extrapolated point of intersection of the linear mixer output and the third order IM output, which can be defined in terms of RF signal power or IF signal power (IIP3 and OIP3, for input and output third-order intercept point). Post layout spectreRF simulation of the Gilbert mixer shows IIP3 to be 7.65dBm and OIP3 to be 15.09dBm, which are evident from the Figure 6.13[b].

Passive mixers often suffer from conversion loss during frequency translation from the RF to IF signal. However, the conversion gain (defined as the ratio of the output IF signal to the value of the input RF signal) in the case of an active mixer such as Gilbert cell type is greater than unity. Hence these type of mixers also provide signal amplification, in addition to efficient frequency translation. The Figure 6.14 plots the variation of the conversion gain of the mixer circuit obtained using post-layout spectreRF simulation.

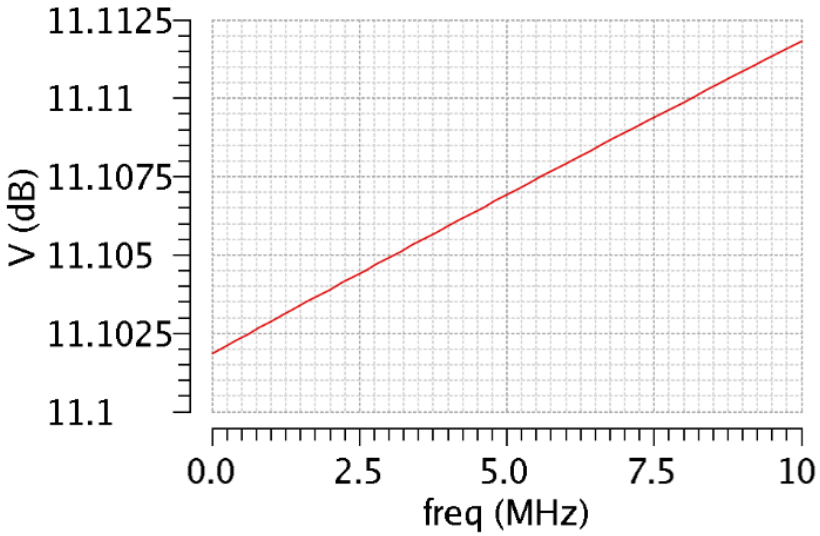

Figure 6.14. Plot showing the variation of the mixer conversion gain with the passband frequency.

6.9 Associated drive circuitry

The output of the double balanced Gilbert mixer being a dual-ended signal, there is a need for converting it into a single-ended one, for ease of connection as well as to simplify the drive circuitry for capturing the sensor signal easily. As the useful frequency output from the mixer lies within 50 MHz range, it is quite easy and straightforward to capture this low frequency signal using an active balun, instead of using a passive balun. In fact, active baluns always use reduced chip area when compared to passive ones, and also they provide certain amplification when compared to passive types. A simple differential pair with a single-ended output connected to a source-follower [186] has been utilized in this ASIC chip. The schematic of the differential amplifier is presented in Figure 6 of Appendix A. The current mirror provides a reference bias current of 40 μA to the differential amplifier stage. The use of a low frequency differential pair as a balun is that, it not only convert a dual-ended signal to a single-ended one, but also provides an initial stage of filtering to the unwanted high frequency third order IM components appearing at the IF output of the mixer. The gain magnitude and the bandwidth of the differential amplifier is presented in Figure 7 of Appendix A, which shows that there is a high closed-loop gain of 26dB.

A second stage of filtering of the unwanted high frequency signals is provided by an active low pass filter implemented using an operational amplifier circuitry. This Low Pass Filter (LPF) stage utilizes the second order Sallen-Key topology [187], designed for an upper cut off frequency of 30 MHz. Such a continuous time filter forms a crucial component in analogue signal processing, because it can be used in antialiasing the carrier frequency, harmonics and noise that are passed and aliased into the differential IF signal. This filter has been designed for a unity gain with infinite input resistance and a zero output resistance [188]. The differential amplifier circuit used in the previous stage (Figure 6 of Appendix A) has been utilized for the implementation of this second-order filter. The schematic of the second-order Sallen-Key LPF has been presented in Figure 8 of Appendix A. Magnitude response plot of the LPF (Figure 9 of Appendix A) confirms the designed upper-cut off frequency of 30 MHz.

The sinusoidal output signal from the low pass filter contains only the desired differential sensor signal, which should be converted to a square wave having the same frequency, for digital processing. This circuit utilizes a comparator that switches its output between either positive or negative supply rails, depending on the polarity of the difference between its two input terminals. The comparator used here is an analogue cell from the AMS CMOS 0.35 μm library of cells, which requires an external bias current of 15μA [189]. The sinusoidal low pass filter output is applied at the positive input of the comparator, while the negative input is provided with an external dc voltage reference of 1.65V. As a result, the output of the comparator will be a square signal, which in turn is fed to a microcontroller input. The schematic of the comparator used in the design is presented in Figure 10 of Appendix A. The Figure 11 of Appendix A shows the comparison of the transient response of the LPF output and the comparator output. This figure indicates that the comparator output is obtained as a rail-to-rail square wave signal.

Frequency counting of the differential sensor output square signal is achieved by using a low-cost microcontroller Teensy 3.1, which log the acquired data to a computer through USB serial communication. This data acquisition and the real time visualization of the data was carried out with virtual instrument developed [175] using LabVIEW software.

6.10 Post-fabrication results

6.10.1 Output spectrum of FBAR-CMOS oscillators

The performance of the ASIC oscillator has been verified using high frequency oscilloscopes and spectrum analysers with the help of high impedance active probes. The output frequency spectrum of the oscillator obtained using the Tektronix MDO3012 Mixed Domain Oscilloscope is shown in Figure 6.15[a]. A narrow peak is clearly visible in the figure, which demonstrates the fundamental oscillator frequency of 887.43 MHz, This is the nominal frequency at which the FBAR sensor will be operated, so as to drive the signal conditioning circuitry which includes the down conversion mixer and the output comparator. In addition, this is an important validation of the basic operation of the ASIC circuitry as well as the steady-state behaviour of the ASIC based FBAR oscillator design.

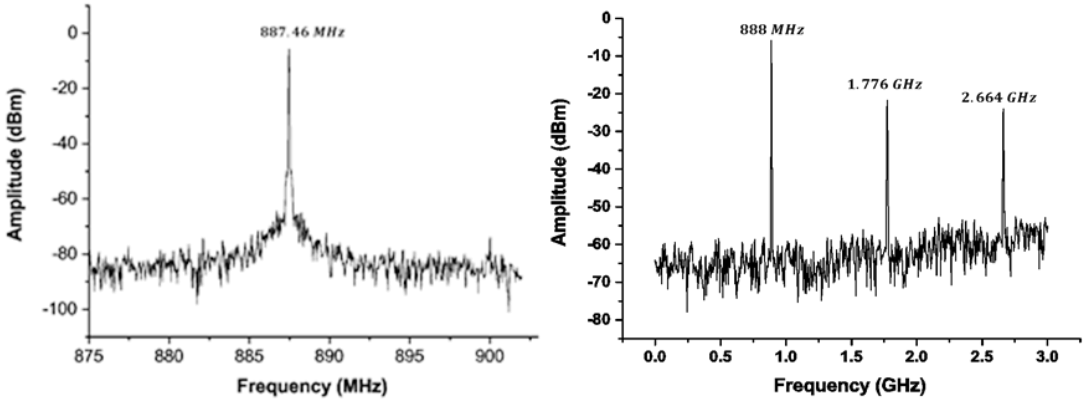

Figure 6.15. (a) Frequency spectrum measured for the FBAR-CMOS oscillator showing the oscillation frequency of 887.6 MHz. (b) Measured oscillator output spectrum showing the fundamental frequency (888 MHz), the first and the second harmonic peaks (1776 MHz and 2664 MHz), respectively.

The Figure 6.15[b] shows a broader spectrum for the CMOS FBAR oscillator which demonstrates peaks at 888 MHz, 1.776 GHz, and 2.664 GHz. These peaks indicate the fundamental frequency, the first and the second harmonics, respectively. These oscillator harmonics are formed not due to the FBAR resonator itself, but are caused by the non-linearities of the restoring inverting amplifier used [167]. It can be observed that the signal amplitude of the fundamental oscillation frequency is much higher (>15 dB) than the harmonics of the oscillator circuit, which allows the

amplifier to select the fundamental frequency even after the addition of ligands on to the sensor surface, which could degrade the amplitude of the sensor output voltage.

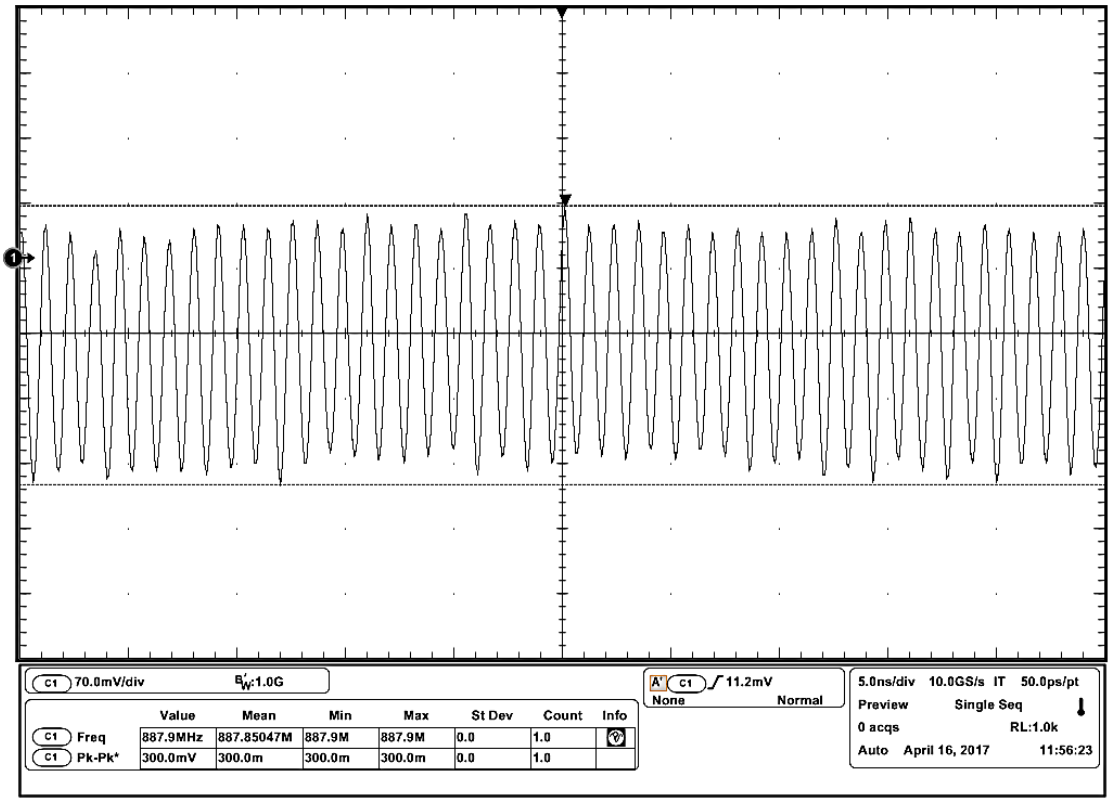

Figure 6.16. Measured transient signals from the CMOS FBAR oscillator using a high-impedance active probe showing the fundamental frequency at 887.9 MHz, with the aid of a high speed oscilloscope.

Transient oscillator signals were measured from the CMOS FBAR oscillator using a high-impedance active probe and a high-speed oscilloscope. Figure 6.16 shows the screen captured plot of the buffered Pierce oscillator output signal, measured as it enters the mixer circuitry. From this figure, it can be observed that the oscillator output frequency is 886.9 MHz, with a peak-to-peak voltage swing of 300 mV. This oscillator output frequency verifies that the designed Pierce oscillator is operating at the fundamental resonant frequency of the FBAR device, thus creating a CMOS driven FBAR sensor.

6.10.2 Comparator differential output

The differential sensor output from the mixer is driven by a LPF to remove the high frequency harmonics and other inter-modulation components at the mixer output. This output from the LPF is obtained as a digital signal with voltage level compatible

to that of the microcontroller digital input pin voltage level, which is of 0 – 3.3V. A typical time-varying output of the comparator circuit when two FBARs are driven by the ASIC circuitry is obtained as shown in the Figure 6.17. The square pulse was observed to have a base differential frequency of 3.73 MHz at a 3.3V supply. It can be observed that there is some amount of high-frequency noise present at the comparator output.

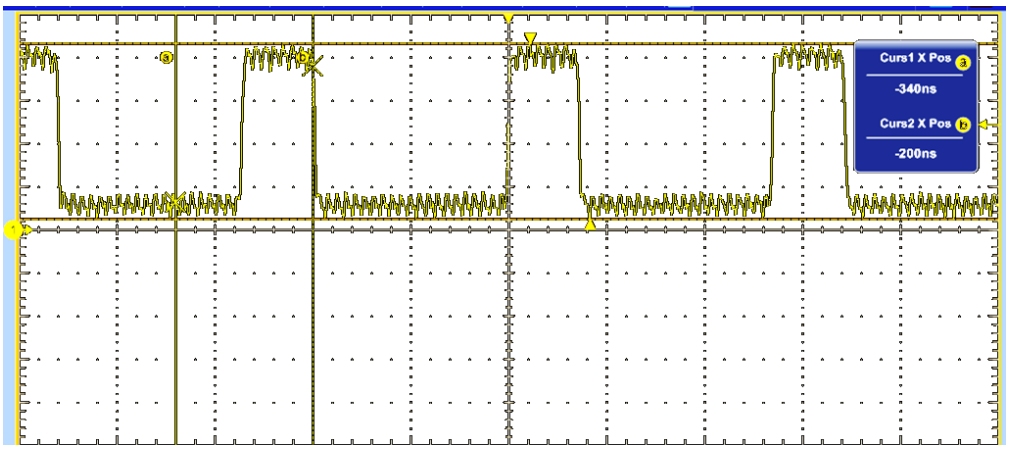

Figure 6.17. The output differential sensor response obtained as a time-varying square signal from the comparator output of the ASIC FBAR sensor system.

6.11 Phase noise Analysis of CMOS-FBAR Oscillator

Phase noise, can be described as a short-term random frequency fluctuations of a signal. Because it has an impact on overall sensor system performance, it is a major concern in oscillator circuit design. The phase noise is a measurement of uncertainty in phase of the output of a feedback oscillator, and is measured as the ratio of the signal power P_{sig} at the frequency of oscillation ω_o to the power at a frequency offset $\Delta\omega$ from the oscillation frequency [167].

Consider a lossy resonator connected to an energy restoration amplifier. The positive resistance of the resonator will be cancelled out by an average negative resistance of the restoring amplifier, resulting in the creation of a lossless *LC* network. The phase noise due to the resistance *R*, relative to the carrier frequency is given by:

$$L\{\Delta\omega\} = 10\log\left[\frac{2kT}{P_{sig}}.\left(\frac{\omega_0}{2Q\Delta\omega}\right)^2\right] \qquad 6.12$$

where *k* is Boltzmann's constant, *T* is absolute temperature, and *Q* is the quality factor of the resonant tank [182]. This equation shows that the thermal noise of the tank conductance exhibits *1/f²* behaviour because of the filtering action of the resonator tank, reducing with the inverse square of the offset frequency [190]. This equation demonstrates that at a particular offset, as the carrier power and *Q* increases, the phase noise of the system gets reduced. But, in addition to the *1/f²* region, a real phase noise spectrum consists of a region where the phase noise flatten out for a large $\Delta\omega$, resulting in a white noise floor region. Such a floor may be due to the noise associated with active elements within the sensor system (such as buffers, mixer, filter), or even the noise performance of the measurement system. Additionally, there is a *1/f³* region as well, at smaller $\Delta\omega$, nearer to the centre frequency. Thus, a modification to the above equation was proposed by Leeson in 1966, which accounts for all the above-said observations, given by:

$$L\{\Delta\omega\} = 10\log\left[\frac{2FkT}{P_{sig}}.\left\{1+\left(\frac{\omega_0}{2Q\Delta\omega}\right)^2\right\}\left(1+\frac{\Delta\omega_{1/f^3}}{|\Delta\omega|}\right)\right] \qquad 6.13$$

The equation includes an empirical fitting parameter *F*, causing the increased noise in the *1/f²* region and is determined from the measurements. The noise floor is accounted for by the additive factor of unity and the $1/|\Delta\omega|^3$ behaviour at lower offset frequencies is accounted for by a multiplicative factor (the term in the second set of parenthesis). Figure 6.18(a) gives the sketch of the phase noise behaviour based on ideal oscillator model and Leeson Model.

Phase noise measurements have been carried out using the Tektronix MDO3012 Mixed Domain Oscilloscope for the 888 MHz FBAR CMOS oscillator and is as plotted in Figure 6.18(b). This figure shows the phase noise in dBc/Hz plotted as a function of frequency offset, with the frequency axis on a log scale. It can be observed that the actual plot is approximated by three distinct regions; a $1/f^3$ region near the resonant frequency, a $1/f^2$ region and a white noise floor region with larger $\Delta\omega$. The $1/f^3$ region is formed due to the upconversion of the *1/f* noise to the vicinity of the oscillator resonant frequency, while the $1/f^2$ region is formed due to the resistive noise associated with the resonant FBAR. The white noise floor is obtained from the flicker noise caused due to the circuit elements and also due to the thermal noise floor.

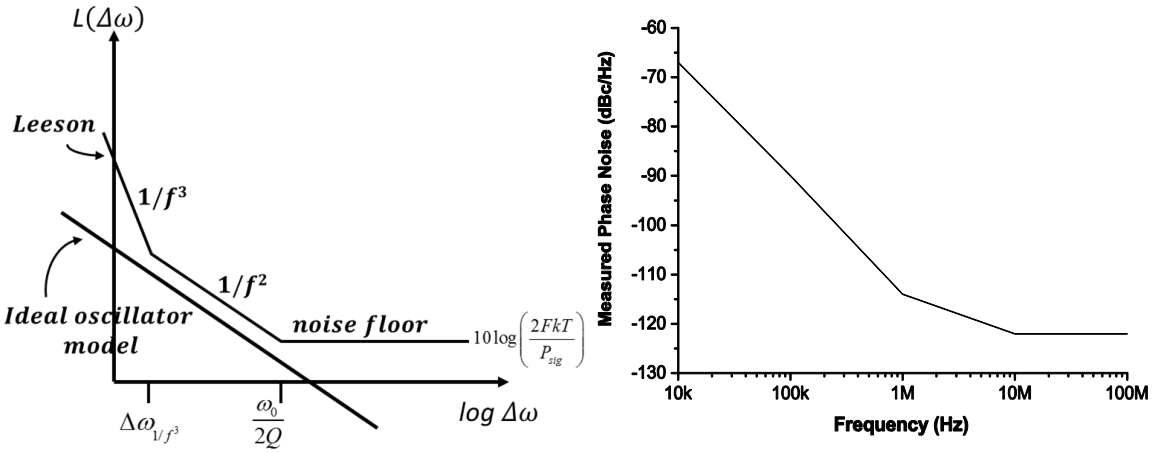

Figure 6.18. (a): Illustration of the shape of the phase noise behaviour based on ideal oscillator model and Leeson Model. (b): Measured phase noise from FBAR-CMOS oscillator having oscillation frequency near 888 MHz, which shows a similarity with the Leeson behaviour.

6.12 Complete ASIC design

The spatial and parasitic load limitations of externally coupled oscillators, have been eliminated by the hybrid integration of the FBAR devices with CMOS oscillator circuitry. The composite micrograph of the fabricated ASIC die is shown in Figure 6.19. The layout for the complete ASIC circuit required an area of 1.65 mm × 1.55 mm including I/O pads. The ASIC chip was fabricated at AMS using a 0.35µm CMOS process. It has the capability of supporting a single sensor system in which two single-

ended FBARs are driven using inverter-based Pierce oscillator circuits and a single differential sensor response (square signal) is provided at the comparator output.

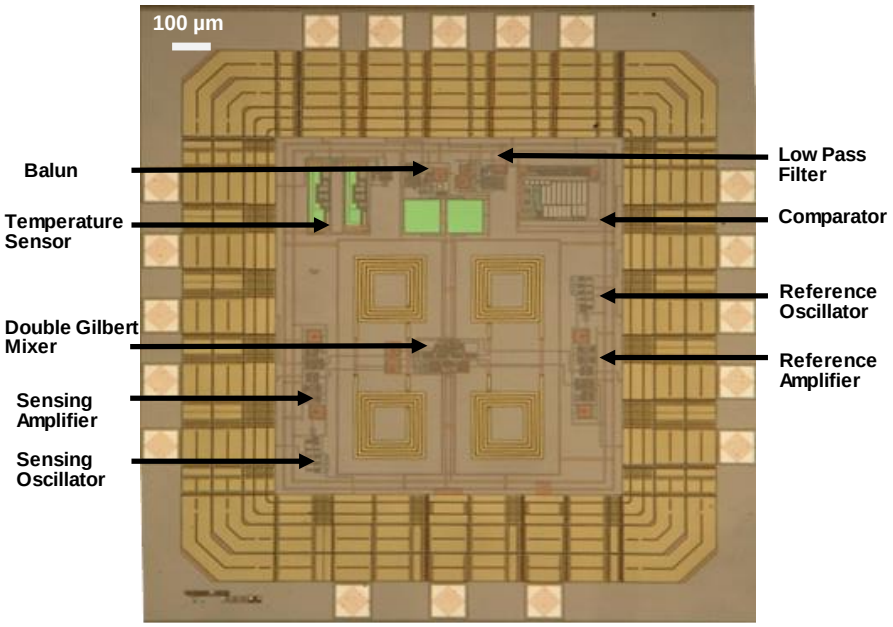

Figure 6.19. Composite micrograph of fabricated ASIC die

6.13 Application of MEMS-FBAR Sensor System

6.13.1 Particulate Matter Detection

A hybrid MEMS-FBAR based microsensor system utilizing high frequency acoustic wave devices for the real time monitoring of airborne fine particulates (< 2.5 µm) has been developed to evaluate the performance of the designed AVLSI chip. The hybrid particle sensor is made up of dual high frequency zinc oxide (ZnO) based solidly mounted FBAR device interfaced to the fabricated CMOS ASIC chip. The experimental results proved that the particulate mass loading is delivered as a resonant frequency shift of the FBAR resonating at 890MHz. Figure 6.20(a) shows the photograph of the CMOS-FBAR particle sensor system consisting of the dual FBAR sensors driven by the ASIC chip placed on the PCB along with a virtual impactor to sample 2.5 µm sized particles. The virtual impactor was developed by Farah H. Villa-López, University of Warwick, UK.

A high-frequency PCB has been designed to house the AVLSI ASIC chip and the dual FBAR sensors, as shown in Figure 6.20(b). The PCB design and particle

sensor testing were carried out in collaboration with Geraint Rhys Jones, University of Warwick, UK. The PCB is a four-layer board with grounding layers to reduce the noise associated with high frequencies signals. It also takes account of the phase shifts associated with the RF signal paths to the individual FBAR sensors. The ASIC chip was wire-bonded on to the PCB and was covered with glue for protection, as shown in Figure 6.20(c).

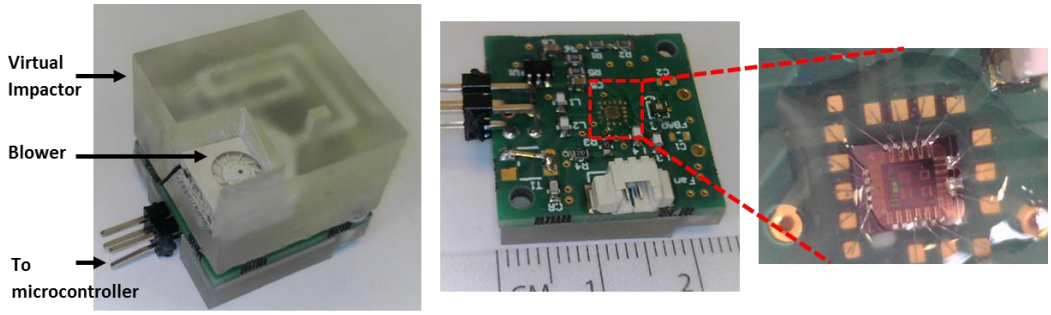

Figure 6.20. (a) Photograph of the CMOS-FBAR particle sensor system. (b) The printed circuit board which houses the AVLSI Chip and the sensors. (c) Inset shows the ASIC chip wire-bonded on to PCB and covered with glue for protection.

The FBAR based particle sensor was characterised and tested in the sensor testing chamber. The microsensor system was placed inside the testing chamber together with a reference commercial instrument (DC1700 Air Quality Monitor, Dylos Corporation) for real-time monitoring of particle deposition within the test chamber. The sensors were exposed to PTFE artificial aerosols to monitor the $PM_{2.5}$ concentration levels inside the test chamber. The deposition of particles onto the sensor surface resulted in a shift in the oscillator resonant frequency. This shift in frequency is measured as a differential square wave signal from the ASIC chip via a Teensy 3.2 microcontroller. The difference between the output frequency before and after injection of particles indicate the sensor response to the particles being introduced. The virtual impactor samples air in where $PM_{2.5}$ particles are separated and then deposited onto the SMR surface, as shown in Figure 6.20(a).

The Figure 6.21 shows the filtered output frequency of the sensor for a period before and after particles are introduced. There is a delay of approximately 2 minutes between particle injection and the response of the chip, which is due to the extra time taken by the particles to travel through the impactor to reach the sensor surface. From the Figure 6.21 it is clear that, the output frequency increases from 46 kHz to 56 kHz (Δf = 10kHz) for the first injection. For the second injection, the change is from 56 kHz to 60 kHz (Δf = 4 kHz). Photographs shown in Figure 6.22 indicates the sensor surface before and after the injection of particles, which prove that particles have been deposited on the sensor surface after particle injection. Frequency response of the FBAR particle sensor corresponds to the particle concentration within the chamber shown by Dylos AQM, which demonstrates that the FBAR responds to the addition of micro particles being deposited on to the sensor surface.

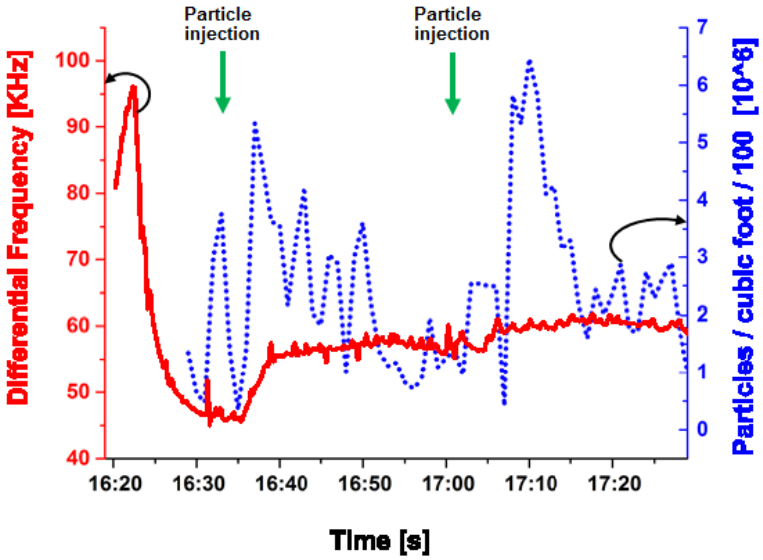

Figure 6.21. Frequency response of the FBAR particle sensor, shown along with data from Dylos AQM, showing that the FBAR responds to the addition of microparticles being deposited on the sensor surface. (The green arrows shows the points of injection of the microparticles).

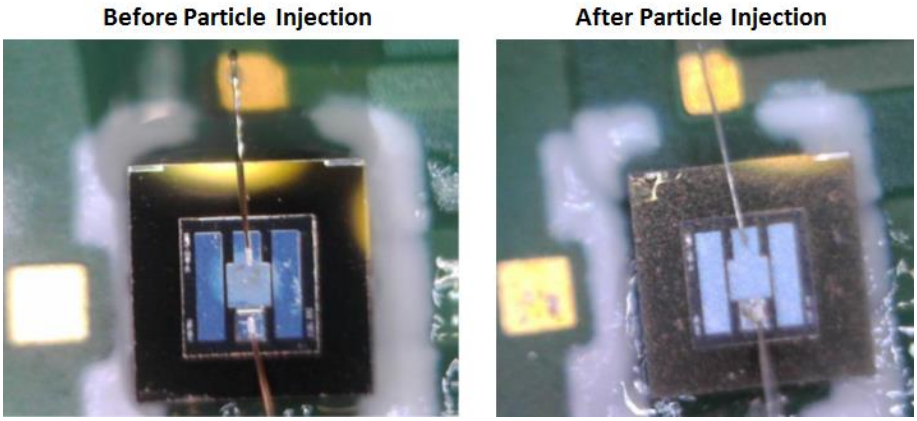

Figure 6.22. Microscopic view of FBAR surface before and after particle injection, shows that white PTFE particles have been deposited throughout the sensor surface.

6.14 Hybrid CMOS-MEMS integration

As part of the development of a compact and low-power portable microsensor system, the sensor drive, control and interface circuitry was deployed in an analog VLSI Chip. The ASIC comprises of an analog module containing the oscillator and the associated signal processing circuitry to sense the differential block as shown on the system architecture diagram in Figure 6.1 in the section 6.2.

The analogue VLSI chip is capable of supporting of dual detection channels and replaces the entire discrete oscillator and mixer modules described in Appendix B. To facilitate the use of SAW/FBAR acoustic sensors of different device characteristics and varying operating conditions, the inverter based Pierce oscillator circuit has been designed to support sensors with a maximum cutoff frequency of around 1 GHz, enabling the use of ultra-high frequency sensors. The analog oscillator output signals can be measured through a buffer stage, and also the balanced mixer generates a common mode-free differential output signal, with the aid of the on-chip low pass filter circuits that remove the unwanted overtones. In addition, a diode-based temperature sensor is also implemented on-chip to provide moderate-precision measurement of the chip temperature.

A low-cost acoustic system-in-a-package microsensor for biochemical/microparticle detection has been developed by packaging the dual FBAR microsensors and the AVLSI CMOS chip in a small RF based QFN package and wire bonding them together, to form a hybrid integrated sensor system. This package will be mounted onto the PCB which in-turn is connected to a data capture circuitry. The Figure 6.23 shows a SiP solution of the CMOS-FBAR sensor in which a sensing FBAR, reference FBAR and the drive Chip are placed in a 6 mm x 6 mm QFN package. This system forms the foundation of a fully integrated portable smart microsensor based on CMOS-FBAR devices for the continuous, real-time and low-cost monitoring of biological, chemical and particulate matter [191].

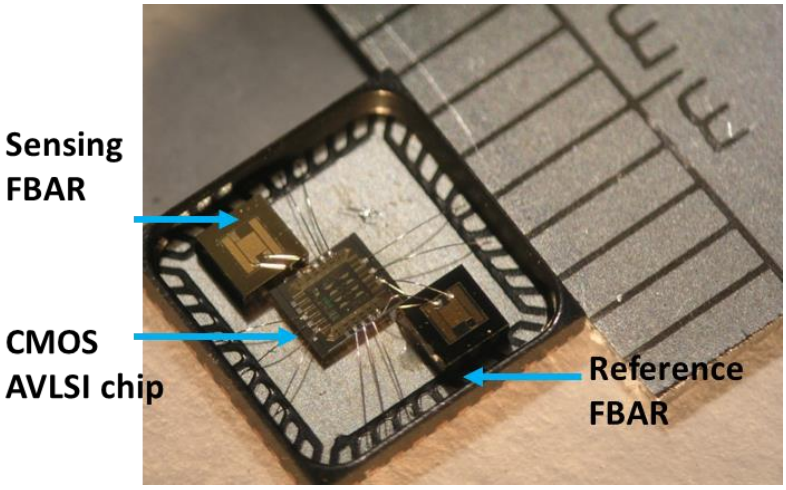

Figure 6.23. Photograph of the hybrid ASIC-FBAR SiP solution.

6.15 VLSI Integration of Acoustic Sensor System

In order to enhance the performance and accuracy of measurements and to develop a miniaturized portable acoustic sensor system, the entire oscillator circuitry including the mixer circuitry which has been implemented using discrete components was replaced by a single ASIC Chip. Figure 6.24 shows a comparison of the discrete oscillator and mixer circuitry combined together and the on-chip resonator circuitry, detailing the overall size of the two circuits. The ASIC solution developed here shows that variation in the baseline oscillator frequencies and subsequent sensor drift can be easily removed through differential operation of the system. Furthermore, it allows the

sensor system to be miniaturized and serves as subsystem for further integration. The ultimate goal is to create a single acoustic based monolithic chemoreceiver-on-a-chip.

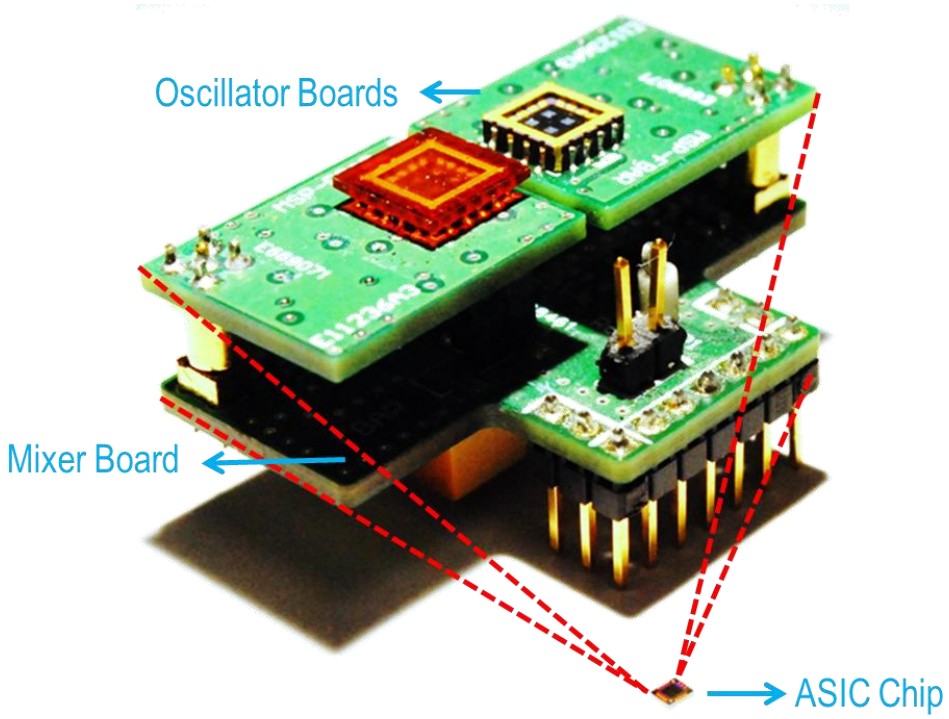

Figure 6.24. Acoustic oscillator circuitry overview showing the actual size comparison of discrete circuitry and ASIC chip.

6.16 Design limitations and future work

A design methodology for the development of an ASIC oscillator chip for a high-frequency acoustic sensor using the CMOS platform has been presented in this thesis. Further optimization could be achieved in the area of power consumption and overall chip size, which could largely improve the cost efficiency of the system. An improvement in the design of the RF mixer could bring about a considerable reduction in the chip size, providing room for accommodating several interface circuits to drive a sensor array. The versatility of the ASIC chip could be improved by designing an oscillator circuit with a wideband capability, so that a wide range of high-frequency sensors could be operated using the chip. Given the fact that it is in the early stages of development and already shows a good response in particle sensing applications, this ASIC circuitry will have great prospects in current and future applications. The bandwidth limitations and noise associated with the CMOS design could be largely removed by the adaptation of the SiGe BiCMOS process, which has superior

performance than its CMOS counterpart, with better area and power efficiency. In the future, a smart and portable sensor system could be designed by integrating the acoustic wave sensors and the associated CMOS oscillator circuitry into a single monolithic system.

6.17 Summary

The goal of this chapter is to explore the feasibility of the integration of the sensor and associated interface circuitry into a single hybrid SiP sensor. As part of this, a VLSI chip has been designed and fabricated. This section described the design and simulation of the different sections of the ASIC chip, in addition to commenting about the actual output of the chip after fabrication. An application of the CMOS-MEMS sensor system has been described, which details the analysis of operation of the ASIC chip thereby showing the differential sensor output. This chapter is concluded by emphasizing the importance of the development of a hybrid CMOS-MEMS integrated sensor SiP, as part of the development of a portable, low-cost and smart sensor system.

CHAPTER 7

Conclusion and Future Work

7.1 Summary of contributions

This dissertation describes a body of work conducted to develop a smart, label-free cell-based chemoreceiver for artificial insect olfaction. The central challenge of the thesis was to mimic nature in both cellular and molecular levels on to a technological platform which aids in the development of a new class of technology for infochemical communication. A surface acoustic wave based microsensor has been used to develop functional technological equivalents of the cellular and molecular mechanisms that mimics the pathway between pheromone production and detection in insects. The concept of chemical info communication has been initially explored with the aid of polymer-based gas-phase measurements, which imitates the molecular machinery of chemical olfaction. This was followed by the investigation of the feasibility of using the prototype cell-based biosensor system in a static mode for artificial insect olfaction mimicking the cellular detection in the receptor/antenna apparatus of insects. Finally, as part of the development of a compact and low-power portable chemoreceiver system, the sensor drive and interface circuitry was deployed in an analogue VLSI chip, thereby overcoming the associated measurement complexity and equipment cost.

The work carried out in this thesis has made several original contributions to the development of a smart, low-cost, portable and label-free acoustic resonator based chemoreceiver, which are summarized below:

- An info-chemical communication system has been developed, which employs uniquely ratiometrically encoded chemical signals. The system consists of a chemoemitter module, which is capable of releasing a predefined ratio of

volatile compounds utilizing an artificial gland. An array of polymer-coated piezoelectric SAWR sensors forms the chemoreceiver module, which helped in the detection of vapor-phase chemical blends released into the environment.

- The encoding, transmission, and decoding of ratiometric information based upon volatile based binary mixtures of info chemicals firstly using fruit volatiles and later with insect pheromones has been demonstrated through the recovery of blend ratios by obtaining a classification of chemical ratios. Ratiometric information has been successfully recovered based on both the stationary and the transient sensor responses. Small scale, high-throughput infochemical communication has been made possible by a combination of precise spatiotemporal signal generation using plant volatiles and sex pheromones with highly sensitive detection and signal processing.
- A dual surface acoustic wave based whole cell sensor system has been developed, utilizing transfected odorant receptors, with the aid of an automated microfluidic ligand delivery system. This resulted in the development of a SH-SAW sensor functionalized with specific insect ORs (such as Or22a and Or67d) that are introduced into Sf9 cells, which allowed the acousto-electric detection of the binding of associated ligands.
- Successfully deposited and attached live Sf9 cells on to the SAWR sensors, which formed a functionalized biolayer for specific ligand detection and also detected the change in intra-cellular calcium levels when the ligand binds to the receptors. The cell adherence and growth pattern witnessed in SAW resonators proves the aptness of Sf9 cells for use as a biological functional layer on MEMS based acoustic resonators.
- An ASIC chip has been developed for the integration of the olfactory sensor drive, control and interface circuitry, as part of the development of a compact and low-power portable chemoreceiver system. This AVLSI chip has been developed using the standard CMOS 0.35 µm process which has the ability to allow the monolithic integration of CMOS circuitry with acoustic MEMS sensors.

7.2 Future Work

The work presented in this thesis has opened up the opportunity for the work to be extended in other future projects. Other prospective projects that may arise from this work are listed below:

7.2.1 Ultrafine Particle Sensing

This thesis has paved the way for the development of a particle sensor based on acoustic sensors such as SAWs and FBARs as they can be used for mass-sensing applications. As part of this development, miniaturised particle sensors have been designed and developed utilizing SAW sensors and SMR devices for the detection of particulate matter ($PM_{2.5}$ and PM_{10}). This resulted in the development of a particle sensor SiP, capable of performing air quality monitoring. Further work is being carried out towards the development of a CMOS monolithic low-cost and low-power miniaturised particle sensor based on FBAR technology, for the real-time monitoring of particulate matter.

7.2.2 Liquid phase detection with different cell types

In conclusion, there is an opportunity to investigate the use of immobilised receptors on the acoustic sensor surface, possibly based upon locusts that have been shown to survive in dry conditions and so may be used for airborne molecular detection. Additionally, other forms of acoustic wave micro sensors such as FBAR devices could be explored instead of SAW sensors in order to design the cell-based chemoreceiver to be used in artificial olfaction. Thus the polymer coated SAWR sensor array can be substituted by a polymer FBAR array for improved sensitivity. This could allow the exploration of immobilised proteins on the surface of the FBAR sensors resulting in the development of a BioMEMS chip to create an artificial biosensing unit. The use of FBAR devices improves the sensitivity of the sensors due to their higher frequency of operation. Due to their compact size and CMOS compatibility, it is possible to develop a monolithic FBAR-CMOS based BioMEMS

chip with oscillator array employing different types of immobilised cells that will enhance the chemical selectivity of the chemoreceiver sensors.

The contributions from this thesis have resulted in conference and journal publications as listed in Appendix D.

References

[1] J. Yang, Z. Rácz, J. W. Gardner, M. Cole, and H. Chen, "Ratiometric info-chemical communication system based on polymer-coated surface acoustic wave microsensors," *Sensors Actuators B Chem.*, vol. 173, pp. 547–554, Oct. 2012.

[2] T. Nakagawa and L. B. Vosshall, "Controversy and consensus: noncanonical signaling mechanisms in the insect olfactory system.," *Curr. Opin. Neurobiol.*, vol. 19, no. 3, pp. 284–92, Jun. 2009.

[3] P. B. Sklar, R. R. Anholt, and S. H. Snyder, "The odorant-sensitive adenylate cyclase of olfactory receptor cells. Differential stimulation by distinct classes of odorants.," *J. Biol. Chem.*, vol. 261, no. 33, pp. 15538–43, Nov. 1986.

[4] U. Pace, E. Hanski, Y. Salomon, and D. Lancet, "Odorant-sensitive adenylate cyclase may mediate olfactory reception," *Nature*, vol. 316, no. 6025, pp. 255–258, Jul. 1985.

[5] D. T. Jones and R. R. Reed, "Golf: An olfactory neuron specific-G protein involved in odorant signal transduction.," *Science*, vol. 244, no. 4906, pp. 790–795, May 1989.

[6] L. Buck and R. Axel, "A novel multigene family may encode odorant receptors: a molecular basis for odor recognition.," *Cell*, vol. 65, no. 1, pp. 175–87, Apr. 1991.

[7] R. Glatz and K. Bailey-hill, "Progress in neurobiology mimicking nature's noses : from receptor deorphaning to olfactory biosensing," *Prog. Neurobiol.*, vol. 93, no. 2, pp. 270–296, 2011.

[8] P. Ramdya and R. Benton, "Evolving olfactory systems on the fly.," *Trends Genet.*, vol. 26, no. 7, pp. 307–16, Jul. 2010.

[9] D. Wicher, R. Schäfer, R. Bauernfeind, M. C. Stensmyr, R. Heller, S. H. Heinemann, and B. S. Hansson, "Drosophila odorant receptors are both ligand-gated and cyclic-nucleotide-activated cation channels.," *Nature*, vol. 452, no. 7190, pp. 1007–1011, 2008.

[10] K. Sato, M. Pellegrino, T. Nakagawa, T. Nakagawa, L. B. Vosshall, and K. Touhara, "Insect olfactory receptors are heteromeric ligand-gated ion channels.," *Nature*, vol. 452, no. 7190, pp. 1002–1006, 2008.

[11] M. Cole, J. W. Gardner, S. Pathak, Z. Rácz, R. A. J. Challiss, and D. Markovic, "Cell-Based Acoustic Sensors For Biomedical Applications," *Biomed. Eng. (NY).*, 2010.

[12] T. S. Ha, "Odorant and pheromone receptors in insects," *Front. Cell. Neurosci.*, vol. 3, no. September, pp. 1–6, 2009.

[13] W. Carey and B. Kowalski, "Chemical piezoelectric sensor and sensor array characterization," *Anal. Chem.*, no. 14, pp. 3077–3084, 1986.

[14] I. Avramov, "Design of rayleigh SAW resonators for applications as gas sensors in highly reactive chemical environments," in *2006 IEEE International*

Frequency Control Symposium and Exposition, 2006, pp. 381–388.

[15] S. Thomas, M. Cole, A. De Luca, F. Torrisi, A. C. Ferrari, F. Udrea, and J. W. Gardner, "Graphene-coated rayleigh SAW resonators for NO2 detection," in *Procedia Engineering*, 2014, vol. 87, no. 2, pp. 999–1002.

[16] S. Thomas, Z. Rácz, M. Cole, and J. W. Gardner, "Dual high-frequency surface acoustic wave resonator for ultrafine particle sensing," in *IEEE Sensors - Proceedings*, 2013, pp. 1–4.

[17] I. D. Avramov, A. Voigt, and M. Rapp, "Rayleigh SAW resonators using gold electrode structure for gas sensor applications in chemically reactive environments," *Electron. Lett.*, vol. 41, no. 7, pp. 30–31, 2005.

[18] I. Leonte, G. Sehra, M. Cole, P. Hesketh, and J. W. Gardner, "Taste sensors utilizing high-frequency SH-SAW devices," *Sensors Actuators B Chem.*, vol. 118, no. 1–2, pp. 349–355, 2006.

[19] W. Wang, S. He, and H. Li, "Theoretical sensitivity evaluation of a shear-horizontal SAW based micro rate sensor," in *Ultrasonics*, 2009, pp. 1684–1687.

[20] K. Mitsakakis, A. Tsortos, J. Kondoh, and E. Gizeli, "Parametric study of SH-SAW device response to various types of surface perturbations," *Sensors Actuators B Chem.*, vol. 138, no. 2, pp. 408–416, May 2009.

[21] J. Weber, W. Albers, J. Tuppurainen, M. Link, R. Gabl, W. Wersing, and M. Schreiter, "Shear mode FBARs as highly sensitive liquid biosensors," *Sensors Actuators A Phys.*, vol. 128, no. 1, pp. 84–88, Mar. 2006.

[22] M. L. Johnston, I. Kymissis, and K. L. Shepard, "FBAR-CMOS oscillator array for mass-sensing applications," *IEEE Sens. J.*, vol. 10, no. 6, pp. 1042–1047, Jun. 2010.

[23] M. Nirschl, M. Schreiter, and J. Vörös, "Physical comparison of FBAR and QCM-D sensitivity dependence on adlayer thickness and viscosity," *Sensors Actuators A. Phys.*, vol. 165, no. 2, pp. 415–421, 2011.

[24] C. Wu, L. Du, D. Wang, L. Zhao, and P. Wang, "A biomimetic olfactory-based biosensor with high efficiency immobilization of molecular detectors.," *Biosens. Bioelectron.*, vol. 31, no. 1, pp. 44–8, Jan. 2012.

[25] G. J. Price, A. a. Clifton, V. J. Burton, and T. C. Hunter, "Piezoelectric chemical sensors based on morpholine containing polymers," *Sensors Actuators, B Chem.*, vol. 84, no. 2–3, pp. 208–213, 2002.

[26] M. V. Voinova, M. Jonson, and B. Kasemo, "'Missing mass' effect in biosensor's QCM applications," *Biosens. Bioelectron.*, vol. 17, no. 10, pp. 835–841, Oct. 2002.

[27] Y. Q. Fu, J. K. Luo, X. Y. Du, A. J. Flewitt, Y. Li, G. H. Markx, A. J. Walton, and W. I. Milne, "Recent developments on ZnO films for acoustic wave based bio-sensing and microfluidic applications: a review," *Sensors Actuators B Chem.*, vol. 143, no. 2, pp. 606–619, Jan. 2010.

[28] R. Lucklum and P. Hauptmann, "Transduction mechanism of acoustic-wave based chemical and biochemical sensors," *Meas. Sci. Technol.*, vol. 14, no. 11, pp. 1854–1864, 2003.

[29] K. Saha, F. Bender, a. Rasmusson, and E. Gizeli, “Probing the viscoelasticity and mass of a surface-bound protein layer with an acoustic waveguide device,” *Langmuir*, vol. 19, no. 4, pp. 1304–1311, 2003.

[30] Z. A. Shana, D. E. Radtke, U. R. Kelkar, F. Josse, and D. T. Haworth, “Short communication: Theory and application of a quartz resonator as a sensor for viscous liquids,” *Anal. Chim. Acta*, vol. 231, no. 2, pp. 317–320, 1990.

[31] K. Keiji Kanazawa and J. G. Gordon, “The oscillation frequency of a quartz resonator in contact with liquid,” *Anal. Chim. Acta*, vol. 175, no. C, pp. 99–105, 1985.

[32] D. S. Ballantine, S. J. Martin, A. J. Ricco, G. C. Frye, H. Wohltjen, R. M. White, and E. T. Zellers, *Acoustic wave sensors-theory, design, and physico-chemical applications*. London: Academic Press, 1997.

[33] S. Shiokawa and J. Kondoh, “Surface acoustic wave sensors,” *Jpn. J. Appl. Phys.*, vol. 43, no. 5B, pp. 2799–2802, 2004.

[34] S. J. Martin, a. J. Ricco, T. M. Niemczyk, and G. C. Frye, “Characterization of SH acoustic plate mode liquid sensors,” *Sensors and Actuators*, vol. 20, no. 3, pp. 253–268, 1989.

[35] M. Saitakis, A. Tsortos, and E. Gizeli, “Probing the interaction of a membrane receptor with a surface-attached ligand using whole cells on acoustic biosensors.,” *Biosens. Bioelectron.*, vol. 25, no. 7, pp. 1688–93, Mar. 2010.

[36] G. Papadakis, A. Tsortos, and E. Gizeli, “Triple-helix DNA structural studies using a Love wave acoustic biosensor,” *Biosens. Bioelectron.*, vol. 25, no. 4, pp. 702–707, 2009.

[37] K. M. M. Aung, X. Ho, and X. Su, “DNA assembly on streptavidin modified surface: A study using quartz crystal microbalance with dissipation or resistance measurements,” *Sensors Actuators, B Chem.*, vol. 131, no. 2, pp. 371–378, 2008.

[38] A. Tsortos, G. Papadakis, and E. Gizeli, “Shear acoustic wave biosensor for detecting DNA intrinsic viscosity and conformation: A study with QCM-D,” *Biosens. Bioelectron.*, vol. 24, no. 4, pp. 836–841, 2008.

[39] A. Tsortos, G. Papadakis, K. Mitsakakis, K. A. Melzak, and E. Gizeli, “Quantitative determination of size and shape of surface-bound DNA using an acoustic wave sensor.,” *Biophys. J.*, vol. 94, no. 7, pp. 2706–2715, 2008.

[40] M. Rodahl and B. Kasemo, “On the measurement of thin liquid overlayers with the quartz-crystal microbalance,” *Sensors Actuators A Phys.*, vol. 54, no. 1–3, pp. 448–456, Jun. 1996.

[41] C. Di Natale, R. Paolesse, A. Macagnano, A. Mantini, A. D’Amico, A. Legin, L. Lvova, A. Rudnitskaya, and Y. Vlasov, “Electronic nose and electronic tongue integration for improved classification of clinical and food samples,” *Sensors Actuators B Chem.*, vol. 64, no. 1–3, pp. 15–21, Jun. 2000.

[42] S. P. Sakti, S. Rösler, R. Lucklum, P. Hauptmann, F. Bühling, and S. Ansorge, “Thick polystyrene-coated quartz crystal microbalance as a basis of a cost effective immunosensor,” *Sensors Actuators A Phys.*, vol. 76, no. 1–3, pp. 98–

102, Aug. 1999.

[43] A. Hengerer, J. Decker, E. Prohaska, S. Hauck, C. Kößlinger, and H. Wolf, “Quartz crystal microbalance (QCM) as a device for the screening of phage libraries,” *Biosens. Bioelectron.*, vol. 14, no. 2, pp. 139–144, Feb. 1999.

[44] C. Köβlinger, E. Uttenthaler, S. Drost, F. Aberl, H. Wolf, G. Brink, A. Stanglmaier, and E. Sackmann, “Comparison of the QCM and the SPR method for surface studies and immunological applications,” *Sensors Actuators B Chem.*, vol. 24, no. 1–3, pp. 107–112, Mar. 1995.

[45] D. A. Buttry, “The quartz crystal microbalance as an situ tool in electrochemistry,” in *In Situ Studies of the Electrochemical Interface Situ Studies of the Electrochemical Interface*, Arlington, 1989, p. 35.

[46] M. Rodahl, F. Höök, C. Fredriksson, C. A. Keller, A. Krozer, P. Brzezinski, M. Voinova, and B. Kasemo, “Simultaneous frequency and dissipation factor QCM measurements of biomolecular adsorption and cell adhesion.,” *Faraday Discuss.*, no. 107, pp. 229–246, 1997.

[47] C. Fredriksson, S. Kihlman, M. Rodahl, and B. Kasemo, “The piezoelectric quartz crystal mass and dissipation sensor: a means of studying cell adhesion,” *Langmuir*, vol. 14, no. 2, pp. 248–251, 1998.

[48] F. Hook, M. Rodahl, C. Keller, K. Glasmastar, C. Fredriksson, P. Dahiqvist, and B. Kasemo, “The dissipative QCM-D technique: interfacial phenomena and sensor applications for proteins, biomembranes, living cells and polymers,” in *European Frequency and Time Forum and the IEEE International Frequency Control Symposium*, 1999, vol. 2, pp. 966–972.

[49] C. A. Keller and B. Kasemo, “Surface specific kinetics of lipid vesicle adsorption measured with a quartz crystal microbalance.,” *Biophys. J.*, vol. 75, no. 3, pp. 1397–1402, Sep. 1998.

[50] M.-I. Rocha-Gaso, C. March-Iborra, Á. Montoya-Baides, and A. Arnau-Vives, “Surface generated acoustic wave biosensors for the detection of pathogens: a review,” *Sensors*, vol. 9, no. 12, pp. 5740–5769, Jul. 2009.

[51] W. P. Jakubik, “Surface acoustic wave-based gas sensors,” *Thin Solid Films*, vol. 520, no. 3, pp. 986–993, 2011.

[52] S. Ahmadi, C. Korman, and M. Zaghloul, “CMOS integrated gas sensor chip using SAW technology,” *Proc. 2003 Int. Symp. Circuits Syst. 2003. ISCAS ’03.*, p. IV-848-IV-851, 2003.

[53] S. Thomas, Z. Rácz, M. Cole, and J. W. Gardner, “High-frequency one-port colpitts SAW oscillator for chemical sensing,” in *CENICS 2013: International Conference on Advances in Circuits, Electronics and Micro-electronics*, 2013, pp. 13–17.

[54] I. Voiculescu and A. N. Nordin, “Acoustic wave based MEMS devices for biosensing applications,” *Biosens. Bioelectron.*, vol. 33, no. 1, pp. 1–9, 2012.

[55] K. Länge, B. E. Rapp, and M. Rapp, “Surface acoustic wave biosensors: a review.,” *Anal. Bioanal. Chem.*, vol. 391, no. 5, pp. 1509–19, Jul. 2008.

[56] B. Jakoby and M. J. Vellekoop, “Properties of Love waves: applications in

sensors," *Smart Mater. Struct.*, vol. 6, no. 6, pp. 668–679, 1999.

[57] M. Nirschl, A. Blüher, C. Erler, B. Katzschner, I. Vikholm-Lundin, S. Auer, J. Vörös, W. Pompe, M. Schreiter, and M. Mertig, "Film bulk acoustic resonators for DNA and protein detection and investigation of in vitro bacterial S-layer formation," *Sensors Actuators A Phys.*, vol. 156, no. 1, pp. 180–184, Nov. 2009.

[58] R. Gabl, "First results on label-free detection of DNA and protein molecules using a novel integrated sensor technology based on gravimetric detection principles," *Biosens. Bioelectron.*, vol. 19, no. 6, pp. 615–620, Jan. 2004.

[59] J. Bjurström, G. Wingqvist, V. Yantchev, and I. Katardjiev, "Temperature compensation of liquid FBAR sensors," *J. Micromechanics Microengineering*, vol. 17, no. 3, Mar. 2007.

[60] H. Zhang, M. S. Marma, S. K. Bahl, E. S. Kim, and C. E. Mckenna, "Sequence specific label-free DNA sensing using film-bulk-acoustic-resonators," vol. 7, no. 12, pp. 1587–1588, 2007.

[61] T. Tsung Tan, V. O. Schmitt, Q. Lucas, and S. Isz, "Electronic noses and electronic tongues," *LabPlus International*, no. October, pp. 1–4, 2001.

[62] Y. Zou, H. Wan, X. Zhang, D. Ha, and P. Wang, "Electronic nose and electronic tongue," in *Bioinspired Smell and Taste Sensors*, P. Wang, Q. Liu, C. Wu, and K. . Hsia, Eds. 2015, p. 328.

[63] F. Di Pietrantonio, M. Benetti, D. Cannatà, E. Verona, a. Palla-Papavlu, J. M. Fernández-Pradas, P. Serra, M. Staiano, a. Varriale, and S. D'Auria, "A surface acoustic wave bio-electronic nose for detection of volatile odorant molecules," *Biosens. Bioelectron.*, vol. 67, pp. 516–523, 2015.

[64] M. Cole, J. A. Covington, and J. W. Gardner, "Combined electronic nose and tongue for a flavour sensing system," *Sensors Actuators B Chem.*, vol. 156, no. 2, pp. 832–839, 2011.

[65] G. Sehra, M. Cole, and J. W. Gardner, "Miniature taste sensing system based on dual SH-SAW sensor device: an electronic tongue," *Sensors Actuators B Chem.*, vol. 103, no. 1–2, pp. 233–239, 2004.

[66] A. J. Pointon, "Piezoelectric devices," *IEE Proc. A Phys. Sci. Meas. Instrumentation, Manag. Educ. Rev.*, vol. 129, no. 5, p. 285, 1982.

[67] D. James, S. M. Scott, Z. Ali, and W. T. O'Hare, "Chemical sensors for electronic nose systems," *Microchim. Acta*, vol. 149, no. 1–2, pp. 1–17, 2005.

[68] J. W. Gardner, V. K. Varadan, and O. O. Awadelkarim, *Microsensors, MEMS and Smart Devices*. Winchester: Wiley, 2001.

[69] G. S. Sehra, "Surface acoustic wave based flavour sensor system," University of Warwick, 2004.

[70] R. Weigel, D. P. Morgan, J. M. Owens, a. Ballato, K. M. Lakin, K. Hashimoto, and C. C. W. Ruppel, "Microwave acoustic materials, devices, and applications," *IEEE Trans. Microw. Theory Tech.*, vol. 50, no. 3, pp. 738–749, Mar. 2002.

[71] K.-Y. Hashimoto, *Surface acoustic wave devices in telecommunications-*

modelling and simulations. Berlin: Springer, 2000.

[72] Ballantine D. S., *Acoustic wave sensors: theory, design, and physico-chemical applications*. London: Academic Press, 1997.

[73] A. Janshoff, H. J. Galla, and C. Steinem, "Piezoelectric mass-sensing devices as biosensors - An alternative to optical biosensors?," *Angew. Chemie - Int. Ed.*, vol. 39, no. 22, pp. 4004–4032, 2000.

[74] B. Drafts, "Acoustic wave technology sensors," *IEEE Trans. Microw. Theory Tech.*, vol. 49, no. 4 II, pp. 795–802, 2001.

[75] S. W. Wenzel and R. M. White, "Analytic comparison of the sensitivities of bulk-wave, surface-wave, and flexural plate-wave ultrasonic gravimetric sensors," *Appl. Phys. Lett.*, vol. 54, no. 20, p. 1976, 1989.

[76] J. Kondoh, Y. Matsui, and S. Shiokawa, "New biosensor using shear horizontal surface acoustic wave device," *Jpn. J. Appl. Phys.*, vol. 32, pp. 2376–2379, 1993.

[77] G. N. M. Ferreira, A.-C. da-Silva, and B. Tomé, "Acoustic wave biosensors: physical models and biological applications of quartz crystal microbalance.," *Trends Biotechnol.*, vol. 27, no. 12, pp. 689–697, 2009.

[78] J. C. Andle, J. F. Vetelino, M. W. Lade, and D. J. McAllister, "An acoustic plate mode device for biosensor applications," in *Solid-State Sensors and Actuators*, 1991.

[79] A. J. Ricco and S. J. Martin, "Acoustic wave viscosity sensor," *Appl. Phys. Lett.*, vol. 50, no. 21, pp. 1474–1476, 1987.

[80] M. G. Schweyer, J. C. Andle, D. J. McAllister, L. a. French, and J. F. Vetelino, "An acoustic plate mode sensor for aqueous mercury," *1996 IEEE Ultrason. Symp. Proc.*, vol. 1, pp. 355–358, 1996.

[81] C. Déjous, M. Savart, D. Rebière, and J. Pistré, "A shear-horizontal acoustic plate mode (SH-APM) sensor for biological media," *Sensors Actuators B Chem.*, vol. 27, no. 1–3, pp. 452–456, 1995.

[82] M. Hoummady, A. Campitelli, and W. Wlodarski, "Acoustic wave sensors: design, sensing mechanisms and applications," *Smart Mater. Struct.*, vol. 6, pp. 647–657, 1997.

[83] S. J. Martin, G. C. Frye, J. J. Spares, and M. A. Butler, "Gas sensing with acoustic devices," *IEEE Ultrason. Symp. Proc.*, vol. 1, pp. 423–434, 1996.

[84] G. Sauerbrey, "Verwendung von Schwingquarzen zur Wägung dünner Schichten und zur Mikrowägung," *Zeitschrift für Phys.*, vol. 155, no. 2, pp. 206–222, 1959.

[85] K. K. Kanazawa and J. G. Gordon, "Frequency of a quartz microbalance in contact with liquid," *Anal. Chem.*, vol. 57, no. 8, pp. 1770–1771, 1985.

[86] H. Wohltjen and R. Dessy, "Surface acoustic wave probe for chemical analysis. I. Introduction and instrument description," *Anal. Chem.*, vol. 51, no. 9, pp. 1458–1464, 1979.

[87] D. D. Stubbs, L. Sang-Hun, and W. D. Hunt, "Molecular recognition for

electronic noses using surface acoustic wave immunoassay sensors," *Sensors Journal, IEEE*, vol. 2, no. 4, pp. 294–300, 2002.

[88] V. K. Varadan, Y. Ma, and V. V. Varadan, "Scattering and attenuation of elastic waves in random media," *Pure Appl. Geophys.*, vol. 131, no. 4, 1989.

[89] E. Gizeli, N. J. Goddard, C. R. Lowe, and A. C. Stevenson, "A Love plate biosensor utilising a polymer layer," *Sensors Actuators B Chem.*, vol. 6, no. 1–3, pp. 131–137, 1992.

[90] V. M. Yantchev, S. Member, V. L. Strashilov, M. Rapp, U. Stahl, and I. D. Avramov, "Theoretical and experimental mass-sensitivity analysis of polymer-coated SAW and STW resonators for gas sensing applications," *IEEE Sens. J.*, vol. 2, no. 4, pp. 307–313.

[91] Z. Rácz, M. Cole, J. W. Gardner, M. F. Chowdhury, W. P. Bula, J. G. E. Gardeniers, S. Karout, A. Capurro, and T. C. Pearce, "Design and umplementation of a modular biomimetic infochemical communication system," *Int. J. Circuit Theory Appl.*, vol. 41, no. 6, pp. 653–667, 2013.

[92] T. M. A. Gronewold, "Surface acoustic wave sensors in the bioanalytical field: Recent trends and challenges," *Anal. Chim. Acta*, vol. 603, no. 2, pp. 119–128, Nov. 2007.

[93] G. N. M. Ferreira, A.-C. da-Silva, and B. Tomé, "Acoustic wave biosensors: physical models and biological applications of quartz crystal microbalance.," *Trends Biotechnol.*, vol. 27, no. 12, pp. 689–97, Dec. 2009.

[94] P. S. Cross, W. H. Haydl, and R. S. Smith, "Design and applications of two-port SAW Resonators on YZ-lithium niobate," *Proc. IEEE*, vol. 64, no. 5, pp. 682–685, 1976.

[95] I. I. Leonte, "High Frequency Acousto-Electric Microsensors for Liquid Analysis.," University of Warwick, 2008.

[96] G. Kovacs, M. Anhorn, H. E. Engan, G. Visintini, and C. C. W. Ruppel, "Improved material constants for LiNbO3 and LiTaO3," *IEEE Symp. Ultrason.*, pp. 435–438, 1990.

[97] F. S. A. Talbi, "Zero TCF ZnO/quartz SAW structure for gas sensing applications," *Proc. 2004 IEEE Int. Freq. Control Symp. Expo. 2004.*, vol. 0, no. 1, pp. 542–545, 2004.

[98] S. Pathak, "Piezoelectric Microsensors for Semiochemical Communication," University of Warwick, 2012.

[99] F. H. Villa-Lopez, S. Thomas, M. Cole, and J. W. Gardner, "Finite Element Modelling of particle sensors based on Solidly Mounted Resonators," in *IEEE Sensors- Proceedings*, 2014, pp. 574–577.

[100] C. K. Campbell, *Surface accoustic wave devices for mobile and wireless communications*, vol. 9, no. 8. Academic Press, San Diego., 1998.

[101] T. B. Pollard, T. D. Kenny, J. F. Vetelino, and M. P. Da Cunha, "Pure SH-SAW propagation, transduction and measurements on KNbO3," *IEEE Trans. Ultrason. Ferroelectr. Freq. Control*, vol. 53, no. 1, pp. 199–207, 2006.

[102] T. Pastureaud, M. Solal, B. Biasse, B. Aspar, J. B. Briot, W. Daniau, W. Steichen, R. Lardat, V. Laude, A. Laens, J. M. Friedt, and S. Ballandras, "High-frequency surface acoustic waves excited on thin-oriented LiNbO/sub 3/ single-crystal layers transferred onto silicon," *IEEE Trans. Ultrason. Ferroelectr. Freq. Control*, vol. 54, no. 4, pp. 870–876, 2007.

[103] A. Mauder, "SAW gas sensors: comparison between delay line and two-port resonator," *Sensors Actuators B Chem.*, vol. 26, no. 1–3, pp. 187–190, 1995.

[104] W. Soluch, "Design of SAW synchronous resonators on ST cut quartz.," *IEEE Trans. Ultrason. Ferroelectr. Freq. Control*, vol. 46, no. 5, pp. 1324–6, Jan. 1999.

[105] A. R. Katritzky, G. P. Savage, and M. Pilarska, "The response to vapor challenges of new Microsensor coatings: Thiadiazole derivatives," *Cheminform - Wiley*, vol. 21, no. 43, 1989.

[106] D. L. Bartley and D. D. Dominguez, "Elastic effects of polymer coatings on surface acoustic waves.," *Anal. Chem.*, vol. 62, no. 15, pp. 1649–56, 1990.

[107] S. Martin and A. Ricco, "Effective utilization of acoustic wave sensor responses: simultaneous measurement of velocity and attenuation," *Ultrason. Symp. 1989.*, pp. 621–625, 1989.

[108] S. M. Dunphy, "Design and fabrication of filters based on surface acoustic wave devices," Kate Gleason College of Engineering, Rochester Institute of Technology, 2010.

[109] I. Satoh, *Chemical sensor technology, Volume2*. Amsterdam: Elsivier, 1989.

[110] K. Mosbach and B. Danielsson, "Thermal bioanalyzers in flow streams. Enzyme thermistor devices," *Anal. Chem.*, vol. 53, no. 1, pp. 83–94, 1981.

[111] A. J. Slobodnik, E. D. Convay, and R. T. Delmonico, "Microwave Acoustics Handbook, vol. 1A Surface wave Velocities," 1973.

[112] S. J. Martin, G. C. Frye, and S. D. Senturla, "Dynamics and response of polymer-coated surface and film resonance," *Anal. Chem.*, vol. 66, no. 14, pp. 2201–2219, 1994.

[113] S. J. Martin, G. C. Frye, and S. D. Senturia, "Dynamics and Response of Polymer-Coated Surface Acoustic Wave Devices: Effect of Viscoelastic Properties and Film Resonance," *Anal. Chem.*, vol. 66, no. 14, pp. 2201–2219, 1994.

[114] M. Cole, G. Sehra, J. W. Gardner, and V. K. Varadan, "Development of smart tongue devices for measurement of liquid properties," *IEEE Sens. J.*, vol. 4, no. 5, pp. 543–550, 2004.

[115] J. Kondoh, K. Saito, S. Shiokawa, and H. Suzuki, "Simultaneous measurements of liquid properties using multichannel shear horizontal surface acoustic wave microsensor," *Jpn. J. Appl. Phys.*, vol. 35, no. Part 1, No. 5B, pp. 3093–3096, 1996.

[116] E. Gizeli, "Study of the sensitivity of the acoustic waveguide sensor," *Anal. Chem.*, vol. 72, no. 24, pp. 5967–5972, 2000.

[117] B. A. Auld, *Acoustic fields and waves in solids*, Volume II. John Wiley and Sons, Inc, 1973.

[118] J. Kondoh and S. Shiokawa, "New application of shear horizontal surface acoustic wave sensors to identifying fruit juices," *Jpn. J. Appl. Phys.*, vol. 33, no. Part 1, No. 5B, pp. 3095–3099, 1994.

[119] R. M. White and F. W. Voltmer, "Direct piezoelectric coupling to surface elastic waves," *Appl. Phys. Lett.*, vol. 7, no. 12, p. 314, 1965.

[120] D.-P. Chen and H. A. Haus, "Analysis of metal-strip SAW gratings and transducers," *IEEE Trans. Sonics Ultrason.*, vol. 32, no. 3, pp. 395–408, 1985.

[121] D. W. Branch and S. M. Brozik, "Low-level detection of a Bacillus anthracis simulant using Love-Wave Biosensors on 36° YX LiTaO3," California, 2003.

[122] E. A. Malo, M. Renou, and A. Guerrero, "Analytical studies of spodoptera littoralis sex pheromone components by electroantennography and coupled gas chromatography – electroantennographic detection," *Talanta*, vol. 52, pp. 525–532, 2000.

[123] H. Ljungberg, P. Anderson, and B. S. Hansson, "Physiology and morphology of pheromone-specific sensilla on the antennae of male and female Spodoptera littoralis (Lepidoptera, Noctuidae)," *J. Insect Physiol.*, vol. 39, no. 3, pp. 253–260, 1993.

[124] T. Sakurai, H. Mitsuno, S. S. Haupt, K. Uchino, F. Yokohari, T. Nishioka, I. Kobayashi, H. Sezutsu, T. Tamura, and R. Kanzaki, "A single sex pheromone receptor determines chemical response specificity of sexual behavior in the silkmoth Bombyx mori.," *PLoS Genet.*, vol. 7, no. 6, p. e1002115, Jun. 2011.

[125] C. Löfstedt, "Population variation and genetic control of pheromone communication systems in moths," *Entomol. exp. appl.*, vol. 54, pp. 199–218, 1990.

[126] L. S. Kuebler, S. B. Olsson, and B. S. Hansson, "First order processing of complex olfactory information in the moth brain," in *Procedia Computer Science*, 2011, vol. 7, pp. 258–260.

[127] S. B. Olsson, R. A. J. Challiss, M. Cole, J. G. E. Gardeniers, J. W. Gardner, A. Guerrero, B. S. Hansson, and T. C. Pearce, "Biosynthetic infochemical communication.," *Bioinspir. Biomim.*, vol. 10, no. 4, p. 43001, 2015.

[128] M. Cole, Z. Rácz, J. W. Gardner, and T. C. Pearce, "A novel biomimetic infochemical communication technology : from insects to robots," in *IEEE Sensors Conference - Proceedings*, 2012, pp. 12–15.

[129] B. T. Sullivan, J. D. Allison, R. A. Goyer, and W. P. Shepherd, "Sex pheromone of the baldcypress leafroller (lepidoptera: tortricidae)," *J. Econ. Entomol.*, vol. 108, no. 1, pp. 166–172, 2015.

[130] C. Y. Yang, K. S. Han, and K. S. Boo, "Sex pheromones and reproductive isolation of three species in genus adoxophyes," *J. Chem. Ecol.*, vol. 35, no. 3, pp. 342–348, 2009.

[131] M. J. Domingue, C. J. Musto, C. E. Linn, W. L. Roelofs, and T. C. Baker, "Altered olfactory receptor neuron responsiveness in rare Ostrinia nubilalis

males attracted to the O. furnacalis pheromone blend," *J. Insect Physiol.*, vol. 53, no. 10, pp. 1063–1071, 2007.

[132] J. R. Miller and W. L. Roelofs, "Individual variation in sex pheromone component ratios in two populations of the redbanded leafroller moth, argyrotaenia velutinana," *Environ. Entomol.*, vol. 9, no. 3, pp. 359–363, 1980.

[133] W. H. King, "Piezoelectric sorption detector.," *Anal. Chem.*, vol. 36, no. 9, pp. 1735–1739, 1964.

[134] S. Thomas, S. L. T. Leong, Z. Rácz, M. Cole, and J. W. Gardner, "Design and implementation of a high-frequency surface acoustic wave sensor array for pheromone detection in an insect-inspired infochemical communication system," in *14th International Meeting on Chemical Sensors*, 2012, pp. 11–14.

[135] Z. Rácz, S. B. Olsson, J. W. Gardner, T. C. Pearce, B. S. Hansson, and M. Cole, "Challenges of biomimetic infochemical communication," in *Procedia Computer Science*, 2011, vol. 7, pp. 106–109.

[136] Z. Rácz, J. W. Gardner, and M. Cole, "Volatile-based ratiometric infochemical communication system using polymer-coated piezoelectric sensor arrays," in *IEEE Sensors Conference*, 2011, pp. 3–5.

[137] W. P. Bula, N. G. Dimov, and A. Guerrero, "Artificial gland for precise release of semiochemicals for chemical communication," *14th Int. Conf. Miniaturized Syst. Chem. Life Sci.*, pp. 671–673, 2010.

[138] N. G. Dimov, L. Muñoz, W. P. Bula, A. Guerrero, and J. G. E. Gardeniers, "A chemoemitter system mimicking chemical communication in insects," *Procedia Comput. Sci.*, pp. 142–143, 2011.

[139] J. W. Gardner and P. N. Bartlett, *Electronic noses: Principles and applications*. Oxford: Oxford University Press, 1999.

[140] J. W. Grate, R. A. McGill, and M. H. Abraham, "Chemically selective polymer coatings for acoustic vapor sensors and arrays," *IEEE 1992 Ultrason. Symp. Proc.*, pp. 275–279, 1992.

[141] J. W. Grate and H. Abraham, "Solubility interactions and the design of chemically selective sorbent coatings for chemical sensor arrays," *Sensors Actuators B*, vol. 3, pp. 85–111, 1991.

[142] M. H. Abraham, C. F. Poole, and S. K. Poole, "Classification of stationary phases and other materials by gas chromatography," *J. Chromatogr. A*, vol. 842, no. 1–2, pp. 79–114, 1999.

[143] H. Wohltjen, "Mechanism of operation and design considerations for surface acoustic wave device vapour sensors," *Sensors and Actuators*, vol. 5, no. 4, pp. 307–325, 1984.

[144] A. Yamamoto, R. Saguchi, and S. Nagura, "Sustained-release pheromone dispenser," 4,923,119, 1990.

[145] Y. W, Kim, S. E. Sardari, M. T. Meyer, A. Iliadis, H. C. Wu, W. E. Bentley, and R. Ghodssi, "An ALD aluminum oxide passivated Surface Acoustic Wave sensor for early biofilm detection," *Sensors Actuators B Chem.*, vol. 163, no. 1, pp. 136–145, Mar. 2012.

[146] C. Wu, L. Du, D. Wang, L. Wang, L. Zhao, and P. Wang, “A novel surface acoustic wave-based biosensor for highly sensitive functional assays of olfactory receptors.,” *Biochem. Biophys. Res. Commun.*, vol. 407, no. 1, pp. 18–22, Feb. 2011.

[147] M. Saitakis and E. Gizeli, “Acoustic sensors as a biophysical tool for probing cell attachment and cell /surface interactions,” *Cell. Mol. Life Sci.*, pp. 357–371, 2012.

[148] N. Dimov, L. Muñoz, G. Carot-Sans, M. L. P. M. Verhoeven, W. P. Bula, G. Kocer, A. Guerrero, and H. J. G. E. Gardeniers, “Pheromone synthesis in a biomicroreactor coated with anti-adsorption polyelectrolyte multilayer,” *Biomicrofluidics*, vol. 5, no. 3, pp. 1–12, 2011.

[149] L. Muñoz, N. Dimov, G. Carot-Sans, W. P. Bula, A. Guerrero, and H. J. G. E. Gardeniers, “Mimicking insect communication: release and detection of pheromone, biosynthesized by an alcohol acetyl transferase immobilized in a microreactor,” *PLoS One*, vol. 7, no. 11, pp. 11–14, 2012.

[150] U. B. Kaupp, “Olfactory signalling in vertebrates and insects: differences and commonalities,” *Nat. Rev. Neurosci.*, vol. 11, no. March, pp. 188–200, 2010.

[151] A. J. Ricco, S. J. Martin, and T. E. Zipperian, “Surface acoustic wave gas sensor based on film conductivity changes,” *Sensors and Actuators*, vol. 8, no. 4, pp. 319–333, 1985.

[152] A. Kiely, A. Authier, A. V. Kralicek, C. G. Warr, and R. D. Newcomb, “Functional analysis of a Drosophila melanogaster olfactory receptor expressed in Sf9 cells.,” *J. Neurosci. Methods*, vol. 159, no. 2, pp. 189–94, Jan. 2007.

[153] R. Smart, A. Kiely, M. Beale, E. Vargas, C. Carraher, A. V. Kralicek, D. L. Christie, C. Chen, R. D. Newcomb, and C. G. Warr, “Drosophila odorant receptors are novel seven transmembrane domain proteins that can signal independently of heterotrimeric G proteins,” *Insect Biochem. Mol. Biol.*, vol. 38, no. 8, pp. 770–780, 2008.

[154] M. D. Jordan, A. Anderson, D. Begum, C. Carraher, A. Authier, S. D. G. Marshall, A. Kiely, L. N. Gatehouse, D. R. Greenwood, D. L. Christie, A. V. Kralicek, S. C. Trowell, and R. D. Newcomb, “Odorant receptors from the light brown apple moth (Epiphyas postvittana) recognize important volatile compounds produced by plants,” *Chem. Senses*, vol. 34, no. 5, pp. 383–394, 2009.

[155] A. R. Anderson, K. W. Wanner, S. C. Trowell, C. G. Warr, E. Jaquin-Joly, P. Zagatti, H. Robertson, and R. D. Newcomb, “Molecular basis of female-specific odorant responses in Bombyx mori,” *Insect Biochem. Mol. Biol.*, vol. 39, no. 3, pp. 189–197, 2009.

[156] B. S. Hansson, M. Knaden, S. Sachse, M. C. Stensmyr, and D. Wicher, “Towards plant-odor-related olfactory neuroethology in Drosophila,” *Chemoecology*, vol. 20, no. 2, pp. 51–61, 2010.

[157] V. Sargsyan, M. N. Getahun, S. L. Llanos, S. B. Olsson, B. S. Hansson, and D. Wicher, “Phosphorylation via PKC regulates the function of the Drosophila odorant co-receptor.,” *Front. Cell. Neurosci.*, vol. 5, no. June, p. 5, 2011.

[158] S. Pathak, M. D. Jordan, Z. Rácz, R. J. Challiss, J. W. Gardner, and M. Cole, "Detection of ligand-elicited cellular responses using surface acoustic wave biosensors," *Procedia Comput. Sci.*, vol. 7, pp. 346–347, Jan. 2011.

[159] Z. Rácz, M. Cole, J. W. Gardner, S. Pathak, M. D. Jordan, and R. A. J. Challiss, "Cell-based surface acoustic wave resonant microsensor for biomolecular agent detection," in *The 16th International Conference on Solid-State Sensors, Actuators and Microsystems*, pp. 2168–2171.

[160] E. A. Hallem, M. G. Ho, and J. R. Carlson, "The molecular basis of odor coding in the Drosophila Antenna," *Cell*, vol. 117, pp. 965–979, 2004.

[161] A. Kurtovic, A. Widmer, and B. J. Dickson, "A single class of olfactory neurons mediates behavioural responses to a Drosophila sex pheromone.," *Nature*, vol. 446, no. 7135, pp. 542–6, Mar. 2007.

[162] D. S. Ronderos and D. P. Smith, "Diverse signaling mechanisms mediate volatile odorant detection in Drosophila.," *Fly (Austin).*, vol. 3, no. 4, pp. 290–7, 2009.

[163] M. D. Jordan and R. A. J. Challiss, "Expression of insect olfactory receptors for biosensing on SAW sensors," *Procedia Comput. Sci.*, vol. 7, pp. 281–282, Jan. 2011.

[164] G. W. Pierce, "Piezoelectric Crystal Resonators and Crystal Oscillators Applied to the Precision Calibration of Wavemeters," *Am. Acad. Arts Sci.*, vol. 59, no. 4, pp. 81–106, 1923.

[165] J. D. Larson, P. D. Bradley, S. Wartenberg, and R. C. Ruby, "Modified Butterworth-Van Dyke circuit for FBAR resonators and automated measurement system," *2000 IEEE Ultrason. Symp. Proceedings. An Int. Symp. (Cat. No.00CH37121)*, pp. 863–868, 2000.

[166] F. H. Villa-López, G. Rughoobur, S. Thomas, A. J. Flewitt, M. Cole, and J. W. Gardner, "Design and modelling of solidly mounted resonators for low-cost particle sensing," *Meas. Sci. Technol.*, vol. 27, no. 2, p. 25101, 2016.

[167] M. L. Johnston, "Thin-film bulk acoustic resonators on integrated circuits for physical sensing applications," Columbia University, 2012.

[168] M. Chatras, S. Bila, S. Giraud, L. Catherinot, J. Fan, D. Cros, M. Aubourg, A. Flament, A. Frapp, B. Stefanelli, A. Kaiser, A. Cathelin, J. Baptiste, A. Reinhardt, L. Leyssenne, and E. Kerherv, "Modeling and design of BAW resonators and filters for integration in a UMTS transmitter," in *Modeling and Measurement Methods for Acoustic Waves and for Acoustic Microdevices*, 2013.

[169] MX.COM Inc., "Crystal oscillator circuit design," North Carolina, USA, 1997.

[170] A. T. Nimal, M. Singh, U. Mittal, and R. D. S. Yadava, "A comparative analysis of one-port Colpitt and two-port Pierce SAW oscillators for DMMP vapor sensing," *Sensors Actuators B Chem.*, vol. 114, no. 1, pp. 316–325, Mar. 2006.

[171] B. Duane, "Making your oscillator work," Microchip Technology Inc., Arizona, USA, 2004.

[172] EPCOS AG, "Design-guide for the SAW oscillator," Munich, Germany, 2008.

[173] B. P. Otis, “Ultra-low power wireless technologies for sensor networks,” University of California, Berkeley, 2005.

[174] B. P. Otis and J. M. Rabaey, “A 300-μW 1.9-ghz cmos oscillator utilizing micromachined resonators,” *IEEE J. Solid-State Circuits*, vol. 38, no. 7, pp. 1271–1274, Jul. 2003.

[175] S. Thomas, F. H. Villa-López, J. Theunis, J. Peters, M. Cole, and J. W. Gardner, “Particle sensor using solidly mounted resonators,” *IEEE Sens. J.*, vol. 16, no. 8, pp. 2282–2289, 2016.

[176] A. Paidimarri, “Architecture for Ultra-low Power Multi-channel Transmitters for Body Area Networks using RF,” 2011.

[177] Y. H. Chee, A. M. Niknejad, J. Rabaey, B. Wireless, and U. C. Berkeley, “A Sub-100uW 1.9-GHz CMOS Oscillator Using FBAR Resonator,” *IEEE Radio Freq. Integr. Circuits Symp.*, pp. 1–4, 2005.

[178] V. S. Yadav and A. Chaturvedi, “Conversion gain and linearity enhancement of active CMOS mixer for wireless applications,” in *International Conference on Signal Processing and Integrated Networks*, 2014, pp. 397–401.

[179] P. J. Sullivan, B. A. Xavier, and W. H. Ku, “Low voltage performance of a microwave CMOS Gilbert cell mixer,” *IEEE J. Solid-State Circuits*, vol. 32, no. 7, pp. 1151–1155, 1997.

[180] B. Razavi, “RF Microelectronics.” Prentice Hall, p. 916 pages, 2012.

[181] F. Azevedo, F. Fortes, and M. J. Rosario, “A New On-Chip CMOS Active Balun Integrated With LNA,” *2007 14th IEEE Int. Conf. Electron. Circuits Syst.*, pp. 1213–1216, 2007.

[182] T. Lee, “The design of CMOS radio - Frequency integrated circuits.” .

[183] D. Pietron, K. Siwiec, J. Kopanski, and W. A. Pleskacz, “Implementation of the Bluetooth receiver RF front-end in the CMOS-RF 130 nm technology,” *Proc. 21st Int. Conf. Mix. Des. Integr. Circuits Syst. Mix. 2014*, pp. 230–235, 2014.

[184] B. Gilbert, “A Precise Four-Quadrant Multiplier with Subnanosecond Response,” *IEEE J. Solid-State Circuits*, vol. 3, no. 4, pp. 365–373, 1968.

[185] J. Everard, *Fundamentals of RF circuit design: with low noise oscillators*. West Sussex, England: John Wiley & Sons Ltd, 2001.

[186] B. R. Jackson and C. E. Saavedra, “A CMOS Subharmonic mixer with input and output active baluns,” *Microw. Opt. Technol. Lett.*, vol. 48, no. 12, pp. 2472–2478, 2006.

[187] R. P. Sallen and E. L. Key, “A Practical Method of Designing RC Active Filters,” *Ire Tct*, vol. 2, no. 1, pp. 74–85, 1955.

[188] P. E. Allen and D. R. Holberg, *CMOS analog circuit design*, 2nd Editio. Oxford: Oxford University Press, 2002.

[189] Austria Microsystems, “Analog Standard Cell: COMP – CMOS Comparator,” 2015.

[190] T. H. Lee and A. Hajimiri, “Oscillator phase noise : A tutorial,” vol. 35, no. 3,

pp. 326–336, 2000.

[191] S. Thomas, M. Cole, F. H. Villa-lopez, J. W. Gardner, J. Peters, and J. Theunis, “A low-cost acoustic microsensor based system in package for air quality monitoring,” in *IEEE Sensors - Proceedings*, 2016, pp. 4–6.

[192] M. Cole, Z. Rácz, J. W. Gardner, and T. C. Pearce, “A novel biomimetic infochemical communication technology: From insects to robots,” in *Proceedings of IEEE Sensors*, 2012, pp. 12–15.

Appendix A CMOS ASIC Chip Specification

1. General System Overview

The goal of this document is to provide information about the CMOS ASIC interface Chip designed to drive the acoustic SMR sensors and provide a differential low frequency output to be used for analysis.

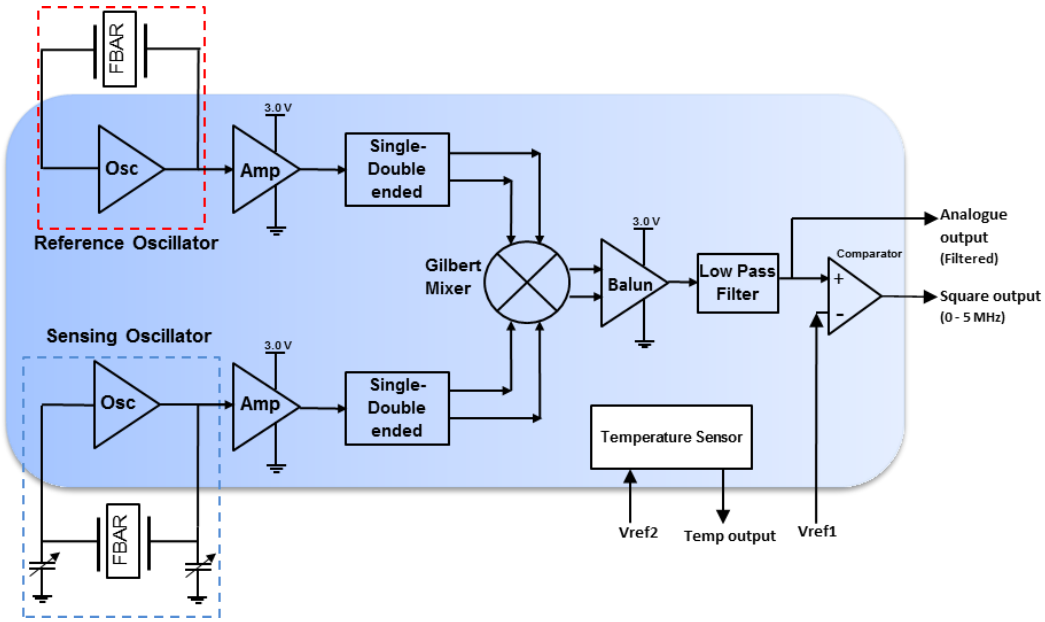

Figure 1: Block Diagram of Acoustic Sensor and the associated drive circuitry

The CMOS ASIC chip consists of:

- Two oscillator circuits (see Figure 2) with amplifiers, one for a reference sensor and the other for the active sensor.
- An RF Double Gilbert Mixer circuit provides the sum and difference of the reference and sensing oscillators.
- Double to Single ended converters (active opamp based Balun) provide a single ended mixer output, which also provides an initial filtering of the HF signals. This circuit is used to convert the double ended mixer output to a single ended signal, so that it could be easily filtered using an active LPF.

- The single ended balun output is taken to a Sallen Key 2nd Order Low Pass Filter, which provides the mixer differential signal (i.e., the low frequency signal) at its output.
- The LPF output is converted to a square wave output using an analogue comparator circuit, which is fed out of the ASIC chip. This is a bit stream output, which could be fed to a counter.
- Frequency tuning of the oscillator circuits could be done using external capacitors.
- A temperature sensor (p-n diode) with voltage amplifier is also provided on-chip, requires an external reference precision voltage.

Table 1: ASIC Chip specification

Parameter	Details
Die size	1.55 mm x 1.65 mm
Number of Particle sensor Channels	Single differential analogue output signal.
Oscillator Frequency	~ 970 MHz centre
Differential output Signal[1]	Difference frequency from the mixer output is fed to comparator to get a square wave output. (range: 0 – 5 MHz)

Table 2: Specification of pin-out for demo board

PIN No:	SIGNAL	DESCRIPTION
1	AGND	Analogue Ground
2	AVDD	Analogue Power Supply (3.3 V)
5	Comp_out	Comparator output (Square wave of 0 – 5 MHz) DO1

2. AVLSI Chip Description

Figure 2 shows the AVLSI Oscillator Chip for driving the particle sensor. The receiver is designed to process two FBAR sensors and deliver a differential output.

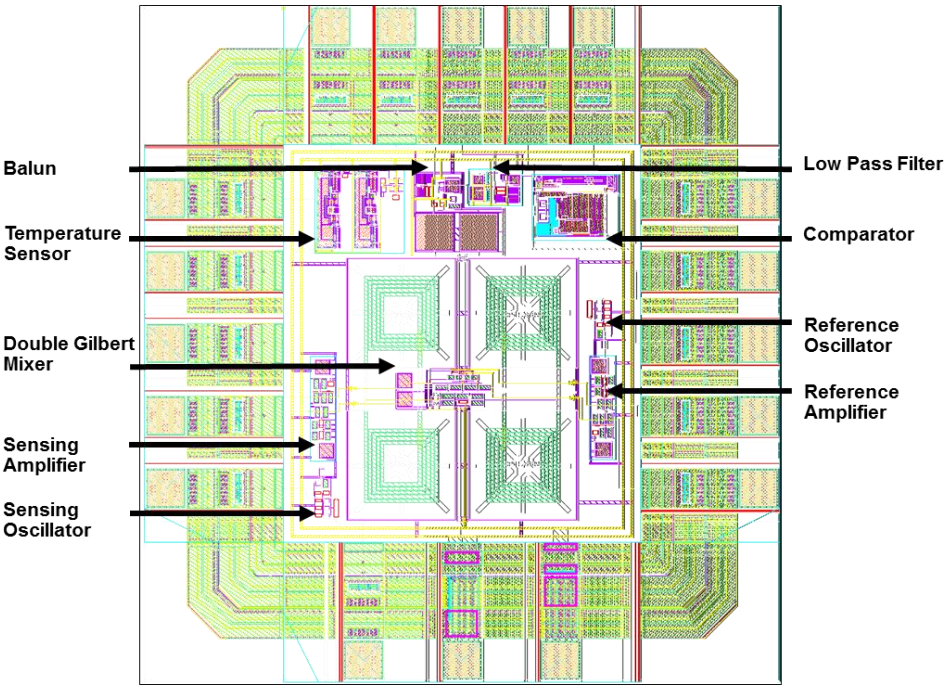

Figure 2. AVLSI Oscillator Chip Floor Plan

3. Layout of Pads

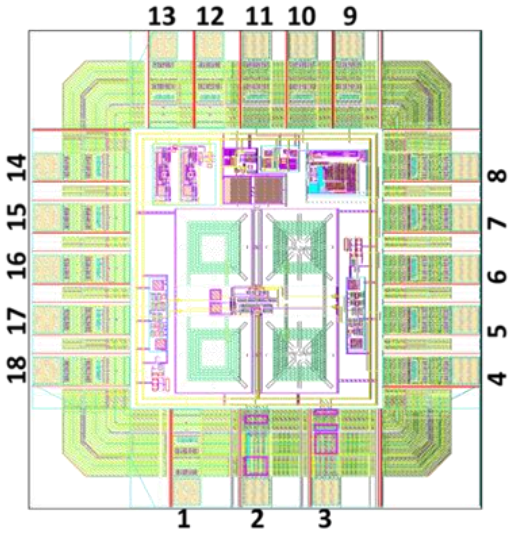

Figure 3: Layout of Pads

4. Detailed Pad list of the ASIC Chip

Table 3: Pin-out of ASIC Chip

PAD	SIGNAL Name	DESCRIPTION	Signal Type
1	FBAR2_P1	Sensing oscillator PORT 1	Analogue
2	GND	Analogue ground	Analogue
3	VDD	Analogue supply	Analogue
4	LO_indn	Connect a 20nH inductor between this pin and VCC to supply current to internal transistors.	Analogue
5	LO_indp	Connect a 20nH inductor between this pin and VCC to supply current to internal transistors.	Analogue
6	FBAR1_P2	Reference oscillator PORT 2	Analogue
7	FBAR1_P1	Reference oscillator PORT 1	Analogue
8	ST	Comparator enable	Analogue
9	CMPR_O	Comparator square wave output	Digital
10	CPR_Vref	Reference voltage to comparator	Analogue
11	LPF_O	Low pass filter output	Analogue
12	MIX_OUT	Amplified mixer output	Analogue
13	TEMP_Vref	Reference voltage to temperature sensor	Analogue
14	TEMP_O	Temperature sensor output	Analogue
15	NC	-	-
16	RF_indn	Connect a 20nH inductor between this pin and VCC to supply current to internal transistors.	Analogue
17	RF_indp	Connect a 20nH inductor between this pin and VCC to supply current.	Analogue
18	FBAR2_P2	Sensing oscillator PORT 2	Analogue

5. Packaged ASIC Chip

QFN 24 pin Package used Size: 5 x 5 mm

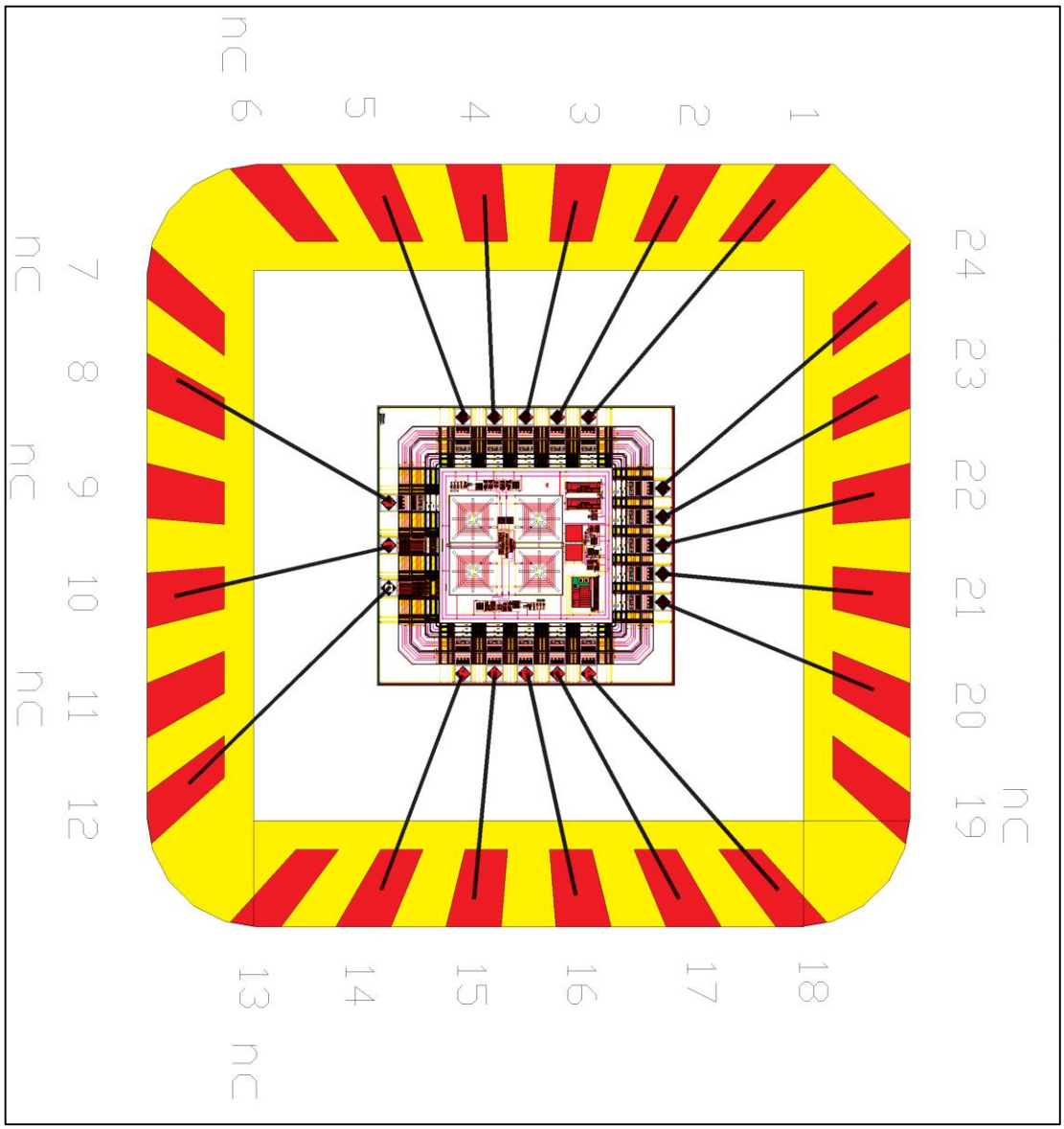

Figure 4: Schematic of Packaged CMOS Die

6. Pin Specifications of QFN (24) pin ASIC Package

Table 4: Pin-out of the ASIC Package

Package PIN	ASIC Pad	DESCRIPTION	Signal name
1	14	Temperature sensor output	TEMP_O
2	15	Pad not connected internally	-
3	16	Connect a 20nH inductor between this pin and VCC to supply current to the internal output transistors.	RF_indn
4	17	Connect a 20nH inductor between this pin and VCC to supply current to the internal output transistors.	RF_indp
5	18	Sensing oscillator PORT 2	FBAR2_P2
6	NC	No connection	
7	NC	No connection	
8	1	Sensing oscillator PORT 1	FBAR2_P1
9	NC	No connection	
10	2	Analogue ground	GND
11	NC	No connection	-
12	3	Analogue supply	VDD
13	NC	No connection	-
14	4	Connect a 20nH inductor between this pin and VCC to supply current to the internal output transistors.	LO_indn
15	5	Connect a 20nH inductor between this pin and VCC to supply current to the internal output transistors.	LO_indp
16	6	Reference oscillator PORT 2	FBAR1_P2
17	7	Reference oscillator PORT 1	FBAR1_P1
18	8	Comparator enable	ST

19	NC	No connection	-
20	9	Comparator square wave output	CMPR_O
21	10	Reference voltage to comparator	CPR_Vref
22	11	Low pass Filter output	LPF_O
23	12	Amplified mixer output	MIX_OUT
24	13	Reference voltage to temperature sensor	TEMP_Vref

7. Overall Chip Schematic

The schematics of the overall chip and the sub-blocks are shown below.

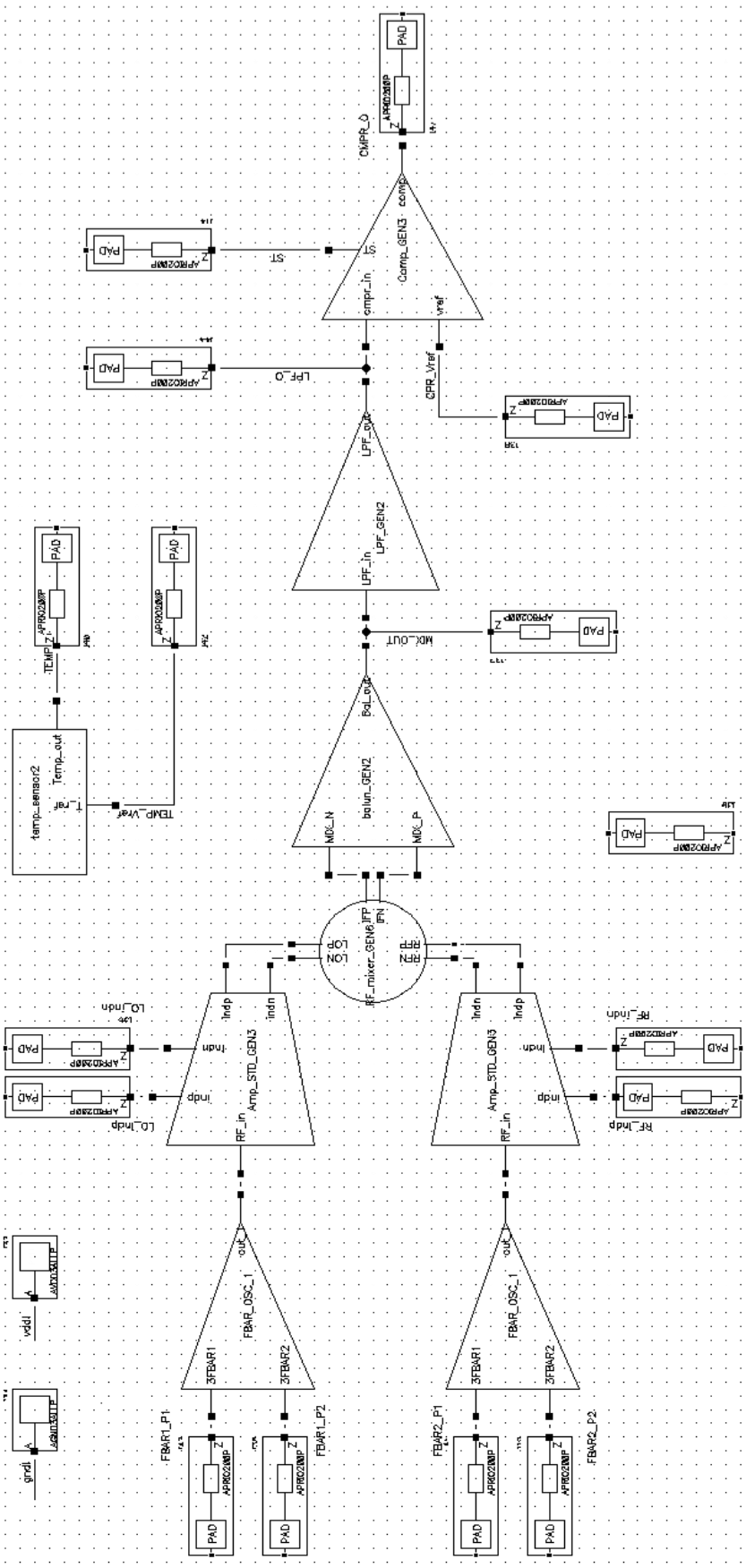

Figure 5: Block diagram of overall ASIC Chip

8. Associated drive circuitry

This document summarizes the specifications of the drive circuitry associated with the oscillator circuitry for the generation of low-frequency differential signal at the output of the ASIC chip. As part of this drive circuitry design, a low pass filter and a comparator has been utilized to generate the differential sensor signal. The design schematics of the differential amplifier involved, LPF and the comparator has been detailed here. The SpectreRF simulations of these blocks have also been incorporated in this section.

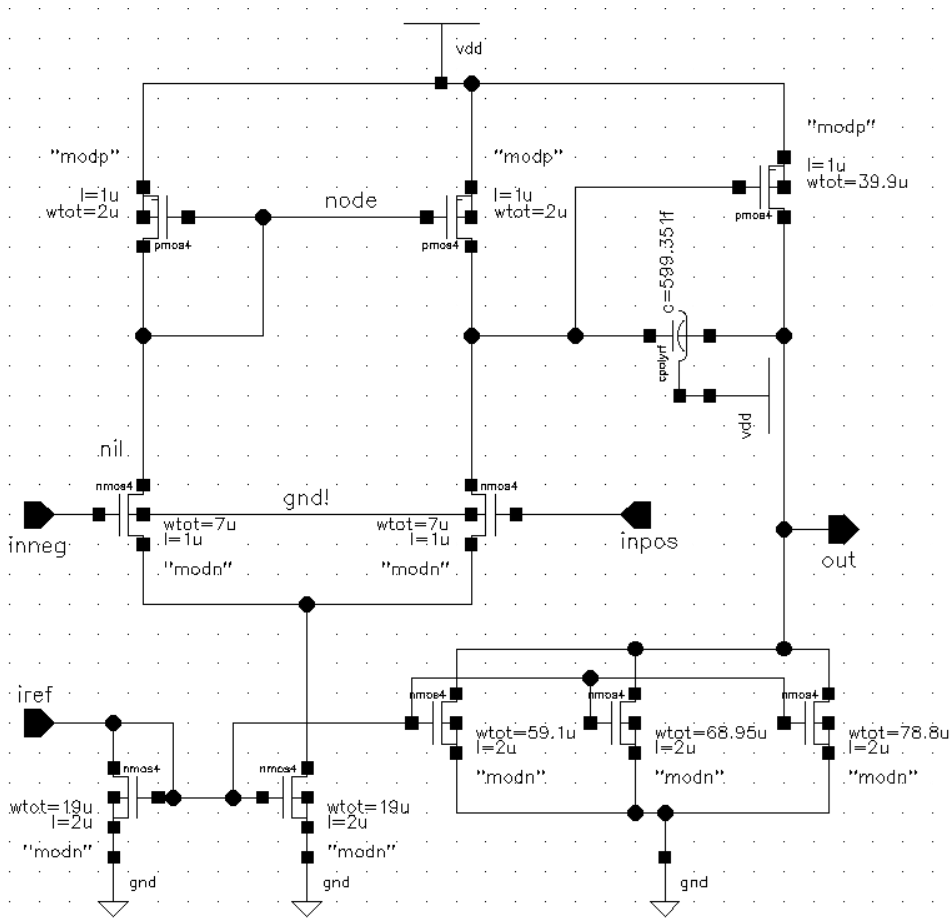

Figure 6. Schematic of the differential amplifier used for the realization of double-to-single ended conversion of mixer output.

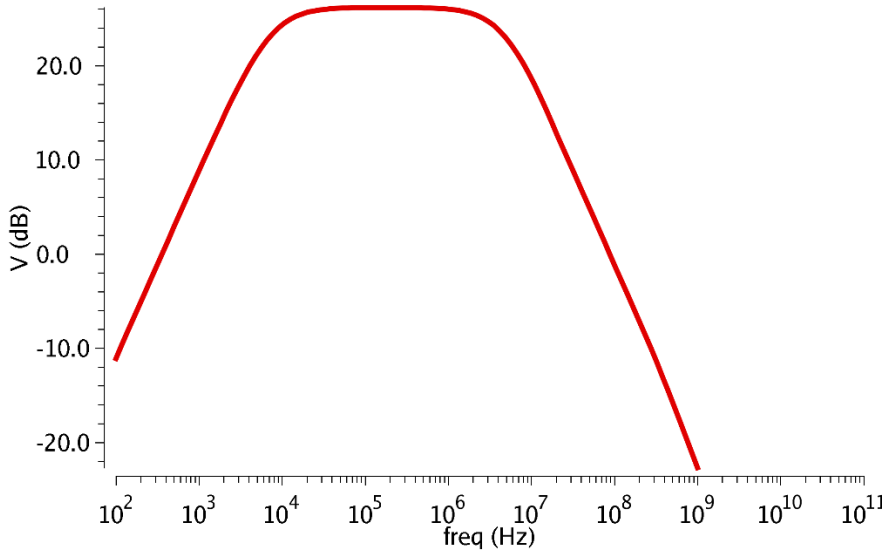

Figure 7. Frequency response of the differential amplifier

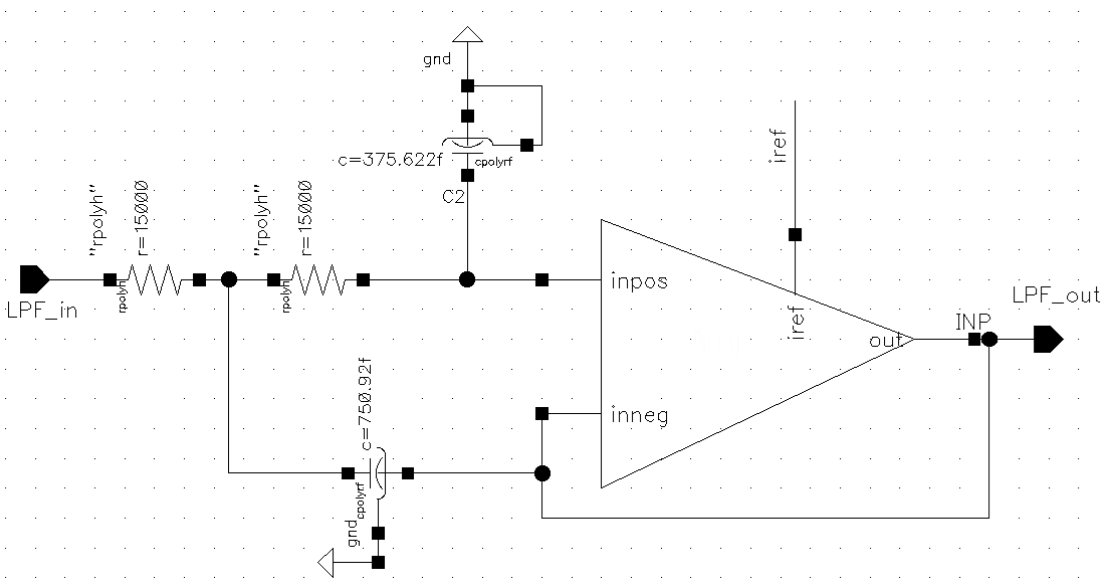

Figure 8. Schematic of the second-order Sallen-Key low pass filter utilizing a differential amplifier.

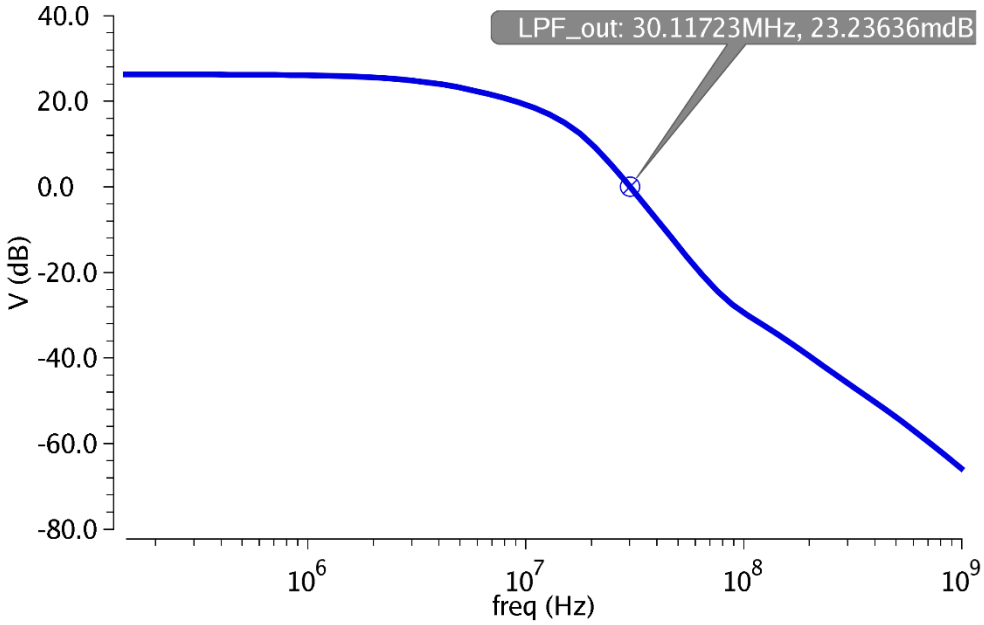

Figure 9. Magnitude response plot of the low pass filter confirming the designed 30MHz upper-cut off frequency.

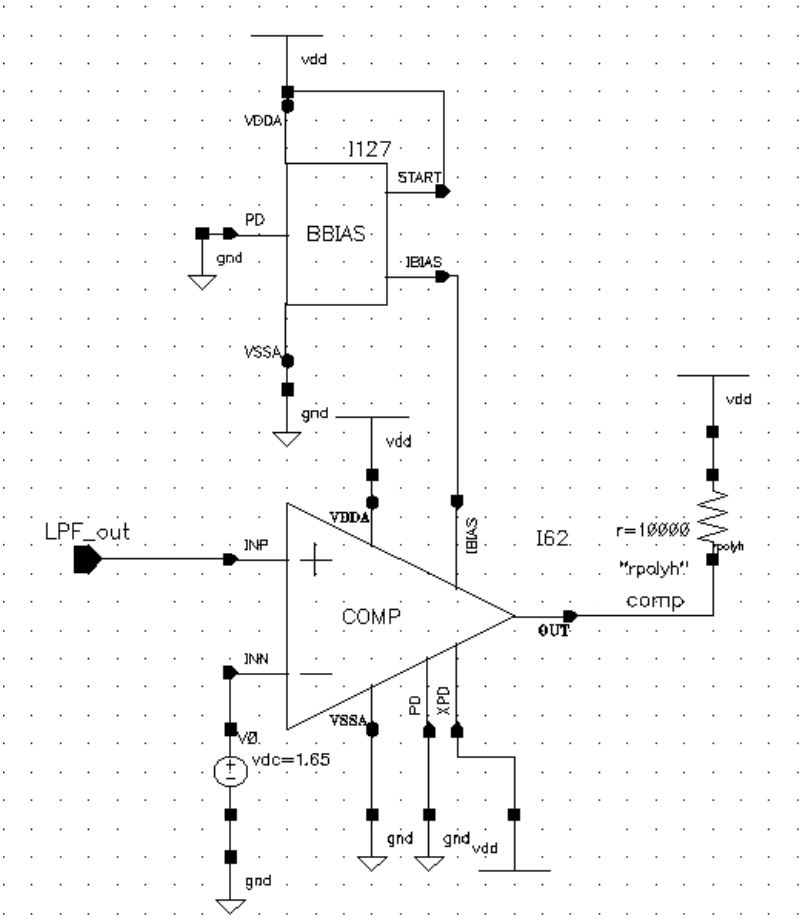

Figure 10. The schematic of the comparator used in the design

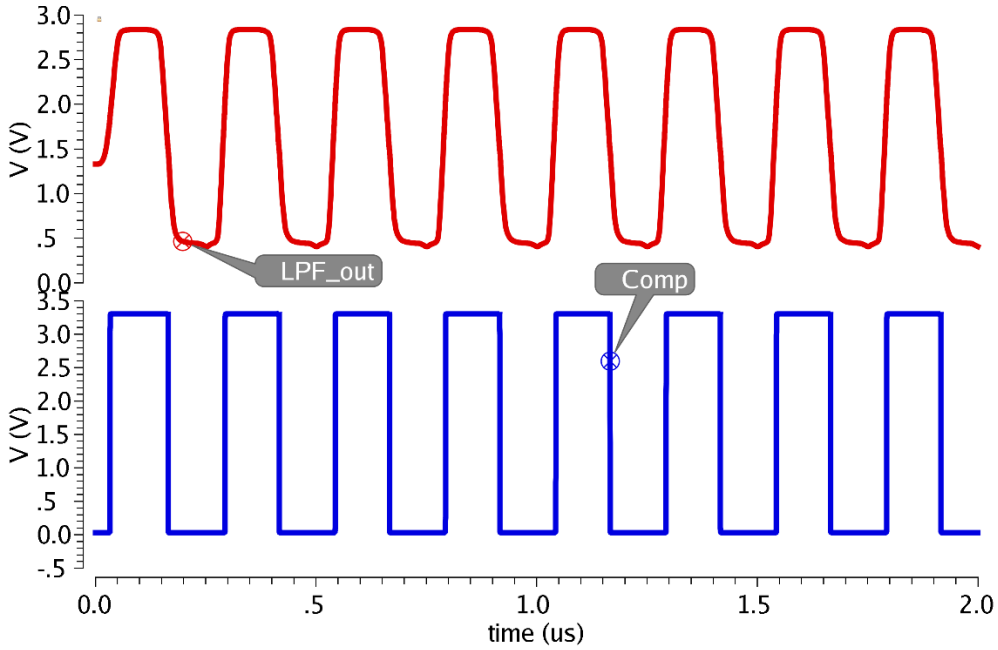

Figure 11. Comparison of transient response amplitudes of filter output and comparator output.

9. Conclusions

This document summarizes the specification of the second generation ASIC Chip for driving the FBAR based Particle Sensor. ASIC chip design, simulations and layout has been carried out using Cadence IC6 tools. The chip has been manufactured and packaged using Europractice MPW services using the AMS (AustriaMicroSystems) foundry. 30 unpackaged and 10 packaged dies were produced by AMS.

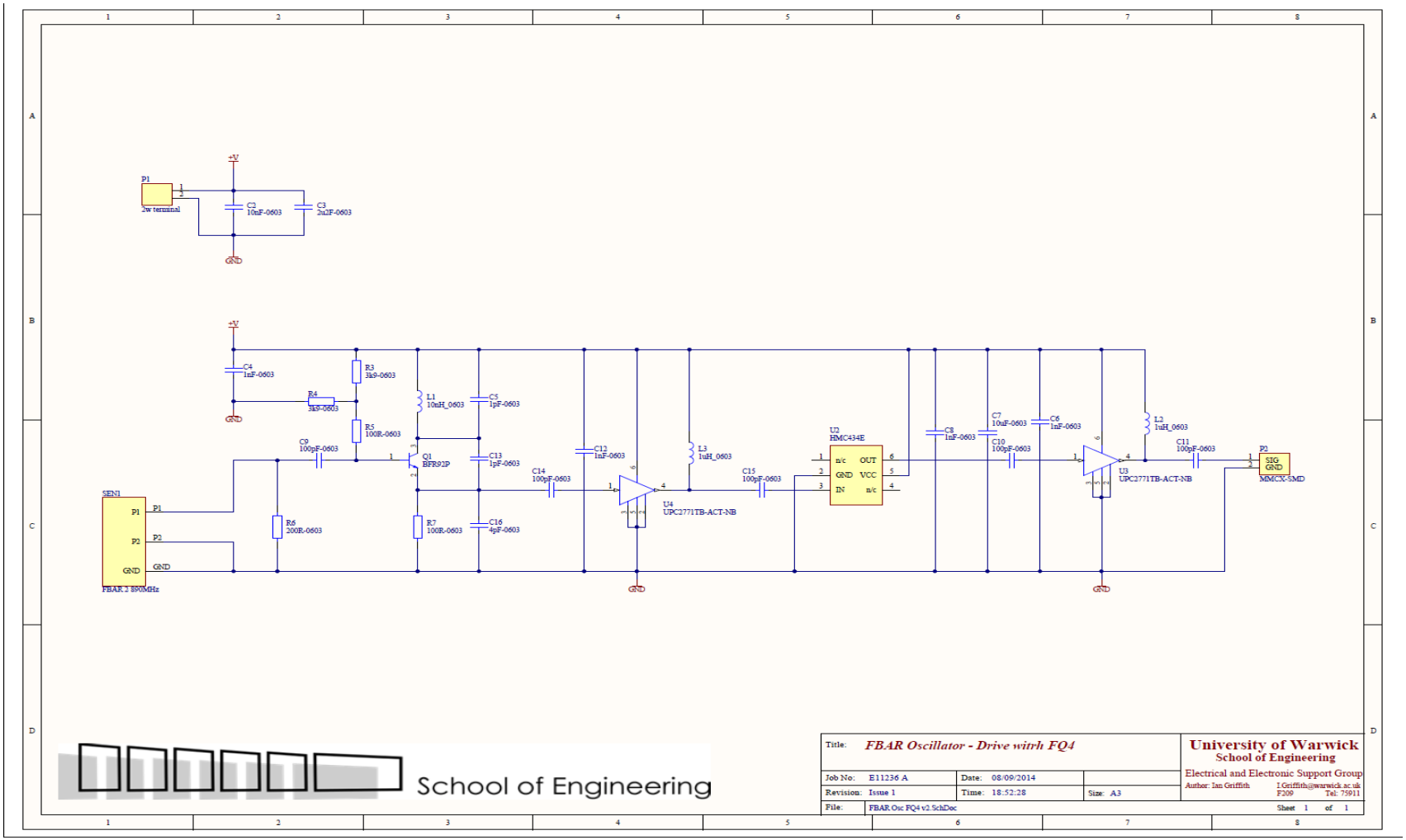

Appendix B Discrete oscillator circuitry for SMR.

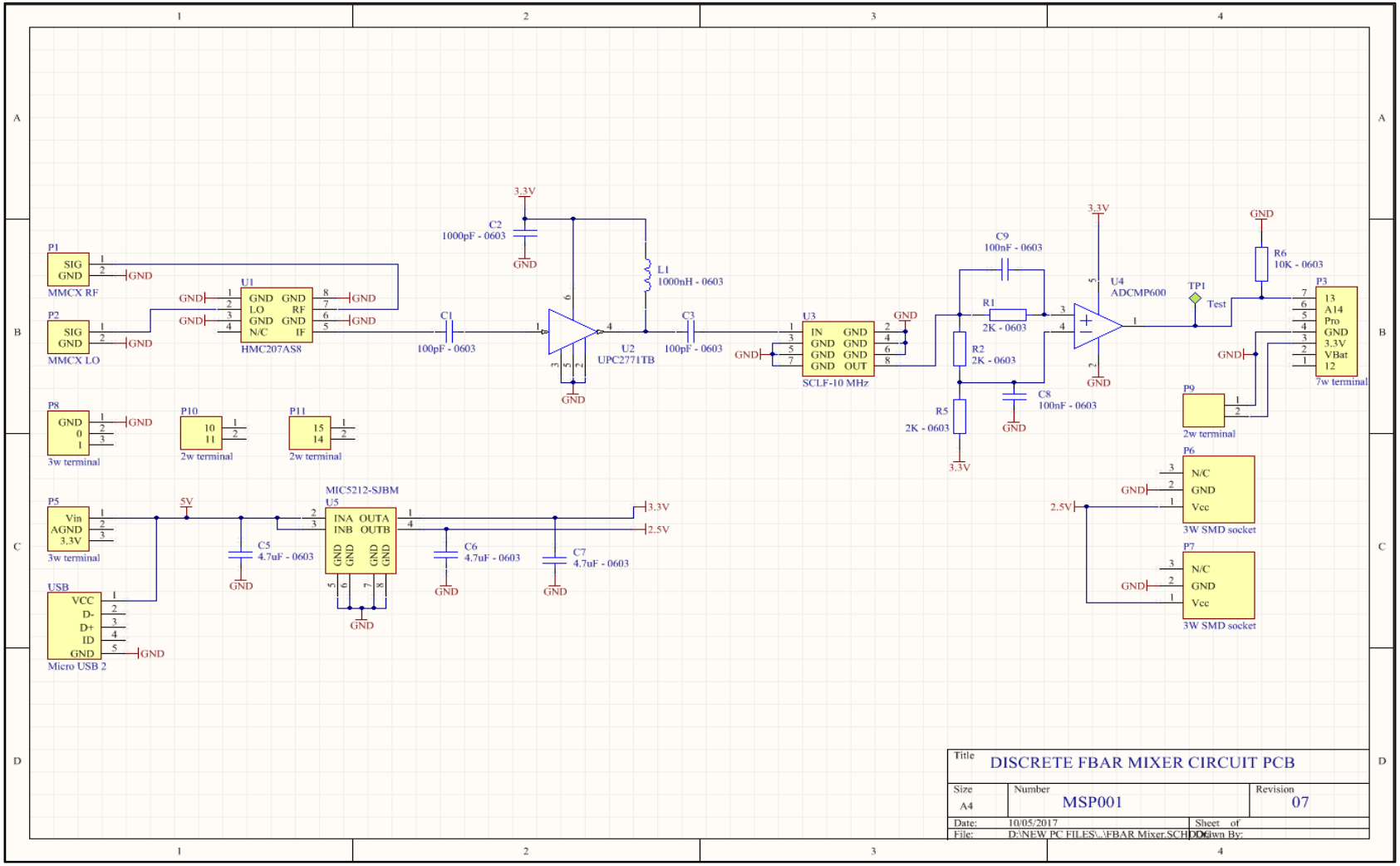

Appendix C Discrete RF Mixer circuitry

Appendix D Publications

APPENDIX D

DOI 10.5162/IMCS2012/P2.2.12

Design and Implementation of a High-Frequency Surface Acoustic Wave Sensor Array for Pheromone Detection in an Insect-inspired Infochemical Communication System

S. Thomas, S. Li Tai Leong, Z. Rácz, M. Cole, and J.W. Gardner
Microsensors & Bioelectronics Laboratory, University of Warwick, Coventry, United Kingdom,
J.W.Gardner@warwick.ac.uk

Abstract

This paper reports on the design and development of a novel pheromone detection biosensor module that forms part of an infochemical communication system. Infochemical communication in insects is based upon the use of sex pheromones for the tenacity of attracting conspecific mates. Our system involves three functional blocks: a chemoemitter module comprising a high-precision syringe pump and a micro-machined artificial gland; a chemoreceiver module comprising an array of four polymer-coated dual Surface Acoustic Wave Resonator (SAWR) sensors with associated oscillator drive circuitry; located inside a small odour chamber. Chemical information takes the form of insect pheromone compounds that are released inside the odour chamber by a silicon-based micro-evaporator and then detected by the sensor array. The design and fabrication of a high frequency 262 MHz oscillator circuit is described giving stable Surface Acoustic Wave (SAW) signals with reference SAWRs used to offset drift.

Key words: SAWR Sensors, pheromone, infochemical communication, high frequency, oscillator circuit.

Introduction

It is of fundamental significance for a wide variety of living organisms to exchange molecular information and process it in a unique way. Intraspecific communication in insects is achieved by the use of *semiochemicals*; these odour cues are able to modify behavior such as conspecific mate finding, location of food, and other social interactions [1]. This is due to the fact that, for example, moths utilize their olfactory system that enables them to translate odour signals to a complex behavioural pattern within the antenna lobe, which is at the bottom of the detecting organ (antenna). The work presented here mimics chemical communication in insects in which a female moth releases a sex pheromone and the male moth detects it remotely and arises from an EU-funded Framework project called "iCHEM" [2].

Pheromones play an important role in the behaviour of an insect by triggering a pre-encoded behaviour that enables the male to locate the calling female. These pheromone components, usually released by the female moths as a blend of different compounds, are biosynthesized in the insect's pheromone gland.

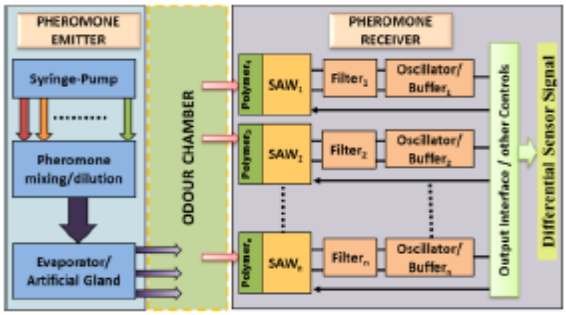

Fig. 1. Schematic block diagram of the biosynthetic insect-inspired communication system.

In order to accomplish species-specificity, these pheromone components are blended with variation in molecular chain length, unsaturation level, functional group and total number of compounds. The olfaction system of the moth *Spodoptera littoralis* has been studied extensively in recent years, both from a behavioral and neurophysiological view [3]. Since (Z,E)-9,11-tetradecadienyl acetate (ZE-9,11- 14:OAc) forms the main component in the sex pheromone of this moth [4], we have employed this pheromone compound for the establishment of insect-based communication protocol in our work.

APPENDIX D

DOI 10.5162/IMCS2012/P2.2.12

Figure 1 shows a schematic block diagram that is analogous to pheromone communication of insects. Our experimental set-up consists of a chemoemitter that generates a set of semiochemical signals, an odour chamber simulating a wind tunnel and a piezoelectric chemoreceiver containing an array of SAWR sensors coated with different types of polymers. The differential signal generated by the SAWR sensors produce varied responses allowing us to detect and decode the pheromone mixtures.

Insect-inspired Communication System

I. Biosynthetic Pheromone Emission

The artificial pheromone-emitter gland is driven by a syringe pump and an evaporation controller system used to control a micromachined evaporator [5] for the release of pheromone into the chamber. This artificial gland imitates the functionality of the biological mechanism that allows the moth *S. littoralis* to release pheromones in specific dosing. Our chemoemitter is crucial for the labeling of information before they are transmitted into the real world based on relative proportions between compounds [5].

As the normal solution of pheromone Z,E-9,11-14:OAc is highly concentrated, hexane was used as the solvent for diluting the pheromone. The microevaporator temperature was set to a temperature of 90°C and different volumes of this pheromone solution was delivered to the chip by a syringe pump at a flow rate of 5 µL/sec, in order to input the odour stimulus into the wind tunnel.

II. Chemoreception using SAWR Sensors

A highly-sensitive (ppb level), polymer-coated RF-based SAWR oscillator array was employed to detect the semiochemical concentrations in the gas phase, which electronically simulates the complex olfactory system of the night-active insects. More specifically, the SAWR sensor array mimics the insect's antenna with different types of sensilla designed for detection of various olfactory stimuli [4]. The SAW resonator based sensors are not only highly sensitive, but also simpler in operation having only frequency output and so require a much simpler interface circuitry for data processing.

The dual SAWR arrangement enables the generation of differential signals that help ameliorate common mode variations, e.g. drift.

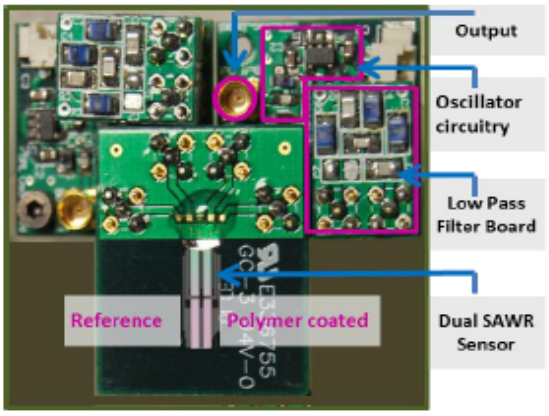

Fig. 2. Photograph of a dual 262 MHz SAW resonator sensor with surface mount amplifier, filter and buffer circuitry.

The X-propagating ST-cut quartz based gas phase dual SAW Resonator sensors with aluminum electrodes are designed to resonate at 262 MHz in a feedback loop of a simple radio frequency (RF) oscillator circuit. The design specifications of the SAWR are 60.5 pairs of interdigitated transducers (IDTs) with 3 µm finger width, acoustic aperture of 720 µm and a cavity length of 1764 µm. 550 reflector gratings surround the IDTs for creating a standing wave pattern. Figure 2 shows the photograph of the dual 262 MHz SAWR sensor with surface mount oscillator circuitry.

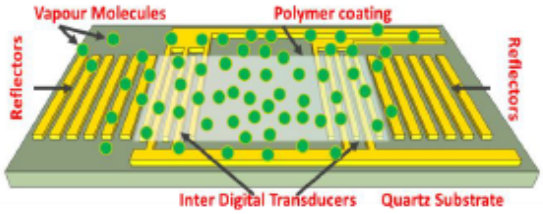

Fig. 3. Schematic diagram of the SAWR sensor coated with a polymer based functional layer and exposed to gas molecules.

Four different polymers, namely poly-caprolactone (PCL), poly(9-vinylcarbazole) (PVK), poly(styrene-co-butadiene) (PSB) and poly(ethylene-co-vinyl acetate) (PEVA) were recognized as the optimal polymers that were stable, reasonably sensitive and selective to the insect pheromones. Therefore, one side of each dual SAWR was functionalized with these polymers (schematic shown in figure 3) while the other side served as a reference, thus enabling the decryption of the encoded information. Figure 4 [A] shows an optical microscopy image specifying the locus of the polymer coating on a dual SAWR sensor and figure 4 [B] shows the magnified view of the polymer coating.

APPENDIX D

DOI 10.5162/IMCS2012/P2.2.12

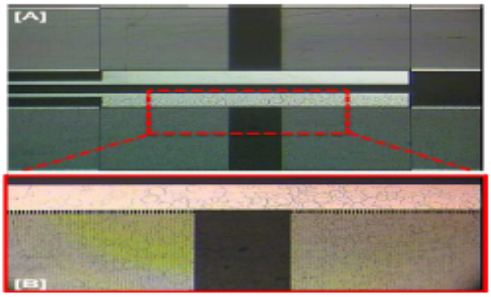

Fig. 4 [A]. Optical micrograph specifying the locus of the polymer coating on one side of a dual SAWR sensor [B]. Magnified view of the polymer coating.

III. Oscillator Circuit Design

The SAWR sensors were driven by amplifier based independent feedback-oscillator circuits consisting of surface mount amplifiers, a low pass filter, and the buffer circuitry. The oscillator Printed Circuit Board (PCB) is a four layer board with separate grounding planes which takes account of the phase shifts associated with the RF signal path within the resonator-circuitry loop. It also reduces the RF cross talk, thereby improving noise sensitivity. A schematic layout of the RF oscillator circuit is shown in Figure 5 comprising low pass filter, amplifier and buffer stages.

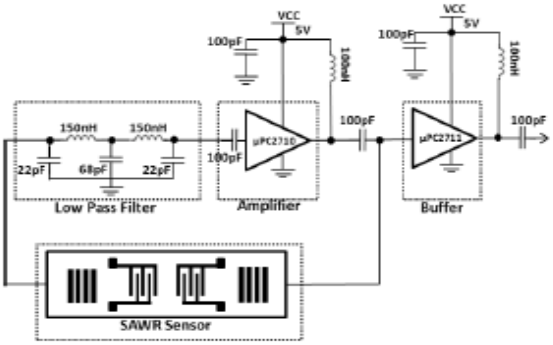

Fig. 5. Schematic diagram of circuitry to drive the SAWR sensor and buffer the read-out signal.

The SAWR devices are used as the frequency and phase selective elements in the feedback loop of the oscillator circuit because they provide a maximum signal transmission at the designed frequency (262 MHz) with very low, typically 12 dB attenuation as indicated by the scattering parameter analysis in figure 6. In addition to the SAWR attenuation, approximately 2 dB is also lost through the filters and cables in the circuit. The amplifier gain should always exceed the total signal loss in the feedback loop of the oscillator circuit elements by a typical gain margin of 5 dB [2], for maintaining a stable operation of the SAWR resonator. Therefore the circuit employs a commercial high gain monolithic microwave integrated circuit (MMIC) wide-band amplifier μPC2710 (NEC), having a gain of 33 dB, with a maximum input power of 10 dBm and a maximum output power of 13.5 dBm allowing the device to be operated safely with a loop loss of 3.5 dB or more. The low pass filter consisting of passive elements suppresses the oscillations at other spurious frequencies. A commercial bipolar MMIC wide band amplifier μPC2711 (NEC) forms the buffer stage with a gain of 13 dB in order to measure the differential analogue oscillator output signal.

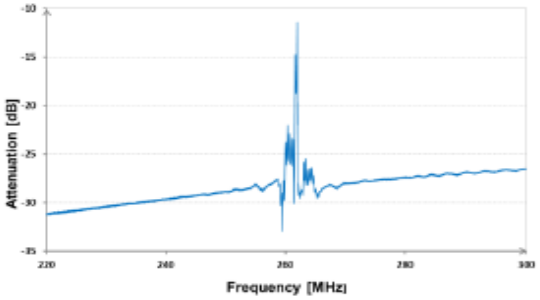

Fig. 6. Attenuation vs. frequency plot for a 262 MHz SAW resonator Sensor.

Experimental Setup

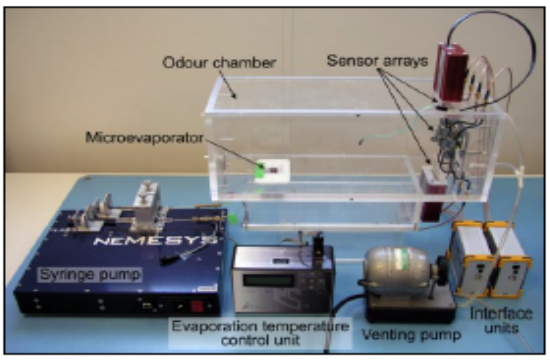

Fig. 7. Test chamber containing pheromone micro-evaporator and array of four polymer-coated SAWR sensors.

A prototype of the insect-based pheromone detection system has been constructed as shown in the figure 7. The chemoemitter module consists of a neMESYS high-precision dual channel syringe pump (cetoni GmbH, Germany) that drives a micro-machined artificial gland, releasing pheromone into the 14x14x40 cm^3 Perspex odour chamber. The polymer coated 4-sensor dual SAWR array, with the related RF oscillator circuitries and interfaces make up the chemoreceiver module. Using a

APPENDIX D

DOI 10.5162/IMCS2012/P2.2.12

commercial FQ4 interface instrument (JLM Innovation, Tubingen, Germany) and a desktop computer within the experimental system, the output of each sensor was measured and recorded independently.

Results

In this paper we have shown the response of a SAWR sensor array to a biosynthetic pheromone compound and the development of a custom high-frequency oscillator circuit to drive four dual SAWR sensors. The differential frequency response of the polymer coated SAWR sensors to the pheromone was successfully measured as shown in Figure 8.

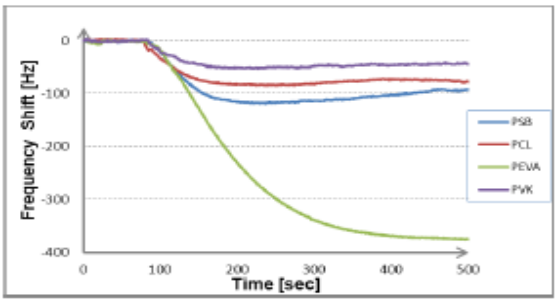

Fig. 8. Differential frequency response of four different polymer-coated SAWR sensors to pheromone Z,E-9,11-14:OAc.

In random repeated sequences, 5, 10, 15 and 20 µl of a solution of Z,E-9,11-14:OAc (10% volume in hexane) were introduced into the odour chamber using the microevaporator and the responses obtained were approximately linear (see Figure 9) and can be classified using a simple linear statistical classifier. Moreover, it can be also observed that variations in blend concentrations are clearly visible and separable as well. This also proves that the pheromones can be transmitted and detected by the different SAWR sensors. Thus proportionately-encoded signals can be transmitted in our infochemical communication system.

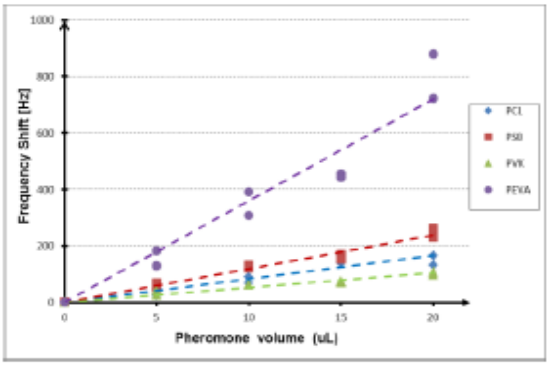

Fig. 9. Response of four polymer coated SAWR sensors to different volumes of odour pulse.

Conclusions

We have presented an integrated chemoemitter and chemoreceiver system that simulates infochemical communication in insects, thereby forming a new branch of expertise for information transmission using only molecules. The differential sensor outputs can be directly fed into a field-programmable gate array for neuromorphic signal processing permitting autonomous robot control for search and rescue, and has become an intricate scheme for encoded message transmission. In addition to providing the required selectivity that is necessary for pheromone blend specificity, the SAW sensors offer low-cost and low-power, and offer a route to full CMOS integration with the driving, data acquisition and processing circuitry.

Future development of this work is being directed towards testing and optimizing the capability of the system to generate and detect a precise mix of pheromone compounds in programmable ratios of concentration. Moreover, further advances include the integration of the olfactory sensor drive and interface circuitry into an application-specific integrated circuit (ASIC) chip boosting them to full system-on-chip (SoC) implementation of chemoreceiver system.

Acknowledgements

This work was supported by the EC 6th Framework Programme, and FET project no. FP6-032275 called "Biosynthetic Infochemical Communication".

References

[1] E. Hartlieb, et al., "Appetitive Learning of Odours With Different Behavioural Meaning in Moths," Physiology & behavior, vol. 67, no. 5, 671-677 (1999).

[2] iCHEM Project, EU FP6 STREP project, see www.go.warwick.ac.uk/iCHEM

[3] R. J. Fan and B. S. Hansson, "Olfactory Discrimination Conditioning in the Moth Spodoptera littoralis," Physiology & behavior, vol. 72, no. 1-2, 159-165 (2001).

[4] P. Anderson et al., "Increased Behavioral and Neuronal Sensitivity to sex Pheromone After Brief Odor Experience in a Moth," Chemical senses, vol. 32, no. 5, 483-491 (2007); doi:10.1093/chemse/bjm017

[5] W. P. Bula et al., "Artificial Gland for Precise Release of Semiochemicals for Chemical Communication," 14th International Conference on Miniaturized Systems for Chemistry and Life Sciences, 671-673 (2010).

APPENDIX D

CENICS 2013 : The Sixth International Conference on Advances in Circuits, Electronics and Micro-electronics

High-frequency One-port Colpitts SAW Oscillator for Chemical Sensing

S. Thomas, Z. Rácz, M. Cole and J.W. Gardner
Microsensors and Bioelectronics Laboratory
University of Warwick
Coventry, UK
J.W.Gardner@warwick.ac.uk

Abstract—**This paper reports upon the design and development of a low cost, high sensitivity, high frequency surface acoustic wave resonator (SAWR) based system for gas sensing applications. The 262 MHz one-port SAWR operates in a grounded-base Colpitts oscillator arrangement that was developed based on an equivalent circuit model. Electrical characteristics of the fabricated SAWR show good agreement with its equivalent device model at the resonant frequencies, and it was found to have good stability and sensitivity with a Q-factor in air of about 2,870 at its fundamental resonant frequency. The sensor system is designed to operate in a dual configuration in which one resonator is coated with a gas-sensitive polymer (polyethylene) coating, whilst the second one is used as a reference channel; thereby eliminating common mode interferences on the baseline signal. Mass sensitivity was found to be ca. 1 Hz/ng, which corresponds to sub-ppm sensitivity to gas/odour concentration.**

Keywords-acoustic waves; one-port; Colpitts oscillator; BVD model; SAW resonator;polymer coating

I. INTRODUCTION

Both bulk acoustic and surface acoustic wave (SAW) based sensor systems have been reported in chemical sensing applications over the past few decades [1–4]. Due to their high sensitivity and simple drive/readout circuitry, more recent focus has been on surface acoustic wave based devices where a SAW device forms the frequency selective component within an oscillator circuit. Polymer-coated SAW based chemical sensors impart high sensitivity and selectivity to specific volatile compounds. The absorption of the ligand molecule onto the polymer changes the physicochemical and electrical behavior of the SAW device resulting in a change in its oscillation frequency.

Common methods to implement SAW oscillator circuits are typically based on the feedback loop method or the negative resistance method [5], [6]. The frequency stability and vapor sensitivity of the SAW sensor system directly depends on the type of the employed oscillator circuit. Nimal *et al.* [7] have recently reported that one-port Colpitts oscillators are more sensitive, but less stable, than two-port Pierce oscillators. The sensitivity can also be improved by tuning the phase point set within the SAWR in the pass band thereby reducing the noise performance of the oscillator circuit [8].

In this study, we present one-port polymer-coated Rayleigh wave based SAW resonators, fabricated on an ST-cut quartz wafer, for application in low-cost chemical sensors. An investigation into different equivalent circuit models is also presented, which lead to the conclusion that the most suitable oscillator circuit for one-port SAWR sensors is a Colpitts oscillator configuration.

II. ONE PORT SAW RESONATOR

SAW resonators are commonly available as one-port and two-port devices employing either delay line or resonator configurations. Because of the potential for high Q-value, low noise level and higher stability, we have selected a one-port resonator structure. These resonators are designed to operate at a baseline frequency of 262 MHz in a dual configuration to obtain differential measurements (Fig. 1).

The design and modeling of surface acoustic devices are normally carried out using the well-established Coupling of Modes (COM) theory [9], [10]. Although a COM model allows for an accurate description of the SAW resonator by simulating the admittance behaviour, the formulas are somewhat cumbersome and are not very informative - as far as circuit analysis and simulation is concerned. In addition, the accuracy of this model is limited to a narrow frequency band around the resonance region. Hence, the COM theory must assume *near-resonance* frequencies in order to derive a simplified electrical model of the SAW resonator [11].

The Butterworth Van Dyke (BVD) model, as a simple electrical equivalent circuit model, is more suitable for circuit designers. Morgan [12] established that the electrical acoustic impedance behavior of a SAW device, obtained using a lumped-element equivalent circuit model, is in good agreement with conventional COM analysis. This equivalent circuit model conveniently relates the acoustic perturbations due to surface mass loading in a SAW device to its electrical behavior.

A BVD model [11] was developed for the 262 MHz one-port SAWR, shown in Fig. 2., allowing quick simulation and design of the associated oscillator circuitry. The motional and static arm parameters were extracted using the transmission parameters of the SAWR. As shown in Fig. 2, the electrical components R, L and C are the motional inductance, capacitance and resistance respectively, which form the *motional arm* producing the resonant frequency while the capacitor C_o forms the *static arm* providing the anti-resonant frequency. The motional arm signifies the electro-acoustic properties [13] of the piezoelectric material and it models the vibration of the crystal. R represents the

 ISBN: 978-1-61208-302-5

APPENDIX D

acoustic attenuation in the resonator and capacitance C_o the capacitance of the piezoelectric crystal.

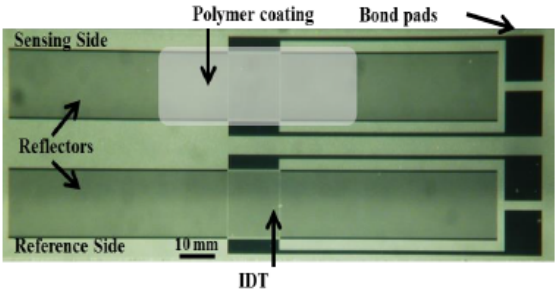

Fig.1. Optical micrograph of the 262 MHz one-port dual SAW resonator sensor, fabricated in aluminium on a ST-cut quartz wafer substrate. The top resonator is coated with a chemically-sensitive non-conductive polymer (polyethylene) and the bottom resonator is uncoated thus acting as a reference channel.

The designed 1-port SAWR comprises 60.25 finger pairs with 3 μm finger width forming the inter-digitated-transducer (IDT), and 500 reflectors on each side to create a standing wave pattern with an overall die size of 7.4 mm × 2.4 mm. The dual resonator configuration [14] with a reference channel eliminates common mode interferences on the baseline signal, such as changes in ambient temperature or pressure. The SAWRs were fabricated on an ST-cut quartz substrate with aluminum IDTs using UV lithography (PacTech, Germany).

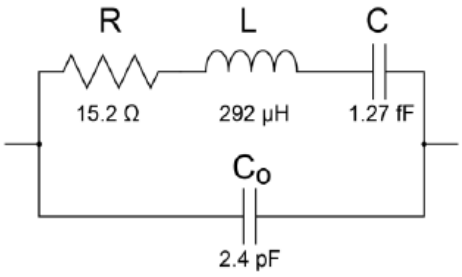

Fig.2. Illustration of the BVD equivalent circuit lumped element model of a one-port SAW resonator.

In addition to the fundamental mode of operation, the SAWR exhibits several overtone frequencies, which can be modelled by adding additional series-resonant branches to the BVD model. For operation around a certain resonant frequency, the crystal can be modelled by the circuit with a single motional arm. The impedance of this modelled circuit is given by [15]:

$$Z(s)=\frac{s^2+\left(\frac{R}{L}\right)s+\omega_s^2}{sC_o\left[s^2+\left(\frac{R}{L}\right)s+\left(1+\frac{C}{C_o}\right)\omega_s^2\right]} \quad (1)$$

where

$$\omega_s=2\pi f_s=\frac{1}{\sqrt{LC}}, \quad (2)$$

$$f_s=\frac{1}{2\pi\sqrt{LC}} \quad (3)$$

Here, f_s is the series resonance frequency of the SAWR, modeled by the motional arm. The unloaded quality factor of a SAWR is given by

$$Q_u=\frac{\omega_s L}{R} \quad (4)$$

Due to the high Q-factor of a SAWR, R can be neglected. Thus (1) becomes,

$$Z(s)=\frac{s^2+\omega_s^2}{sC_o\left[s^2+\left(1+\frac{C}{C_o}\right)\omega_s^2\right]} \quad (5)$$

This shows that the resonator exhibits a parallel resonance at:

$$f_a=\frac{1}{2\pi\sqrt{LC_T}} \quad (6)$$

where

$$C_T=\frac{CC_o}{C+C_o} \quad (7)$$

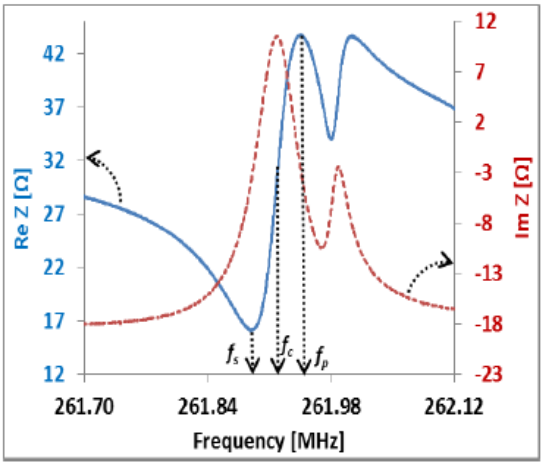

Fig.3. Real (Solid line) and imaginary parts (dotted line) of the impedance presented by 262 MHz one-port SAWR. The series, parallel and center frequencies are marked on the diagram.

The real and imaginary parts of the one-port SAWR impedance exhibiting a minimum resistance at resonance and a maximum resistance at anti-resonance frequencies, obtained by an RF network analyzer (E5071B, Agilent Technologies), is shown in Fig. 3. The series resonance frequency, f_s, is 261.91 MHz, the parallel resonance, f_a is 261.94 MHz and the center frequency, f_c is 261.92 MHz. This also demonstrates that the SAWR center frequency lies

 ISBN: 978-1-61208-302-5

APPENDIX D

as expected between the series and parallel resonant frequencies. The phase curve in Fig. 3 also shows that the Barkhausen criterion of 0° phase condition for oscillation is satisfied at the center frequency of the SAWR.

III. COLPITTS OSCILLATOR DESIGN

Several similar transistor-based circuit configurations are available for the realisation of SAW oscillators, such as Pierce, Colpitts, and Clapp, with the main difference lying in the transistor grounding options. The performance of the three configurations varies with the difference in the position of the biasing resistors and capacitances. The most desirable option is the Pierce configuration due to its simplicity, robustness and ability to work at higher frequencies (> 500 MHz) because it is arguably the least affected by stray capacitances [15]. However, the Pierce oscillator can only work with a two-port SAW resonator within a feedback loop to attain the required 180° phase shift.

The Colpitts oscillator, however, allows the SAWR to operate in a 1-port configuration [7], and therefore was selected for this work. The schematic of the Colpitts SAW oscillator circuit with a grounded base configuration, where the SAWR input is connected to the transistor's base and the output port is connected to the ground, is shown in Fig. 4.

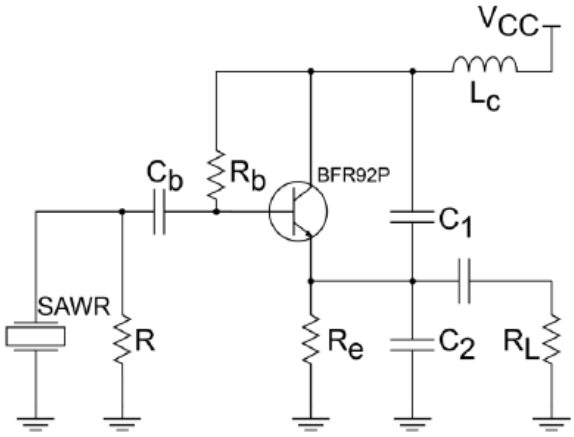

Fig. 4. Simplified schematic of the Colpitts oscillator circuitry used to drive the 1-port SAW resonator sensor.

The Colpitts oscillator offers good stability at higher frequencies, lower harmonics, lower component count and hence lower cost than other types including feedback-based oscillator. The transition frequency of the transistor, f_T, limits its frequency of operation, when the capacitors needed for obtaining the oscillation frequency are comparable to the transistor's terminal capacitances. This may be avoided by using a high f_T value (a few gigahertz) BJT in the oscillator circuit or by using the crystal in a series resonance configuration [15]. The use of RF transistor (BFR92P, Infineon) rather than an operational amplifier also reduces parasitic capacitances allowing radio frequency (RF) oscillator operation. To obtain the tuned oscillation frequency close to the SAWR Q-factor, tight tolerance components were selected for the capacitor and the inductor values.

In this configuration, the resonator shows an inductive behavior between the series (f_s) and parallel resonances (f_p). The transistor along with the feedback capacitors C_1 and C_2 provides the negative resistance to compensate for resistive losses in the resonator. The major limitation of such an oscillator circuit is that the parasitic capacitances begin to affect the effective operation of the circuit at frequencies above 500 MHz.

IV. CHEMICAL DETECTION SYSTEM SETUP

A robust, high-sensitivity chemical detection system based on polymer-coated one port SAW sensor has been designed and implemented. The SAW oscillator has been realized by interfacing the dual SAW resonators to Colpitts oscillator circuitry. A two layered Printed Circuit Board (PCB) has been designed using Altium Designer software. Figure 5 shows the photograph of the dual Colpitts SAW oscillator based chemical sensor system. The PCB ensures minimal cross-talk associated with high frequency signals. The phase shifts linked with the RF signal paths to the resonators have also been taken into account during the PCB design.

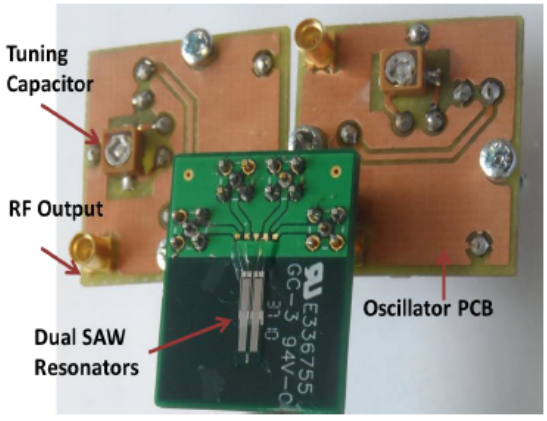

Fig.5. Photograph of the SAW resonator with associated Colpitts oscillator circuit on the backside of a custom PCB.

The experimental arrangement demonstrating chemical detection using SAWR oscillator consists of a 14×14×40 cm^3 gas/odor chamber (photograph of the setup is shown in Fig. 6) to which a neMESYS multi-channel syringe pump (Cetoni GmbH, Germany) is attached. The microliter precision syringe delivers the chemicals into the chamber via capillary lines, where it gets vaporised. The SAW sensors, arranged in dual configuration, where one is coated with the sensing polymer *polyethylene* and the other

 ISBN: 978-1-61208-302-5

APPENDIX D

sensor forms the reference channel are attached to the far end of the chamber. A commercial FQ4 interface instrument (JLM Innovation, Tubingen, Germany) was connected to the oscillator output for frequency measurement. The oscillation frequencies of the individual sensors were monitored to obtain the SAWR differential signal.

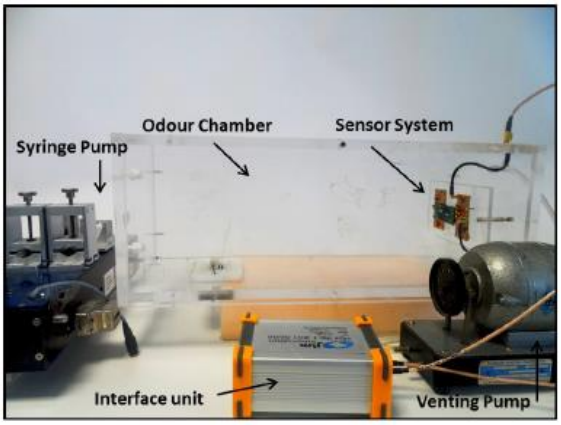

Fig.6. Experimental arrangement for chemical detection sensor system consisting of an odour chamber, a venting pump, syringe pump, and SAW sensors with the Colpitts circuitry.

V. EXPERIMENTAL RESULTS

Figure 7 shows the oscillator's resonant frequency output obtained by an RF oscilloscope (LeCroy LT342 Waverunner). The measured frequency value is in good agreement with the theoretically modeled value. The load sensitivity is significantly less for this oscillator circuit. The output of the SAWR oscillator is practically noise and distortion free.

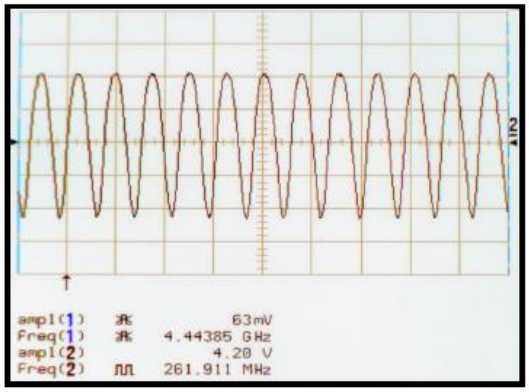

Fig.7. Photograph of the baseline frequency (261.9 MHz with amplitude of 4.2 V) of a Colpitts SAW oscillator sensor system shown at the channel 2 of an RF Oscilloscope.

The typical frequency shifts of a dual SAWR sensor after the detection of a volatile chemical compound (here an insect sex pheromone) shows that the one-port SAW oscillator provides a highly-sensitive system for chemical detection. The response has a low level of noise as shown in Fig. 8. On the introduction of 10 µl of the insect pheromone Z9-14:OAc into the odor chamber, a differential frequency shift of about 6 kHz was measured at the SAW output, which shows that the average sensor response to the pheromone compound is about 0.6 *Hz/nl* of liquid, i.e., sub-ppm levels of phermone in air.

The response time of the system is relatively slow (~100 s) and it is associated with the evaporation and diffusion of the volatile compound inside the chamber. However, the actual response time of the SAWR itself is below one second.

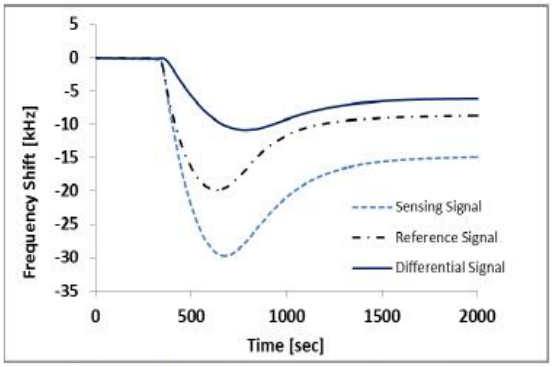

Fig.8. *Differential frequency response of polymer-coated SAWR sensor to pheromone Z9-14:OAc demonstrating the high sensitivity of the polymer-coated SAWR sensor.*

VI. CONCLUSION

A high frequency one-port Colpitts SAWR oscillator has been designed and fabricated for application in a low-cost, low-power gas sensor. An equivalent model has been developed, which formed the basis of an oscillator circuit design for a highly sensitive chemical sensor. The SAWR exhibits a high quality factor of 2,870 and has an estimated 0.5 Hz/ng mass sensitivity after coating with a thin gas sensitive non-conducting polymer film.

Further studies are being carried out on the detection of specific blends (i.e. mixtures) of chemical compounds. In addition, technological developments of this work include the creation of a smart low-cost, low-power chemical sensor on a chip - by the integration of the SAWR sensor with full custom CMOS oscillator circuitry thus resulting in an application-specific integrated circuit (ASIC) BioMEMS chip.

ACKNOWLEDGMENT

The authors wish to thank first Mr. Frank Courtney (Warwick University, UK) for his assistance in all mechanical and technical matters and secondly Mr. Ian Griffith (Warwick University, UK) for his help in the manufacturing of the oscillator PCB.

 ISBN: 978-1-61208-302-5

APPENDIX D

REFERENCES

[1] I. Avramov, "Design of Rayleigh SAW Resonators for Applications as Gas Sensors in Highly Reactive Chemical Environments," 2006 IEEE International Frequency Control Symposium and Exposition, Jun. 2006, pp. 381–388, doi: 10.1109/FREQ.2006.275415.

[2] K. Mitsakakis, A. Tserepi, and E. Gizeli, "SAW device integrated with microfluidics for array-type biosensing," Microelectronic Engineering, vol. 86, no. 4–6, Apr. 2009, pp. 1416–1418, doi: 10.1016/j.mee.2008.12.063.

[3] V. M. Yantchev, S. Member, V. L. Strashilov, M. Rapp, U. Stahl, and I. D. Avramov, "Theoretical and Experimental Mass-Sensitivity Analysis of Polymer-Coated SAW and STW Resonators for Gas Sensing Applications," IEEE Sensors Journal, vol. 2, no. 4, Aug. 2002, pp. 307–313, doi: 10.1109/JSEN.2002.804039.

[4] Z. Rácz, M. Cole, J. W. Gardner, S. Pathak, M. D. Jordan, and R. A. J. Challiss, "Cell-Based Surface Acoustic Wave Resonant Microsensor for Biomolecular Agent Detection," 16th International Conference on Solid-State Sensors, Actuators and Microsystems, June 2011, pp. 2168-2171, doi: 10.1109/TRANSDUCERS.2011. 5969348.

[5] M.-I. Rocha-Gaso, C. March-Iborra, Á. Montoya-Baides, and A. Arnau-Vives, "Surface Generated Acoustic Wave Biosensors for the Detection of Pathogens: A Review," Sensors, vol. 9, no. 12, Jul. 2009, pp. 5740–5769, doi: 10.3390/s90705740.

[6] M. ElBarkouky, P. Wambacq, and Y. Rolain, "A low-power 6.3 GHz FBAR overtone-based oscillator in 90 nm CMOS technology," Research in Microelectronics and Electronics Conference, July 2007, pp.61-64, doi: 10.1109/RME.2007.4401811.

[7] A. T. Nimal, M. Singh, U. Mittal, and R. D. S. Yadava, "A comparative analysis of one-port Colpitt and two-port Pierce SAW oscillators for DMMP vapor sensing," Sensors and Actuators B: Chemical, vol. 114, no. 1, Mar. 2006, pp. 316–325, doi: 10.1016/j.snb.2005.05.021.

[8] S. Stier, A. Voigt, M. Rapp, F. K. Gmbh, P. O. Box, and D.-Karlsruhe, "Influence of Phase Position on the Performance of Chemical Sensors Based on SAW Device oscillators," Analytical Chemistry, vol. 70, no. 24, 1998, pp. 5190–5197, doi: 10.1021/ac9805504.

[9] P. V. Wright, "Analysis and design of low-loss SAW devices with internal reflections using coupling-of-modes theory," Proc. IEEE Ultrasonics Symp., 1989, pp. 141–152, doi: 10.1109/ULTSYM.1989.66974.

[10] C. S. Hartmann, D. P. Chen, and J. Heighway, "Modeling of SAW transversely coupled resonators filters using coupling-of-modes modeling technique" in Ultrasonics Symposium, 1992, pp. 39–44, doi: 10.1109/ULTSYM.1992.276067.

[11] R. Kshetrimayum, R. D. S. Yadava, and R. P. Tandon, "Modeling electrical response of polymer-coated SAW resonators by equivalent circuit representation.," Ultrasonics, vol. 51, no. 5, Jul. 2011, pp. 547–553, doi: 10.1016/j.ultras.2010.12.006.

[12] D. P. Morgan, "Simplified analysis of surface acoustic wave one-port resonators," Electronics Letters, vol. 39, no. 18, Sept. 2003, pp. 4–5, doi: 10.1049/el.

[13] C. K. Campbell, Surface Acoustic Wave Devices for Mobile and Wireless Communications, vol. 9, no. 8. Academic Press, San Diego., 1998.

[14] S. Thomas, S. L. T. Leong, Z. Rácz, M. Cole, and J. W. Gardner, "Design and Implementation of a High-Frequency Surface Acoustic Wave Sensor Array for Pheromone Detection in an Insect-inspired Infochemical Communication System," 14th International Meeting on Chemical Sensors, 2012, pp. 11–14, doi: 10.5162/IMCS2012/P2.2.12.

[15] G. Gonzalez, Foundations of Oscillator Circuit Design, Artech House, 2007.

 ISBN: 978-1-61208-302-5

Dual High-Frequency Surface Acoustic Wave Resonator for Ultrafine Particle Sensing

Sanju Thomas, Zoltán Rácz, Marina Cole, Julian W. Gardner
Microsensors & Bioelectronics Laboratory,
University of Warwick
Coventry, United Kingdom
J.W.Gardner@warwick.ac.uk

Abstract— **This paper describes the development of a low-cost robust Surface Acoustic Wave Resonator (SAWR) micro sensor capable of detecting sub-micron size particles below 1 ng. The device comprises two 262 MHz Rayleigh wave SAW resonators fabricated on ST-cut quartz where one is used for particle sensing and the other as a reference channel. Electro-acoustic detection of different particles (including carbon, gold, sucrose, silicon, and PTFE) with different diameters was studied. The mass sensitivity of the SAWR was found to be typically 275 Hz/ng or 4 pg/Hz for the detection of 750 nm diameter gold particles. We believe that the device could be used as a low-cost and low power microsensor for the real-time and ubiquitous monitoring of airborne particulate matter. In particular, our SAWR sensor can be used to detect the typical levels of ultrafine particulate pollutants (PM2.5) found in city air today.**

I. INTRODUCTION

Cities play a critical role in the regional and global air pollution due to multiple sources of emission including transportation and various industrial activities. This could bring about several direct and indirect, serious and immediate concerns related to human health and to the environment [1]. As a result, there is a significant need to detect atmospheric particulate matter (PM) (e.g. fine particles such as dust, soot and pollen) related to increasing pollution levels in our city centers. More stringent requirements by legislators for indoor and outdoor air quality monitoring and recent advances in nanoparticle based technologies have generated an increased interest in the precise measurement of ultrafine particles.

Commonly used sensors for monitoring airborne-particle size distribution and concentration are based on optical measurement techniques including nephelometry, polychromatic LED method, Scanning Electron Microscopy or MEMS based resonant mass sensors [2]. Unlike optical methods, SAW devices do not require sophisticated and expensive setups and can be operated with low cost electronic circuitry, providing the desired sensitivity level [3]. High frequency SAW resonators are known to be simple devices that are very sensitive to mass loading, because of the acoustoelectric coupling between the acoustic wave and materials deposited on the device surface.

In this paper, we report the development of a highly sensitive 262 MHz Surface Acoustic Wave (SAW) based sensor capable of detecting sub-micron size particles with masses below 1 ng. The nanoparticle sensor fabricated on a quartz substrate utilizes Rayleigh waves with a penetration depth of around 5 µm, i.e. comparable to the size of the particles being probed as illustrated in Figure 1. The SAWR devices can be integrated with analogue circuitry (e.g. Pierce oscillators) to obtain sensitive, low-power, low-cost particle detectors.

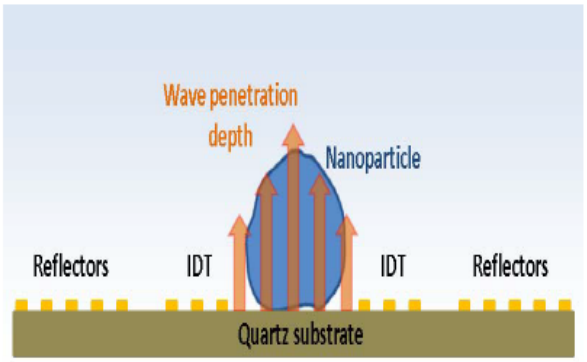

Figure 1. Penetration depths of Rayleigh waves from a SAWR can be tailored to the nanoparticle diameters of interest here.

II. SENSOR DESIGN

The acousto-electric transducer used in this work was batch fabricated on a 4" ST-cut quartz substrate wafer using UV lithography (PacTech, Germany). The high temperature stability of ST cut based Rayleigh SAW devices eliminates the need of using temperature control circuitry [4]. These sensors resonates at a frequency of 262 MHz consists of aluminum based inter-digital-transducers (IDT) in order to produce a

Rayleigh wave in the crystallographic X-direction. Each IDT comprises a set of 60.5 finger pairs with a finger width of 3 μm and an acoustic aperture of 720 μm. The distance between the two IDT structures was set at 303 μm, to create a standing wave pattern. The IDTs are surrounded by 600 shorted reflector gratings on each side with a 6 μm pitch.

Since the use of a comparable reference sensor is the most popular method for compensation [5], the designed 2-port SAW sensor operates in a dual configuration with an overall die size of 9.6 × 3.6 mm^2. The dual resonator configuration eliminates common mode interferences on the sensing signal, such as changes in ambient temperature or pressure. One side of each dual device acts as a reference signal, while the other side is used for the detection of the nanoparticles. This differential signal have reduced noise level and improved signal stability by maintaining a high signal to noise ratio. The typical device insertion loss is *ca.* 9 dB which shows that the electrical power dissipation due to acousto-electric conversion at the IDT/substrate interface is very low.

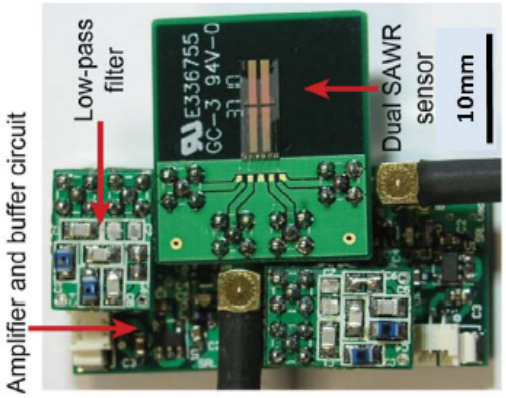

Figure 2. Photograph of a dual 262 MHzSAW sensor and the associated electronics including RF amplifiers, filters and buffer.

The SAW resonators operate in an oscillator configuration (feedback loop based) consisting of RF amplifier, a low pass filter, and the buffer circuitry. In order to avoid the problem of frequency locking of SAW resonators, the oscillator boards are arranged separately for each resonator structure, providing frequency stability. Separation of the power and ground planes on the oscillator board reduces the RF cross talk, thereby improving noise sensitivity. The low pass filter included in the feedback loop suppresses oscillations at spurious frequencies. As the SAW resonators were designed for both input and output impedances of 50Ω, the need of impedance matching circuits were avoided. The dual two-port SAWR sensor (with reference channel) and its associated electronic circuitry for excitation, amplification, buffering and read-out are shown in Figure 2.

III. Mass Sensitivity Analysis

The sensitivity of SAW sensors depends on several factors including operating frequency of SAW device, change in the wave velocity due to surface mass loading and density of the substrate material. In general, the mass sensitivity for surface acoustic mode sensors can be defined as [6]

$$S_m = \lim_{m \to 0} \frac{1}{V_o} \frac{\Delta V}{\Delta m} \tag{1}$$

where V_o and V are the wave velocities before and after loading respectively and ΔV is the difference between them produced by adding a mass per unit area, Δm, uniformly on the sensing area of the device. Since a SAW device operates in an oscillator mode, due to negligible oscillator phase shift, and by rearranging equation (1), it can be shown that [4]

$$S_m \Delta m = \Delta V / V_o = \Delta f / f_o \tag{2}$$

where f_o and f are the resonant frequencies before and after mass loading respectively and Δf is the difference between them.

The mass sensitivity of a piezoelectric device could also be expressed as [7]

$$\Delta f = \alpha f_o^2 \Delta m / A \tag{3}$$

where α is a mechanical sensitivity constant and A is the portion of sensing area covered by the mass deposited on the device. This shows that the mass sensitivity is directly proportional to the square of the resonant frequency of the sensor. Additionally, Wenzel et al. [6] utilized Auld's perturbation theory to derive a simple expression for mass sensitivity focusing on resonance wavelength, rather than frequency of operation. Thus,

$$S_m = -K(\sigma)\frac{1}{\rho \lambda} \tag{4}$$

where, ρ is the density of the substrate and λ is the SAW wavelength. $K(\sigma)$ is a parameter that ranges from 1 to 2 for most isotropic solids and is dependent on the rayleigh and shear wave velocities.

Hence, from equations (3) and (4), it can be deduced that, in order to obtain higher sensitivity for SAW devices, the operating wavelength of the sensor must be reduced. In other words, by increasing the resonant frequency of the SAW resonator, a higher sensitivity can be obtained. As a result, we have designed and fabricated a high frequency (262 MHz) SAW resonator for particle detection at ppb level.

IV. Experimental Procedure

The experimental setup for the detection of ultrafine particles have been developed utilizing a dual SAW based sensor as shown in Figure 3. A precision linear translation stage (LS Starrett Co., USA) which incorporates three micrometers with 0.5" travel range along each axis, was placed on top of the sensor system. The deposition of the micro and nano particles on the active area of the SAW sensor was done using a 0.25 μm thick wire attached to the translation stage. The stage allows the micro scale movement of the particles placed on the tip of the wire in all the three axes, prior to their deposition on the SAW sensing area.

APPENDIX D

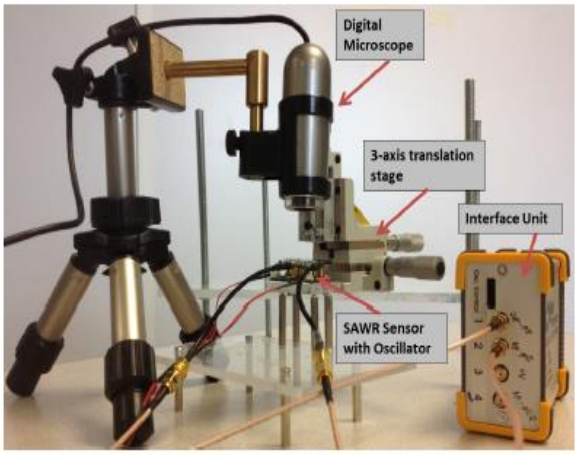

Figure 3. Experimental setup for particle testing consisting of s SAW based sensor system and associated drive and interface circuitries, a digital microscope and a translation stage used for particle deposition.

A digital microscope (Dino-Lite Europe, The Netherlands) enabled the real-time visual monitoring of the particle deposition on the sensor surface. The sensor system was placed inside a housing specifically designed to ensure temperature stability and to eliminate any effects due to environmental variations. It also insured avoidance of deposition of any foreign particulate matter on the sensing area. This in turn ensured a stable SAW baseline signal and reduced noise level. The oscillators are connected to a commercial four channel interface (JLM Innovation, Germany) unit to measure the resonant frequency of the dual SAW device and record it onto a personal computer.

V. Particle Deposition

In order to measure the mass sensitivity of the SAW based resonators, fine particles with known size and composition were deposited and the change in frequencies was monitored. The frequency response of the sensors to particles of different materials and various sizes including 0.75 µm gold powder, 6 µm sugar crystals, 10 µm silicon powder, 20 µm gold and 30 µm PTFE beads was measured. Effects of particle deposition on both the *free* sensing area of the SAWR sensor and between the aluminum inter digital transducers (IDTs) was studied.

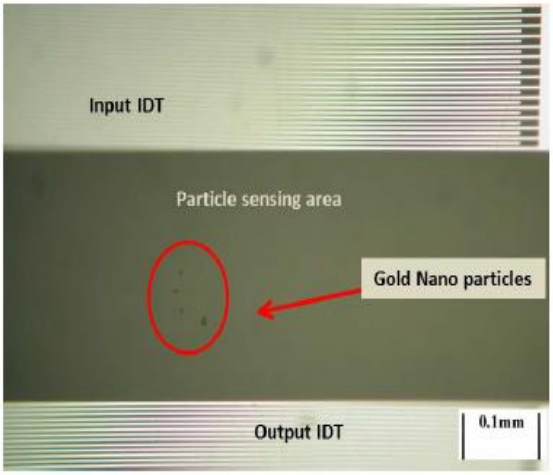

Figure 4. Optical image of gold particles deposited correctly within the free sensing area between the IDTs.

Figure 4 shows the sensor after the deposition of gold particles (diameters less than 1 µm) on the active area of the SAW based particle sensor and Figure 5 shows the SEM image of the gold nanoparticles deposited on the SAW IDT area.

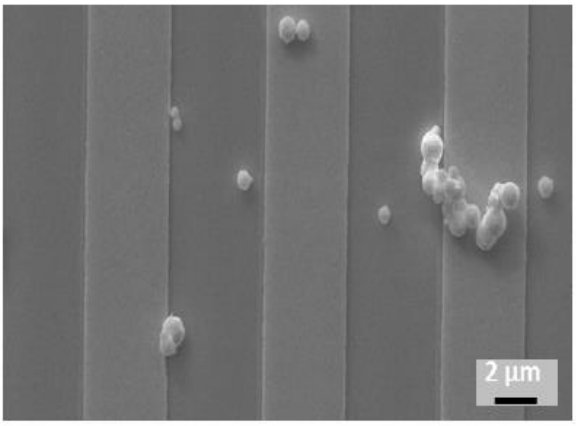

Figure 5. SEM image of gold nanoparticles placed across the 3 µm wide aluminum electrodes of the SAWR IDTs in order to test positional sensitivity.

VI. Results and Discussion

A typical differential frequency output produced by the deposition of fine gold particles (750 nm) on the sensing side of the dual SAWR sensors is as shown in Figure 6. From this, it can be seen that the SAW sensor has a fast and low noise response. In a similar manner, the frequency response due to other types of particles including carbon, gold, sucrose, silicon, and PTFE were also obtained in an attempt to obtain the mass sensitivity of the SAW particle sensor.

The mass sensitivity of the particle sensor was calculated for each particle type, utilizing the value of the particle density and diameter. The relationship between the mass sensitivity, $\Delta f/\Delta m$, and particle diameter has been established as shown in Figure 7. It can be noted that the SAW sensor displayed the highest mass sensitivity for the particles of less than ca. 5 µm in diameter. For all other particle diameters outside this range, the sensitivity was significantly smaller.

The change in mass sensitivity with particle dimensions could be explained by the knowledge of acoustic penetration depth of the SAW resonator. Rayleigh waves travel along the surface of the substrate with the particle vibration in the vertical plane. This particle motion consists of a combination of P (compressive) and SV (shear vertical) vibrations in the axis normal to the direction of wave. The penetration depth is the depth at which the signal amplitude is degraded to e-1 of its value at its surface [8], and it changes inversely with the

APPENDIX D

frequency of operation of SAW sensor. Thus, in a highly sensitive SAWR particle sensor, surface interactions occur in the close proximity, resulting in increased mass sensitivity [9].

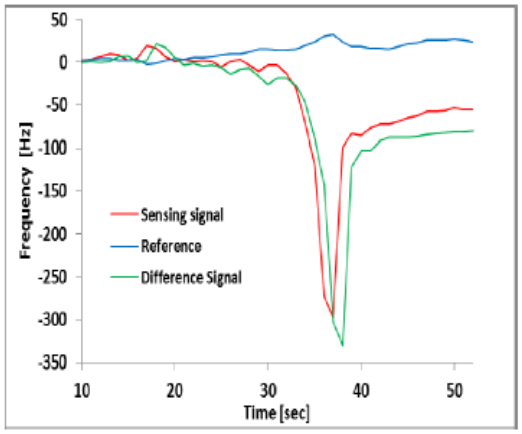

Figure 6. Typical frequency shifts of a dual SAWR sensor after the addition of gold nanoparticles in sensing region.

As the particle diameter decreases, a high frequency Rayleigh based particle sensor allows particle monitoring in the close proximity of sensor surface. Hence the particle size must be less than the acoustic penetration depth to allow acoustic coupling of the entire particle volume. Otherwise, the sensor only probes the part of the particle near its surface.

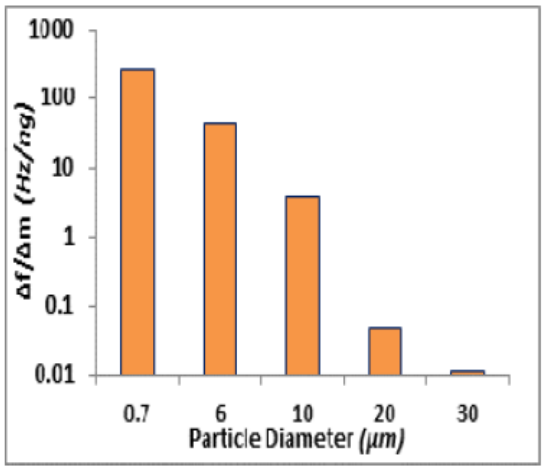

Figure 7. Plot showing the relationship between SAWR sensitivity Δf/Δm and particle diameter for different sized particles.

For a Rayleigh SAW device with a wave length λ, the penetration depth is typically about 0.4λ [8] and therefore a characteristic penetration depth of 262 MHz SAWR sensor is in the range of ca. 5 µm. This phenomenon may be utilized to monitor pollutants with different particle size distribution by employing SAWRs operating at different frequencies.

Ideally, if the size of a gold particle is within the penetration depth range, e.g. 4 µm, then the mass of that particle detected by the sensor is calculated to be *ca.* 0.65 ng. Thus by using sub-micron size particles, masses in the picogram range could be detected by the sensor.

VII. Conclusion

A low cost SAW based particle sensor capable of detecting ultrafine particulate matter with masses below 1 ng has been developed and discussed. A high sensitivity of 275 Hz/ng was measured which shows good close agreement with the theoretically estimated value. Work is under progress to develop a compact and low power particle sensor system by implementing the oscillator circuit in a silicon CMOS process.

Acknowledgment

The authors wish to thank first Mr. Frank Courtney (Warwick University, UK) for his assistance in constructing the particle deposition unit and secondly Mr. Martin Davis (Microscopy and Analysis Laboratory, Warwick University, UK) for his help with the SEM imaging of the SAW based particle sensors.

References

[1] M. L. Melamed et al., "Detection of pollution transport events southeast of Mexico City using ground-based visible spectroscopy measurements of nitrogen dioxide," Atmospheric Chemistry and Physics, pp. 4827–4840, 2009.

[2] A. Hajjam, J. C. Wilson, A. Rahafrooz, and S. Pourkamali, "Fabrication and characterization of thermally actuated micromechanical resonators for airborne particle mass sensing: II. Device fabrication and characterization," Journal of Micromechanics and Microengineering, vol. 20, no. 12, Dec. 2010.

[3] K. Länge, B. E. Rapp, and M. Rapp, "Surface acoustic wave biosensors: a review," Analytical and bioanalytical chemistry, vol. 391, no. 5, pp. 1509–1519, Jul. 2008.

[4] Ballantine D. S., Acoustic Wave Sensors: Theory, Design, and Physico-Chemical Applications. Academic Press, 1997.

[5] M. Hoummady, A. Campitelli, and W. Wlodarski, "Acoustic wave sensors: design, sensing mechanisms and applications," Smart Materials and Structures, vol. 6, no. 6, pp. 647–657, Dec. 1997.

[6] S. W. Wenzel and R. M. White, "Analytic comparison of the sensitivities of bulk-wave, surface-wave, and flexural plate-wave ultrasonic gravimetric sensors," Applied Physics Letters, vol. 54, no. 20, pp. 1976-1978, 1989.

[7] W. D. Bowers and R. L. Chuan, "Surface acoustic-wave piezoelectric crystal aerosol mass microbalance," Review of Scientific Instruments, vol. 60, no. 7, pp. 1297-1302, 1989.

[8] W. Lowrie, Fundamentals of geophysics, 2nd Ed., Cambridge: Cambridge University Press, 2007.

[9] T. M. A Gronewold, "Surface acoustic wave sensors in the bioanalytical field: recent trends and challenges," Analytica chimica acta, vol. 603, no. 2, pp. 119–128, Nov. 2007.

APPENDIX D

A Low-Cost Acoustic Microsensor based System in Package for Air Quality Monitoring

Sanju Thomas, Marina Cole, Farah H. Villa-Lopez, Julian W. Gardner
Microsensors and Bioelectronics Laboratory
University of Warwick
Coventry, United Kingdom

Jan Peters, Jan Theunis
Laboratory of Air Quality Measurements
Flemish Institute of Technological Development (VITO)
Mol, Belgium

Abstract—**In this paper we report on the development of a novel hybrid System in Package (SiP) microsensor utilizing high frequency acoustic wave devices for the real time monitoring of airborne fine particulates. The hybrid particle sensing system consists of a zinc oxide (ZnO) based solidly mounted resonator (SMR) device interfaced to a CMOS application-specific integrated circuit (ASIC) chip. Air is drawn into a virtual impactor where $PM_{2.5}$ particles are separated and then deposited onto the SMR surface. The mass loading due to the fine particles is measured as a shift in the resonant frequency of the SMR working at 894 MHz. Experimental results performed in both laboratory conditions and real outdoor environment showed that the hybrid system is capable of detecting fine particles with a sensitivity of 7.5 kHz per µg/m³. This system is used as a basis towards a fully integrated portable smart particle sensor based on CMOS-SMR devices for the continuous, real-time and low-cost monitoring of airborne particulate matter.**

Keywords— air quality monitoring, CMOS sensor, particle sensing, particulate matter, solidly mounted resonator.

I. INTRODUCTION

Air pollution due to particulate matter (PM) pose a significant threat not only for the environment but also to human health causing several diseases and reducing the life expectancy of the population worldwide. Airborne particles found in indoor and outdoor environments can stem from human activities such as domestic and industrial processes, road traffic and solvents use. It is their size that make these pollutants particularly hazardous as fine particles with diameters of 2.5 µm or smaller ($PM_{2.5}$) can penetrate deeply into the lungs. Trying to minimize human exposure to PM and the related adverse health effects, exposure limits of $PM_{2.5}$ have been established by organizations such as the European Commission (EC) and the World Health Organization (WHO) [1].

There is an increased need of monitoring personal exposure to particulate matter. Commercial instruments such as the tapered element oscillating microbalance (TEOM) analyser and optical based instruments have been used for a long time. However, they are complex, costly and bulky [2]. Acoustic wave based devices have been proposed as an alternative approach for particle detection.

In this work we use solidly mounted resonators as they offer significant advantages with respect to size, cost and complexity. Furthermore, their compatibility with low-cost silicon technologies and small footprint make them suitable candidates for fully CMOS integration as opposed to other acoustic wave devices such as Surface Acoustic Wave (SAW) devices and Quartz Crystal Microbalances (QCM).

This work was funded under the EC 7th Framework Program, Project No. 611887, "Multi-Sensor-Platform for Smart Building Management: MSP".

II. DESCRIPTION OF THE SYSTEM IN PACKAGE

A. Overall description of the microsensor system

A novel low-cost acoustic SiP microsensor for particulate matter ($PM_{2.5}$) detection has been developed as part of a study into environmental air quality monitoring. The microsensor system is based on a thin film Solidly Mounted Resonator vibrating at 894 MHz driven by a CMOS Pierce oscillator circuit, which forms part of an ASIC chip. The pictorial illustration of a SiP particle sensor for PM detection is shown in Fig. 1.

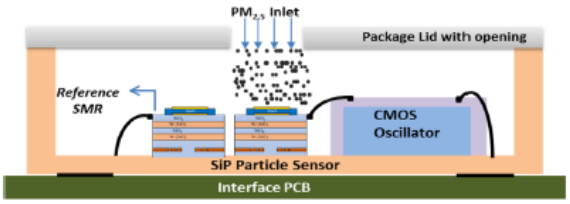

Fig. 1. Block diagram representation of a SMR microsensor system for the detection of particulate matter.

The particle sensor SiP employs a dual mode configuration in order to eliminate common mode interferences, where one SMR forms the sensing device while the other one forms the reference sensor. The ASIC oscillator chip is designed using the standard AMS (Austria Micro Systems) 0.35 um CMOS process and with the help of an on-chip RF Mixer, a differential output is obtained (0-5 MHz). Fig. 2 shows the schematic block diagram of the components inside the ASIC chip along with the off-chip dual SMR devices.

B. Solidly Mounted Resonator

The SMRs consisted of a 2.96 µm thick ZnO piezoelectric layer with top and bottom aluminium electrodes with a thickness of 200 nm. Three pairs of Molybdenum and silicon dioxide layers formed an acoustic mirror that reflects and traps the acoustic wave over the resonant frequency range. The device was fabricated on a 500 µm thick 4-inch p-type silicon substrate using standard micro fabrication technologies.

APPENDIX D

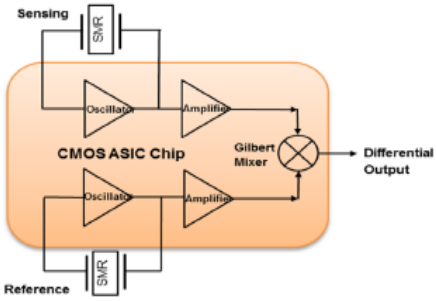

Fig. 2. Block diagram of the hybrid ASIC-SMR SiP.

The SMRs were designed in a coplanar waveguide (CPW) structure with a characteristic impedance of 50 Ω for maximum power transfer. The electrodes are linked to the coplanar transmission line, which helps in reducing the parasitic effects of the structure. A top view micrograph of the fabricated SMR is shown in Fig. 3[a].

C. CMOS Oscillator ASIC

Hybrid integration of SMR devices with CMOS oscillator circuitry minimizes the spatial and parasitic load limitations of externally coupled oscillators. The composite micrograph of the fabricated ASIC die with a size of *2.5* x *2.5 mm* is shown in Fig. 3[b]. The ASIC chip fabricated at AustiaMicroSystems (AMS) using a 0.35µm 3.3v CMOS process, has the capability of supporting two single-ended SMRs using inverter-based Pierce oscillator circuits and providing a differential signal using a gilbert mixer circuitry. The output of the Pierce oscillator is fed to a 2-stage CMOS inverter amplifier which amplifies the weak signal, before it is fed to the analogue mixer.

The ASIC chip also contains an analogue mixer based on Double Balanced Gilbert cell topology. The sensing SMR is connected to the RF input port while the reference SMR is connected to the LO (local oscillator) port of the mixer.

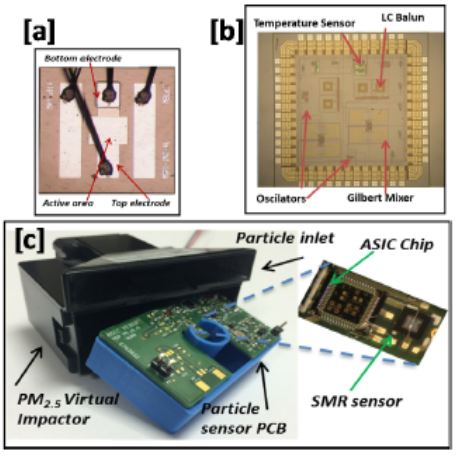

Fig. 3. [a] Top view of fabricated SMR. Device is 1 mm x 1 mm; [b] Composite micrograpgh of the ASIC die and [c] Photograph of the hybrid SMR-ASIC system placed inside the $PM_{2.5}$ virtual impactor.

A differential output frequency is obtained at the IF (intermediate frequency) port of the mixer, which is further amplified and sent to an off-chip low-pass filter and comparator to obtain a low frequency square signal that can be fed to a microcontroller.

The particle system was placed inside a commercial $PM_{2.5}$ virtual impactor (Sharp Microelectronics) and the complete system is as shown in Fig. 3[c]. The impactor separates the $PM_{2.5}$ fraction from the air flow and $PM_{2.5}$ particles are fed to the sensor surface for detection, providing an active sampling rather than a pure gravimetric deposition.

III. SPECTRERF SIMULATION RESULTS

The simulation of CMOS ASIC oscillator chip has been performed using Cadence® Design Systems Spectre®RF circuit simulator. The schematic of the 3-inverter Pierce oscillator is shown in Fig. 4.

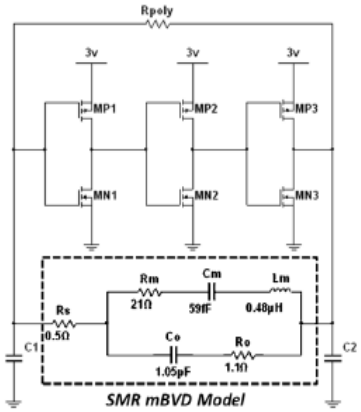

Fig. 4. Inverter based CMOS pierce oscillator schematic showing the mBVD model of the SMR device.

The SMR is connected to an inverting CMOS amplifier to form a hybrid integrated CMOS-SMR oscillator. The inverting amplifier is formed by three RF MOSFET-based CMOS inverters, which ensures sufficient gain to overcome the SMR insertion losses and to provide sustained oscillations [3]. The resistor *Rpoly* provides sufficient biasing to the MOSFETs. C1 and C2 along with the parasitic capacitances and inductances within the loop, helps in oscillator start-up. This helps to generate continuous noise energy within the SMR, resulting in increased current flow into the resonator [4]. The modified Butterworth-Van Dyke circuit model of the SMR is described in Fig. 4, which serves as a resonant tank for the oscillator.

The Spectre®RF simulations of the oscillator circuit after layout are shown in the Fig. 5. The output voltage levels during transient simulation are shown in Fig. 5[a]. The voltage gain (20dB modifier) at the fundamental resonant frequency is 0 dB, obtained from the periodic steady state analysis of the oscillator circuit, as shown in Fig. 5[b]. Fig. 5[c] and Fig. 5[d] show the loop gain magnitude and phase at the oscillator frequency, respectively. Close inspection of the magnitude and phase curves shows that the oscillator satisfies the Barkhausen criterion for sustained oscillations, because there is a gain of 0 dB (unity) and a phase of 0 degree, occurring simultaneously at the oscillator frequency.

APPENDIX D

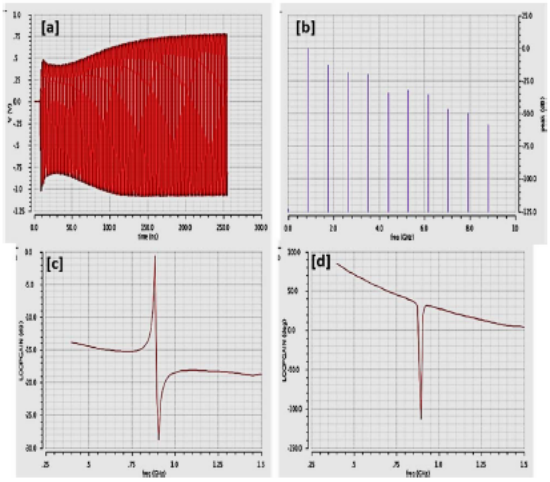

Fig. 5. Post layout SpectreRF simulation results of CMOS Oscillator detailing [a] Transient stability; [b] Periodic Steady state; [c] Loop gain magnitude and [d] Loop gain phase.

The performance of the ASIC oscillator has been verified using the Tektronix MDO3012 Mixed Domain Oscilloscope, which produced the output spectrum of the oscillator as shown in Fig. 6. This shows the oscillator frequency of 893.6 MHz, which is similar to that of SMR resonant frequency.

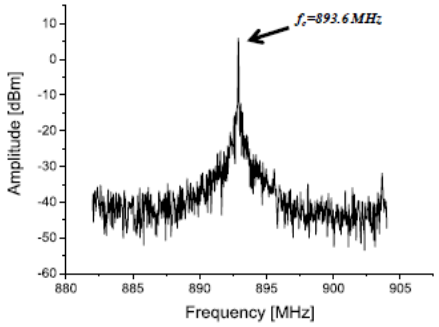

Fig. 6. Output Spectrum of the SMR-CMOS oscillator resonating at frequency (fc) of 893.6 MHz.

IV. EXPERIMENTAL RESULTS

In order to demonstrate particulate matter detection, an experimental setup was constructed that comprises of a test chamber and a dust generator system. Commercial instruments such as Grimm dust monitor (model 1.108), DC1700 AQM (Dylos Corporation) and a QCM sensor (Vitrocell Systems GmbH) were also employed for benchmarking. The sensors were exposed to artificial aerosols such as Dolomite powder (0–20µm) and Ultrafine Test Dust (UFTD) (1–20µm) and $PM_{2.5}$ concentration levels were monitored inside the test chamber. The deposition of micro-particles onto the SMR surface causes a shift in the resonant frequency of the oscillator, which is measured as a differential signal.

Preliminary results were also obtained for outdoor $PM_{2.5}$ monitoring, when the SMR-based SiP was exposed to car exhaust at VITO campus.

Fig. 7 shows the response of the SMR-based SiP together with the reference instruments. Grimm and Dylos monitors showed similar response curves as they both are optical based devices. On the other hand, the QCM device and the SMR-based SiP, both acoustic resonators, presented a similar response pattern as their resonant frequencies decreased after the addition of micro particles. After a series of laboratory and outdoor experiments, the sensitivity of the SMR-based SiP was found to be 7.5 kHz per µg/m^3, considerably high compared to that of the commercial QCM device.

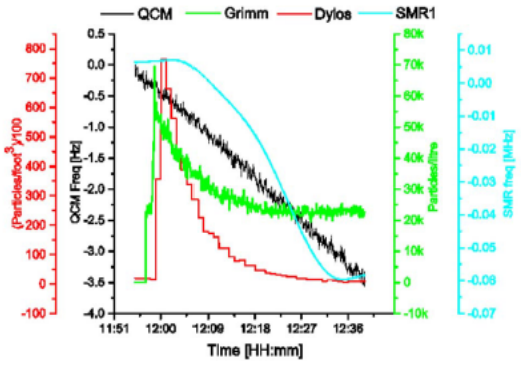

Fig. 7. Frequency response of the SMR particle sensor, due to particle deposition, shown along with data from Grimm, Dylos and QCM Devices.

V. CONCLUSIONS

We have reported the development of a low-cost hybrid SMR microsensor based SiP for particulate matter ($PM_{2.5}$) detection. A 0.35um CMOS ASIC chip containing Pierce inverter based oscillators and a gilbert mixed circuit, produces a differential low frequency output signal. The ASIC SMR shows a superior sensitivity of 7.5 kHz per µg/m^3 compared to the QCM device. In order to provide UFP, $PM_{2.5}$ and PM_{10} detection, it is possible to tailor the frequency dependent sensitivity based on the size of particles. Further work is underway towards the monolithic integration of both SMR and interface ASIC into a smart, portable, low-power and low-cost nano-particle sensor.

ACKNOWLEDGMENT

The authors would like to thank Mr. Frank Courtney (University of Warwick) for the development of a package for the particle sensor and Mr. Jo Van Laer (VITO) for his assistance in performing both laboratory and outdoor testing of the SMR particle sensor system.

REFERENCES

[1] World Health Organisation, "Health effects of Particulate Matter," 2013.

[2] A. Hajjam, J.C. Wilson and S. Pourkamali, "Individual Air-Borne Particle Mass Measurement Using High-Frequency Micromechanical Resonators". IEEE Sensors Journal, vol. 11, no. 11, pp. 2883-2890, 2011.

[3] M. L. Johnston and I. Kymissis, "An array of Monolithic FBAR-CMOS oscillators for Mass sensing Applications," pp. 1626–1629, 2009.

[4] EPCOS, "Design-guide for the SAW oscillator," 2008.

APPENDIX D

Available online at www.sciencedirect.com

ScienceDirect

Procedia Engineering 87 (2014) 999 – 1002

Procedia Engineering

www.elsevier.com/locate/procedia

EUROSENSORS 2014, the XXVIII edition of the conference series

Graphene-coated Rayleigh SAW Resonators for NO_2 Detection

S. Thomas[1], M. Cole[1], A. De Luca[2], F. Torrisi[3], A.C. Ferrari[3], F. Udrea[2], J.W. Gardner[1]*

[1]*School of Engineering, University of Warwick, Coventry, UK*
[2]*Department of Engineering, University of Cambridge, Cambridge, UK*
[3]*Cambridge Graphene Centre, University of Cambridge, Cambridge, UK*

Abstract

This paper describes the development of a novel low-cost Rayleigh Surface Acoustic Wave Resonator (SAWR) device coated with a graphene layer that is capable of detecting PPM levels of NO_2 in air. The sensor comprises two 262 MHz ST-cut quartz based Rayleigh SAWRs arranged in a dual oscillator configuration; where one resonator is coated with gas-sensitive graphene, and the other left uncoated to act as a reference. An array of NMP-dispersed exfoliated reduced graphene oxide dots was deposited in the active area inside the SAWR IDTs by a non-contacting, micro ink-jet printing system. An automated Mass Flow Controller system has been developed that delivers gases to the SAWR sensors with circuitry for excitation, amplification, buffering and signal read-out. This SAW-based graphene sensor has sensitivity to NO_2 of *ca.* 25 Hz/ppm and could be implemented in a low-power low-cost gas sensor.

Peer-review under responsibility of the scientific committee of Eurosensors 2014

Keywords: Surface Acoustic Sensor; NO_2 detection; Graphene oxide; SAW Resonator; Dual SAW

1. Introduction

Significant research has been carried out in the development of low-cost sensors for monitoring and controlling toxic gases responsible for global pollution. Among the various toxic chemicals studied, NO_2 is one of the most dangerous pollutants that contributes to several environmental effects, such as acid rain and ozone formation and can cause health problems at very low concentrations. Due to the drastic impact of NO_2 on public health and

* Corresponding author. Tel.: +44-2476-523695; fax: +44-2476-418922.
E-mail address: j.w.gardner@warwick.ac.uk

Peer-review under responsibility of the scientific committee of Eurosensors 2014
doi:10.1016/j.proeng.2014.11.328

APPENDIX D

environment, extensive research is being carried out in the field of NO_2 detection. In this paper, NO_2 detection mechanism using graphene based surface acoustic wave resonators (SAWR) is discussed. Even though SAWRs ($LiTaO_3$-based) incorporating graphene-coating have been previously used for sensing hydrogen, carbon monoxide, carbon dioxide, and ambient humidity [1], practically no work has been carried out in the detection of NO_2 gas.

We exhibit, for the first time, the response of graphene based Rayleigh SAW Resonators fabricated on quartz substrate to NO_2, as they are good candidates for monitoring changes in surface acoustic properties due to mass loading (Fig.1). The system described here is capable of demonstrating the dependence of the acoustic impedance of graphene on NO_2 in air utilizing quartz-based SAWR sensors [2]. Exfoliated reduced graphene oxide (RGO), which is not pure graphene have been used as the coating layer for the sensor. Hernandez *et al*. [3] commented that RGO is not perfect graphene but functionalized with hydroxyls and epoxides. Furthermore, Gardner *et al*. [4] confirmed the presence of defects or oxides for the graphene studied here by Raman spectroscopy.

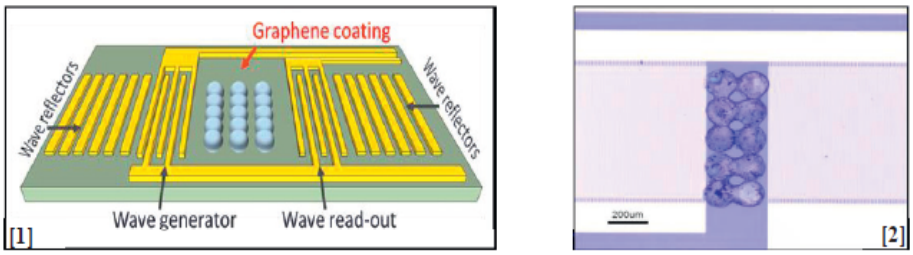

Fig. 1. Schematic of a two-port quartz-based Rayleigh SAW resonant device coated with an array of exfoliated graphene oxide micro-dots.
Fig. 2. Optical micrograph of the 262 MHz SAWR sensor coated with an array of graphene dots in *free* sensing area. Dot diameter is 150

2. Materials and Methods

2.1. SAW Resonator Design

The two-port SAWR sensors used in this work was batch fabricated on a 4" ST-cut quartz substrate wafer using UV lithography (PacTech, Germany) as explained in [2]. These dual sensors with an overall die size of 9.6 mm × 3.6 mm have a resonant frequency of 262 MHz and consists of aluminium based inter-digital-transducers (IDT), producing a Rayleigh wave in the crystallographic X-direction. Each IDT comprises a set of 60.5 finger pairs with a finger width of 3 µm and an acoustic aperture of 720 µm. A distance of 303 µm, between the input and output IDTs produce a standing wave pattern. 600 shorted reflector gratings surround each IDT with a 6 µm pitch [2]. The dual SAWR sensor (with reference channel) arrangement enables a differential operation that removes common mode variations such as temperature and humidity. Graphene was deposited on one side of each dual device (Fig.2), while the other side was left blank to act as a reference signal, in order to produce a low-noise differential signal.

2.2. Graphene ink formulation

We prepare the graphene-based printable ink as explained in [5]. Graphite flakes (NGS Naturgraphit) are sonicated (Decon bath, 100W) in NMP for 9 hours. The un-exfoliated flakes are left to settle for 10 minutes after sonication. The decanted dispersions are then ultra-centrifuged using a TH-641 swinging bucket rotor in a Sorvall WX-100 Ultra-centrifuge at 10,000 rpm (~15,000g) for an hour and filtered to remove flakes >1µm, that might clog the nozzle. The resulting ink is characterized by Optical Absorption Spectroscopy (OAS), High Resolution Transmission Electron Microscopy (HRTEM), Electron diffraction and Raman spectroscopy.

A Perkin-Elmer Lambda 950 spectrometer with 1nm resolution is used for the OAS measurements. OAS can be used to estimate the concentration of graphene [3], [5], [6] using the Beer-Lambert Law according to the relation $A=\alpha cl$, where A is the absorbance, l [m] is the light path length, c [g/L] the concentration of dispersed graphitic material and α [L g-1m-1] the absorption coefficient.

APPENDIX D

From α~1390Lg-1m-1 at 660nm [6], [7] and measured A~0.8, we estimate c~0.11±0.02g/L. A combination of HRTEM and Raman Spectroscopy analysis showed that the graphene-ink mostly consists of SLGs, Bi-Layers (BLG) and FLGs, with lateral size~300-1000nm. We find that ~35\% SLGs are larger than 300nm; ~40\% BLGs are larger than 350nm; ~55\% FLGs are larger than 450nm. In particular, we have 33\% SLG with c~0.11g/L [5].

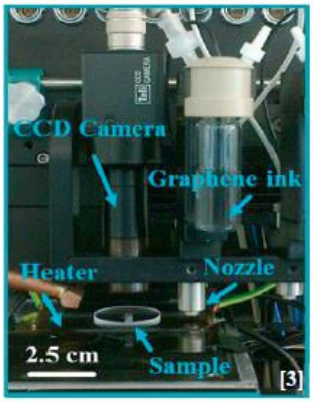

Fig. 3: Photograph of micro inkjet deposition system along with SAWR sample.

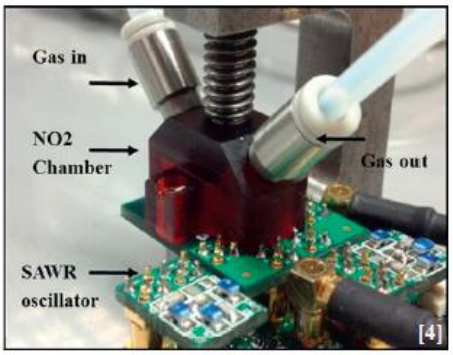

Fig. 4: The experimental setup for the detection of NO_2 vapour, showing the gas chamber with the in/out openings, placed over the SAWR oscillator system.

2.3. Graphene Deposition

Graphene was deposited onto the *free* sensing area of the SAWR sensor. A matrix of 2×5 dots (*ca*. 120um diameter with a centre-to-centre spacing of 200 μm) of NMP-dispersed exfoliated graphene was deposited by micro ink-jet printing as shown in Fig. 3. (Microdrop Tech.). The system is fitted with (i) a PC controlled stage and a CCD camera, which guarantees very accurate positioning of the sample under the ink dispensing nozzle; (ii) a strobe monitoring unit used to verify in time the drop stability and the absence of satellites drops, which might be responsible for a detrimental worsening of the process reproducibility; (iii) an in-house built heater, used to raise the temperature of the sample above ambient temperature (approx. 80°C) [4] in order to control the dimension of the deposited dots. A script for automatic dispensing of the ink in predefined location of the sample was realized. 500 drops of graphene ink were dispensed for a total of roughly 50 nL for each dot and a deposition time of approx. 10 minutes.

2.4. Experimental

The experimental setup for vapour detection using a graphene-SAWR device is shown in Fig. 4. The gas delivery system comprises high purity gas cylinders equipped with regulators and safety shut-off valves, inline particle and moisture filters, high-precision digital mass flow controllers to set the required gas concentrations to the sensor and inline check valves to prevent reverse gas flow. A gas chamber comprising of inlet and outlet holes, is attached to the sensor board, which allows the NO_2 gas mixture at various concentrations (ppm levels) to interact with the graphene layer coated on the sensing area. The gas mixture had a constant flow rate, and zero grade air was used as the reference (baseline) gas. These sensors resonate in a feedback loop of a simple RF oscillator circuit containing a high gain amplifier and a buffer with a low-pass filter in order to suppress oscillations at unwanted frequencies. The oscillation frequency of the SAWR oscillator circuit was recorded using a commercial instrument (JLM Innovation, Tubingen, Germany).

3. Results

The electro-acoustic interaction of NO_2 on graphene has been demonstrated as a frequency response of the SAWR sensors. On the binding of NO_2 molecules with graphene-SAWR, the oscillation frequency of the resonator decreases, which will be measured and recorded as a differential signal. The typical frequency output (Fig. 5) of a dual SAWR to four subsequent injections of 3 ppm NO_2 in air shows that the sensor response is fast, reproducible

APPENDIX D

and low noise. In a similar manner, the frequency response of the graphene-coated SAWR sensors was measured to various levels of NO2 concentrations to establish the minimum sensitivity of the sensors. The relationship between the graphene-SAWR sensitivity and NO_2 concentrations has been established to be approx. a log-linear response (Fig. 6), which modelled the sensor response linearly with volatile concentration confirming to have the sensor to be operating in the non-saturated regime.

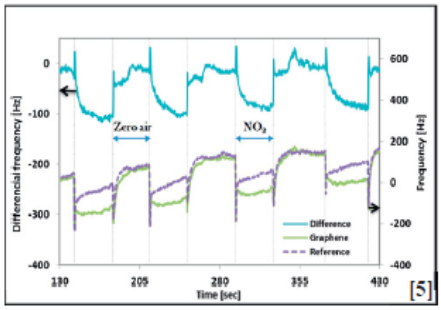

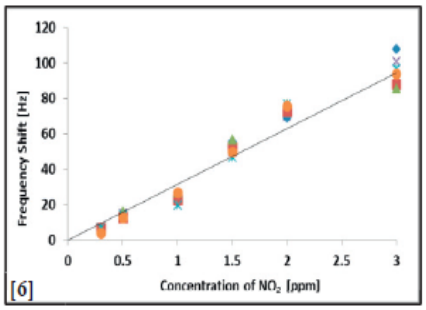

Fig. 5: Typical frequency output of a dual SAWR sensor in response to sequential injections of 3 ppm of NO_2 in air. Fig. 6: Linear frequency response of graphene SAWR sensor towards different low concentrations of NO_2 gas in air.

We believe that the defects in graphene oxide produced a higher sensitivity to reactive gases, such as NO_2. The extent of the surface acoustic wave penetration into the adjacent medium (exfoliated graphene oxide layer) determines the frequency change to the detected NO_2 concentration. In general, the frequency response, 'f' of a graphene-SAW sensor is given by $f = kc^n$ where k is the sensitivity constant, the exponent n is close to unity, and c is the concentration of reactive gas. Thus the sensitivity k of the graphene-SAWR is given by $\Delta f/\Delta c \approx 25$ Hz/ppm.

4. Conclusion

In conclusion, we have presented a novel grapheme-based SAWR sensor system, capable of detecting sub-ppm levels of NO_2. We believe that our SAWR based gas sensor can be used a sensitive, selective, low-power and low-cost gas sensor. In addition, sensitivity can also be improved by using an ultra-thin exfoliated graphene oxide layer with thicknesses comparable to the SAWR radiation depth. However, it has been identified that these sensors have cross sensitivity to water vapour, resulting in sensitivity degradation. Further studies are being carried out in the detection of other reactive gases (e.g. CO) and their cross-sensitivities. The integration of graphene with Rayleigh wave sensors could form a revolution in low-cost low-power chemical and environmental applications.

Acknowledgements

The authors thank Mr F. Courtney (University of Warwick) for the fabrication of the gas sensing chamber.

References

[1] V.S. Chivukula, Č. Daumantas, J.H. Kim, R. Rimeika, J.M. Xu, and M.S. Shur, Surface Acoustic Wave Response to Optical Absorption by Graphene Composite Film, IEEE Trans. Ultrason. Ferroelectr. Freq. Control, vol. 59, no. 2, 2012.
[2] S. Thomas, Z. Rácz, M. Cole, and J.W. Gardner, Dual High-Frequency Surface Acoustic Wave Resonator for Ultrafine Particle Sensing, IEEE Sensors Conference, 2013, pp. 4–7.
[3] Y. Hernandez, V. Nicolosi, M. Lotya et al., "High-yield production of graphene by liquid-phase exfoliation of graphite," Nat. Nano. 3, 563-568 (2008).
[4] J.W. Gardner, M.T. Cole, A. De Luca, P. Clément, E. Llobet, S. Z. Ali, and F. Udrea, Graphene SOI CMOS Sensors for Detection of PPB Levels of NO_2 in air," Transducers Conference, 2013, pp. 2055–2058.
[5] F. Torrisi, T. Hasan, W. Wu et al., "Inkjet-Printed Graphene Electronics," ACS Nano 6 (4), 2992-3006 (2012).
[6] M. Lotya, Y. Hernandez, P. J. King et al., "Liquid Phase Production of Graphene by Exfoliation of Graphite in Surfactant/Water Solutions," J. Am. Chem. Soc. 131 (10), 3611-3620 (2009).
[7] T. Hasan, F. Torrisi, Z. Sun et al., "Solution-phase exfoliation of graphite for ultrafast photonics," Physica Status Solidi (b) 247 (11-12), 2953-2957 (2010).

APPENDIX D

ASIC for Hybrid Biosynthetic Infochemical Chemoreceiver

M.F. Chowdhury, Z. Rácz, M. Cole, S. Thomas, J.W. Gardner
Microsensors & Bioelectronics Laboratory, School of Engineering
University of Warwick, Coventry CV4 7AL, United Kingdom
j.w.gardner@warwick.ac.uk

Abstract— In this paper we report upon the design of an application-specific integrated circuit (ASIC) that forms part of a single-board implementation of a smart chemoreceiver within an infochemical communication system. The ASIC, comprising four differential surface acoustic wave resonator (SAWR) circuits, enables the sensing of odour blend ratios of either fruit volatiles or sex pheromones for insects. The ASIC chip has a digital interface to an FPGA containing a neuromorphic blend model developed in order to classify specific ratios of chemical compounds in the odour blends and used to control a mobile robot. The ASIC measures small changes in the resonant frequency of functionalized piezoelectric sensors with a resolution of 20 Hz and where the base SAW frequency is selected in the range of 60 to 969 MHz. The BiCMOS ASIC chip has dimensions 3 mm × 3 mm and was fabricated at AustiaMicroSystems (AMS). The smart chemoreceiver can be integrated with a chemoemitter to create a novel insect based infochemical communication system.

I. INTRODUCTION

This ASIC chip has been designed as part of an EU funded project [1] to demonstrate, in real-time, the neuromorphic processing of chemical sensor signals to extract blend specificity information in a system that emulates both insect olfaction and infochemical communication. The complete system consists of chemoemitter for the deployment of chemicals in specific ratios into the communication channel and chemoreceiver able not just to detect different chemicals but to recover their specific ratios. This system uses either biological sensors based on insect cells expressing relevant olfactory receptors or organic sensors based upon polymers.

Our current work presents an intermediate hybrid stage between previous system comprising PCBs and discrete components (Figures 1) and the final portable monolithic chemoreceiver device. It is capable of supporting experimental studies using an array of up to four biosensors to detect blends of chemical compounds and replaces the entire discrete sensor module shown in Figure 1(b).

The ASIC has been developed as a part of compact portable system with four chemical detection channels that can be placed on a mobile robot and interfaced to the back-end FPGA block where neuromorphic computation is carried out.

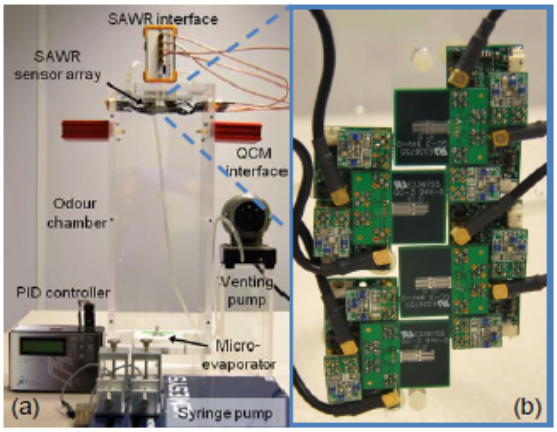

Figure 1: (a) Experimental setup for infochemical communication with micro-evaporator and SAWR chemo-receiver, and (b) the SAWR sensor array and its associated circuitry.

II. PROTOTYPE SYSTEM

Prior to the implementation of the ASIC system, an initial prototype system has been developed using discrete components, including SAWR sensors, filters, amplifier circuits and buffers as shown in the Figure 1b. The basic concept and preliminary results of biological sensors have been reported previously [2,3]. However, whilst performing measurements on discrete components it was realized that there were two main problems: (1) variation in the resonant frequencies of nominally identical SAW resonators and (2) drift of the resonant frequency over time with changes in ambient temperature and cell properties.

For a resonant system, small changes/differences in ideal closed-loop phase shift lead to a shift in the resonance frequency of the sensor and a change in the amplitude of the returned sensor signal [4]. As a result, it is evident that the acoustic resonator oscillator design should be tailored to compensate for the phase characteristics of the acoustic sensor. The drift in the normal oscillating frequency of an acoustic sensor is generally caused by parametric variation

978-1-4244-9289-3/11/$26.00 ©2011 Crown

due to temperature changes in either the SAW piezoelectric substrate or the circuit components.

III. VLSI Chemoreceiver Integration

In order to enhance the performance and accuracy of measurements in the SAW based biosensor system, the resonator circuitry which has been implemented using discrete components was replaced by a single VLSI chip. This ASIC chip can drive up to four pairs of differential SAWR sensors and can be interfaced to an FPGA containing a neuromorphic computational block. The entire ASIC oscillator chip is about 3 mm by 3 mm. Figure 2 shows a comparison of the discrete oscillator circuitry and the on-chip resonator circuitry, detailing the overall size of the two circuits. A Printed Circuit Board (PCB) has been designed as shown in the Figure 3, which forms a full hybrid system including the ASIC chip, and is currently being characterised using the SAW based sensor system. The PCB is a four layer board with grounding layers to reduce the cross-talk associated with high frequency signals. It also takes account of the phase shifts associated with the RF signal paths to the individual SAWR sensors.

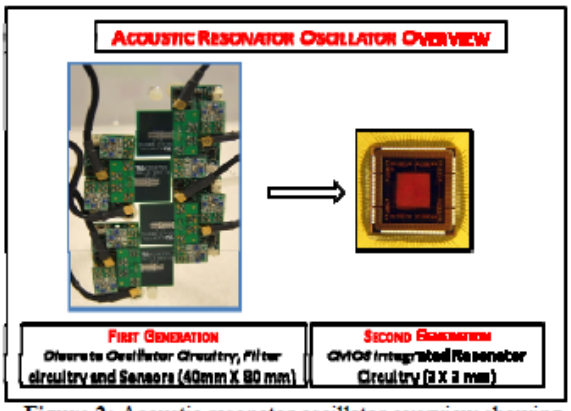

Figure 2: Acoustic resonator oscillator overview showing discrete circuitry and ASIC chip.

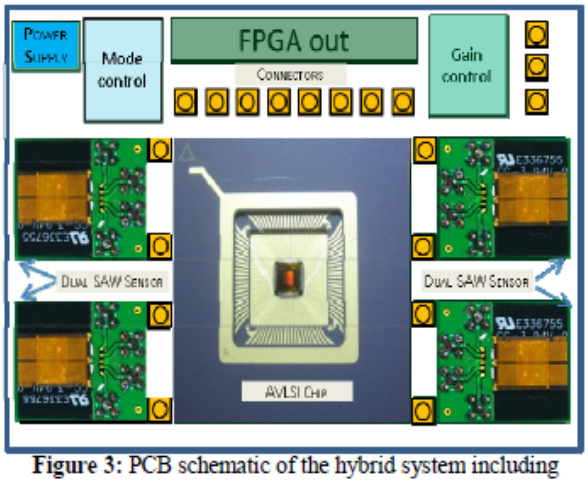

Figure 3: PCB schematic of the hybrid system including sensors, ASIC chip and digital output.

IV. ASIC Implementation

The ASIC has been developed using a 0.35µm 3.6V HF SiGe BiCMOS AMS process and has the capability of supporting up to eight single-ended channels (SAWRs). The chip can operate at frequencies of up to 1 GHz, has a number of on-chip mode selection options to compensate for any mismatching of the SAW oscillator frequencies and can readily measure frequencies to a 32-bit accuracy. Figure 4, shows the basic block diagram of the overall system.

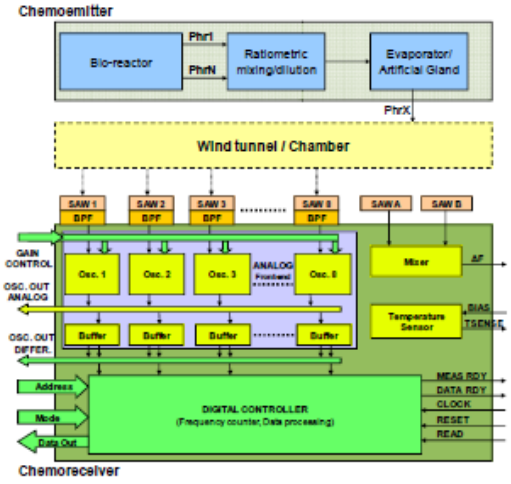

Figure 4: Schematic block diagram of the biosynthetic infochemical communication system.

It comprises of a chemoemitter in which a chemical blend is formulated and transmitted via an artificial evaporator/gland via a wind tunnel to the chemoreceiver. The chemoreceiver block contains SAW resonators that are placed outside the ASIC chip for detecting the transmitted blend. Sensor signals are processed by the chip and converted into digital form to be interfaced with a field-programmable gate array (FPGA) block, where the final neuromorphic computation is carried out and blend ratios recovered. A photograph of the fabricated 9 mm^2 chip is shown in Figure 5.

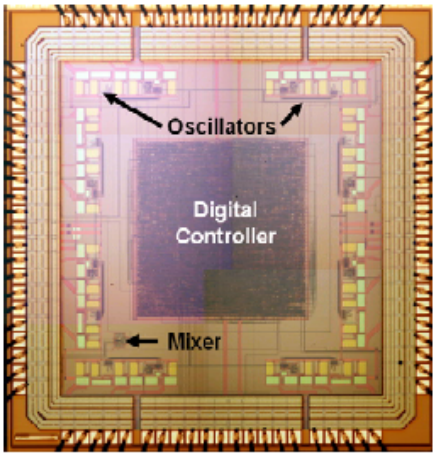

Figure 5: Composite micrograph of fabricated die.

APPENDIX D

A. The Oscillators

The basic building blocks for the oscillator circuit are shown in Figure 6. The oscillator was designed to ensure that it operated from 60 MHz to 869 MHz, and thus needed to have wideband capability. To achieve such performance capability and given that the oscillator needed to be configured for a 2-port SAW resonator together with selected AMS S35 BiCMOS process, a simple constant base current bias circuit topology with programmable gain control was found to be most suitable for this purpose. It is well known that such topology has two main limitations: (1) temperature stability and (2) bias resistance is Rb is dependent on the β parameter of the transistor. However, the latter issue can be resolved by programmable gain control and thus provides a degree of flexibility in terms of oscillation adjustment.

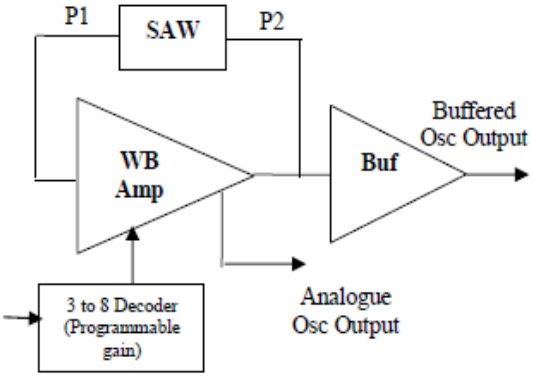

Figure 6: Oscillator Block

The actual amplifier (WB Amp, Figure 6) required 4-stages within the oscillator block and 2-stage buffering at the output that provides input to the digital control block where 32-bit frequency measurements are recorded. The final output buffer stage was designed to provide differential output and simulated to show its operation of more than 1GHz.

The ASIC provides seven levels of gain control options, ranging from 10 dB to 30dB, plus a choice of external control via resistor R (Figure 7).

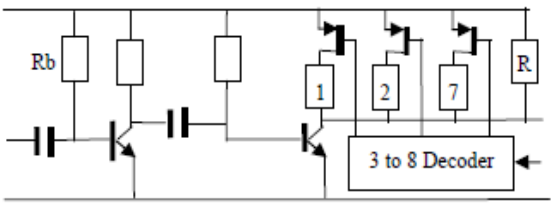

Figure 7: Wideband amplifier stage with programmable gain control

B. The Mixer

The ASIC chip also contains an analogue mixer based on Double Balanced Gilbert cell topology. This mixer has been included as a platform to check any mis-matching errors between two identical SAW devices or oscillators. Here, the differential output from the buffer stage can be applied to the mixer input to reduce noise interferences.

C. The Digital Controller

The digital controller block performs: (1) the frequency measurement on all eight channels to 32-bit accuracy, (2) computes difference between base and measured frequency (3) stores computed difference between two channels and (4) allows data to be read in 4 × 8 bit block.

The block diagram of the digital controller is shown below in Figure 8.

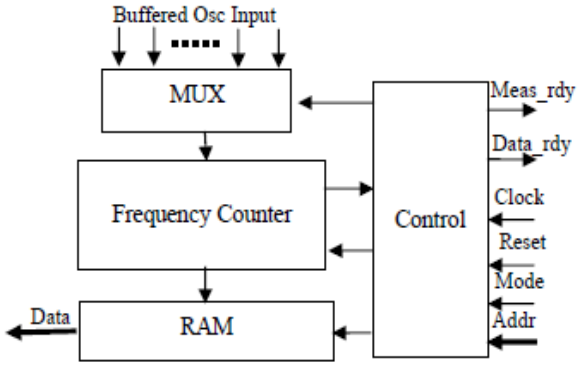

Figure 8: Digital controller

The controller is driven by a 10 MHz input clock. The frequency measurement is performed by gating clock at 50 ms. Here, the multiplexed oscillator input from each of the eight channels is applied to the counter to measure the frequency. With 50 ms gating we can achieve a measurement resolution of just 20 Hz. However, for increased resolution, it was found that a large divider is needed and this significantly increased the number of registers and logic gates required. The timing diagram of the frequency counter is shown in Figure 9.

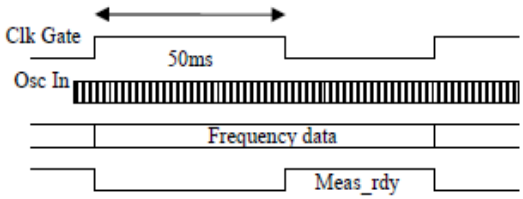

Figure 9: Gated frequency counter

V. Simulation Results

Simulations of the oscillator blocks and the amplifier with programmable gain control are shown in Figure 10 for a base frequency of 869 MHz. The measured and actual outputs of the chip are given in Figure 11.

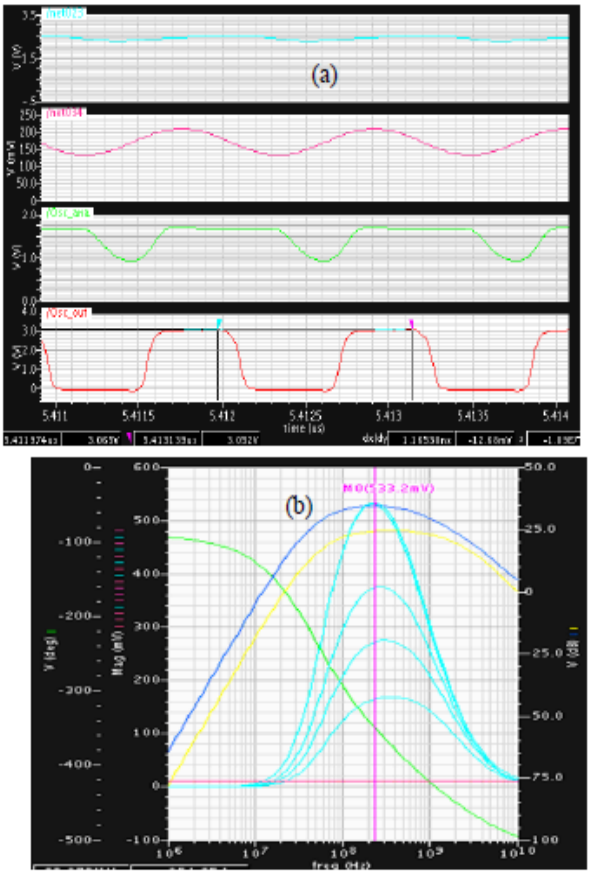

Figure 10: Simulation outputs: (a) the oscillator block at 869 MHz and (b) programmable gain control amplifier

The simulations shown in Figure 11, verified that it is possible to measure the input frequency accurately to 20 Hz resolution and retrieve the store the data in the addressable memory locations. The data can be read within the READ cycle. This process can be performed asynchronously when Meas_rdy is set, but it is recommended to synchronize with Data_rdy cyc

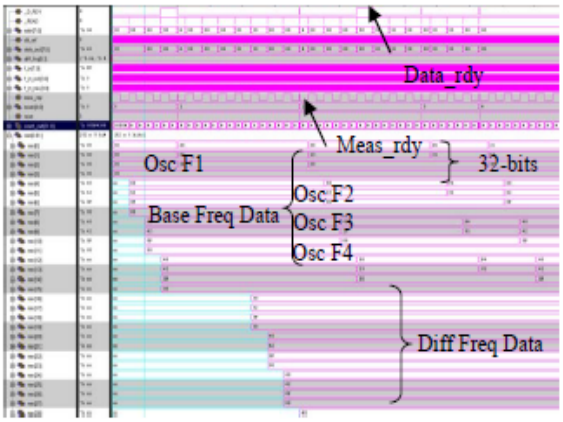

Figure 11: Measured actual and difference frequency data to 32-bit accuracy

The baseline oscillator miss-match is cancelled by initially storing the base frequency F1, F2 .. Fn in the register. During the measurement cycle, any drift in frequency can be monitored by checking the difference value during the calibration phase and then used to compensate for any error.

By selecting the appropriate mode on the ASIC chip, the difference between two oscillators can be calculated as ΔF=F1-F2 and stored in memory. For subsequent measurements, this data can be accessed and subtracted from any new measured frequency to remove the offset.

VI. CONCLUSIONS

An ASIC chip has been designed for application in an infochemical communication system employed 2-port SAW resonator sensors. The ASIC solution developed here shows that variation in the baseline oscillator frequencies and subsequent sensor drift can be digitally removed. This gives a greater flexibility in terms performing of more advanced on-chip signal processing. Furthermore, it allows the infochemical communication system to be miniaturized and serves as subsystem for further integration. The ultimate goal is to create a single chemoreceiver-on-a-chip solution for a mobile robot.

ACKNOWLEDGMENTS

This work was funded by EU as part of a STREP project no. FP6-032275 called "Biosynthetic Infochemical Communication" and Engineering and Physical Sciences Research Council UK (for PhD studentship).

REFERENCES

[1] iCHEM project, EU FP6 STREP project. See www.go.warwick.ac.uk/iCHEM.

[2] Z. Rácz, M. Cole, J.W. Gardner, S. Pathak, M.D. Jordan, and R.A.J. Challiss, "Cell-based surface acoustic wave resonant microsensor for biomolecular agent detection," *The 16th International Conference on Solid-State Sensors*, 2011, pp. 1-4.

[3] M. Cole, J.W. Gardner, S. Pathak, T.C. Pearce, and Z. Rácz, "Towards a biosynthetic infochemical communication system," *Procedia Chemistry*, vol. 1, (1), Sep. 2009, pp. 305-308.

[4] M. Binhack, W. Buff, S. Klett, M. Hamsch, and J. Ehrenpfordt, "A combination of SAW-Resonators and conventional sensing elements for wireless passive remote sensing," *IEEE Ultrasonics Symposium*, 2000, pp. 495-498.

APPENDIX D

Sensors and Actuators A 244 (2016) 138–145

Contents lists available at ScienceDirect

Sensors and Actuators A: Physical

journal homepage: www.elsevier.com/locate/sna

High frequency surface acoustic wave resonator-based sensor for particulate matter detection

Sanju Thomas, Marina Cole, Farah H. Villa-López, Julian W. Gardner*

Microsensors and Bioelectronics Laboratory, School of Engineering, University of Warwick, Coventry CV4 7AL, UK

ARTICLE INFO

Article history:
Received 23 June 2015
Received in revised form 22 January 2016
Accepted 4 April 2016
Available online 6 April 2016

Keywords:
Particulate matter detection
Surface acoustic wave resonator
Particle sensor
Ultrafine particles
High frequency SAWR sensor
PM_{10}
$PM_{2.5}$

ABSTRACT

This paper describes the characterization of high frequency Surface Acoustic Wave Resonator based (SAWR) sensors, for the detection of micron and sub-micron sized particles. The sensor comprises two 262 MHz ST-cut quartz based Rayleigh wave SAWRs where one is used for particle detection and the other as reference. Electro-acoustic detection of different sized particles shows a strong relationship between mass sensitivity ($\Delta f/\Delta m$) and particle diameter (D_p). This enables frequency-dependent SAWR sensitivity to be tailored to the size of particles, thus making these types of sensors good candidates for PM_{10}, $PM_{2.5}$ and ultrafine particle (UFP) sensing. Our initial characterisation demonstrated a typical SAWR frequency shift of 60 Hz in response to a deposition of *ca.* 0.21 ng of 0.75 μm-sized gold particles (~50 particles) on the sensor surface. Sensor responses to different sized particles, such as ~30 μm diameter silicon, gold (diameters of ~0.75 μm and ~20 μm), ~8 μm fine sugar, PTFE (~1 μm and ~15 μm), ~4 μm talcum powder, and ~2 μm molybdenum powder were evaluated, and an average mass sensitivity of 275 Hz/ng was obtained. Based on the results obtained in this study we believe that acoustic wave technology has great potential for application in airborne particle detection. Moreover, acoustic resonator devices can be integrated with CMOS interface circuitry to obtain sensitive, robust, low-power and low-cost particle detectors for a variety of applications including outdoor environmental monitoring.

1. Introduction

Air pollution is a common problem in both developed and developing countries and it has a major effect on human health. Particulate matter (PM), carbon monoxide, ozone, nitrogen dioxide and sulphur dioxide are some of the major pollutants affecting human health. Small airborne particulate matter having diameters of 10 μm or less are commonly classified as PM_{10} (defined as particles equal to and less than 10 μm in diameter), $PM_{2.5}$ (defined as fine particles that consist of particles equal to or less than 2.5 μm in diameter) and UFPs (defined as particles with an diameter smaller than 0.1 μm). The latter ones are of particular concern due to their ability to penetrate deep into the lungs and blood streams, causing major health related problems including DNA mutations, heart attacks, and premature deaths [1]. In addition, PM pollution also has various environmental effects including visibility impairment and acid rain causing damages to the natural ecosystem and aesthetic damage to buildings and monuments. Since, even at relatively low concentrations, the burden of air pollution on health and ecosystem is significant, effective management of air quality is absolutely necessary [2]. More stringent regulations for indoor and outdoor air quality have been introduced by various environmental agencies and research organisations worldwide in order to set air quality standards at the level that effectively protects both public health and welfare. The European Commission has adopted a Clean Air Policy Package in December 2013, consisting of a new Clean Air Programme for Europe with new air quality objectives for the period up to 2030. In this, $PM_{2.5}$ exposure reduction target is set to reach 18 μg/m^3 based on the average exposure indicator (AEI) [3]. As a result, there is an urgent need to identify and measure atmospheric PM (e.g. dust, soot, and pollen) by developing and validating strategies and monitoring systems for air quality measurements based on the latest measuring techniques with low detection limits.

Currently, PM measurements are typically carried out using aerosol monitoring instruments based on the principles of optical absorbance and filtration, quartz crystal microbalance, light scattering and pulse counting, tapered element oscillating microbalance and gravimetry [4–8]. Despite the fact that conventional PM sampling methods provide certain advantages including

* Corresponding author at: School of Engineering, University of Warwick, Coventry CV4 7AL, UK.
E-mail addresses: S.Thomas.1@warwick.ac.uk (S. Thomas), Marina.Cole@warwick.ac.uk (M. Cole), F.H.Villa-Lopez@warwick.ac.uk (F.H. Villa-López), J.W.Gardner@warwick.ac.uk (J.W. Gardner).

http://dx.doi.org/10.1016/j.sna.2016.04.003
0924-4247/

APPENDIX D

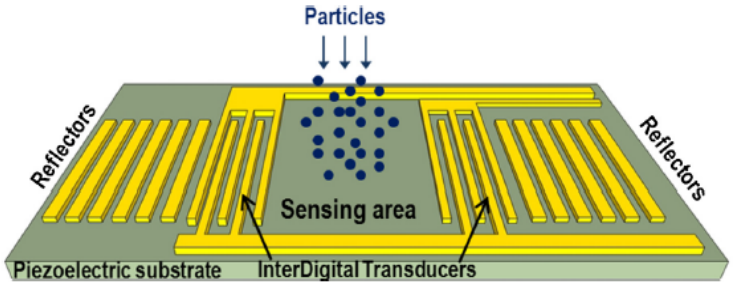

Fig 1. Basic principle of SAWR particle detection: schematic of a surface acoustic wave resonator based sensor with sub-micron sized particles deposited on the active sensing area.

real time data with short time resolution (<1 h) [9], most of these prevailing systems are bulky, expensive, and energy inefficient. Recent advances in nanoparticle based technologies have generated an increased interest in the development of smart, compact and low cost sensors for the precise measurement of ultra-fine particles as well as PM_{10} and $PM_{2.5}$.

This paper outlines the development of a two-port SAWR-based particle microsensor. High frequency SAWRs are well known to be simple devices that are very sensitive to mass loading, with mass sensitivity levels several times higher than that of quartz crystal microbalance (QCM) devices [10,11]. In addition, they can be operated with low-cost drive and signal conditioning circuitry; unlike optical devices which require sophisticated and expensive setups. The particle sensor described here is a Rayleigh wave surface acoustic wave device capable of detecting micron and submicron sized particles, using sensitivity-tailored frequency-dependant designs of acoustoelectric sensors. The main advantages of SAWR devices include a simple and low cost fabrication procedure, high sensitivity and a fast response time—in addition to their compact size and robustness [12].

2. SAWR sensor theory and principle of operation

In this paper, we present the characterization of a novel, miniature particle detection sensor using a conventional high frequency two-port surface acoustic wave resonator operating in an oscillator configuration. The basic configuration of a SAWR sensor shown with sub-micron sized particles deposited on the active sensing area is illustrated in Fig. 1. The figure depicts a device based upon a piezoelectric substrate with inter-digital-transducers (IDT) and reflectors on each side of the device patterned in order to produce a standing Rayleigh-type acoustic wave.

For a Rayleigh SAWR sensor, the sensing region lying between the two IDTs constitutes the central mass sensitive region referred to here as the active area. The reflector gratings on both sides of the SAWR IDTs form a resonant acoustic cavity. At the resonant frequency, this cavity will trap the acoustic wave in the form of standing waves between the two reflector gratings. With diminished standing wave amplitude away from the SAWR central cavity gap (active area), remote reflector gratings have a smaller effect on the resonator frequency [13]. Thus, the sensitivity will be highest at the central active area between the two IDTs.

When the particles fall on the sensor surface the propagation of the acoustic waves is perturbed and as a result, both the velocity and attenuation of the wave change. If the devices are placed in an oscillator configuration these changes can be measured with high accuracy as a change in resonant frequency. The sensing mechanism of the surface acoustic wave sensor depends on various factors including mechanical and electrical properties of the particles under test [14,15]. The mechanical effects include mass density and visco-elasticity of the particles, while the electrical effects include their conductivity and dielectric permittivity [16].

The theory behind SAWR sensors in general shows that SAW perturbations on a non-metallized active area, so-called *free* sensing area, are related to both the mechanical and the acoustoelectric properties of the adjacent medium [17]. However, by covering the sensing area with a thin conducting layer such as gold, an electrically-*shorted* SAWR device is formed, resulting in negligible effect due to electric potential [18]; therefore, the sensor response is dominated by only the mechanical properties of the medium under test. For a *free* SAWR particle sensor, a change in SAW frequency could be associated with the following variables including mass density ρ, viscosity η, conductivity σ, and dielectric permittivity ε of the particles under test. The total frequency shift, Δf, can be expressed using the differential theorem as shown below:

$$\Delta f_{Free} = \left\{ \frac{\partial f_{particle}}{\partial \rho_{particle}} \Delta \rho_{particle} + \frac{\partial f_{particle}}{\partial \eta_{particle}} \Delta \eta_{particle} + \frac{\partial f_{particle}}{\partial \sigma_{particle}} \Delta \sigma_{particle} + \frac{\partial f_{particle}}{\partial \varepsilon_{particle}} \Delta \varepsilon_{particle} \right\} \quad (1)$$

For an electrically *shorted* SAWR device, the electrical terms may be neglected thus leaving:

$$\Delta f_{Shorted} = \left\{ \frac{\partial f_{particle}}{\partial \rho_{particle}} \Delta \rho_{particle} + \frac{\partial f_{particle}}{\partial \eta_{particle}} \Delta \eta_{particle} \right\} \quad (2)$$

The difference between the two frequency parameters gives the electrical terms, thus permitting the separation out of both purely mechanical and purely electrical properties of the particles under test. In this work both configurations of the two-port SAWR devices were utilized: *free* (with non-metallized active areas) and *shorted* (with metallized active areas).

Depending on the nature of the SAWR sensor surface, i.e. metallized (*shorted*) or non-metallized (*free*), the generated acoustic waves possess both mechanical and electrical penetration depths. This means that, when a Rayleigh wave is generated on a piezoelectric substrate, it has an associated acousto-electric potential that extends into the adjacent medium. It is the distance of this wave penetration (called skin or penetration depth) that determines how far into the adjacent medium a measurable property can be detected. In the case of particle sensors, the acousto-electric potential of the SAW sensor extends into the particulate matter and the extent of penetration of this potential determines how far from the sensor/particle interface electrical and mechanical properties of the deposited particles can be detected by the sensor.

For the case of a metallized device, the electrical penetration depth is negligible; as the device is electrically *shorted*. But for a *free* device, both the mechanical and electrical skin depths are visible. The electrical skin depth δ_e was calculated by Kondoh et al. [17]

APPENDIX D

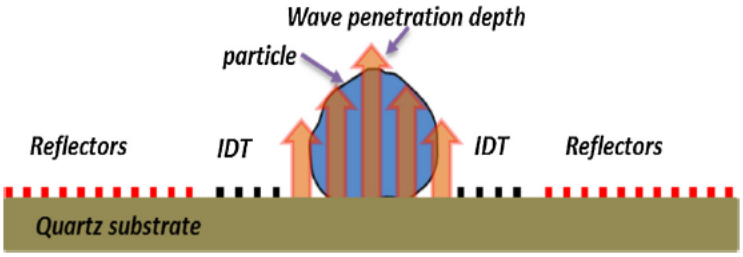

Fig. 2. SAWR mass detection mechanism: cartoon of a surface acoustic wave resonator based sensor for detection of sub-micron sized particles; shown with penetration depths extending into the adjacent medium.

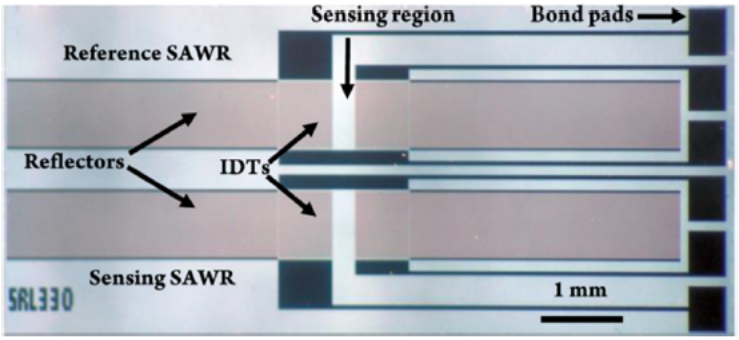

Fig. 3. Dual SAWR sensor photograph: optical micrograph of a 262 MHz Dual Rayleigh SAWR (free) sensor fabricated on x-propagating ST-cut quartz with aluminium electrodes for particle measurements.

to be approximately 1/7th of the SAWR sensor wavelength and is given by:

$$\delta_e = \frac{\lambda_0}{7} \tag{3}$$

The effective mechanical penetration depth δ_m of a SAWR sensor is given by the equation [19]:

$$\delta_m = \sqrt{\frac{\eta}{\pi f_0 \rho}} \tag{4}$$

where η and ρ are the viscosity and density of the adjacent medium respectively, and f_0 is the resonant frequency of the device.

From the above two equations, it is obvious that the penetration depths are inversely proportional to the resonant frequency of the SAWR device and hence, the limit of particle detection using SAWR devices can be tailored to the particle diameters of interest by varying the resonant frequency of the sensor; thus in turn changing the penetration depths. In order to have an effective detection of UFPs, $PM_{2.5}$ and PM_{10}s, sensors with different operating frequencies need to be used having the optimal penetration depths to suite the size of the particles. Fig. 2 shows the pictorial representation of a SAWR based sensor illustrating the mass detection mechanism for detection of particulate matter; shown with penetration depths extending into the adjacent medium.

The change in resonant frequency of a SAWR due to mass loading (neglecting the viscoelastic and electrical effects) has been characterized by the classic Sauerbrey equation, which is given by

$$\Delta f = -\frac{2f_0^2}{\sqrt{\rho_s \mu_s}} \frac{\Delta m}{A} \tag{5}$$

where f_0 is the resonant frequency of the SAW device, A is the active area of the sensor, ρ_s is the substrate density, μ_s is the substrate shear modulus and Δm is the change in mass.

The above formula will be used to calculate mass sensitivities of *free* and *shorted* SAWR devices due to mass loading of different types of particles.

3. Materials and methods

3.1. SAWR particle sensor design

The particle sensors were designed to resonate at a frequency of 262 MHz (optimised for the acoustic penetration depth of ~3 μm). They were made up of aluminium based inter-digital-transducers (IDTs) patterned on top of ST-cut quartz substrate, resulting in generation of Rayleigh waves propagating in the crystallographic x-direction. The SAWR devices were fabricated at SAWTech (Germany) employing 4″ ST-cut quartz wafers, using UV lithography. The IDTs consist of 60.5 finger pairs with 3 μm finger width. The acoustic aperture is 720 μm, while the cavity length is 1764 μm constituting an overall die size of 9.6 mm × 3.6 mm. The IDTs are surrounded by a total of 1200 reflector gratings (600 on each side) with 6 μm pitch, to create a standing wave pattern between the IDTs. ST-cut quartz substrates were chosen in order to eliminate the need for temperature control circuitry due to their high temperature stability.

The use of a reference sensor is a standard method of compensation, hence the SAWRs are employed to operate in a dual sensor configuration, as shown in Fig. 3 [11,20]; where this differential structure provides better signal stability and reduced noise by compensating for atmospheric effects such as change in pressure, temperature, humidity and other common mode variations.

The SAW sensors have been designed to resonate in a feedback loop of a simple radio frequency oscillator circuit at 262 MHz. Fig. 4[A] shows a block diagram representation of the dual sensor and its associated interface circuitry. The characteristics of the SAW resonators are dependent upon the accuracy of the

APPENDIX D

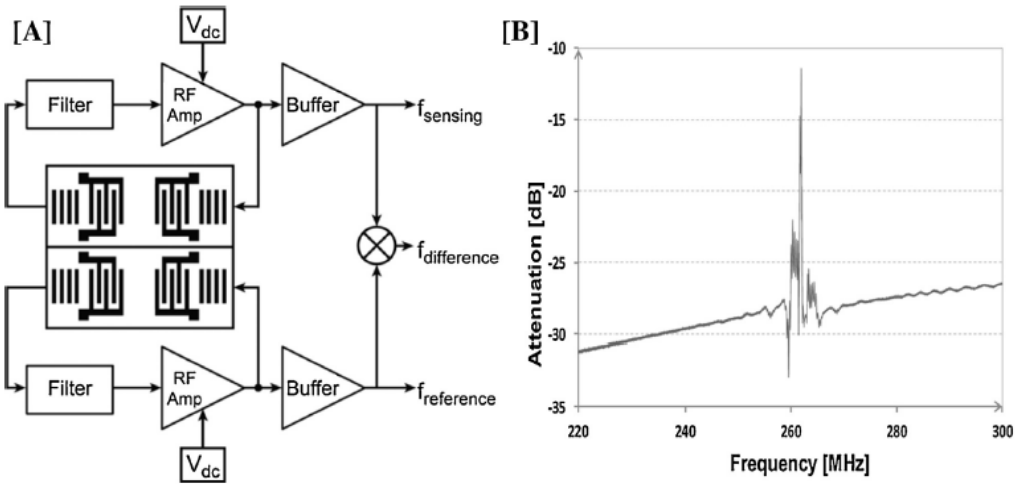

Fig. 4. [A] SAWR Oscillator: Block diagram of Dual SAWR sensor, each SAWRs forming part of separate oscillator circuits. [B] SAWR Transmission characteristics: Attenuation vs. frequency plot of a 262 MHz free SAW resonator.

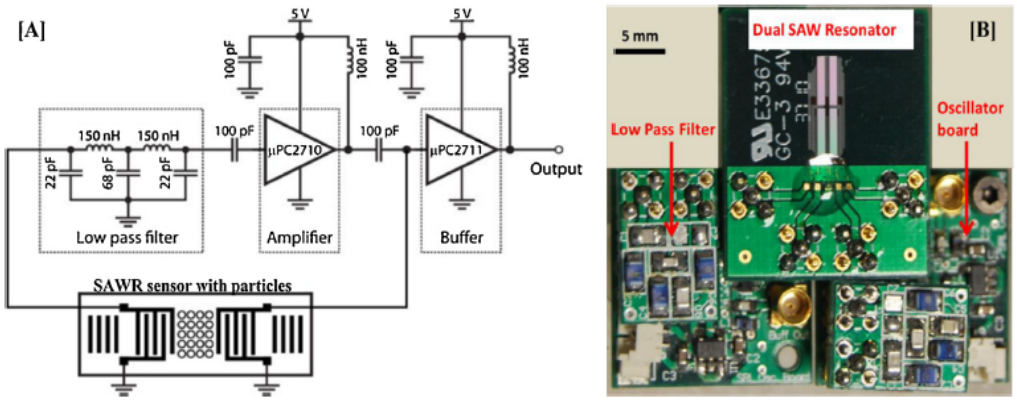

Fig. 5. Particle sensor circuitry and photograph: [A] schematic of SAWR oscillator including the filter, amplifier and buffer stages. [B] Photograph of a dual 262 MHz (free) SAWR oscillator based sensor with surface mount amplifier, filter and buffer circuitry.

fabrication process; consequently, there can be variation between the designed electrical characteristics of frequency, attenuation, phase shift, input impedance and the actual obtained values. The S21 scattering parameter analysis shows that a maximum signal transmission occurs at 261.9 MHz frequency (as presented in Fig. 4[B]) and shows good agreement with the SAWR design parameters. The acoustic wave attenuation at the IDT/substrate interface is very low [11] and the loss is only about 11 dB for the fabricated Rayleigh SAWR devices. As the SAW resonators were designed for both input and output impedances of 50 Ω, the need of additional impedance matching circuits were avoided.

3.2. Oscillator circuit

The choice of an optimal circuit to drive the SAWRs depends on the electrical characteristics of the fabricated resonator devices. In addition to the commonly used attenuation and phase based measurement techniques, SAWRs can be used for frequency based measurements when employed as frequency control elements in an oscillator circuit. Detection of the micron and sub-micron sized particles is characterised by changes in the oscillator frequency of the SAWR oscillator system. A modular feedback based oscillator topology was chosen as this allows the 262 MHz SAWR to operate in a two-port configuration and also offers good stability and robustness at higher frequencies [21].

The oscillator was designed for operation in the 60–800 MHz frequency range, providing a wide-band, high gain capability. Low power RF Amplifiers (μPC2710, NEC) which are matched to 50 Ω internally provide required gain to compensate for loop losses including SAWR insertion loss, mass loading and filter losses. Passive low pass filter boards are used for noise reduction, phase tuning and overtone suppression at higher frequencies. An oscillator board containing the basic oscillator circuit components (i.e. inductors and capacitors) and boards containing the filter and the dual sensor has been implemented using a four layer PCB with separate grounding planes which reduces the radio frequency (RF) cross talk, thereby improving noise sensitivity [22]. An output from each stage, sensing and reference, is provided by the buffer amplifier (μPC2711, NEC), which is sent to the commercial frequency counter interface board (JLM Innovation, Germany) that in turn connects to a computer USB port to perform data acquisition and processing. The two-port SAWR sensor (with reference channel) and the schematic of the associated electronic circuitry for excitation, amplification, buffering and read-out are shown in Fig. 5[A], while the photograph of the entire sensor setup with surface mount amplifier, filter and buffer circuitry is shown in Fig. 5[B].

APPENDIX D

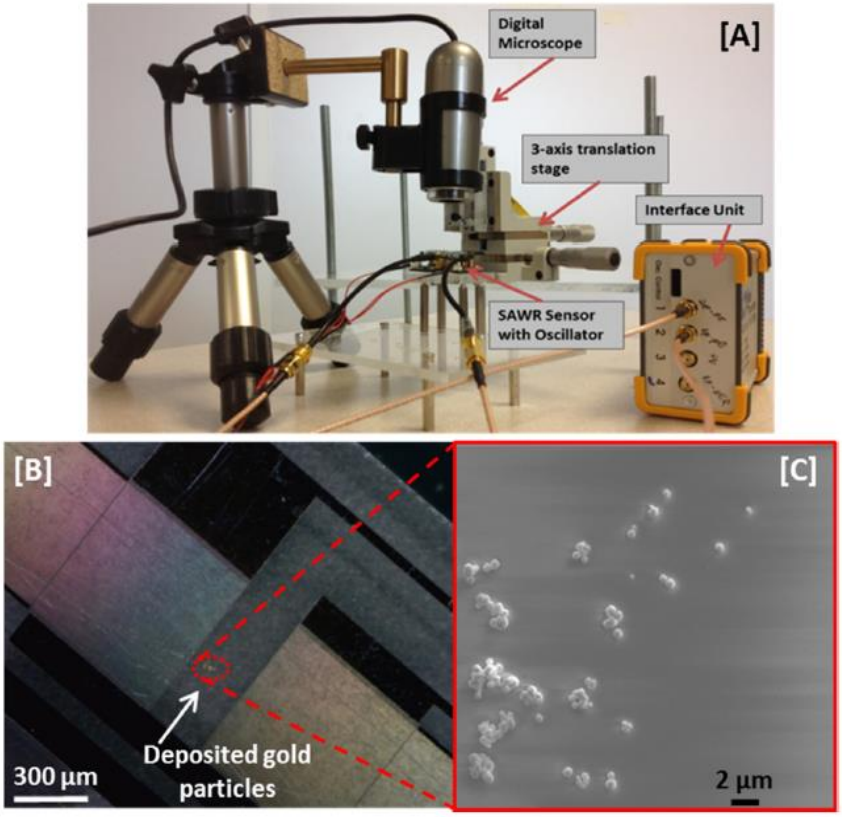

Fig. 6. Particulate matter deposition: [A] experimental setup for particle deposition on SAWR sensor. [B] Photograph showing gold particles (<1 µm diameter) deposited on the sensing area of the free SAWR particle sensor. [C] SEM image of the deposited particles.

4. Experimental procedure

The experimental setup for determining the particle detection capability of the SAWR sensor is shown in Fig. 6[A]. This setup comprises a precision linear translation stage (LS Starrett Co., USA), the SAWR particle sensor with the oscillator circuitry and a digital microscope (Dino-Lite Europe, The Netherlands), in addition to the commercial interface board for PC interfacing. The linear translational stage integrates three micrometres with 12.5 mm travel range along x, y and z axes and is connected to one end of a suspended metallic rod. The other end of this rod is attached to a 25 µm thick gold bondwire. The micro scale movement of the linear stage helps to move the bondwire in all the three axes for the accurate deposition of particles on to the sensor surface.

The bondwire is plunged into a bottle containing micrometre-sized particle powder (with known particle diameter) so that some particles adhere on to it due to the attractive interparticle forces that exist in micron and sub-micron sized particles [23]. With the aid of the linear translation stage, this bondwire (containing the adherent particles) is then gently rubbed onto the sensor surface, allowing the particles to fall on to the sensor surface. The deposition of this particle mass onto the sensor surface produces a shift in frequency at the SAWR oscillator output. The entire deposition process was visually monitored in real time through the digital microscope, to guide the placement of particulate mass on to the sensor surface. In addition, a photomicrograph of the sensor surface with the deposited particles was also captured, which was used to count the number of particles deposited onto the sensing area. Fig. 6[B] shows the photograph of gold particles with diameter of <1 µm deposited on the sensing area of the SAWR particle sensor. The scanning electron microscope images of these gold particles are shown in Fig. 6[C]. The sensor unit is placed inside an environmental chamber to ensure ambient temperature stability, to avoid both air current effects and the deposition of any foreign material on the sensor within the laboratory environment.

5. Results and discussion

In order to evaluate the particle sensing capability of the SAWR sensor and to establish the mass sensitivity of the sensor, different types of micro particles with known diameters were deposited onto the different regions within the total sensor surface area (including the sensor active area, IDT regions, and reflector regions of the SAWR sensor). The different types of controlled artificial aerosols, with an aerodynamic diameter range of approximately 1–30 µm, were used in the characterisation of devices.

The parameters under investigation also included particle number and particle mass, in addition to the frequency shift observed from the SAWR sensor. The frequency response of the sensor is related to the number of particulate matter present on the sensor surface, which in turn depends on the particle diameter. The photograph of the sensor surface (with the deposited particles) was processed using the image processing and analysis software ImageJ 1.46r (National Institutes of Health, USA) in order to define the number of deposited particles; thereby determining the total mass deposited onto the sensor surface. A typical free SAWR sensor response to the deposition of *ca.* 0.21 ng of 0.75 µm-sized gold particles (~50 particles) on to the central active region of the sensor is

APPENDIX D

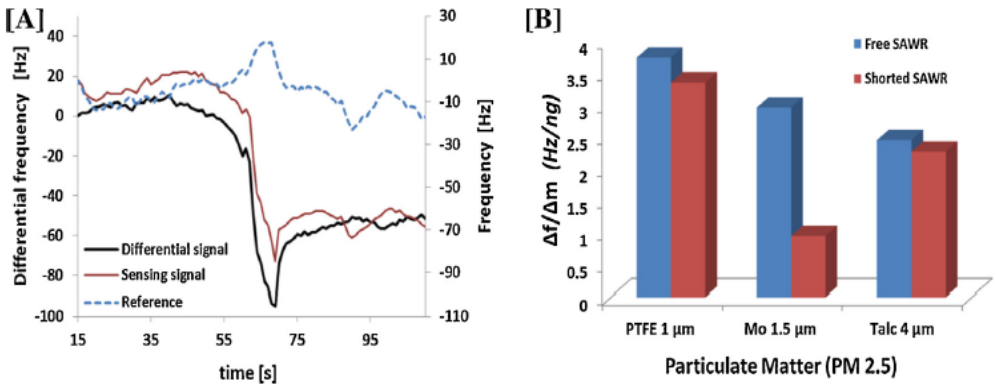

Fig. 7. SAWR response to PM deposition: [A] typical frequency outputs (differential to left; single to right shifted by reference value at t = 0) of a dual free SAWR sensors in response to a deposition of ca. 0.21 ng of 0.75 µm-sized gold particles (~50 particles), on to the central active area. [B] Sensitivity analysis obtained using free SAWR devices and shorted SAWR devices for a variety of particles.

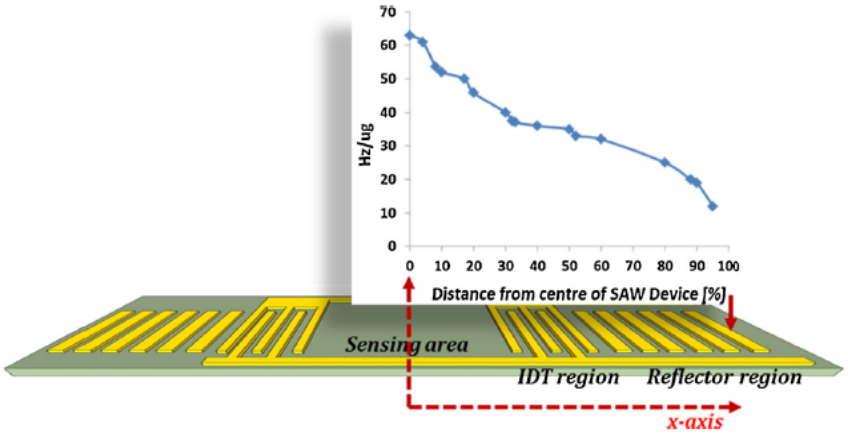

Fig. 8. SAWR sensitivity analysis: relationship between mass sensitivity and the distance from the central active region throughout the length of the free SAWR sensor along the *x*-axis. The dotted line indicates the axis direction starting from the central sensing region (origin) towards the outer end of the reflector.

shown in Fig. 7[A], which produces a differential frequency shift of 60 Hz.

The artificial aerosols used in the investigation included silicon powder, fine sugar crystals, PTFE with two different diameters, fine talcum powder, molybdenum micro particles and gold micro particles with 2 different diameters. As explained in SAWR theory Section 2, the total frequency shift of a SAWR device is dependent on different physical factors including mass density, viscosity, conductivity, and dielectric permittivity of the deposited particles (Eq.(1) and (2)); as a result, the frequency shift can be related to one or all of these dependent variables, depending on whether the active sensing area is *free* or *shorted*. Particles like PTFE (~1 µm diameter), molybdenum (~1.5 µm diameter) and talcum powder (~4 µm diameter) were deposited onto both *free* and *shorted* dual SAWR devices separately and the differential frequency shifts were recorded against time. The mass sensitivities have been calculated each time based on Eq. (5) and Fig. 7[B] shows the mass sensitivities obtained using these *free* and *shorted* SAWR devices for the above-mentioned particles. This figure shows that the frequency shift obtained for a *free* SAWR device is larger, when compared to a *shorted* device. This is because both the mechanical and electrical interactions contribute to the *free* SAWR measurement; while only mechanical effects contribute to the *shorted* SAWR response.

In order to evaluate the particle sensing capability of the different sensor regions, the same type of particle mass (~0.75 µm diameter gold) have been deposited onto different locations (sensor active area, IDT regions, and reflector regions) on separate *free* SAWR devices; and the resulting mass sensitivity of the SAWR sensor was measured. The experimental data obtained show that mass sensitivity diminishes as expected, while moving away from the central sensing area towards the furthest reflector gratings. This sensitivity distribution is shown in Fig. 8. From the figure, it is clear that the mass sensitivity will be at the maximum when the particles are deposited onto the central cavity area (origin of *x*-axis) of the SAWR device, and it will be the minimum when the particles fall onto the far outer end of the reflectors.

In order to establish the minimum sensitivity and the linearity of the sensors, the frequency response of the SAWR sensor was measured to various levels of particle concentration. In random trials, 0.75 µm sized gold particles were deposited on to the active area of a free 262 MHz SAWR device. As seen from Fig. 9, the average SAW mass sensitivity to 0.75 µm sized gold particles is 250–275 Hz/ng and the response of the sensors is almost linear indicating the reliability of the sensor setup and confirming that the sensors operated in the non-saturated regime.

For Rayleigh wave surface acoustic wave devices, acoustic waves travel along the quartz substrate surface in a vertical plane. According to Gronewold [24], surface interactions occur in the close proximity of the SAWR sensor where there is an increased mass sensitivity behaviour. Hence during particle sensing, if the particle

APPENDIX D

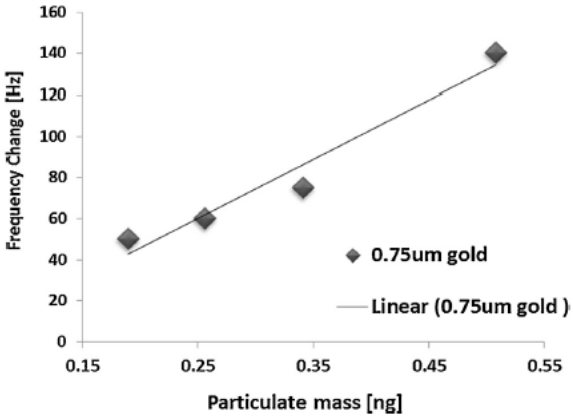

Fig. 9. Mass-dependency of SAWR: linear relationship of mass-dependent differential frequency responses for a dual free SAW resonator to gold particles of diameter 0.75 μm.

diameter is within the penetration depth of the SAWR device, then the entire particle will be probed, resulting in improved sensitivity. However, if the particle size is greater than the penetration depth of the device, then acoustic waves will not penetrate the region outside the penetration depth boundary; resulting in partial sensing of the particles.

Hence, in order to allow acoustic coupling of the entire particle volume, the particle size must be less than the acoustic penetration depth (~3 μm) of the designed SAWRs; otherwise the sensor probes only a part of the particle near its surface. Thus, the SAWR sensitivity $\Delta f/\Delta m$ will be higher (in the range of Hz/ng) for particles having sizes smaller than the penetration depth, whilst the sensitivity will be much smaller (in the range of Hz/μg) for those particles with size range greater than the penetration depth. In order to confirm such device sensitivity/particle size dependency, initial experiments were conducted where the same types of particles with different diameters (one with size < penetration depth and another with size > penetration depth) were in turn deposited onto different *free* SAWR devices and the mass sensitivity was measured in each case. Fig. 10[A] shows the sensitivity (log scale) obtained using two different types of particles (gold and PTFE) having diameters within and outside the penetration depth of the SAWR sensor.

Due to the strong dependency of particle number concentrations on the cut-off characteristic of the acoustic sensor, it is possible to optimize the sensor design for high frequency operation in order to achieve required sensitivity for particles with different diameters.

Mass sensitivities were obtained by depositing different types of particle masses with varying sizes like ~30 μm diameter silicon, gold (sizes of ~0.75 μm and ~20 μm), ~8 μm fine sugar, PTFE (~1 μm and ~15 μm), ~4 μm talcum powder, and ~2 μm molybdenum powder on to different SAWR devices. The relation between SAWR sensitivity $\Delta f/\Delta m$ and different sized particles of one type has been established to be approximately a power law distribution on a log–log plot, where the sensitivity varies as a power of the particle diameter as shown in Fig. 10[B]. The figure also shows the closeness of the experimental data to the power law fitting cure, which is a straight line.

It could be observed that sensors exhibited higher mass sensitivity to particles of sizes smaller than penetration depth (~3 μm) thus confirming that sensors designed to operate at 262 MHz are optimised for $PM_{2.5}$ detection. This in turn confirms that the frequency-dependent sensitivity of the SAW resonators can be tailored to different particle sizes and therefore making them potentially capable of $PM_{10,}$ $PM_{2.5}$ and UFPs detection.

In order to further explore the use of acoustic wave technology for particle, detection experiments have also been carried out using Solidly Mounted Resonator (SMR) based bulk acoustic wave devices operating at a higher frequency of 970 MHz. The results were benchmarked against two other commercial particle detectors (one optical and one QCM), using controlled aerosols and results are reported elsewhere [25,26].

6. Conclusions and further work

We have presented the development of a low cost and robust microsensor for particle detection based upon high frequency SAWR devices. A 262 MHz SAW particle sensor was found to be capable of detecting masses below 1 ng with a high mass sensitivity of 275 Hz/ng. The characterization of these SAWR based devices has been performed in laboratory conditions, in order to explore their sensitivity to particulate matter of different sizes and different composition (e.g. metal, insulator, organic etc.). Furthermore, this has helped to establish the relation between the mass sensitivity and particle size for the effective detection of micron and sub-micron particles. We have established that tailoring of the frequency-dependent sensitivity is possible, which makes SAW resonators promising technology for detection of PM_{10}, $PM_{2.5}$ and UFPs.

Further work is being carried out on the development of a monolithic acoustic wave based particle sensor integrated with CMOS circuitry and designed for 3D-SiP solution whose sensitivity is determined by the operating frequency. The sensor design is being optimized for high frequency applications (~1 GHz) in order to achieve required sensitivity for possible application as a smart, low-cost PM monitor.

References

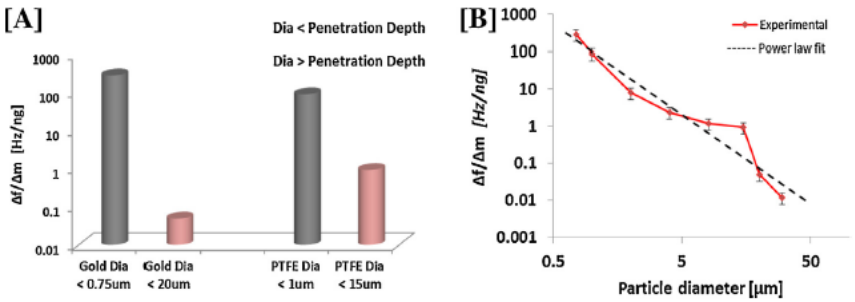

Fig. 10. Effect of particle size on sensitivity: [A] sensitivity study using particles having diameters within and outside the penetration depth of similar types of free SAWR sensor. [B] The relationship between SAWR sensitivity Δf/Δm and particle diameter for one type of particle.

APPENDIX D

[1] United States Environmental Protection Agency, Particulate Matter, 2011 (accessed 17.6.15) http://www.epa.gov/airquality/particlepollution/health.html.
[2] World Health Organisation, Health Effects of Particulate Matter, 2013 http://www.euro.who.int/__data/assets/pdf_file/0006/189051/Health-effects-of-particulate-matter-final-Eng.pdf.
[3] European Commission, Air Quality Standards, 2015 (accessed 9.6.15) http://ec.europa.eu/environment/air/quality/standards.htm.
[4] J.P. Black, MEMS-based System for Particle Exposure Assessment Using Thin-Film Bulk Acoustic Wave Resonators and IR/UV Optical Discrimination, Ph.D. Thesis, University of California at Berkeley, 2006.
[5] S. Steinle, S. Reis, C.E. Sabel, S. Semple, M.M. Twigg, C.F. Braban, et al., Personal exposure monitoring of PM2.5 in indoor and outdoor microenvironments, Sci. Total Environ. 508 (2015) 383–394, http://dx.doi.org/10.1016/j.scitotenv.2014.12.003.
[6] D.C. Green, G.W. Fuller, T. Baker, Development and validation of the volatile correction model for PM_{10}—an empirical method for adjusting TEOM measurements for their loss of volatile particulate matter, Atmos. Environ. 43 (2009) 2132–2141, http://dx.doi.org/10.1016/j.atmosenv.2009.01.024.
[7] H.S. Wasisto, S. Merzsch, A. Stranz, A. Waag, I. Kirsch, E. Uhde, et al., A resonant cantilever sensor for monitoring airborne nanoparticles, in: Transducers, IEEE, Beijing, 2011, pp. 1116–1119, http://dx.doi.org/10.1109/TRANSDUCERS.2011.5969233.
[8] A. Hajjam, J.C. Wilson, A. Rahafrooz, S. Pourkamali, Fabrication and characterization of thermally actuated micromechanical resonators for airborne particle mass sensing: il. Device fabrication and characterization, J. Micromech. Microeng. 20 (2010), http://dx.doi.org/10.1088/0960-1317/20/12/125019.
[9] Air Quality Expert Group, Particulate Matter in the United Kingdom, Defra, London, 2005.
[10] W.D. Bowers, R.L. Chuan, T.M. Duong, A 200 MHz surface acoustic wave resonator mass microbalance, Rev. Sci. Instrum. 62 (1991) 1624–1629, http://dx.doi.org/10.1063/1.1142442.
[11] S. Thomas, Z. Rácz, M. Cole, J.W. Gardner, Dual high-frequency surface acoustic wave resonator for ultrafine particle sensing, in: IEEE Sensors- Proc., Baltimore, MD, 2013, pp. 1–4, http://dx.doi.org/10.1109/ICSENS.2013.6688319.
[12] J. Yang, Z. Rácz, J.W. Gardner, M. Cole, H. Chen, Ratiometric info-chemical communication system based on polymer-coated surface acoustic wave microsensors, Sens. Actuators B 173 (2012) 547–554, http://dx.doi.org/10.1016/j.snb.2012.07.043.
[13] C.K. Campbell, Surface acoustic wave devices for mobile and wireless communications, Academic Press, San Diego, 1998, http://dx.doi.org/10.1016/j.jacr.2012.01.004.
[14] C. Tasaltin, M.A. Ebeoglu, Z.Z. Ozturk, Acoustoelectric effect on the responses of saw sensors coated with electrospun ZnO nanostructured thin film, Sensors 12 (2012) 12006–12015, http://dx.doi.org/10.3390/s120912006.
[15] Z. Rácz, M. Cole, J.W. Gardner, M.F. Chowdhury, W.P. Bula, J.G.E. Gardeniers, et al., Design and implementation of a modular biomimetic infochemical communication system, Int. J. Circuit Theory Appl. 41 (2013) 653–667, http://dx.doi.org/10.1002/cta.1829.
[16] L. Fan, H. Ge, S. Zhang, H. Zhang, J. Zhu, Optimization of sensitivity induced by surface conductivity and sorbed mass in surface acoustic wave gas sensors, Sens. Actuators B 161 (2012) 114–123, http://dx.doi.org/10.1016/j.snb.2011.09.077.
[17] J. Kondoh, Y. Matsui, S. Shiokawa, New biosensor using shear horizontal surface acoustic wave device, Jpn. J. Appl. Phys. 32 (1993) 2376–2379, http://dx.doi.org/10.1143/JJAP.32.2376.
[18] M. Cole, G. Sehra, J.W. Gardner, V.K. Varadan, Development of smart tongue devices for measurement of liquid properties, IEEE Sens. J. 4 (2004) 543–550, http://dx.doi.org/10.1109/JSEN.2004.832855.
[19] E. Gizeli, Study of the sensitivity of the acoustic waveguide sensor, Anal. Chem. 72 (2000) 5967–5972, http://dx.doi.org/10.1021/ac000694u.
[20] M. Hoummady, A. Campitelli, W. Wlodarski, Acoustic wave sensors: design, sensing mechanisms and applications, Smart Mater. Struct. 6 (1997) 647–657, http://dx.doi.org/10.1088/0964-1726/6/6/001.
[21] R.F. Schmitt, J.W. Allen, R. Wright, Rapid design of SAW oscillator electronics for sensor applications, Sens. Actuators B 76 (2001) 80–85, http://dx.doi.org/10.1016/S0925-4005(01)00576-7.
[22] S. Thomas, Z. Rácz, M. Cole, J.W. Gardner, High-frequency one-port Colpitts SAW oscillator for chemical sensing, in: CENICS 2013 Int. Conf. Adv. Circuits, Electron. Micro-Electronics, Barcelona, 2013, pp. 13–17.
[23] A. Castellanos, The relationship between attractive interparticle forces and bulk behaviour in dry and uncharged fine powders, Adv. Phys. 54 (2005), http://dx.doi.org/10.1080/17461390500402657.
[24] T.M.A. Gronewold, Surface acoustic wave sensors in the bioanalytical field: recent trends and challenges, Anal. Chim. Acta. 603 (2007) 119–128, http://dx.doi.org/10.1016/j.aca.2007.09.056.
[25] S. Thomas, F. Villa-Lopez, J. Theunis, J. Peters, M. Cole, J.W. Gardner, Particle system using solidly mounted resonators, IEEE Sens. J. (2015), http://dx.doi.org/10.1109/JSEN.2015.2512303.
[26] F. Helue, G. Rughoobur, S. Thomas, A.J. Flewitt, M. Cole, J.W. Gardner, Design and modelling of solidly-mounted resonators for low-cost particle sensing, Meas. Sci. Technol. 27 (2016), http://dx.doi.org/10.1088/0957-0233/27/2/025101.

Biographies

Sanju Thomas received the B.Eng. degree in electronic engineering from the Visveswaraiah Technological University, Karnataka, India and M.Sc. in Biomedical Engineering from University of Warwick, Coventry, U.K. He is currently working towards the completion of his Ph.D. degree in acoustic biosensors and is also a research staff at the Microsensors and Bioelectronics Laboratory, Warwick University, U.K. His main research interests are Chemical Sensing and Artificial Olfaction, Acoustic wave sensors (SAW/FBAR), analog CMOS/ASIC circuit design, smart sensors and microsystems.

Marina Cole received the B.Sc. degree from the University of Montenegro, Yugoslavia, and the Ph.D. degree from Coventry University, Coventry, U.K. She joined the School of Engineering at Warwick University, Coventry, U.K., in 1996 as a Postdoctoral Research Assistant and she was appointed to a lectureship in electronic engineering in 1998. Her main research interests are integrated silicon-based sensors, SAW-based sensors, analog and mixed-signal ASICs, smart sensors, actuators, and microsystems.

Farah H. Villa-Lopez received the B.Sc. degree (Hons) in mechanical and electrical engineering from Universidad Veracruzana, Xalapa, Mexico in 2012. She is currently working towards her Ph.D. degree at the Microsensors and Bioelectronics Laboratory, University of Warwick, Coventry, UK. Her research interests includes acoustic wave sensors and microsystems.

Julian W. Gardner, BSc PhD DSc FIET SMIEEE FREng, is Professor of Electronic Engineering in the School of Engineering, Warwick University, UK. He is also the Head of Microsensors and Bioelectronics Laboratory and is author or coauthor of over 500 technical papers and patents, as well as six technical books in the area of microsensors and machine olfaction. His research interests include the modelling of silicon microsensors, chemical sensor array devices, biomimetic MEMS devices, and electronic noses.